

High-resolution measurements of temperature
and humidity fields in the atmospheric
boundary layer with scanning rotational
Raman lidar

Dissertation zur Erlangung des Doktorgrades
der Naturwissenschaften (Dr. rer. nat.)

Fakultät Naturwissenschaften
Universität Hohenheim

Institut für Physik und Meteorologie

vorgelegt von Eva Hammann

aus Stuttgart

2016

Dekan bzw. Dekanin: Prof. Dr. rer. nat. Heinz Breer

1. berichtende Person: Prof. Dr. rer. nat. Volker Wulfmeyer

2. berichtende Person: Prof. Dr. Paolo Di Girolamo

Eingereicht am: 18.02.2016

Mündliche Prüfung am: 29.04.2016

Die vorliegende Arbeit wurde am 15.04.2016 von der Fakultät Naturwissenschaften der Universität Hohenheim als „Dissertation zur Erlangung des Doktorgrades der Naturwissenschaften“ angenommen.

Abstract

The Institute of Physics and Meteorology of the University of Hohenheim (UHOH) operates a scanning rotational Raman lidar (RRL) for high-resolution temperature and water vapor measurements. The measurement performance of the RRL was improved in several aspects. The statistical error of temperature measurements was reduced by up to 70% through optimization of the filter passbands for various solar background conditions. The optimization method, based on detailed simulations, was written for one specific wavelength and was not applicable to other Raman lidar systems. Therefore the simulation results were parametrized in respect to temperature and background level and expressed in units of wavenumbers. A new interference filter transmitting rotational Raman lines near the excitation wavelength was installed, resulting in a higher transmission and eliminating possible leakage signal. A detection channel for the vibrational Raman line of water vapor was added for the retrieval of water vapor mixing ratios during day-and nighttime. More than 300 hours of temperature and more than 200 hours of water vapor measurements were performed and the acquired profiles used in several publications. Atmospheric variance and higher order moment profiles of the daytime atmospheric boundary layer were derived. In the following the improvements are described in more detail.

The measurement performance was increased with new interference filters and an optimized alignment of the filter passbands. For this purpose the wavelength of the Nd:YAG laser (GCR290-50, Newport Spectra Physics) was determined as 354.83 nm and the frequency stability over a longer time period investigated. The absolute wavelength changed only a few femtometers during 4 hours of measurement, probably due to thermal issues. This is sufficient for application in a rotational Raman lidar. The simulations concerning the optimum shifts of the filter passband were performed independently of wavelength. This is possible due to the fact that the shift of the Raman lines with respect to energy and frequency is the same

for all wavelengths. The impact of temperature, background count rate, and shape of filter transmission curve on the optimum shifts was studied in detail. Temperature and background were identified as the essential parameters and equations for the shifts were determined with respect to these variables [52]. By application of these equations, the optimum shifts can be derived for other lidars without repetition of the simulation. The accuracy of the derived passbands shifts of the parametrization in respect to the simulation is better than 2% for all studied temperatures.

The two combined interference filters, which were used to select the first transmitted wavelength range, were exchanged with a new single filter with higher transmission and a better blocking capability of the excitation wavelength. Thus, additional signal due to leakage of elastic backscatter in this channel is completely avoided.

With the implementation of one additional detection channel, the water vapor mixing ratio can be determined. The intensity of the vibrational Raman line of water vapor was measured and set in relation to a molecular reference signal. A temperature independent combination of the two rotational Raman line measurements was applied as reference signal. If an excitation wavelength of 354.83 nm is used, the water vapor lines are found around 407.7 nm. Calibration was performed similar to the temperature calibration by comparison with a radiosonde profile. A correction concerning the different extinction of the two wavelengths was applied. The resulting water vapor mixing ratio can be used to derive relative and absolute humidity if a temperature profile is available. The water vapor channel was implemented successfully and the corresponding measurement error was derived.

Measurements were performed vertically in most cases, but a beam steering unit makes measurements in other directions possible. The whole system is mounted on a mobile platform, which can be transported easily to measurement sites. The UHOH RRL participated in three campaigns with more than 300 hours of acquired data. During the campaigns, the water vapor measurements as well as the according to solar background tuned filter positions were characterized [53]. The interruption of the measurement due to the change of positions was around 5 minutes, and is justified by the improvement.

Profiles of turbulence characteristics were determined from the vertical high resolution measurements. With an analysis of the auto-covariance function, instrumental and atmospheric variations were separated. In a fully developed convective boundary layer, turbulent eddies can be observed. They have a size between 50 and 100 seconds, and the temporal resolution of the measurements has to be significantly higher. This is the case with a temporal resolution of 10 s. One of the products are atmospheric variance profiles, which could be derived the first time from temperature lidar data [17]. Other products are the higher order moments, which describe the overall distribution of the variance in detail. A complete characterization also includes the variance profiles of water vapor and horizontal wind. Former were derived from the water vapor mixing ratio profiles measured by the UHOH RRL. In comparison with the simultaneous acquired temperature variance profiles, data from the 19 May 2013 in the time periods from 13:00 to 13:40 UTC and from 15:00 to 16:00 UTC was investigated. The highest variance values were expected at the top of the boundary layer. The mean altitude of the boundary layer is called z_i . In case of temperature, variances of $0.23 \pm 0.03 \text{ K}^2$ and $1.23 \pm 0.71 \text{ K}^2$, respectively, were found at z_i . For the water vapor mixing ratio, the derived values were $0.94 \pm 0.05 (\text{g/kg})^2$ and $1.41 \pm 0.22 (\text{g/kg})^2$, respectively. The third order moment of temperature was slightly negative in the boundary layer with positive values just below the boundary layer top and negative above. The opposite behavior could be observed for water vapor third order moments. The fourth-order moments were positive in the observed altitudes. From scanning measurements near the surface, vertical temperature profiles and the potential temperature gradient were derived.

The derived turbulence characteristics were used as parameters in equations for weather modeling [122]. Sensible heat fluxes were derived from averaged profiles. Temperature profiles were assimilated into the WRF model to study the impact on the boundary layer in the model.

Zusammenfassung

Das Institut für Physik und Meteorologie der Universität Hohenheim (UHOH) betreibt ein scannendes Rotations-Raman-Lidar (RRL) für hochaufgelöste Messungen von Temperatur- und Wasserdampf-feldern. Die Leistungsfähigkeit des Systems bezüglich der Genauigkeit und statistischer Messungenauigkeit konnte erheblich verbessert werden. Der statistische Messfehler wurde bis zu 70% reduziert durch die Abstimmung der detektierten Wellenlängenbereiche auf den Tageslichthintergrund. Die Optimierung basiert auf einer detaillierten Simulation der Rotations-Raman-Linien und der Filterkurven. Die Berechnungen wurden zuerst wellenlängenabhängig durchgeführt und waren daher nicht direkt übertragbar auf andere Ramanlidarsysteme. Deshalb wurden die Ergebnisse der Simulation parametrisiert bezüglich der Temperatur und dem Signalhintergrund und in Wellenzahleinheiten angegeben. Ein neuer Interferenzfilter für den Wellenlängenbereich nahe der Anregungswellenlänge wurde eingebaut. Dieser besitzt eine höhere Maximaltransmission und eine erhöhte optische Dichte für die Anregungswellenlänge. Damit kann ein zusätzliches Fehlersignal in Bereichen mit hoher Rückstreuung vermieden werden. Ein Empfangskanal für das Vibrations-Raman-Signal von Wasserdampf ermöglicht die Messung des Wasserdampfmischungsverhältnisses. Mehr als 300 Stunden Temperaturmessungen und 200 Stunden Wasserdampfmessungen wurden durchgeführt und waren die Basis für mehrere Publikationen. Messdaten mit hoher zeitlicher Auflösung wurden verwendet um Varianzprofile und Profile der höheren Momente in der planetaren Grenzschicht zu ermitteln. Im Folgenden werden die vorgenommenen Verbesserungen im Detail beschrieben. Die Leistungsfähigkeit des Systems konnte durch neue Interferenzfilter und eine optimierte Einstellung der transmittierten Wellenlängenbereiche verbessert werden. Dazu wurde die Wellenlänge des frequenzstabilisierten Nd:YAG-Lasers (GCR290-50 von Newport Spectra Physics) gemessen (354.83 nm). Zusätzlich wurde die Langzeitstabilität untersucht. Es zeigte sich, dass die Wellenlänge nur wenige Femtometer über einen Zeitraum von 4 Stunden variiert. Dies ist für die Anwendung in Ramanlidarmessungen ausreichend. Die Simula-

tionen zur Bestimmung der optimalen Wellenlängenbereiche wurde für beliebige Wellenlängen erweitert. Dies ist möglich, da die Verschiebung der Ramanlinien bezüglich der Energie und damit der Frequenz wellenlängenunabhängig sind. Der Einfluss von Temperatur, Messhintergrund und Form der Transmissionskurve des Filters wurde im Detail untersucht. Temperatur und Hintergrund wurden als die entscheidenden Faktoren identifiziert und Gleichungen ermittelt, die von diesen Parametern abhängen [52]. Mit den Gleichungen lassen sich die optimalen Wellenlängenbereiche für andere Systeme bestimmen, ohne die Simulation im Detail zu wiederholen. Die Abweichung der Näherung von der Simulation bezüglich der Verschiebung liegt unter 2%.

Zudem wurde die bestehende Filterkombination zur Selektion des ersten Wellenlängenbereiches durch einen neuwertigen Interferenzfilter mit höherer Transmission und besserer Blockung der Anregungswellenlänge ersetzt. Damit kann ein Fehlersignal durch elastische Rückstreuung in diesem Kanal ausgeschlossen werden.

Neben den Temperatur konnte durch den Einbau eines weiteren Detektionskanales auch das Wasserdampfmischungsverhältnis ermittelt werden. Dabei wurde die Intensität der Vibrations-Ramanlinie von Wasserdampf gemessen und in Relation zu einem molekularen Referenzsignal gesetzt. Das Referenzsignal bestand aus einer temperaturunabhängigen Kombination aus den beiden Rotations-Raman-Signalen. Die Wasserdampflinien können bei einer Anregungswellenlänge von 354.83 nm bei 407.7 nm gefunden werden. Vergleichbar mit den Temperaturmessungen wurde das Verhältnis der Signale mit einem Wasserdampfprofil kalibriert. Es wurde eine Korrektur für die unterschiedliche Extinktion der beiden Wellenlängen angewendet. Der Wasserdampfkanal konnte erfolgreich betrieben werden und der statistische Fehler bestimmt werden.

Zusätzlich zu den Messungen von Vertikalprofilen konnten mit zwei beweglichen Spiegeln Profile in andere Richtungen aufgenommen werden. Das komplette System ist in einem mobilen Messfahrzeug eingebaut. Es wurden drei Kampagnen durchgeführt, mit mehr als 300 Stunden gemessener Daten. Es wurden sowohl die Wasserdampfmessungen als auch die hintergrundabhängigen Filterpositionen getestet und charakterisiert [53]. Die dazu nötige Unterbrechung der Messungen um 5 Minuten war durch die erreichte Reduktion des

Fehlers gerechtfertigt.

Aus den hochaufgelösten Messdaten konnten Profile von wichtigen Turbulenzeigenschaften ermittelt werden. Mit Autokovarianzrechnungen wurden atmosphärische und instrumentelle Schwankungen separiert. In einer vollständig entwickelten konvektiven Grenzschicht sind Turbulenzen und Wirbel zu beobachten. Da diese im Mittel zwischen 50 und 100 Sekunden bestehen, muss die zeitliche Auflösung der Messungen wesentlich höher sein. Das ist mit 10 Sekunden Auflösung erfüllt. Ein Resultat waren Varianzprofile, welche mit diesem Lidarsystem zum ersten Mal aus Temperaturlidardaten bestimmt werden konnten [17]. Weitere Produkte waren Profile der höheren Momente, welche die Form der Varianz im Detail beschreiben. Um die Grenzschicht vollständig zu charakterisieren, benötigt man auch Varianzprofile von Wasserdampf und Wind. Erstere konnten ebenfalls aus den Messungen des UHOH RRLs gewonnen werden. Im Vergleich mit den simultan gemessenen Temperaturprofilen wurden Daten vom 19. Mai 2013 aus dem Zeitraum 13:00 bis 13:40 UTC und dem Zeitraum 15:00 bis 16:00 UTC untersucht. Die höchsten Varianzwerte werden auf Höhe der Grenzschichtoberkante z_i erwartet. Für die Temperaturvarianz konnten Werte von $0.23 \pm 0.03 \text{ K}^2$ und $1.23 \pm 0.71 \text{ K}^2$ ermittelt werden. Bei der Wasserdampfvarianz wurden die Werte $0.94 \pm 0.05 \text{ (g/kg)}^2$ und $1.41 \pm 0.22 \text{ (g/kg)}^2$ gemessen. Das Moment dritter Ordnung der Temperatur zeigte leicht negative Werte in der Grenzschicht mit positiven Werten direkt unterhalb der Grenzschichtoberkante und negativen Werten oberhalb der Grenzschicht. Das entgegengesetzte Verhalten konnte für Wasserdampf beobachtet werden. Das Moment vierter Ordnung war für beide Messgrößen positiv in der Grenzschicht. Aus Messungen in der Atmosphärenschicht nahe der Oberfläche mit Hilfe des Scanners wurden Vertikalprofile nahe der Oberfläche erstellt. Ein weiterer Schritt war es, die ermittelten Turbulenzeigenschaften als Eingangsparameter in Gleichungen für Wettermodellierungen zu verwenden [122]. Der sensible Wärmefluss wurde aus gemittelten Profilen bestimmt. Temperaturprofile wurden in das WRF-Modell assimiliert und der Einfluß auf die Grenzschicht ermittelt.

Contents

1	Importance of temperature and water vapor in atmospheric studies	1
2	Temperature and water vapor measurements with lidar	6
2.1	Lidar	6
2.2	Temperature measurements with lidar	11
2.3	Rotational Raman lidar (RRL)	12
2.4	Hammann and Behrendt, 2015, Optics Express . . .	15
2.5	Vibrational Raman technique for water vapor measurements	32
3	The rotational Raman lidar system of University of Hohenheim	34
3.1	Laser performance	35
3.2	New design of the polychromator	36
3.2.1	Water vapor channel	37
3.2.2	Design of a new interference filter for the lowJ channel	38
3.3	Resulting system	40
4	Temperature and water vapor mixing ratio measurements	42
4.1	Vertical temperature measurements	42
4.2	Hammann et al., 2015, Atmospheric Chemistry and Physics	44
4.3	Blocking capabilities of the new interference filter . .	60

4.4	Water vapor measurements	60
5	Planetary boundary layer and turbulence theory	64
5.1	Behrendt et al., 2015, Atmospheric Chemistry and Physics	66
5.2	Noise error of water vapor measurements	83
5.3	Higher order moments of temperature and water va- por mixing ratio	83
5.4	Wulfmeyer et al., 2016, Journal of Atmospheric Sciences	90
6	Measurement of surface layer temperature gradients	117
6.1	Surface flux theory	117
6.2	Low level scans	119
7	Discussions	122
7.1	Comparison between the performance in the years 2007 and 2014	122
7.2	Outline of possible further technical improvements .	124
7.2.1	Increase of laser power	124
7.2.2	Detection	126
7.2.3	Additional wavelengths	127
8	Summary and outlook	128
	List of Figures	148
	List of Tables	152
	Appendices	153
A	Updated programs and data acquisition	154
A.1	Choice of discriminator level	154
A.2	Data Acquisition and beam steering	156
A.3	Program to glue analog and photon-counting data .	156
A.4	Retrieval of water vapor mixing ratio	158

B Measurement plans	159
B.1 HOPE, April and May 2013	159
B.2 Hohenheim, September and October 2013	162
B.3 SABLE, August 2014	163

List of Abbreviations

AOI	Angle of Incidence
BASIL	University of Basilicata Raman lidar system
BSU	Beam Steering Unit
CAPE	Convection Available Potential Energy
CIN	Convection Inhibition
COPS	Convective and Orographically-induced Precipitation Study
DIAL	Differential Absorption Lidar
EC	Eddy Covariance
FOM	Fourth-Order Moment
FTIR	Fourier transform infrared spectroscopy
FWHM	Full Width at Half Maximum
HD(CP) ²	High Definition of Clouds and Precipitation for advancing Climate Prediction
HOPE	HD(CP) ² Observation Prototype Experiment
HRS�	High Resolution Lidar
IASI	Infrared Atmospheric Sounding Interferometer
ICON	Icosahedral non-hydrostatic (general circulation model), DWD
IDL	Interactive Data Language
IF	Interference Filter
IL	Integral Scale
IOP	Intensive Observation Period
KIT	Karlsruhe Institute of Technology
LES	Large Eddy simulation
MR	(water vapor) Mixing ratio
OD	Optical Density
PBL	Planetary Boundary Layer
PRINCE	PRediction, Identification and trackiNg of Convective cElls
lowJ	first rotational Raman channel, also RR1
highJ	second rotational Raman channel, also RR2
RRL	Rotational Raman Lidar
SABLE	Surface-Atmospheric Boundary Layer Exchange
SOP	Special Observation Period
SRL	Scanning Raman Lidar (NASA/GSFC)

TOM	Third Order Moment
<i>Tr</i>	Transmission
u_*	friction velocity
UHOH	University of Hohenheim
UTC	Universal Standard Time

Chapter 1 Importance of temperature and water vapor in atmospheric studies

The Earth's atmosphere is a complex system with highly fluctuating variables like temperature, wind velocity or trace gas concentrations, e.g. of water vapor or carbon dioxide. There are processes which cover the whole Earth (large wind systems) and processes in length scales of a few meters and less (turbulence). On time scale, processes range from several thousands of years (climatic changes, ice ages) to seconds and less (turbulence).

Temperature is one of the main variables describing the state of the atmosphere. The temperature profile determines the division of the atmosphere into troposphere, stratosphere, mesosphere and thermosphere, since the boundaries between these divisions are marked by a change of the sign of the vertical temperature gradient. The main energy source of the atmosphere is the sun. Incoming energy is absorbed by the surface and atmospheric constituents like ozone. From the Earth's surface long wave radiation is emitted and is partly absorbed by water vapor and other trace gases (greenhouse effect). Along with the transport of water vapor, temperature changes are a sign for energy fluxes. In case of energy transport through warm air masses, one speaks of sensible heat flux whereas in case of energy transport through water vapor one speaks of latent heat flux. Temperature differences drive many processes throughout the whole atmosphere and are an indicator of thermodynamic instability.

Temperature measurements are necessary for different purposes like weather and climate monitoring, verification of LES models or the investigation of boundary layer schemes. The requirements for ac-

curacy and resolution depend strongly on the purpose [121]. Of special interest are profiles. Therefore the observation of temperatures should be done not only in-situ but also by remote sensing instrumentation to cover larger altitude ranges with a sufficient repetition rate and accuracy [49, 121] for boundary layer studies and as input data for weather forecast models.

An in-situ method to acquire profiles are radio soundings, but they are launched routinely only twice a day by the national weather services and the global coverage is poor. Additionally the ascent rate of the radio sounding balloon is approximately 5 m/s. The result is not an instantaneous profile, but higher altitudes are sampled significantly later than lower altitudes. It is therefore not representative if the measured volume contains fast changing processes like eddies in the boundary layer or fast developing clouds. Temperature can also be retrieved by microwave radiometers (MWR) and infrared (IR) spectrometers, which measure the thermal emission of all molecules in the line of sight. In the retrieval the temperature profile is based on a first guess. Only the relative intensity of wavelengths gives an indication of the altitude range and therefore the vertical resolution is coarse (100 m to 1 km above 1 km altitude [22, 121]). Additionally the whole retrieval is based on cost-functions, whose minima are supposed to represent the best solution [70]. Such profiles are not useful for boundary layer studies as they cannot resolve temperature gradients or inversions in detail. There are satellite based measurements like by IASI (FTIR), but they also do not reach the resolution near the surface required for boundary layer studies. Other disadvantages are that their footprint can cover several kilometers and clouds inhibit measurements at the surface. In consequence, there is a data gap for high-resolution temperature profiles in the atmospheric boundary layer.

The same issues apply to water vapor measurements. Water vapor is the most important greenhouse gas [63] and is temporally and spatially highly variable. Most of the water vapor content is located in the boundary layer, which is in direct exchange with the surface and the vegetation. Next to the absolute humidity content also the relative humidity is of importance. The relative humidity is temperature dependent. If a relative humidity of 100% is reached and condensation nuclei are available, water vapor condensates at

the condensation nuclei and clouds are developing. As condensation releases energy, ascending water vapor is a significant energy transport mechanism. Especially the development of thunderstorms is often accompanied with large latent heat fluxes. Atmospheric variables describing the convection and the stored energy are CAPE (Convective Available Potential Energy) and CIN (Convection Inhibition). High CAPE values without high CIN are indicators for a high probability of convective thunderstorms. Passive instruments for water vapor profiles are microwave radiometer or GPS, but they rely on complex retrieval algorithms and need primary assumptions. One solution to reduce the lack of atmospheric data is the lidar technology. Lidar is an abbreviation for 'LIght Detection And Ranging'. Lidar can provide profiles of the troposphere in high temporal resolutions between seconds to hours. Like described in the following chapter, lidar is capable of measuring many important atmospheric variables. As an active remote sensing instrument lidar delivers directly range-resolved profiles without the need of assumptions and best-guess retrievals like the described passive instruments. From the lidar signals even the noise error of a measurement can be estimated. Unfortunately, there is no wide spread lidar network yet except for ceilometers (detection of cloud base height e.g. for air traffic) and a few continental aerosol lidar networks (e.g. EARLINET [19], ALINET [66]). Wind farms and airports apply Doppler lidar for wind monitoring. Variables like temperature or water vapor are not yet measured routinely by lidar. Fully automatic lidars which provide the data on a operational base would be a big step on the way to a more reliable forecast of weather, extreme events and the evaluation of climate models.

Another aspect of lidar measurements is to provide high resolution data sets for LES model improvement. High resolution data sets are needed to initialize the model and furthermore to verify the results after a certain run time. Due to the lack of operational systems, such data sets are mostly acquired during extensive observation campaigns or at measurements sites like Lindenberg (Germany)[84], Cabauw (the Netherlands)[8] or the ARM sites in Oklahoma (USA) and Darwin (Australia)[93, 100]. Data is also used to improve the understanding of short time scale processes of the atmospheric boundary layer and for other purposes.

A main research focus of the Institute of Physics and Meteorology of the University of Hohenheim (UHOH) is Land-Atmosphere feedback, which takes place in the planetary boundary layer. Of interest are fluxes and turbulent features in this layer and especially the surface layer. While for the measurement of surface fluxes it is necessary to measure near the surface, a temporal resolution of several seconds and a vertical resolution of around 100 meter is needed for the derivation of turbulence characteristics. The Institute of Physics and Meteorology developed therefore a mobile scanning rotational Raman lidar (RRL) to measure three-dimensional temperature fields [81, 82]. It was first applied in the Convective and Orographically induced Precipitation Study (COPS) campaign. With three detection channels, the system could provide temperature profiles and profiles of the backscatter and the extinction coefficient in high temporal resolution. The system was optimized for daytime measurements in the boundary layer, which are challenging with Raman lidar due to the low signal to noise ratio. The scanning ability is especially useful to measure temperature fields near the surface.

Purpose of this doctoral thesis was the system improvement including a reduction of the statistical error to decrease the necessary temporal averaging. This goal could be reached by implementation of a new interference filter and an optimization of the filter passbands in relation to the signal background. I implemented a switch to use different filter passbands for daytime and nighttime solar background. The optimization was based on detailed simulations, which I generalized for arbitrary laser wavelengths (see section 2.4). After the addition of a detection channel for the vibrational Raman signal of water vapor, the water vapor mixing ratio is measured simultaneous to temperature profiles [53]. Additional to vertical profiles of temperature and water vapor for atmosphere characterization, there is a possibility to measure parallel to the surface by directing the laser beam horizontally. Scans can be performed to measure two or three-dimensional fields of temperature or moisture.

The lidar participated with the new setup in three measurement campaigns, collecting more than 300 hours of atmospheric profiles. These data were evaluated and used for several publications [53, 17, 52, 122]. Furthermore, high resolution measurements of tempera-

ture and water vapor mixing ratio were used to derive simultaneous profiles of the atmospheric variance and the higher order moments (section 5.3). Averaged temperature profiles were assimilated in WRF and the impact on profiles investigated [5, 4]. Scanning measurements near the surface delivered for the first time temperature surface layer gradients measured by lidar. These data sets can be useful for the derivation of surface layer sensible heat fluxes.

The thesis summarizes knowledge of lidar technology and shows in detail how temperature is measured with the rotational Raman technique. Furthermore, the optimization of the UHOH Raman lidar and the performance in several measurement campaigns is described. The recently added vibrational Raman water vapor channel is characterized. A summary of the results and a classification of the obtained improvements can be found in chapter 8.

Chapter 2 Temperature and water vapor measurements with lidar

2.1 Lidar

Lidar is an abbreviation for “LIght Detection And Ranging” and is the optical equivalent to radar [37]. The basic principle is to send a short laser pulse (few nanoseconds) into the test volume and detect the backscattered signal in dependency of the time of flight to the emitted laser pulse. The time of flight is in the following transferred into distance to the scattering volume. Scatterers are molecules and particles; the probability of a scattering event depends on the laser wavelength since it determines if the scatter process is in the Mie or Rayleigh scatter regime. Both are results of the same scattering equation, but simplifications for certain assumptions like the size of the scatterer. Mie scattering takes place when the scattering object has a similar size to the excitation wavelength λ_0 (particles in case of wavelengths in the visible region); this process is independent on the wavelength λ . If the object is much smaller than λ_0 (e.g. molecules), it is in the regime of Rayleigh scattering. There the scattering cross section is dependent on λ^{-4} . The scatter process can change the state of the scatterer and also the wavelength of the scattered photon. Prior and after the scattering the photons can be absorbed and different lidar types are able to measure the effects of these processes. In the subsequent data analysis, properties of the observed atmospheric volume are derived.

The lidar equation describes the detected fraction $P_{\lambda_0}(z)$ of the outgoing laser power which is backscattered in a scattering volume

in the distance z , e.g. [64, 87]:

$$P_{\lambda_0}(z) = \eta_{\lambda_0} P_{\lambda_0} \frac{c\Delta t}{2} \frac{A_T}{z^2} O(z) \beta_{\lambda_0}(z) \exp \left[-2 \int_0^z \alpha_{\lambda_0}(z') dz' \right]. \quad (2.1)$$

In this equation, P_{λ_0} is the power of a laser pulse, Δt the pulse length, $O(z)$ the overlap function between beam and telescope field-of-view [73], A_T the telescope area, η_{λ_0} the system efficiency for λ_0 , β_{λ_0} the backscatter coefficient, and α_{λ_0} the extinction coefficient for both ways. This equation is valid for a lidar which detects the elastic backscattered light (λ_0 is the wavelength of the outgoing and the detected signal). For lidar types with an interest in inelastic backscattered signal the equation has to be modified. It has to be taken into account that on the way back to the receiver, a photon has another wavelength, here λ_R . In this case the backscatter coefficient β_{λ_R} also includes the effective differential Raman scatter cross section $\frac{d\sigma}{d\Omega}$. The cross section contains the temperature dependency, the abundance of the scattering molecule and other intramolecular parameters (compare [52]). Then the equation reads

$$P_{\lambda_R}(z) = \eta_{\lambda_R} P_{\lambda_0} \frac{c\Delta t}{2} \frac{A_T}{z^2} O(z) \beta_{\lambda_R}(z) \exp \left[- \int_0^z (\alpha_{\lambda_0}(z') + \alpha_{\lambda_R}(z')) dz' \right]. \quad (2.2)$$

In most lidar types the ratio of two detected signals is used with the advantage, that many factors in Eq. 2.1 like P_{λ_0} cancel. In case of close-by wavelengths even the system efficiency and the extinction coefficients may be equal and only the different backscatter coefficient or absorption coefficient remains.

The simplest lidar type is the one which is used to measure distances like applied in construction work and velocity measurements in traffic controls. Especially in construction the time resolution in the detection has to be quite high, as distances in the range of millimeters to centimeters are of interest. With the speed of light this results in 150 GHz rates for a spatial resolution of 1 mm. There are ceilometers which measure the distance to the cloud base or bases, if the lowest cloud layer is not extinguishing the whole signal. In science other variables like atmospheric temperature or the surface

properties of buildings [83] are derived. Several lidar types focus on the effects of the atmospheric components on the backscattered signal e.g. absorption, inelastic backscattering, change of polarization or fluorescence [87, 88]. These observations are linked to certain properties of the observed volume. The most common lidar types are listed here.

- **Aerosol backscatter lidar**

Most lidar types include the detection of the elastically backscattered signal, but there are also pure backscatter lidars. Backscatter lidars are the main tool to study aerosol particle properties. Most of them apply more than one wavelength [76, 7], as especially the difference of scattering cross section for different wavelengths has a high information content concerning the size of the particles. The polarization of the scattered photon differs in case of symmetrical and asymmetrical particles. Additionally the vibrational Raman scattering of nitrogen is detected for the determination of backscatter and extinction coefficients, as it is a pure molecular signal. Sophisticated aerosol identification schemes are in development to distinguish ice particles from water droplets or biomass burning [7, 44]. Other classes would be dust, marine particles, volcanic ash or so called aged dust transported over long distances. If the back trajectories of air flows are known, the origin of such layers can be determined [44].

- **Differential Absorption Lidar (DIAL)**

DIAL applies two or more adjacent wavelengths, with one on an absorption line of the measured variable and one off this line. The lidar equation only differs in the absorption term and the number density of atmospheric components is retrieved with the knowledge of the specific absorption cross section. The absorption cross section, which depends on temperature and pressure, has to be known exactly [85]. In most cases a standard atmosphere based on ground measurements is sufficient. If the mixing ratio is known (like for nitrogen), temperature or pressure can theoretically be measured [87]. There

were experiments to measure temperature [97, 120], but the performance was not satisfactory. Main measurement variables are trace gases like water vapor [120], CO₂ [47], ozone [86] and methane [110]. By a set of three wavelengths even two trace gases can be measured simultaneously [46].

- **Doppler lidar**

The Doppler Effect is also observable at scattered photons, if the scattering object is moving. A frequency shift proportional to the velocity of the scattering object is observed. Doppler lidars measure this shift using particles or molecules as tracers. The product is the line-of-sight wind velocity. The coherent Doppler lidar technique is dependent on particle backscatter. Therefore their measurement range is limited to the planetary boundary and sometimes low level clouds just above the boundary layer. Incoherent Doppler lidar is based on molecule scattering. It can therefore provide measurements through the whole atmosphere, but the resolution is lower than with the coherent technique due to the weaker backscatter [69]. In vertical pointing mode, Doppler lidar are used to observe up and down drafts in a convective boundary layer. Another application is the observation of horizontal structures [98] or the wake of air planes [65]. In recent years, Doppler lidars have been applied in the determination of suitable sites for wind turbines and the consecutive monitoring of wind velocities on already developed sites.

Doppler Lidar is combined with fluorescence lidar for detection of the velocity of metal atoms in the mesosphere [9].

- **Fluorescence lidar**

Fluorescence lidar or resonance scattering lidar is used to identify layers of metals in the high stratosphere/mesosphere region by transmission of a laser wavelength, which is absorbed by sodium or iron and subsequent detection of the amount of fluorescence. This gives the observer the position of the layer and concentration of the metal atoms within. Additionally, it is possible to derive temperature and wind velocity from

this data [9] with the integration technique and by analysis of the fluorescence line shape [48]. It is therefore the only lidar technique to measure temperature in the mesosphere. Fluorescence lidar is also applied in identification of vegetation state [96] and in modern archeology [109].

- **High Spectral Resolution Lidar (HSRL)**

HSRL resolves the shape of the Brillouin-line surrounding the Cabannes line [35, 50, 51]. From the shape the temperature and pressure is derived. Essential are a frequency stabilized light source and a detection with a high spectral resolution. Very narrow-band filters or interferometer allow to detect selected portions of the line and the complete shape is derived through a fit e.g. [115]. Temperature and wind velocity are determined from the temperature dependent broadening of the molecule line and the Doppler-broadening of the particle backscatter line.

- **Raman lidar**

Raman lidars are based on the inelastic scattering processes on the vibrational and rotational quantum states of molecules. The possible state of a molecule depends on the temperature (available energy) and excitation. The energy shift itself is dependent on intramolecular parameters. Transition between rotational energy states requires less energy than transition between vibrational energy states. The transitions results in rotational Raman lines grouped less than 3 nm around of the excitation line for 355 nm, whereas the vibrational lines are spaced a few tenths of nanometers from the excitation line. Every vibrational line is accompanied by rotational Raman lines. By illumination with 355 nm the vibrational Raman line of nitrogen can be found at 387 nm and the one from liquid water at 403 nm [112] and from water vapor at 408 nm [113]. The details are explained in the following sections. Raman lidar can be used, depending on the detection channels, to measure water vapor mixing ratio, temperature, backscatter and extinctions coefficients. It also delivers by detection of

the nitrogen vibrational line a signal, whose intensity is relative to the incidental laser power and the atmospheric density. Since the relative amount of nitrogen is constant through the troposphere, the vibrational Raman line of nitrogen is used as molecular (temperature independent) reference signal.

Additionally to the mentioned lidar types, also combinations of them were realized, e.g. [105, 23, 100, 29].

2.2 Temperature measurements with lidar

There are several ways to measure the atmospheric temperature with lidar. An overview can be found in [12]. Depending on altitude and temperature range, some methods are more suitable than others [6].

One method is the integration technique [56, 62, 57]. It is based on the hydrostatic equation and needs an exact pressure profile. With the knowledge or educated guess of a temperature in a certain altitude, the temperature profile can be calculated iteratively. The method relies strongly on this first guess and fails if aerosols are present. An advantage is that only one wavelength has to be detected.

HSRL is also a method for temperature measurements. With three or more wavelength sections detected, the broadening of the Rayleigh-Brillouin line due to molecule movement can be characterized [37, 91, 89, 58, 59]. The method is not performing well in case of aerosols contributions. Another approach is the use of a Fabry-Pérot interferometer and a scanning of the laser frequency [116]. While the accuracy is between 0.15 K and 1.5 K up to 15 km with various integration times and heights, Mie-Scattering is still problematic. Therefore this method is not suitable for boundary layer measurements.

It was investigated if DIAL is suitable for temperature measurements. In principle, with a known amount of the atmospheric constituent and the pressure, the only remaining unknown factor in the absorption coefficient is the temperature [36, 97]. Up to now it was not possible to realize DIAL temperature measurements with an accuracy comparable to other techniques [87, 120].

The most suitable technique to measure temperature above the tropopause is fluorescence lidar. Fluorescence is quenched in the lower troposphere due to the high air density. But in altitudes with low molecular density this is not the case. Additionally in the stratosphere and mesosphere the smaller amount of air molecules decreases the Rayleigh backscatter significantly [87, 9], while coincidentally there are layers of atomic sodium or iron. By measurement of the shape of the Doppler-broadened fluorescence line shape of these atoms the temperature is retrieved [48, 40].

The mentioned methods are not suitable for boundary layer measurements due to their sensitivity to aerosols or high measurement errors. Therefore rotational Raman technique [24, 102] is the most suitable for temperature measurements in the lower troposphere. Even daytime measurements are possible with current systems, which are important for land-atmosphere studies. The technique is described in more detail in the next sections.

2.3 Rotational Raman lidar (RRL)

Molecules have intramolecular vibrational and rotational states. The rotational state of the molecule depends on temperature through the Boltzmann distribution. Raman scattering describes the inelastic scattering of photons changing the initial state of the molecule. The equations describing the transition and the corresponding energies and cross sections can be found in [52].

The principle of temperature Raman lidar is that two parts of the pure rotational Raman spectrum with opposite temperature dependency are detected. The ratio of the two signals is calibrated to an independent measured profile to retrieve the absolute temperature. The first filter passband includes lines whose intensity will remain constant or decrease with decreasing temperature while the measured intensity in the second filter passband increases at the same time. The optimum positions of the filter passbands are determined by the measurement scenario. The UHOH RRL for example was optimized for a temperature range of 270 to 300 K, like expected

in subtropical boundary layers, and a daytime signal background. Table 2.1 gives an overview over existing RRLs with focus on tropospheric measurements.

Most rotational Raman lidars detect more than one rotational Raman line in each of the two filter passbands, but there are also approaches to detect only one rotational Raman line per channel [68] or to calculate the exact calibration function, but these show still more deviation than the ones derived by calibration with radiosondes [102]. One has to be aware that radiosondes can show a significant bias and are also not more than a snapshot of the atmospheric state. A lidar profile averaged over several minutes is much more representative. Therefore an exact agreement between lidar and radiosonde profile during calibration is not expected, especially in the boundary layer where processes with short time scales are present. Horizontal measurements over in-situ sensors can also be used for calibration.

Common for all lidar types is a strong, pulsed laser source. Especially in Raman lidar it is advisable to prefer a laser with less frequent, but high energy pulses at the same average power due to the better signal to noise ratio, which can be achieved. In comparison with e.g. DIAL or HSRL, the exact wavelength of the laser is not crucial as long as it is stable and can be determined with a precision of 1 GHz. A limitation is only the specific absorption of atmospheric constituents. Wavelengths which are strongly absorbed by water vapor or ozone should be avoided. For DIAL it is necessary to use exactly the wavelength with or without absorption and also the absorption cross section changes significantly over a small wavelength range. In Raman lidar all shifts can be calculated for arbitrary wavelengths and the detection channels adjusted accordingly. The precision in wavelength is necessary as the detected parts of the pure rotational Raman spectrum have to be determined exactly to extract the most suitable signal. Therefore is it advisable to perform simulations concerning the optimum filter passband combinations for temperature measurements independent of the excitation wavelength like shown in the next section.

Institution	Wavelength, P_{λ_0}	Day/Night	Detail	Reference
UHOH	355 nm, 10 W	both	scanning, mobile	[53]
BASIL	355 nm, 5 W	both	mobile	[29]
Estrange	532 nm, 18 W	night	polar	[1]
Wuhan	532 nm, 18 W	night	interferometer	[68]
JungfrauJoch	532 nm, 5 W	night	alpine	[11]
Xi'an	355 nm, 6 W	both		[71, 108]
Hampton University	355 nm, unknown			[95]
SRL	355 nm, 10.5 W	night	scanning, mobile	[28]
RAMSES	355 nm, 13.5 W	both	autonomous	[84]
RAIMO	355 nm, 9 W	both	autonomous	[31]

Table 2.1: Overview of existing temperature rotational Raman lidars with focus on measurements in the lower troposphere

2.4 Hammann and Behrendt, 2015, Optics Express

Simulations concerning the optimum filter passbands for daytime measurements were performed for the UHOH RRL. The simulation results depended on several lidar parameters like initial laser wavelength, filter passband properties and the atmospheric temperature to be measured. Additionally the background level or signal to background ratio had a high impact on the suitable filter positions. Therefore we studied how the passband centers shift in relation to the different parameters and found simple equations taking temperature and background into account. The effects of the other parameters were found to be negligible. The study was performed in a way, so that the concept can be applied to other laser frequencies without further considerations.

©2015 Optical Society of America. One print or electronic copy may be made for personal use only. Systematic reproduction and distribution, duplication of any material in this paper for a fee or for commercial purposes, or modifications of the content of this paper are prohibited.

Parametrization of optimum filter passbands for rotational Raman temperature measurements

Eva Hammann* and Andreas Behrendt

University of Hohenheim, Institute of Physics and Meteorology, Garbenstrasse 30, 70599 Stuttgart, Germany
*eva.hammann@uni-hohenheim.de

Abstract: We revisit the methodology of rotational Raman temperature measurements covering both lidar and non-range-resolved measurements, e.g., for aircraft control. The results of detailed optimization calculations are presented for the commonly used extraction of signals from the anti-Stokes branch. Different background conditions and realistic shapes of the filter transmission curves are taken into account. Practical uncertainties of the central passbands and widths are discussed. We found a simple parametrization for the optimum filter passband shifts depending on the atmospheric temperature range of interest and the background. The approximation errors of this parametrization are smaller than 2% for temperatures between 200 and 300 K and smaller than 4% between 180 and 200 K.

©2015 Optical Society of America

OCIS codes: (010.0280) Remote sensing and sensors; (280.3640) Lidar; (280.6780) Temperature; (300.6450) Spectroscopy, Raman; (350.2460) Filters, interference

References and links

1. J. Cooney, "Measurement of atmospheric temperature profiles by Raman Backscatter," *J. Appl. Meteorol.* **11**(1), 108–112 (1972).
2. Y. F. Arshinov, S. M. Bobrovnikov, V. E. Zuev, and V. M. Mitev, "Atmospheric temperature measurements using a pure rotational Raman lidar," *Appl. Opt.* **22**(19), 2984–2990 (1983).
3. A. Behrendt, "Temperature Measurements with Lidar" in *Lidar: Range-Resolved Optical Remote Sensing of the Atmosphere* (Springer, 2005), Ch. 10.
4. V. Wulfmeyer, M. Hardesty, D. D. Turner, A. Behrendt, M. Cadetdu, P. Di Girolamo, P. Schlüssel, J. van Baelen, and F. Zus, "A Review of the Remote Sensing of Lower-Tropospheric Thermodynamic Profiles and its Indispensable Role for the Understanding and the Simulation of Water and Energy Cycles," *Rev. Geophys.* **53**(3), 819–895 (2015).
5. M. Frazczek, A. Behrendt, and N. Schmitt, "Laser-based air data system for aircraft control using Raman and elastic backscatter for the measurement of temperature, density, pressure, moisture, and particle backscatter coefficient," *Appl. Opt.* **51**(2), 148–166 (2012).
6. M. Frazczek, A. Behrendt, and N. Schmitt, "Short-range optical air data measurements for aircraft control using rotational Raman backscatter," *Opt. Express* **21**(14), 16398–16414 (2013).
7. A. Behrendt, T. Nakamura, M. Onishi, R. Baumgart, and T. Tsuda, "Combined Raman lidar for the measurement of atmospheric temperature, water vapor, particle extinction coefficient, and particle backscatter coefficient," *Appl. Opt.* **41**(36), 7657–7666 (2002).
8. J. Zeyn, W. Lahmann, and C. Weitkamp, "Remote daytime measurements of tropospheric temperature profiles with a rotational Raman lidar," *Opt. Lett.* **21**(16), 1301–1303 (1996).
9. P. Di Girolamo, R. Marchese, D. N. Whiteman, and B. B. Demoz, "Rotational Raman lidar measurements of atmospheric temperature in the UV," *Geophys. Res. Lett.* **31**(1), L01106 (2004).
10. M. Radlach, A. Behrendt, and V. Wulfmeyer, "Scanning rotational Raman lidar at 355 nm for the measurement of tropospheric temperature fields," *Atmos. Chem. Phys.* **8**(2), 159–169 (2008).
11. P. Di Girolamo, D. Summa, and R. Ferretti, "Multiparameter Raman Lidar Measurements for the Characterization of a Dry Stratospheric Intrusion Event," *J. Atmos. Ocean. Technol.* **26**(9), 1742–1762 (2009).
12. J. Mao, D. Hua, Y. Wang, F. Gao, and L. Wang, "Accurate temperature profiling of the atmospheric boundary layer using an ultraviolet rotational Raman lidar," *Opt. Commun.* **282**(15), 3113–3118 (2009).
13. J. Su, M. McCormick, Y. Wu, R. Lee III, L. Lei, Z. Liu, and K. Leavor, "Cloud temperature measurement using rotational Raman lidar," *J. Quantum Spectrosc. Ra.* **125**, 45–50 (2013).
14. A. Behrendt and J. Reichardt, "Atmospheric temperature profiling in the presence of clouds with a pure rotational Raman lidar by use of an interference-filter-based polychromator," *Appl. Opt.* **39**(9), 1372–1378 (2000).

#247793

(C) 2015 OSA

Received 24 Aug 2015; revised 23 Oct 2015; accepted 29 Oct 2015; published 17 Nov 2015

30 Nov 2015 | Vol. 23, No. 24 | DOI:10.1364/OE.23.030767 | OPTICS EXPRESS 30767

15. M. Alpers, R. Eixmann, C. Fricke-Begemann, M. Gerding, and J. Höffner, "Temperature lidar measurements from 1 to 105 km altitude using resonance, Rayleigh, and Rotational Raman scattering," *Atmos. Chem. Phys.* **4**(3), 793–800 (2004).
16. P. Achtert, M. Khaplanov, F. Khosravi, and J. Gumbel, "Pure rotational-Raman channels of the Esrange lidar for temperature and particle extinction measurements in the troposphere and lower stratosphere," *Atmos. Meas. Tech.* **6**, 91–98 (2013).
17. A. Behrendt, T. Nakamura, and T. Tsuda, "Combined temperature lidar for measurements in the troposphere, stratosphere, and mesosphere," *Appl. Opt.* **43**(14), 2930–2939 (2004).
18. I. Balin, I. Serikov, S. Bobrovnikov, V. Simenonov, B. Calpini, Y. Arshinov, and H. Van den Bergh, "Simultaneous measurement of atmospheric temperature, humidity, and aerosol extinction and backscatter coefficients by a combined vibrational–pure-rotational Raman lidar," *Appl. Phys. B* **79**(6), 775–782 (2004).
19. Y. Arshinov, S. Bobrovnikov, I. Serikov, A. Ansmann, U. Wandinger, D. Althausen, I. Mattis, and D. Müller, "Daytime operation of a pure rotational Raman lidar by use of a Fabry-Perot interferometer," *Appl. Opt.* **44**(17), 3593–3603 (2005).
20. A. Behrendt, S. Pal, V. Wulfmeyer, Á. M. Valdebenito, and G. Lammel, "A novel approach for the characterisation of transport and optical properties of aerosol particles near sources. Part I: measurement of particle backscatter coefficient maps with a scanning UV lidar," *Atmos. Environ.* **45**(16), 2795–2802 (2011).
21. Á. M. Valdebenito, S. Pal, A. Behrendt, V. Wulfmeyer, and G. Lammel, "A novel approach for the characterisation of transport and optical properties of aerosol particles near sources: microphysics-chemistry-transport model development and application," *Atmos. Environ.* **45**(17), 2981–2990 (2011).
22. P. Groenemeijer, C. Barthlott, A. Behrendt, U. Corsmeier, J. Handwerker, M. Kohler, C. Kottmeier, H. Mahlike, S. Pal, M. Radlach, J. Trentmann, A. Wieser, and V. Wulfmeyer, "Multi-sensor measurements of a convective storm cluster over a low mountain range: adaptive observations during PRINCE," *Mon. Weather Rev.* **137**, 585–602 (2009).
23. U. Corsmeier, N. Kalthoff, C. Barthlott, F. Aoshima, A. Behrendt, P. Di Girolamo, M. Dorninger, J. Handwerker, C. Kottmeier, H. Mahlike, S. D. Mobbs, E. G. Norton, J. Wickert, and V. Wulfmeyer, "Processes driving deep convection over complex terrain: a multi-scale analysis of observations from COPS IOP 9c," *Q. J. R. Meteorol. Soc.* **137**(S1), 137–155 (2011).
24. A. Behrendt, S. Pal, F. Aoshima, M. Bender, A. Blyth, U. Corsmeier, J. Cuesta, G. Dick, M. Dorninger, C. Flamant, P. Di Girolamo, T. Gorgas, Y. Huang, N. Kalthoff, S. Khodayar, H. Mamstein, K. Träumler, A. Wieser, and V. Wulfmeyer, "Observation of convection initiation processes with a suite of state-of-the-art research instruments during COPS IOP 8b," *Q. J. R. Meteorol. Soc.* **137**(S1), 81–100 (2011).
25. E. Hammann, A. Behrendt, F. Le Mounier, and V. Wulfmeyer, "Temperature profiling of the atmospheric boundary layer with rotational Raman lidar during the HD(CP)² observational prototype experiment," *Atmos. Chem. Phys.* **15**(5), 2867–2881 (2015).
26. A. Cohen, J. A. Cooney, and K. N. Geller, "Atmospheric temperature profiles from lidar measurements of rotational Raman and elastic scattering," *Appl. Opt.* **15**(11), 2896–2901 (1976).
27. M. A. Buldakov, I. I. Matrosov, and T. N. Papova, "Determination of the anisotropy of the polarisability tensor for N₂ and O₂ molecules," *Opt. Spectrosc.* **46**, 867–869 (1979).
28. G. Vaughan, D. P. Wareing, S. J. Pepler, L. Thomas, and V. Mitev, "Atmospheric temperature measurements made by rotational Raman scattering," *Appl. Opt.* **32**(15), 2758–2764 (1993).
29. A. Behrendt, V. Wulfmeyer, E. Hammann, S. K. Muppa, and S. Pal, "Profiles of second to fourth-order moments of turbulent temperature fluctuations in the convective boundary layer: first measurements with rotational Raman lidar," *Atmos. Chem. Phys.* **15**(10), 5485–5500 (2015).
30. M. Radlach, "A scanning eye-safe rotational Raman lidar in the ultraviolet for measurements of tropospheric temperature fields," doctoral thesis, Stuttgart (2009).
31. F. Liu and F. Yi, "Lidar-measured atmospheric N₂ vibrational rotational Raman spectra and consequent temperature retrieval," *Opt. Express* **22**(23), 27833 (2014).
32. M. Fraczek, "Aircraft air data system based on the measurement of Raman and elastic backscatter via active optical remote-sensing," doctoral thesis, University of Hohenheim, <http://opus.uni-hohenheim.de/volltexte/2014/965/> (2013).

1. Introduction

Atmospheric temperature measurements with rotational Raman lidar (RRL [1–4]) or non-range-resolved temperature measurements, e.g., temperature measurements for aircraft control using rotational Raman backscatter [5, 6], are based on the fact that the relative intensity of rotational Raman lines is temperature-dependent. Q_r , being the ratio between two signals extracted from the spectrum with opposite temperature dependence, can be related to absolute temperature after calibration [7].

The backscatter cross section of the strongest rotational Raman lines is about a factor 1/1500 weaker than the one of elastic molecular scattering [3]. Therefore, the solar background plays an important role for the measurement uncertainties of rotational Raman

temperature lidar. Daytime measurements are more challenging than nighttime measurements. All of today's rotational Raman systems use Nd:YAG lasers as light sources and operate either at the second or third harmonic wavelength near 532 nm or 355 nm, respectively. For daytime measurements, UV systems are generally preferred due to the higher backscatter cross section and lower solar background [3, 8]. Examples for rotational Raman lidars operating in the UV and with interference filter based polychromators are the systems of NASA Goddard Space Flight Center [9], of University of Hohenheim [10], of University of Basilicata [11], of Xi'an University [12] and of Hampton University [13]. Rotational Raman lidars at 532 nm reach larger range at night than UV systems due to the higher laser power available at 532 nm compared to 355 nm, higher efficiency in signal separation, and lower atmospheric extinction. Therefore 532 nm is often used for stratospheric measurements [14–16] and ranges of up to 40 km have been reported [15]. Some of the systems at 532 nm are also based on interference filters [7, 9, 10, 14, 16, 17] and some employ double-grating polychromators [18, 19].

The measurement uncertainty depends critically on which parts of the rotational Raman spectrum are extracted. With interference filters, typically not just one but a few Raman lines are within the filter transmission bands. As the central wavelength of an interference filter is related to the angle of incidence, the central wavelength is adjustable by changing the angle. Depending on temperature, lines with high rotational quantum states J are weak and maybe hardly indistinguishable from the background. On the other hand, these weak high- J lines are more sensitive to temperature changes than low- J lines with higher intensity. Therefore, the optimum combination of the receiver passbands of both rotational Raman channels depends on temperature and signal-to-background ratio. The latter depends then on solar elevation angle, receiver transmission, filter bandwidth, filter out-of-band blocking and laser power.

For the low- J channel, the lowest statistical error can be achieved with a filter passband near the laser wavelength. However, a further demand on the rotational Raman channels is sufficiently high blocking of the elastically scattered light. Thus, low transmission at the laser wavelength is required. But a filter passband close to the laser wavelength shows lower blocking than a filter placed further away. In consequence, both these selection criteria are in conflict to each other and a practical compromise must be found.

Elastic signal leakage in the first rotational Raman channel can be corrected [7, 13]. But leakage correction increases the statistical uncertainty and decreases the accuracy because the correction factor cannot be determined exactly. We therefore recommend putting priority on minimizing the systematic error due to leakage. Experimental results prove that this is indeed possible by positioning the filter passband in sufficient distance to the laser wavelength [14, 17]. After minimizing this systematic error, we recommend minimizing the statistical error with the method presented in this paper.

In order to meet the measurement requirements at daytime, the University of Hohenheim (UHOH) RRL was optimized for high temperature measurement performance in daytime in the convective boundary layer [10]. The data of the UHOH RRL have been used for studies on the characterization of transport and optical properties of aerosol particles near their sources [20, 21], on the initiation of convection [22, 23], and on atmospheric stability indices [24, 25]. Simulations for identifying the optimum pair of central wavelengths for one specific system, the RRL of UHOH, and different signal-to-background ratios were presented already in [25]. It was shown that for the given filter characteristics, a configuration for low and high background levels can be identified, which decreased the relative measurement uncertainty by up to 70%. We present here a concept which explains how to find optimum central wavelengths or shifts of the passband for other lidar systems. This concept avoids the tedious effort of repeating the whole simulations. We investigated whether a parametrization is possible which takes into account all or at least some of the relevant parameters (signal-to-background ratio, temperature range of interest, filter bandwidth, filter shape, etc.). The

results are useful for lidar applications but also beyond, as the rotational Raman technique can also be applied e.g. for temperature sensors for aircraft control [5, 6].

In section 2, the basics of the rotational Raman technique for temperature measurements are recapitulated and the optimization procedure is described. In section 3, the results are discussed. Section 4 contains a summary.

2. Methods

2.1 Rotational Raman temperature measurements

For lidar applications, elastic scattering by particles and molecules can be employed as well as inelastic scattering by molecules. For inelastic scattering, so-called Raman scattering, the vibrational and/or rotational quantum state of the scattering molecule changes and accordingly the energy of the scattered photon differs from the energy of the incident photon. The rotational energy level $E_{rot,i}(J)$ of quantum state J for an atmospheric constituent i is given by

$$E_{rot,i}(J) = [B_{0,i}J(J+1) - D_{0,i}J^2(J+1)^2]hc, \quad J = 0, 1, 2, \dots \quad (1)$$

with Planck's constant h and velocity of light c [3]. $B_{0,i}$ and $D_{0,i}$ are the rotational constant and centrifugal distortion constant for the ground state vibrational level. The selection rule for energy transitions of diatomic molecules like nitrogen and oxygen is $J \pm 2$. As changes of J thus cause both increases and decreases of the energy, the elastic backscatter signal at the excitation frequency is surrounded by a spectrum of rotational Raman lines on both sides. The Stokes branch is found at lower frequencies, corresponding to $J + 2$, with shifts to the excitation frequency of

$$\Delta V_{St,i}(J) = -B_{0,i}2(2J+3) + D_{0,i}[3(2J+3) + (2J+3)^3], \quad J = 0, 1, 2, \dots \quad (2)$$

J is here and in the following the rotational quantum number of the molecule before scattering takes place.

The anti-Stokes branch at higher frequencies, corresponding to $J - 2$, follows

$$\Delta V_{AS,i}(J) = B_{0,i}2(2J-1) + D_{0,i}[3(2J-1) + (2J-1)^3], \quad J = 2, 3, 4, \dots \quad (3)$$

The differential backscatter cross section for a certain rotational quantum state J is temperature-dependent [26] and is given by:

$$\left(\frac{d\sigma}{d\Omega}\right)_s^{RR,i}(J,T) = \frac{112\pi^4}{15} g_i(J)hcB_{0,i}(v_0 + \Delta V_i(J))^2 \gamma_i^2 X(J) \exp\left(-\frac{E_{rot,i}(J)}{kT}\right) \quad (4)$$

where g_i is a statistical weight factor depending on the nuclear spin I_i , v_0 stands for the frequency of the exciting light, γ_i is the anisotropy of the molecular polarizability and k the Boltzmann constant. $X(J)$ differs between the two branches. For the Stokes branch, one must apply

$$X(J) = \frac{(J+1)(J+2)}{2J+3}, \quad J = 0, 1, 2, \dots \quad (5)$$

and for the anti-Stokes branch

$$X(J) = \frac{J(J-1)}{2J-1}, \quad J = 2, 3, 4, \dots \quad (6)$$

Table 1 lists the values used for all constants in Eq. (4) [3, 27]. Only the rotational Raman spectra of nitrogen and oxygen are calculated as these molecules account for more than 95%

even for wet air and the contribution of other molecules (mainly water vapor) is negligible [5]. Figure 1 shows an example of the spectrum calculated for two different temperatures.

Lidar systems transmit laser pulses into the atmosphere and detect the backscattered light with high temporal resolution. From the run time of the signals, the distance to the scatterer is derived. The lidar equation for inelastic scattering describes the portion P_{LR} of the transmitted laser light P_0 , which is detected from distance z

$$P_{LR}(z) = P_0 \frac{c\Delta t}{2} \frac{O(z)}{z^2} \eta_{LR} A_T \beta_{LR}(z) \exp\left[-\int_0^z [\alpha_o(z') + \alpha_R(z')] dz'\right]. \quad (7)$$

In this equation, Δt is the laser pulse duration, $O(z)$ the overlap function, η_{LR} the detection efficiency, A_T the telescope area, β_{LR} the backscatter coefficient, and α_o and α_R are the extinction coefficient for the excitation wavelength and the Raman wavelength, respectively. For rotational Raman lidar, two rotational Raman signals are used. Typically, the one closer to the excitation wavelength is called P_{RR1} and the one further away P_{RR2} . The ratio of rotational Raman signals is then [26]

$$Q(T) = \frac{P_{RR2}}{P_{RR1}} = \frac{\sum_{O_2 N_2} \sum_{J_1} \tau_{RR2}(J_1) \eta_1 \left(\frac{d\sigma}{d\Omega}\right)_x^{RR,2}(J_1)}{\sum_{O_2 N_2} \sum_{J_1} \tau_{RR1}(J_1) \eta_1 \left(\frac{d\sigma}{d\Omega}\right)_x^{RR,1}(J_1)} \quad (8)$$

with P_{RRn} for the background-corrected signal in detection channel n , τ_{RRn} is the transmission for the wavelength of channel n and η_1 the number density of the molecule.

Calibration is usually performed through comparison with an independently measured temperature profile as the uncertainties by analyzing the instrumental parameters and calculating a calibration with these are typically larger [28]. There are several approaches to derive temperature $T(Q)$, depending on the number of detected lines and the temperature range. Details and examples for calibration functions can be found in [3]. In the optimization calculations described here, we apply the exact formulas and not the fit determined by calibration.

The statistical error of a temperature measurement with the rotational Raman technique is mainly determined by shot noise [29]. Thus, ΔT_{stat} can be simulated from the photon numbers by applying Poisson statistics giving [7]

$$\Delta T_{stat} = \frac{dT}{dQ} \Delta Q = \frac{dT}{dQ} \sqrt{\frac{P_{RR1} + P_{R1}}{P_{RR1}^2} + \frac{P_{RR2} + P_{R2}}{P_{RR2}^2}} \quad (9)$$

with P_{Bs} for the background in rotational Raman channel x . Equation (9) is only valid if the background was determined over a high number of range bins and its statistical error is negligible.

Table 1. Values used for the constants in Eqs. (1)-(4)

Molecule	B_0 (cm ⁻¹)	D_0 (cm ⁻¹)	g_u (J odd)	g_l (J even)	l	γ^2 (10 ⁻¹⁶ cm ⁶)
N ₂	1.989500	5.48x10 ⁻⁶	6	3	1	0.509
O ₂	1.437682	4.85x10 ⁻⁶	0	1	0	1.27

2.2 Simulation concept and parameters

For the simulation, the anti-Stokes lines of nitrogen and oxygen were first calculated for two temperatures in order to approximate the differential in Eq. (9) by

$$\frac{dT}{dQ} = \frac{T_1 - T_2}{Q_1 - Q_2} \quad (10)$$

We found that a suitable difference of the two temperatures in the simulation is 5 K. For much larger temperature ranges, non-linear effects of $T(Q)$ may become significant [3]. Then, the simulated photon count rates in the detection for the first and second rotational Raman channel with the passband centers SPC1 and SPC2 respectively, were calculated using different shapes and widths for the transmission bands and different background levels.

The uncertainties for the different combinations of SPCs were calculated for temperatures between 180 and 300 K, which cover the range of typical temperatures in the troposphere and stratosphere, i.e., those altitudes which can be covered with rotational Raman lidar. We varied the SPCs in such a way that the optimum for all of these temperatures is always found. The relative intensities and energy shifts of the rotational Raman spectrum are the same independent of the frequency of the excitation radiation (see Fig. 1). Consequently, we express SPCs and widths in units of wavenumbers, in order to discuss the results in a generalized way independent of the laser wavelength. SPC1 was varied from 0 to 74 cm^{-1} and SPC2 from 66 cm^{-1} to 194 cm^{-1} , both in 0.8 cm^{-1} steps. The corresponding filter parameters in wavelength units for the second to fourth harmonic of Nd:YAG lasers are listed in Table 2. With these ranges, a total of 93 and 161 values were used in the simulation for SPC1 and SPC2, respectively. For each of the value pairs, the statistical uncertainty was calculated resulting in an array of $93 \times 161 = 14\,973$ values for each combination of temperature, filter shape and bandwidth as well as background level. As the aim of this study is to find optimum filter parameters for a given configuration, only the relative errors $d_r T$ in each array have then been investigated further, which means that all the values in each array were divided by the smallest value of the array.

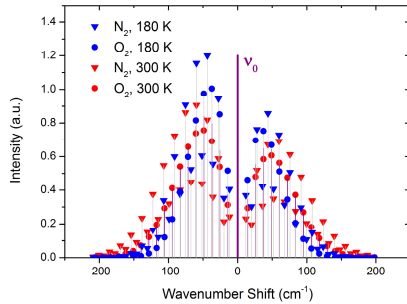


Fig. 1. Shift of pure rotational Raman lines of nitrogen and oxygen relative to the excitation frequency ν_0 and relative intensities of these lines for temperatures of 180 and 300 K.

Table 2. Wavenumber ranges covered by our simulations with corresponding wavelength ranges for the second to fourth harmonic of a Nd:YAG laser. SPC1 and SPC2 are the shifts of the passband centers of the filters for the low- J and high- J rotational Raman channel, respectively, relative to the frequency of the initial radiation.

Wavenumber (cm^{-1})	For 532.0 nm (nm)	For 354.8 nm (nm)	For 266.0 nm (nm)
SPC1 max	529.91	353.90	265.48
SPC1 min	0.0	532.00	266.00
SPC2 max	194.0	526.60	352.40
SPC2 min	66.0	530.14	354.00
Step size	0.8	0.022	0.010
		0.010	0.0055

The bandwidths of the filters, which extract the two rotational Raman signals, must fulfil the following criteria. First, the passbands of both channels should not overlap. Second, they must not include the frequency of the laser. Furthermore, both signals should show an as large as possible sensitivity to temperature. This sensitivity should be opposite for the two channels. Figure 2 shows as example the temperature sensitivity of the extracted signals

$$\frac{dP}{dT} = \frac{P(T_2) - P(T_1)}{T_2 - T_1} \quad (11)$$

as a function of the filter bandwidth for rectangular shaped filter transmission curves at 270 K. One can see that for the RR1 channel with negative temperature sensitivity (decreasing signal intensity with increasing temperature) only bandwidths smaller than about 100 cm^{-1} avoid overlap with the excitation frequency. But it should be noted that typically a very high blocking (transmission less than 10^{-7}) is needed at the excitation frequency [14] in order to avoid contamination of the temperature measurements by elastic backscattering of particles in the atmosphere. These requirements are relaxed for 355 nm compared to 532 nm because of the wavelength dependencies for particle scattering (typically $1/\lambda^4$) and Raman scattering ($1/\lambda^6$). Thus, in practice the optimum SPC1 cannot be used for RR1 and a larger shift is necessary.

But, it is not sufficient to study only temperature sensitivity when selecting optimum filter parameters, the signal intensities relative to the background are also important for the measurement uncertainty like already outlined in the introduction.

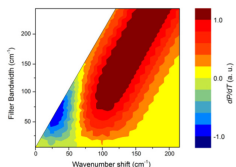


Fig. 2. Temperature sensitivity dP/dT of the extracted rotational Raman signals depending on the wavenumber shift of the center of the filter passband and its bandwidth. Only values for which the excitation frequency is outside of the transmission band are shown.

A full width at half maximum (FWHM) of 23.8 cm^{-1} for the first and 39.6 cm^{-1} for the second channel was used in the first simulations. These bandwidth values were successfully tested in previous experiments [10, 25]. These widths are located in the lower region of Fig. 2, where it is indeed possible to extract signals with opposite temperature sensitivity at 270 K.

The transmission curves of multi-cavity interference filters have Gaussian-like shapes. Thus, we used for the simulation idealized Gaussian curves which were compared with real filter curves. The filter of the UHOH RRL (manufactured by Materion Precision Optics and

Thin Film Coating Inc.) has an optical thickness of 6 at the excitation wavelength and a peak transmission of more than 0.5. (The additional blocking at the laser wavelength by one order of magnitude is achieved by a sequential mount of the rotational Raman channels and the elastic channel [10, 25].) The filter transmission curve F can be approximated by the following equation:

$$F(\nu) = A \exp\left[\frac{-B(\nu - \nu_0)^4}{FWHM}\right]. \quad (12)$$

Parameters A and B are chosen to model the actual curve like described in [10]. In section 2.3 the impact of other transmission curves is discussed. Equation (12) describes the filter passband for a beam divergence of 0° . In practice, however, the beam divergence is not exactly 0° . Therefore a beam divergence of 0.5° was used in the simulation and later it was studied how other values for the divergence influence the results.

For the determination of optimum SPCs, the value P_{Bx} for the background is crucial. It is given here in relation to the intensity P_J^{max} of the strongest rotational Raman line in order to generalize the discussion. The background takes the filter bandwidth $\Delta\nu_{FWHM}$ into account by a factor which is 1 for a filter bandwidth of 8 cm^{-1} (corresponding to 0.10 nm for an excitation wavelength of 355 nm and 0.23 nm for 532 nm) and is correspondingly adjusted for other bandwidths via

$$P_B = S(z) \frac{\Delta\nu_{FWHM}}{8 \text{ cm}^{-1}} P_J^{max}(z). \quad (13)$$

The factor S is then varied for different background levels. At night, values between $S = 0$ and $S = 0.1$ for lower altitudes (up to 2-3 km) are typical for the UHOH RRL. Figure 3 is the result of a derivation of S from experimental data collected with the UHOH RRL (200 mJ pulse energy, laser wavelength of 354.8 nm). At daytime, S is larger and increases quickly with altitude as the backscatter signal decreases exponentially. Typically, S is larger than 1 for altitudes above 2 km at noon. The result of the simulation does not change significantly with higher values of S [30]. Therefore, $S = 1.0$ can be used as a worst-case value at daytime. In the simulation, S was thus varied between 0.0 and 1.0 – also, as larger values will result in very large uncertainties of the temperature measurements anyway and are therefore outside the preferable set of parameters.

P_J^{max} can be estimated from the specific filter passband and the relative intensity of the lines within the passband in comparison with the intensity of the strongest anti-Stokes Raman line. The telescope diameter and further detection efficiencies have no influence on the ratio, as they influence both the signal and the background in the same way.

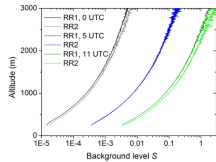


Fig. 3. Background-level S for the two rotational Raman signals RR1 and RR2 at different times of the day (local noon is at 11:40 UTC). The profiles were measured on May 19, 2013 under cloud-free conditions. Total incoming short wave radiation measured by a nearby EC station was 0 W/m^2 at 0 UTC, 128 W/m^2 at 5 UTC and 890 W/m^2 at 11 UTC.

How can the results presented here now be transferred to other systems? The most relevant parameter is laser pulse energy E_{pulse} . For systems with excitation wavelengths near 355 nm and the same filter passband widths as ours (24 cm^{-1} and 40 cm^{-1} for the first and second RR channel, respectively), one will find S' values which scale with the one shown in Fig. 3 with the pulse power of the other system E'_{pulse} relative to the pulse power E_{pulse} used here according to

$$S' = \frac{E_{pulse}}{E'_{pulse}} S. \quad (14)$$

At 532 nm, the daylight background per nm bandwidth is a factor of about 1.6 larger than at 355 nm (see Appendix). Thus S is a factor of $(1.5)^2 \times 1.6 = 3.6$ larger for the same filter passband widths in wavenumber units. The simulation was performed like described in section 2.2 resulting in one array for each pair of temperature and background level. Figure 4 shows as an example the simulation results for 270 K and $S = 0$, i.e. no background radiance. The optimum pair of SPC1 and SPC2 (with $d,T = 1.0$, minimum error per each array) is found at 23 cm^{-1} and 132 cm^{-1} , respectively. It can be seen that a small shift of 8 cm^{-1} (corresponding to 0.1 nm at 355 nm) may result in significant increase of the measurement uncertainty.

A limiting factor for SPC1 is the minimum shift which is sufficient to block the elastic backscattered signal completely. Without this constraint, the optimum is approximately at 25 cm^{-1} for SPC1, which can be found indeed in Fig. 2 in the area of negative correlation. However, current interference filters require a larger shift to the elastic line to guarantee sufficient blocking. Therefore we decided to study not only the parametrization of the shifts for the case $d,T = 1.0$, but to extend the analysis for the SPC pair which provides a relative uncertainty of 1.2 with the largest possible value for SPC1. There are already interference filter which show the required blocking with the resulting SPCs. The performance will be even better if it is possible to choose a smaller value for SPC1, i.e. a passband which is nearer to the frequency of the laser. If a smaller SPC1 is chosen, the already determined SPC2 can be applied without significant increase of the measurement uncertainty.

Figure 5 shows the simulation results for $S = 0$ and temperatures between 180 and 300 K. The wavenumber pairs, which result in $d,T = 1.2$ are marked as spheres to visualize the temperature dependency (for a temperature of 270 K, they correspond to the outer boundary of the yellow area of Fig. 4).

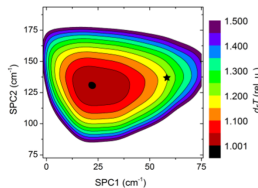


Fig. 4. Example for the simulated temperature measurement uncertainties d,T (relative to the minimum uncertainty of the array shown in black) depending on SPC1 and SPC2, respectively. This case is for a temperature of 270 K and zero background ($S = 0$). The star denotes the largest possible value for SPC1 for which $d,T \leq 1.2$; this point is of practical importance as it marks a setting at which the required blocking of the elastically scattered light at the excitation frequency can be reached.

The optimum wavenumber shifts decrease with decreasing temperature due to the weakening high- J lines. It is also noteworthy that the area within the spheres becomes smaller with decreasing temperatures. The reason for this characteristic is that the rotational Raman spectrum becomes broader with increasing temperature. In consequence, it is more demanding to optimize for measurements at lower than at higher atmospheric temperatures.

2.3 Influence of temperature and background

To clarify the dependency, Figs. 6(a) and 6(b) show the minimum values of the temperature measurement uncertainty of given SPC1 and SPC2, respectively. For all values of the other SPC (if not only $d,T = 1.2$ would be shown in Fig. 5 but all values, Fig. 6a and b would correspond to a projection of the minimum data of Fig. 5 to the T -SPC1 plane and T -SPC2-plane, respectively). Interestingly, the optimum SPC1 changes only by 2 cm^{-1} over the whole temperature range. The SPC1 range with $d,T < 1.2$ becomes larger with higher temperatures. It increases from 42 cm^{-1} at 180 K to 57 cm^{-1} at 300 K. It can be concluded that the optimum SPC1 is not very sensitive to temperature and that the same values can be applied in practice for temperature ranges of several tenths of K. On the other hand, SPC2 shows for the optimum, as well as for the range with $d,T < 1.2$, a quite strong temperature dependency. The optimum position increases by more than 25 cm^{-1} between 180 and 300 K and the $d,T = 1.2$ isolines follow almost parallel. Here the effect of higher relative intensity of high- J lines with higher temperatures becomes significant.

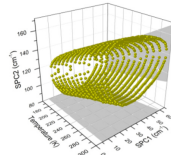


Fig. 5. Spheres mark pairs SPC1 and SPC2 for which the relative temperature measurement uncertainty $d,T = 1.2$. These simulation results are for zero background ($S = 0$). It is interesting to note that the range of both SPC1 and SPC2 for $d,T \leq 1.2$ increases with increasing temperature. Furthermore, these ranges shift to larger values. Gray areas mark the projections of the data points to the parameter planes.

As was done for 270 K above, we investigate now the maximum possible SPC1 for uncertainties $d,T < 1.2$ and non-zero background. Figure 7 shows the results for different background levels and temperatures. Like expected, the SPCs decrease the lower the temperature. The optimum shifts change nearly linearly by 15 cm^{-1} for temperatures between 180 and 300 K (with fixed background level) corresponding to a slope of $0.125\text{ cm}^{-1}/\text{K}$.

Furthermore, the shifts are smaller the higher the background. When changing the background, the whole line shifts approximately by a constant value while the slope is nearly preserved. This shift is 2.9 cm^{-1} , 4.5 cm^{-1} , and 5.5 cm^{-1} from zero background to $S = 0.1$, 0.5 and 1.0 , respectively. Same applies for SPC2, where the shift is about 30 cm^{-1} over the whole temperature range. Here the slope is $0.250\text{ cm}^{-1}/\text{K}$ with shifts of 11.5 cm^{-1} , 20 cm^{-1} , and 23.5 cm^{-1} for $S = 0.1$, 0.5 and 1.0 , respectively.

The next step is to investigate how large the temperature dependence of the shift of SPC1 and SPC2 is. Therefore the SPC difference $d,SPC_{S,240K}$ to the SPCs for 240 K and the same background were calculated with

$$d_s SPC_{s,240K}(T) = \frac{SPC(S=0,T) - SPC(S=0,240K)}{SPC(S=0,240K)} \quad (15)$$

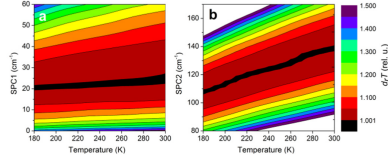


Fig. 6. (a) Minimum values of dT for a combination of SPC1 and temperature T for all values of SPC2 for zero background ($S=0$). (b) Same as (a) but for pairs of SPC2 and T for all values of SPC1. The need of taking the temperature measurement range of interest into account for the filter selection becomes evident.

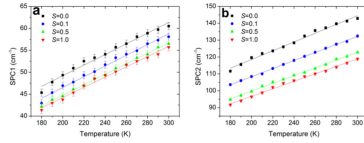


Fig. 7. SPC1 and SPC2 from the excitation wavenumber for $dT = 1.2$ (marked with the star in Fig. 4 for $T = 270$ K and $S = 0$). Points are results of the simulation, thin lines show the best linear fit for each case. These data form the input for the suggested parametrization (see Table 3). Error bars show the uncertainties due to the discretization steps used for SPC1 and SPC2.

The results for $S = 0$ and $S = 1$ are shown in Fig. 8a. Of course, $d_s SPC_{s,240K}$ becomes larger the larger the temperature difference to the reference value of 240 K. Interestingly, all curves are almost linear and nearly coincide. $d_s SPC_{s,240K}$ varies by about 30% over the temperature range of 180 to 300 K giving a mean change of 0.25%/K.

Figure 8b shows in a similar fashion the dependency on the background in relative values $d_s SPC_{s=0,T}$ to $S = 0$ at the same temperature following

$$d_s SPC_{s=0,T}(T) = \frac{SPC(S,T) - SPC(S=0,T)}{SPC(S=0,T)} \quad (16)$$

$d_s SPC_{s=0,T}$ is smaller than about 10% for SPC1 and 20% for SPC2.

In order to illustrate the significance of these results, it is interesting to investigate how much the temperature measurement uncertainties dT increase if these dependencies of the optimum SPCs on temperature and background are neglected. In comparison with Fig. 5 and Fig. 6, the same value of $d_s SPC_{s,240K}$ or $d_s SPC_{s=0,T}$ leads to larger increases in dT the smaller T . This is caused by the narrower rotational Raman spectrum. The same is true for both parameters if S increases because the region of the rotational Raman spectrum, which differs significantly from the background, becomes narrower with increasing background. Consequently, the largest increase of dT for given values of $d_s SPC_{s,240K}$ or $d_s SPC_{s=0,T}$ is found in our study at 180 K and $S = 1$. Here, – as worst case – dT increases drastically by about 170% if SPC1 and SCP2 have been optimized for 240 K and $S = 0$, but measurement are made at 180 K and $S = 1$ with this pair.

2.4 Influence of filter transmission curve and passband widths

There are rotational Raman lidars which detect only single Raman lines (e.g. [31]), but this is not the approach here as the error is definitely larger than using several lines – also for high background, unless the filter bandwidth are narrower than the spectral distance of the rotational Raman lines. As this cannot be realized with interference filters now and in the foreseeable future (and since the maximum transmission becomes also smaller the smaller the bandwidth), we focus the discussions here on filter passbands, which include more than one line.

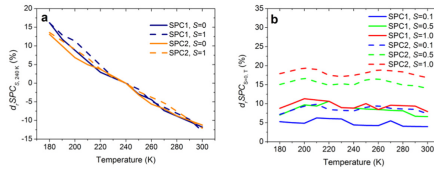


Fig. 8. (a) $dSPC_{S,200K}$ for SPC1 and SPC2 with $S=0$ and $S=1$ respectively (see Eq. (15)).(b) Same as (a), but at same temperatures and relative to zero background ($S=0$).

In section 2.2 and 2.3, the simulations were based on a shape of the filter transmission curve SFT similar to the one of the filters used in the UHOH RRL [25]. As the transmitted passband shifts when changing the angle of incidence on the filter (see [14]), the resulting shape of the filter transmission depends on the divergence of the light passing the filter: The larger the divergence, the broader the transmission band becomes. Figure 9 shows different forms of the transmission band of filter 1.

SFT1 corresponds to the UHOH RRL filters and was used for the simulations above. As the beam divergence in the receiver is about 0.5° , this value was used to derive realistic shapes of the transmission bands (see section 2.2). SFT2 has the same width but a narrower peak and broader tails. This transmission curves corresponds to an older filter we had in use. SFT3 and SFT4 are for beam divergences of 0.1° and 1.0° , respectively, and thus narrower and broader than SFT1. The passband of filter 2 was varied in the same way as filter 1 in the simulations. The difference in optimum SPC for different transmission curve shapes $d_rSPC_{S,T,SFT1}$ is calculated (similar to Eq. (15) and (16)) with

$$d_rSPC_{S,T,SFT1}(T,S) = \frac{SPC(S,T,SFT) - SPC(S,T,SFT1)}{SPC(S,T,SFT1)}. \quad (17)$$

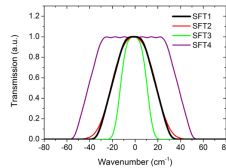


Fig. 9. Filter transmission curves used in the simulation to study the effect of their shape on the optimum filter setting. SFT1 is a Gaussian (see Eq. (12)). SFT2 has the same width as SFT1 but a slightly narrower peak and broader tails. SFT3 and SFT4 are for the same filter as SFT1 but with smaller and higher beam divergence in the receiver, respectively.

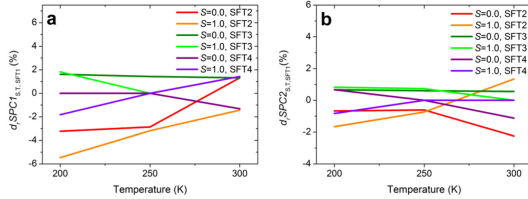


Fig. 10. (a) Relative change $d_{SPC1,T,S,SFT1}$ of selected SPC1s shown in Fig. 7a if the SFT2 to SFT4 are used instead of SFT1. (b) Same as (a) but for SPC2 and Fig. 7b.

Figure 10 shows how SFT2, SFT3 and SFT4 change the results shown for SFT1 in Fig. 7. Temperatures of 200, 250 and 300 K and background value $S = 0$ and $S = 1.0$ were chosen for this test. SPC1 varies within -5.5 and $+1.8\%$, when comparing with the values for same T and S . SPC2 changes only within -2.2 and 1.3% . These changes are very small in comparison to the changes when T and S are varied for the same filter SFT. In addition to these variations, we studied also the effects of keeping SFT1 but changing the bandwidth (see Eq. (12)). For this, we also found small effects (changes of less than $\pm 6\%$). Thus, we conclude that the results obtained with SFT1 and discussed in section 2.3 are representative also for other realistic SFTs and widths which are similar (Gaussian-like, effective widths between 15 and 55 cm^{-1} corresponding to 0.2 and 0.7 nm at 355 nm). As a result it is recommended to focus on expected temperature and background conditions for determining optimum positions of the filter passbands.

3. Resulting parametrization for passband shifts

As discussed in the previous sections, a complete parametrization of the filter parameters taking all effects into account is difficult and also not required in practice. An optimum filter setting can be determined with sufficient accuracy when focusing on the temperature range of interest and on the background level. Therefore, we have investigated whether the presented simulation results can be parametrized with respect to temperature and background only.

In section 2.3, it was shown that the optimum values of SPC1 and SPC2 can be calculated with the linear approximation

$$SPCx(T, S) = m_{SPCx} T + b_{SPCx}(S) \text{ with } x = 1, 2. \quad (18)$$

In this equation m_{SPCx} is the slope depending on the $d_g T$ and the SPCx temperature dependency and b_{SPCx} is a shift which depends on the background. Some parameters were already given in section 2.3 for $d_g T = 1.2$. Table 3 lists these parameters and adds the corresponding values for $d_g T = 1.0$. As discussed above, m_{SPCx} does not depend on the background. The values of b_{SPCx} are given for selected values of S in Table 3. For other values of S , an approximation formula was derived (see Fig. (11)). The values were retrieved by fitting $SPCx(T)$ and determining of the mean slope of the linear fits and the respective background-related shift.

Table 3. Parameters for the suggested parametrization which determines the optimum filter central passbands depending on background S , for $d,T = 1.0$ and $d,T = 1.2$. m_{SPC} : Slope of the linear fit, b_{SPC} : y-intercept of the linear fit.

	m_{SPC} (cm ⁻¹ /K)	b_{SPC} (cm ⁻¹)			
	all S	$S=0$	$S=0.1$	$S=0.5$	$S=1$
SPC1, $d,T=1.2$	0.120	25.5	22.6	21.0	20.0
SPC2, $d,T=1.2$	0.238	72.0	60.5	52.0	48.5
SPC1, $d,T=1.0$	0.051	10.0	11.0	12.0	12.5
SPC2, $d,T=1.0$	0.223	71.0	61.5	53.0	49.5

The fit functions are for SPC1

$$b_{SPC1}(S) = 5.52 \text{ cm}^{-1} \exp\left(\frac{S}{-0.25}\right) + 19.59 \text{ cm}^{-1} \quad (19)$$

and for SPC2

$$b_{SPC2}(S) = 28.20 \text{ cm}^{-1} \exp\left(\frac{S}{-0.36}\right) + 41.28 \text{ cm}^{-1}. \quad (20)$$

In consequence, one obtains the following parametrizations for the passband centers SPC1 of the low- J rotational Raman channel, for which the measurement error is not more than 20% higher than the optimum ($d,T = 1.2$) and required blocking of the elastic backscatter is feasible:

$$SPC1(T, S) = 0.120 \frac{\text{cm}^{-1}}{\text{K}} T + 5.52 \text{ cm}^{-1} \exp\left(\frac{S}{-0.25}\right) + 19.59 \text{ cm}^{-1}. \quad (21)$$

The corresponding equation for SPC2, the passband center of the high- J channel for $d,T = 1.2$, reads

$$SPC2(T, S) = 0.238 \frac{\text{cm}^{-1}}{\text{K}} T + 8.20 \text{ cm}^{-1} \exp\left(\frac{S}{-0.36}\right) + 41.28 \text{ cm}^{-1}. \quad (22)$$

The relative fit error (RFE) between the exact SPCs determined by detailed simulation (SPC_{Sim}) and by the parametrized equations (SPC_{Fit}) were calculated for both approaches with

$$RFE = \frac{SPC_{Fit} - SPC_{Sim}}{SPC_{Sim}}. \quad (23)$$

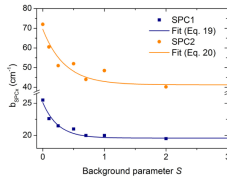


Fig. 11. Mean y-intercept b_{SPC} , of the suggested linear parametrization for SPC1 and SPC2, respectively, versus background parameter S .

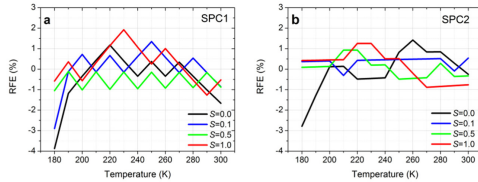


Fig. 12. Performance of the suggested parametrization. (a) Relative fit errors (RFE) for SPC1 for temperatures between 180 and 300 K and background parameters S from 0 to 1. (b) Same as (a) but for SPC2. All deviations are smaller than 2% with the exception of temperatures lower than 200 K for which they are smaller than 4%.

The results for the linear equation are shown in Fig. 12. The fit error RFE is smaller than $\pm 2\%$ for temperatures between 200 and 300 K. For 180 K, the error is larger but still smaller than $\pm 4\%$. A second-order polynomial fit would decrease these errors only marginally by up to 1% (not shown).

What are the related changes in the measurement uncertainty d,T due to the fit errors RFE? A difference of 2% in wavenumber shift results in 1 cm^{-1} for SPC1 of 50 cm^{-1} (corresponding to approximately 0.015 nm for a laser wavelength of 354.83 nm) relative uncertainty values d,T change by only 0.9% for this shift of 1 cm^{-1} . For SPC2, e.g., 2% change of 120 cm^{-1} correspond to 2.4 cm^{-1} . For an excitation wavelength of 354.83 nm this results in a shift of 0.03 nm and in a change in relative uncertainty d,T of only 0.2%. In summary, the errors of the parametrization are indeed small.

4. Conclusions

The statistical measurement uncertainty of atmospheric temperature measurements with the rotational Raman technique depends critically on the choice of the filter passbands for the two rotational Raman channels. We have calculated the relative temperature measurement uncertainties for a range of suitable frequency shifts of the passband centers relative to the excitation frequency for temperatures between 180 and 300 K. Furthermore, different realistic values for the background have been investigated as well different widths and shapes of the passbands.

We found that the effects of differences between realistic filter transmission curves and bandwidths are small (only changes the SPCs by 2 to 5.5%). Consequently, we suggest to neglect these dependencies and to focus the optimization on temperature and background condition because both are responsible for much larger differences.

Then, we have investigated the feasibility of a parametrization for the passband centers, which takes temperature and background into account. We found that two simple parametrizations, one for the SPC of each rotational Raman channel, approximate the optimum shifts well (only differences $<2\%$ between 200 and 300 K; $<4\%$ at 180 K). We suggest using a linear function for the temperature dependency. The crossings with the y-axis depend on the background level. We provide the fit parameters not only for the optimum pair of passband centers but also for the pair with largest shift of the low- J rotational Raman channel for which the measurement error is not more than 20% higher than the optimum. This information is important, because, in practice, the optimum setting cannot be chosen for these filters as it is otherwise too close to the excitation frequency and thus the blocking of the elastic backscatter light is not sufficient.

We conclude that quite a simple parametrization is possible and it is thus not necessary to repeat tedious optimization calculations for each individual rotational Raman receiver. The

parameters of the suggested parametrization are given for temperatures between 180 and 300 K and different relative values of the background. These conditions cover the practical range of atmospheric temperature measurements with the rotational Raman technique for both lidar and non-range-resolved measurements. The suggested parametrization can be used to adapt existing receivers to different temperature and background conditions and has the potential to reduce the statistical measurement uncertainties significantly.

Appendix

A.1 Background values

The background count rate P_B is related to the solar radiance Ψ [32]

$$P_B = \eta_{RR} A_{det} \Psi \omega_{rec} \lambda_{RR} \quad (24)$$

with the detection efficiency k_{RR} , the telescope surface A_{det} , the angle area of view ω_{rec} and the transmission of the filter λ_{RR} . Most of the factors cancel in comparison with the lidar equation (Eq. (7)), as they are equal for the backscattered signal. It follows for a range bin z in the full overlap region

$$\Psi = S \frac{P_0}{8 \text{ cm}^{-1}} \frac{c\Delta t}{2} \beta_{L,max} \exp \left[-\int_0^z (\alpha_a(z') + \alpha_R(z')) dz' \right] \quad (25)$$

Solar radiance Ψ is approximately 250 mW/(m² nm sr) for 355 nm and 400 mW/(m² nm sr) for 532 nm for clear sky and up to a factor 1.25 higher in case of clouds. The extinction and backscatter coefficients of 355 nm and 532 nm can be estimated with [3]

$$P_{RR}(532 \text{ nm}, J) = 0.6 \left(\frac{\tau(532 \text{ nm})(z)}{\tau(355 \text{ nm})(z)} \right)^2 P_{RR}(355 \text{ nm}, J) \quad (26)$$

with the optical transmission τ of both wavelengths at a certain altitude range. Therefore one should solve for S' for the case of high daytime background (250 mW)

$$S' = S \frac{200 \text{ mJ}}{E_{0x}} \frac{P_{RR}(x)}{P_{RR}(355 \text{ nm})} \frac{250 \text{ mW}}{\Psi_x} \quad (27)$$

with the values of the laser system x and the level of expected radiance.

2.5 Vibrational Raman technique for water vapor measurements

Analogous to the rotational Raman technique also vibrational Raman backscatter can be used to gather information about the atmospheric state [74]. The frequency shift of vibrational Raman lines are bigger than the shift of the rotational Raman lines. As the signal intensity of Raman signals is low (cross section is around 10^{-3} lower than the elastic backscatter), only the rotational Raman lines of nitrogen and oxygen and the vibrational Raman lines of nitrogen and water vapor result in signals, which are distinguishable from the background. The total intensity is enhanced by the accompanying rotational Raman lines, which on the other hand introduce a temperature dependency if only some parts of the spectrum are detected. By measuring the signal power at wavelengths, where vibrational Raman lines from a molecule of interest can be found, and normalizing the signal to a molecular reference signal, uncalibrated mixing ratio profiles are determined [74].

The vibrational signal of nitrogen is often used as molecular reference for derivation of particle backscatter coefficient, water vapor mixing ratio or temperature. Another approach is to use a temperature independent signal from the rotational Raman lines around the Cabannes line [16, 15]. To get a temperature independent signal, two signals with temperature dependency are combined in a predefined ratio. This approach is mostly applied if already the rotational Raman lines for temperature measurements are acquired.

The Raman lines of water vapor, liquid water and ice are collocated in a 10 nm spectral range. The shift for water vapor is 3657 cm^{-2} [10] and is 20 cm^{-1} broad. The ratio between the signal P_{WV} (containing the vibrational Raman backscatter) and a molecular reference signal P_{mol} is proportional to the water vapor mixing ratio. With an independent source for a water vapor profile the ratio is calibrated. Several calibration methods are available [100, 90, 104, 39, 118]. Additionally, as there is a significant wavelength difference, a correction $\Gamma(z)$ for the different extinction coefficients has to be applied. The water vapor mixing ratio $MR(z)$

at range z is calculated with the calibration constant cal

$$MR(z) = cal \frac{P_{WV}(z)}{P_{mol}(z)} \Gamma(z). \quad (2.3)$$

It is sometimes necessary to transfer MR in absolute humidity q . By application of pressure p and temperature T profiles from a radio sounding or the respective surface values and the standard atmosphere, the molecular air density ρ_{air} in height z is derived:

$$\rho_{air}(z) = \frac{p(z)100}{R(T(z) + 273.15K)}. \quad (2.4)$$

R is the universal gas constant. q is then calculated by multiplication of the mixing ratio MR with the air density

$$q(z) = MR(z)\rho_{air}(z). \quad (2.5)$$

The statistical error σMR of a water vapor measurement can be expressed as

$$\sigma MR = cal \frac{P_{WV}}{P_{mol}} \sqrt{\frac{P_{WV} + P_{B_{WV}}}{P_{WV}^2} + \frac{P_{mol} + P_{B_{mol}}}{P_{mol}^2}} \quad (2.6)$$

analog to the statistical error of temperature measurements [14, 53]. There are many vibrational Raman lidars measuring water vapor, e.g. [26, 30, 67, 72, 2, 123], even some with scanning abilities [112, 111, 34, 41] or air-borne [114]. Turbulence studies based on water vapor data from vibrational Raman lidars can be found in [119, 123, 99] and [101].

Chapter 3 The rotational Raman lidar system of University of Hohenheim

The rotational Raman lidar (RRL) of the University of Hohenheim was originally designed as a backscatter lidar with 532 nm excitation laser wavelength [79, 80]. The lidar was modified to detect the rotational Raman signal for temperature measurements [81] in 2007 with an excitation wavelength of 355 nm, which is more suitable for daytime temperature measurements than 532 nm [28]. The RRL participated in two measurement campaigns, PRINCE (PREdiction, Identification and trackiNg of Convective cElls, 2006) [79] and COPS (Convective and Orographically-induced Precipitation Study, 2007). The performance of the system during these campaigns was presented in [79, 82] and [81].

The goal of my PhD thesis was the optimization and modification of the RRL. This included a detailed system check and a redesign of the detection section. The exact laser wavelength was determined and its stability over time measured. The central wavelengths (CWL) of the interference filters were adjusted to the recently determined laser wavelength and a simulation performed to identify the best configurations for different background levels. A recent addition is also a detection channel for the vibrational Raman signal of water vapor (compare section 2.5). With this channel is it possible to retrieve the water vapor mixing ratio. Data analysis programs were developed for that purpose. The performance of the new system design was tested during HOPE (HD(CP)² Observation Prototype Experiment) and presented in [53] and section 4.2. The filter extracting the signal for the first Raman channel was exchanged due



Figure 3.1: Photograph of the mobile platform of the UHOH RRL. The beam steering unit is dismounted during the transport.

to insufficient blocking of the laser wavelength of the existing interference filters. As the filter had to have advanced properties, the design was developed with the manufacturer and the resulting filter characterized during the SABLE (Surface-Atmospheric Boundary Layer Exchange) campaign. The system is housed in a small truck simplifying the transport to measurement sites (see Fig. 3.1). A beam steering unit (BSU) mounted on top of the truck enables measurements in other directions than the vertical. The modifications are described in detail in the following sections and in Appendix A. Results of the optimization are presented in chapter 4.

3.1 Laser performance

The laser source of the UHOH RRL is a frequency-tripled Nd:YAG laser (GCR290-50) from Newport Spectra Physics. Specifications according to the manufacturer were a power of 50 W at 1064 nm, repetition rate of 50 Hz, and a pulse length in Q-Switch mode of 5 to 10 ns. The laser was injection-seeded to achieve a line width of 0.003 nm which is necessary for rotational Raman lidar. With KD*P crystals the second (532 nm) and third harmonic (355 nm) were obtained. Laser power was approximately 10 W or 200 mJ

per pulse for 355 nm. For several reasons we are using only 355 nm for lidar measurements. First, the Rayleigh scattering probability depends on λ^{-4} , which gives a benefit using 355 nm over 532 nm. Also, the solar background is smaller in the UV than in the visible spectrum range. Last but not least the human eye is less sensitive in the UV and eye safety is reached at a higher intensity and smaller distance as with 532 nm. With the current beam divergence, eye-safety is achieved in 350 m distance. These beneficial aspects have higher impact than the fact, that in the second harmonic higher laser power (approximately 25 W) would be available.

For the planned improvements of the system the exact wavelength of the laser had to be determined. As the rotational Raman lines of nitrogen are spaced approximately 0.1 nm from each other, the laser wavelength has to be known with a precision of at least 0.01 nm to select the most suitable central wavelengths for temperature retrieval. The stability of the wavelength over a longer time period like 3 hours was also of interest. The wavelength should change less than 1% over this time period. Therefore the laser was characterized using the Wavemeter WSU-432 from High Finesse. It has an absolute accuracy of 1 pm at 355 nm, which is sufficient in this case. The exact wavelength of the third harmonic is 354.83(0) nm (injection-seeded) and the line width is around 0.001 nm. A long-term measurement was performed over 4 hours (starting after a warm up of around half an hour). The wavelength drifted 70 fm in four hours, which is approximately 17 fm per hour. Even longer measurements would show if this trend persists. The results already gave an indication, that the wavelength shift during a measurement of several hours is negligible.

3.2 New design of the polychromator

Like described in detail in section 4.2 simulations for the optimum central wavelengths were performed. Another aspect of the improvement was the length of the signal way in the polychromator. Overlap issues appear if the beam has not equal diameter and divergence at every interference filter and photomultiplier in the sequence. With the original setup the minimal distance between two

filters was approximately 50 cm, which resulted in a total way in the polychromator of 1.5 meters. Limiting is the distance of two filter holders in a right angle to the beam. The ones used had a width of 76 mm mounted on a rotation plate with even larger dimensions and the small angles of incidence (AOI) of about 5° resulted therefore in that long distances. In the workshop designed filter holders, mounted on rails, allow to build more compact with distances between filter surfaces of around 35 cm, which is a reduction of the way of 30%. The AOIs are fixed in this alignment. The filter holders have holes on the bottom, which allow pivot teeth to connect to corresponding holes in the base plates. In the following the filter holders are secured with screws. It is possible with this technique to dismount the filters for transport and mount them again without changing the AOI. In case of the second rotational Raman channel two AOIs were identified for different background levels. One of the pivot teeth can be fixed in two different positions to realize the two settings. Details can be found in [53] and section 4.2.

3.2.1 Water vapor channel

A detection channel for the vibrational Raman signal of water vapor was added. Therefore the exact wavelength of the vibrational Raman line of water vapor including the surrounding rotational Raman lines was determined. Avila et al. calculated a shift in wavenumber for the strongest line of 3657 cm^{-1} [10] with a total width of 20 cm^{-1} , which results in 407.7 nm for an excitation with 354.83 nm for the main line. This wavelength region has to be separated from the excitation line and the accompanying pure rotational Raman lines, therefore a dichroic beam splitter was mounted just after the parallelizing lens and before the daylight rejecting filter ($355\text{ nm} \pm 5\text{ nm}$). The beam splitter was produced by Chroma Technology Corp. and has a transmission of 0.93 at 355 nm and a reflection of about 0.95 at 408 nm. The interference filter in front of the photomultiplier was produced by Materion Precision Optics and Thin Film Coatings Inc. and has a bandwidth of 0.3 nm and a transmission of 0.55 at the central wavelength. As the optical density (OD) is 10^8 at 355 nm, it is not necessary to use an additional filter to reject the laser wavelength. The filter bandwidth of 0.3 nm should make

temperature sensitivity negligible [113]. Originally it was planned to use two equal filters to avoid signal leakage and to reduce the daylight background. But it showed during the measurements that it did not yield a significant advantage as the main solar background source was the filter transmission band itself and not the OD3 for other wavelengths. It has to be mentioned that in case of low level clouds (around 1 km altitude) and sunshine the background level rises significantly, so that the data cannot be used for further analysis anymore. The second filter could also not prohibit this effect, therefore it had to be taken into account at the data analysis. First measurements with the water vapor channel are shown in section 4.2 and more detailed ones in section 4.4.

3.2.2 Design of a new interference filter for the lowJ channel

The optimum position of the first Raman channel (lowJ) is near the excitation wavelength, as the intensity of Raman lines found in this region is almost independent of temperature or even decreasing with increasing temperature (compare section 2.4). As the intensity of the second filter is in every case increasing with increasing temperature, this position is suitable. Separating the signal with interference filters from the Cabannes line is difficult due to two counteracting effects: a high transmission in the passband is preferable but on the other side a sufficient blocking of the elastically scattered excitation wavelength is critical. The elastic backscatter is 10^6 times higher than the Raman signal within optically dense clouds in low altitudes. Therefore a blocking of OD6 is required in a wavelength shift of around 0.5 nm to the passband peak transmission. The construction of such an interference filter is quite challenging. As it was easier to produce ones with OD3, two filters ($Tr=0.6$, FWHM 0.3 nm, OD3) were purchased for PRINCE and implemented in sequence resulting in a peak transmission of approximately $Tr=0.34$.

In actual measurements it became apparent that the summed optical density was less than 6 as signal leakage could be observed within low level clouds. A leakage correction was applied by subtracting a certain percentage of the elastic signal from the Raman signal, but

this adds a possible systematic error to the data product. Therefore it was decided to update the lidar system with an interference filter with sufficient blocking properties. More advanced technology enabled Materion Precision Optics and Thin Film Coating Inc. to design a filter to our specification: $Tr > 0.5$, 0.3 nm bandwidth, central wavelength of 354.20 nm for AOI 5° and $OD > 6$ for 354.83 nm. The new filter consists of two glass plates and is blocking the excitation wavelength with more than OD_6 . First measurements with the new filter took place during the SABLE campaign. Measurements under cloudy conditions verified the optical density of the filter given by the manufacturer (see section 4.3).

3.3 Resulting system

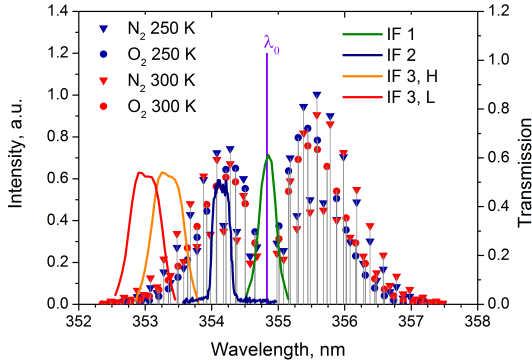


Figure 3.2: Rotational Raman spectrum including the current filter positions and shapes. Two different positions for the highJ filter (IF3) are realized for different background conditions. The lowJ filter (IF2) as the newest has almost a rectangular transmission passband [55].

The system was upgraded to the up-to-date status in August 2014. Most apparent changes to the system of 2007 are the addition of the water vapor channel and the application of only one, superior interference filter in front of the lowJ channel. Additionally the highJ filter can be switched between two distinct angles to increase the performance during different solar backgrounds. The current positions of the filter transmission passbands in comparison with the rotational Raman spectrum can be found in Fig. 3.2.

The impact of the changes on the measurement performance is presented in the following chapter 4. Table 3.1 includes the current filter parameters and selected filter passbands and the corresponding angles of incidence.

Filter	IF0	IF1	IF2	IF3	IF4
AOI, °	0.0	4.8	5.0	4.8/6.2	3.9
CWL, nm	353.65	354.83	354.15	353.30/353.05	407.7
FHWM, nm	8.5	0.29	0.29	0.52	0.30
Peak Transmission, a.u.	0.56	0.62	0.52	0.52	0.79
Transmission at 354.83 nm	0.56	0.62	$<10^{-6}$	$<10^{-6}$	$<10^{-8}$

Table 3.1: Parameters and chosen AOI of the interference filters. CWL: central wavelength, FWHM: full width at half maximum

Chapter 4 Temperature and water vapor mixing ratio measurements

4.1 Vertical temperature measurements

In the frame of the HD(CP)² (High Definition of Clouds and Precipitation for advancing Climate Prediction) project an experiment was performed, called HOPE. HD(CP)² is dealing with the development and validation of a high resolution weather forecast model based on ICON. Goal of the measurement campaign was the acquisition of a data set for atmospheric model verification and to show that state-of-the-art systems are able to acquire data in the required resolution. Therefore several systems were accumulated to measure atmospheric variables in a high spatial and temporal resolution. Included were lidars, microwave radiometers, radio soundings, radars, sun photometers and in-situ measurements. The campaign took place during April and May 2013 near the research center Jülich. The area was chosen because there were already some stationary instruments based in the vicinity. All mobile instruments were divided in three supersites so that a complete data set could be measured at each site. The sites were arranged in a triangle with a base length of approximately 4 km so that the area in between could be sampled from several sides. The instruments of University of Hohenheim were grouped with the KITcube on one supersite. The KITcube is an arrangement of several instruments including a Doppler lidar, microwave radiometer and a 30 meter high mast [61], operated by the Karlsruhe Institute of Technology (KIT). The UHOH RRL and the scanning water vapor DIAL (UHOH WV DIAL) [106] completed

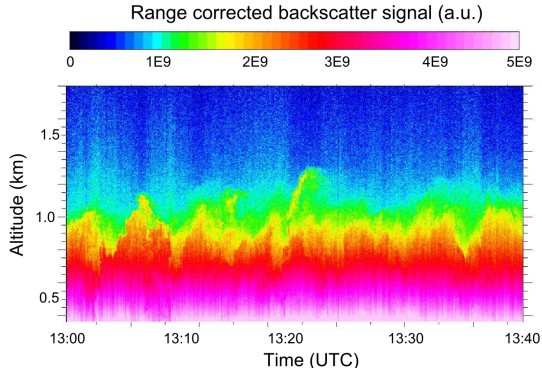


Figure 4.1: Range corrected elastic backscattered signal from 19 May 2013, 13:00-13:40 UTC.

this data set. In Appendix B.1 a table with measurement times and modes can be found. Intensive observation period (IOP) days were announced beforehand if a suitable weather situation was expected. As some instruments including the RRL are not rain safe, IOPs only covered dry days or till a frontal rain event arrived (e.g. IOP 8). Most of the time the RRL was pointing vertical, so that profiles enabled the retrieval of turbulence profiles and sensible heat flux (in combination with data from a Doppler lidar). Details on the system and the measurements can be found in section 4.2. Profiles recorded during IOP 5 were used in section 5.4. Measurements from IOP 6 were used for the turbulence study presented in [17] (section 5.1) and for the master thesis of Stephan Adam [3].

Figure 4.1 shows an example of a measurement of the elastic backscattered signal on 19 May 2013 from 13:00 to 13:40 UTC. These are range and background corrected 1 s profiles and show in detail the turbulent features in the convective boundary layer. This time period was analyzed in respect to temperature, potential temperature, temperature gradient and water vapor mixing ratio. Results are presented in section 4.2 and 5.3.

4.2 Hammann et al., 2015, Atmospheric Chemistry and Physics

This publication contains the measurement configuration and selected measurement examples acquired during the HOPE campaign. The scientific goals were the acquisition of high resolution data sets of several atmospheric variables. Additionally recent changes in the lidar setup could be tested. These were in detail the addition of a detection channel for the vibrational Raman scattering of water vapor and the implementation of a high to low background switch, which increased the measurement performance at day- and nighttime. As examples for the measurement performance, measurements of the temperature gradient and water vapor mixing ratio revealing the development of the atmospheric boundary layer within 25 h are presented.



Temperature profiling of the atmospheric boundary layer with rotational Raman lidar during the HD(CP)² Observational Prototype Experiment

E. Hammann¹, A. Behrendt¹, F. Le Mounier², and V. Wulfmeyer¹

¹University of Hohenheim, Institute of Physics and Meteorology, Garbenstrasse 30, 70599 Stuttgart, Germany

²Laboratoire de Météorologie Dynamique, C.N.R.S, Paris, France

Correspondence to: E. Hammann (eva.hammann@uni-hohenheim.de)

Received: 22 July 2014 – Published in Atmos. Chem. Phys. Discuss.: 21 November 2014

Revised: 6 February 2015 – Accepted: 16 February 2015 – Published: 12 March 2015

Abstract. The temperature measurements of the rotational Raman lidar of the University of Hohenheim (UHOH RRL) during the High Definition of Clouds and Precipitation for advancing Climate Prediction (HD(CP)²) Observation Prototype Experiment (HOPE) in April and May 2013 are discussed. The lidar consists of a frequency-tripled Nd:YAG laser at 355 nm with 10 W average power at 50 Hz, a two-mirror scanner, a 40 cm receiving telescope, and a highly efficient polychromator with cascading interference filters for separating four signals: the elastic backscatter signal, two rotational Raman signals with different temperature dependence, and the vibrational Raman signal of water vapor. The main measurement variable of the UHOH RRL is temperature. For the HOPE campaign, the lidar receiver was optimized for high and low background levels, with a novel switch for the passband of the second rotational Raman channel. The instrument delivers atmospheric profiles of water vapor mixing ratio as well as particle backscatter coefficient and particle extinction coefficient as further products. As examples for the measurement performance, measurements of the temperature gradient and water vapor mixing ratio revealing the development of the atmospheric boundary layer within 25 h are presented. As expected from simulations, a reduction of the measurement uncertainty of 70 % during nighttime was achieved with the new low-background setting. A two-mirror scanner allows for measurements in different directions. When pointing the scanner to low elevation, measurements close to the ground become possible which are otherwise impossible due to the non-total overlap of laser beam and receiving telescope field of view in the near range.

An example of a low-level temperature measurement is presented which resolves the temperature gradient at the top of the stable nighttime boundary layer 100 m above the ground.

1 Introduction

In recent years, different techniques for measuring the atmospheric temperature profile with lidar have been developed, namely the rotational Raman technique, the integration technique (using elastic and Raman signals), and the resonance fluorescence technique, as well as the high-spectral-resolution lidar (HSRL) technique and differential absorption lidar (DIAL) (see Behrendt, 2005, for an overview). For daytime measurements in the troposphere, rotational Raman lidar (RRL) is presently the most reliable technique. Its capabilities in providing temperature profiles with high temporal and spatial resolution and low systematic and noise errors during night- and daytime even within aerosol layers and thin clouds are superior so far to all other techniques, particularly where measurements from the surface to the lower troposphere are concerned (Behrendt and Reichardt, 2000; Behrendt et al., 2002, 2004; Di Girolamo et al., 2004; Arshinov et al., 2005; Radlach et al., 2008).

Most rotational Raman systems operate at wavelengths of 532 or 355 nm, the second and third harmonic wavelengths of Nd:YAG lasers. UV systems are able to perform daytime measurements with lower uncertainties due to the higher backscatter cross section and less solar background (Zeyn et al., 1996; Behrendt, 2005). The rotational Raman lidars of

NASA's Goddard Space Flight Center (Di Girolamo et al., 2004), of the University of Hohenheim (UHOH; Radlach et al., 2008), of the University of Basilicata (Di Girolamo et al., 2009), of Xi'an University (Mao et al., 2009), and of Hampton University (Su et al., 2013) all operate in the UV with interference-filter polychromators. Rotational Raman lidars at 532 nm show lower performance during daytime but reach a larger range at night than an UV system due to the higher laser power available at 532 nm compared to 355 nm, higher efficiency in signal separation, and lower atmospheric extinction. Some of the systems at 532 nm are also based on interference filters (Behrendt and Reichardt, 2000; Behrendt et al., 2002, 2004; Achtert et al., 2013), and some employ double-grating polychromators (Balin et al., 2004; Arshinov et al., 2005).

Daytime temperature measurements are the main focus of the RRL of UHOH. But besides temperature, also the particle backscatter coefficient and the particle extinction coefficient can be measured independently. Furthermore, the system was extended recently with a water vapor Raman channel. For water vapor measurements, two different lidar techniques are available: the DIAL technique and the Raman lidar technique. While water vapor Raman lidar uses the vibrational Raman backscatter signals of water vapor (e.g., Melfi et al., 1969; Whiteman et al., 1992; Turner and Goldsmith, 1999; Leblanc and McDermid, 2008), the DIAL technique (Schotland, 1974; Wulfmeyer and Bösenberg, 1998; Behrendt et al., 2009; Wagner et al., 2013) relies on the different absorption of water vapor at two nearby wavelengths. In contrast to water vapor (WV) DIAL, whose self-calibrating property leads to a high accuracy of the measurements (Bhavar et al., 2011), a water vapor Raman lidar has to be calibrated and shows also lower performance during daytime. However, the laser transmitter is less complex, and, if a certain lidar system already contains rotational Raman channels, only one more detection channel is needed to derive in addition the water vapor mixing ratio (Behrendt et al., 2002). Thus it was decided to extend the UHOH RRL with a water vapor channel. Furthermore, this capability permits relative humidity measurements, which are, e.g., useful for aerosol (Wulfmeyer and Feingold, 2000) and convection initiation studies (Behrendt et al., 2011; Corsmeier et al., 2011). In parallel to the RRL, the UHOH has developed also a water vapor DIAL (Wagner et al., 2013), from which recent measurements are presented in Muppa et al. (2014).

Within the High Definition of Clouds and Precipitation for advancing Climate Prediction (HD(CP)²) project, a new model for high-resolution weather forecasts will be developed (Stevens and Bony, 2013) and other model systems will be tested (Schwitalla and Wulfmeyer, 2014). To verify the model, high-resolution data sets are required. The HD(CP)² Observation Prototype Experiment (HOPE), which provides such a data set, took place during April and May 2013 in the area around the Research Center Jülich in north-

west Germany. The area already had an existing infrastructure of dense standard meteorological instrumentation.

Both systems of UHOH were operated together in the HOPE field campaign and thus provided a synergetic data set of thermodynamic properties of the atmosphere. The lidars were located at one supersite (50°53'50.55" N, 6°27'50.27" E, 110 m above sea level) close to the village of Hambach together with the KITcube, an instrument suite of the Karlsruhe Institute of Technology (KIT) (Kalthoff et al., 2013). The site was on a hillside and elevated above the surroundings by 10 to 15 m. The RRL and the WV DIAL of UHOH were collocated with a Doppler lidar from KIT to acquire a complete data set of temperature, water vapor content, and vertical wind for the determination of fluxes of sensible and latent heat (e.g., Behrendt et al., 2011). It was also the launch site for radiosoundings.

The purpose of this paper is to introduce the measurement performance of the UHOH RRL during HOPE and present highlights of the measurements. One highlight was the application of a novel switch for low- and high-background RRL. During the 18 intensive observation periods more than 200 h of measurements were collected. Measurements took place in the time between sunrise and sunset and were stopped in the case of rain or continuing dense cloud cover. In addition there were two night-long measurements. On one day, RHI (range–height indicator) scans were performed. During one day and one night, the lidar was pointed at a low elevation above the ground. Water vapor measurement started at the beginning of May; therefore only 100 h of water vapor data is available. Case studies using the combination of data from the instrument set – and also from the other two supersites – are in preparation and will be presented later based on the results shown here.

The main research interest of our institute is land–surface–atmosphere feedback, which requires measurements of land–surface exchange, the surface layer, the atmospheric boundary layer, and the lower free troposphere. For investigating not only mean profiles or mean three-dimensional fields but also the turbulent features of the convective boundary layer, instruments providing data with high temporal and spatial resolution in conditions of high-background light are needed. The rotational Raman lidar of UHOH was optimized for such conditions. A new technical feature, which was implemented during the HOPE campaign, was a switch to optimize the performance of the temperature measurements for low- and high-background conditions. Detailed simulations were performed which showed that it is favorable to use another pair of filter center wavelengths in low-background conditions compared to cases with high solar background. The change between the settings can be made in a few minutes. Thus, it was possible to switch easily between the settings and acquire continuous time periods of data which included such changes.

This paper is structured as follows: in Sect. 2 the new setup of the UHOH RRL is explained. Also the simulations for two

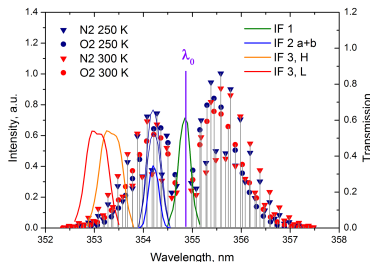


Figure 1. Rotational Raman spectrum of atmospheric nitrogen and oxygen for an excitation wavelength λ_0 of 354.83 nm and for two temperatures (250 and 300 K). Transmission curves of the interference filters are shown for comparison. Although the Stokes lines ($\lambda > \lambda_0$) are more intense, anti-Stokes lines ($\lambda < \lambda_0$) are used by us to avoid possible measurement errors due to fluorescence (Immler et al. 2005). For IF3, the filter positions for both the low- and high-background settings are shown (L and H, respectively).

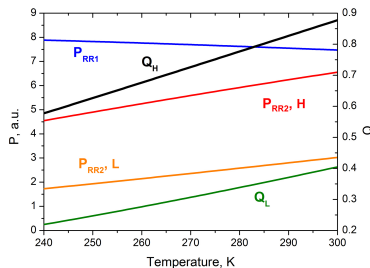


Figure 2. Simulated signal intensities for the filter configurations shown in Fig. 1: rotational Raman signal intensities for the H and L setting and corresponding ratios $Q = P_{RR2}/P_{RR1}$.

settings for the second rotational Raman channel are presented. Section 3 discusses the experimental results of the new system. Section 4 gives a short summary.

2 Methods and performance simulations

2.1 Methods

The rotational Raman lidar of UHOH makes use of the rotational Raman technique for deriving atmospheric temperature profiles (Cooney, 1972). Two parts of the rotational Raman spectrum of air with different temperature depen-

gency are acquired (see Fig. 1). By taking the ratio of the two signals (Fig. 2) and calibrating it, the temperature is obtained without further assumptions about the state of the atmosphere. Figure 2 shows how the rotational Raman signals P_{RR1} and P_{RR2} depend on the temperature. For P_{RR2} there are the two settings shown in Fig. 1 with different central wavelengths CWL2: one for low-background (L) and one for high-background (H) conditions. The setting L results in a lower signal intensity in the second Raman channel. Also the ratio Q between P_{RR2} and P_{RR1} is lower and has a different slope than the one for the H setting. There are several formulas in use for the calibration (Behrendt and Reichardt, 2000; Behrendt, 2005). For temperature measurements up to a few kilometers altitude, the following equation can be used:

$$Q(T) = \exp\left(a - \frac{b}{T}\right), \quad (1)$$

where Q is the ratio between the background-corrected signals in the Raman channels RR2 and RR1, and a and b are calibration constants. This equation is exact for the ratio of two single rotational Raman lines. If several rotational Raman lines are extracted by the two channels, more complicated equations with more constants are needed when temperature measurements are made over a larger range of temperatures (Behrendt and Reichardt, 2000; Behrendt, 2005). This is not the purpose here, so this equation can still be used and results in a high accuracy of the inversion. Therefore the atmospheric temperature can be derived from Q by rearranging Eq. (1) to

$$T = \frac{b}{a - \ln(Q)}. \quad (2)$$

The statistical error of the temperature measurements can be determined from the signal intensities of the photon-counting data and applying Poisson statistics. For a signal with count number s , the 1σ statistical error is

$$\Delta s = \sqrt{s}. \quad (3)$$

This results in a noise error for the temperature ΔT (Behrendt et al., 2002) of

$$\Delta T = \frac{\partial T}{\partial Q} Q \sqrt{\frac{P_{RR1} + P_{B1}}{P_{RR1}^2} + \frac{P_{RR2} + P_{B2}}{P_{RR2}^2}}. \quad (4)$$

P_{RR1} is the background-corrected signal in the first Raman channel, P_{B1} the background in this channel, and P_{RR2} and P_{B2} are the same for the second Raman channel. This equation is valid if ΔP_B is 0, which is a valid approximation if the background is calculated from a high number of bins. One can see from Eq. (4) that the error ΔT scales with

$$\Delta T \sim \frac{1}{\sqrt{P T A \eta}}, \quad (5)$$

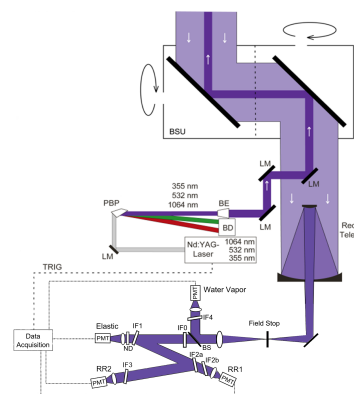


Figure 3. Setup of the rotational Raman lidar of the University of Hohenheim. LM stands for laser mirror, and the wavelengths are separated by a Pellin–Broca prism. Whereas 532 and 1064 nm are sent to a beam dump (BD), 355 nm is expanded by a beam expander (BE) and sent to the atmosphere through the beam steering unit (BSU). Angles in the polychromator are enlarged for clarity. IF0 is a daylight opressing filter (see Table 1 for details). IF1 to IF4 are the interference filters, BS is a beam splitter to separate the vibrational Raman lines from the elastic backscattered and rotational Raman signal. In front of the elastic channel a neutral density filter (ND) is mounted. Photomultipliers are marked with PMT.

where P is the laser power, t the integration time, A the telescope area, and η the overall detection efficiency.

The statistical error ΔT_{Grad} of a temperature gradient measurements is then

$$\Delta T_{\text{Grad}} = \frac{\sqrt{2} \Delta T}{\Delta r}, \quad (6)$$

with Δr being the range interval over which the gradient was calculated.

The two rotational Raman signals can also be used to form a temperature-independent reference signal P_{RR} for the determination of the particle backscatter coefficient, the particle extinction coefficient, or the water vapor mixing ratio (Behrendt et al., 2002, 2004).

The water vapor mixing ratio (MR) at a distance r is calculated with

$$\text{MR}(r) = C \cdot \frac{P_{\text{WV}}(r)}{P_{\text{RR}}(r)} \Gamma(r), \quad (7)$$

where C is a calibration constant, and P_{WV} and P_{RR} are the background-corrected signals of the vibrational Raman line

of water vapor and the rotational Raman lines of nitrogen and oxygen, respectively (Whiteman et al., 1992; Sherlock et al., 1999). $\Gamma(r)$ is a correction for the different atmospheric extinction Γ at the two wavelengths λ_{RR} and $\lambda_{\text{H}_2\text{O}}$:

$$\Gamma(r) = \frac{\exp\left[-\int_{r_0}^r \alpha(\lambda_{\text{RR}}, r') dr'\right]}{\exp\left[-\int_{r_0}^r \alpha(\lambda_{\text{H}_2\text{O}}, r') dr'\right]}. \quad (8)$$

To determine the calibration constant C , a collocated radiosounding can be used. It was found that a correction for the different extinction coefficients of the two wavelengths is negligible for ranges of up to a few kilometers because the difference is less than 0.1 % up to 3 km.

The statistical error of the water vapor measurements can be calculated with Poisson statistics, and one gets

$$\Delta \text{MR} = C \frac{P_{\text{WV}}}{P_{\text{RR}}} \sqrt{\frac{P_{\text{WV}} + P_{\text{BWV}}}{P_{\text{WV}}^2} + \frac{P_{\text{RR}} + P_{\text{BRR}}}{P_{\text{RR}}^2}}. \quad (9)$$

While the error analysis based on Poisson statistics determines the so-called shot noise errors, the total statistical error can be estimated with an analysis of the turbulent fluctuations in the atmosphere (Lenschow et al., 2000). For this, data with high temporal resolution are needed in order to resolve the timescale of these fluctuations. The method based on the analysis of the autocovariance function was developed in Senff et al. (1994) and Wulfmeyer (1999a, b) and summarized in Lenschow et al. (2000). Recently, this technique was applied to WV DIAL (e.g., Muppa et al., 2014) and Doppler lidar data (Lenschow et al., 2012), elastic backscatter lidar data (Pal et al., 2010), and water vapor Raman lidar data (Wulfmeyer et al., 2010; Turner et al., 2014a, b). Recently it was applied for the first time to temperature lidar data by using measurements of the UHOH RRL during HOPE (Behrendt et al., 2014). The comparison between the errors derived with Poisson statistics and turbulence analysis confirms that the total statistical error is mainly due to photon shot noise.

2.2 Current setup

The rotational Raman lidar of UHOH aims at measurements in the atmospheric boundary layer and lower free troposphere during daytime. A scheme of the setup is shown in Fig. 3. As a laser source, an injection-seeded frequency-tripled Nd:YAG laser (Spectra Physics GCR290-50) is used. Only the third harmonic radiation at 354.83 nm is transmitted into the atmosphere. The human eye is less sensitive to UV wavelengths than to wavelengths in the visible spectrum, and therefore eye safety is achieved at even smaller distances for UV lidars than for lidars using, e.g., the second harmonic radiation of a Nd:YAG laser. In consequence, the first and second harmonics are separated in the transmitter from the third using a Pellin–Broca prism and directed into beam dumps. The separation by a prism is preferable to a beam splitter due

Table 1. Parameter of interference filters. AOI: angle of incidence; CWL: central wavelength; FWHM: full width at half maximum.

	IF0	IF1	IF2a	IF2b	IF3	IF4
AOI, deg	0	4.8	6.0	6.0	4.8/6.2	3.9
CWL, nm	355	354.8	354.15	354.15	353.30/353.05	407.7
FWHM	8.5	0.3	0.3	0.3	0.5	0.3
Peak transmission	0.56	0.62	0.53	0.65	0.52	0.75
Refl. at 354.8 nm		< 0.1				
Transm. at 354.8 nm	0.56	0.62	$< 1 \times 10^{-3}$	$< 1 \times 10^{-3}$	$< 1 \times 10^{-6}$	$< 1 \times 10^{-7}$

to the fact that the wavelengths are separated spatially, and definitely no radiation at the other wavelengths remains in the outgoing light. The transmitted power in the UV is around 10 W at a repetition rate of 50 Hz. The beam is expanded by a factor of 6.5 to prevent damage on the transmitting optics and to achieve eye safety in less than 400 m distance (taking also hotspots in the beam profile into account). The expanded beam is directed via three mirrors (10 cm diameter) onto the first mirror of the beam steering unit. Together with a second mirror, this setup enables us to direct the beam to any azimuth and elevation angle of interest. The whole system is mounted on a mobile platform which can be moved to different measurement sites for field campaigns.

The receiving telescope is of the Ritchey–Chrétien–Cassegrain type. Its primary mirror has a diameter of 40 cm. To reduce the daylight background, the focused signal passes a pinhole with selectable diameter. The diameter was set to 3 mm during the HOPE campaign, which results in a full field of view of 0.75 mrad. After passing this field stop, the light is parallelized with a lens and then split by a dichroic beam splitter: while light with wavelengths shorter than 375 nm is transmitted into the main receiver unit, longer wavelengths are reflected. The vibrational-rotational Raman signal of water vapor excited by 354.83 nm is shifted by wavenumbers around 3657.05 cm^{-1} (e.g., Avila et al., 2004) from the excitation wavelength and is thus around 407.7 nm and obtained from the light reflected by the beam splitter. The transmission efficiency of the beam splitter is 0.93 for 355 nm and 0.02 for 408 nm. Reflectivity at 408 nm is above 0.95.

The signal transmitted by the beam splitter passes a daylight-reducing filter IF0 (Eureca, peak transmission of 0.56) and enters the main part of the receiver for the detection of the elastic and rotational Raman signals, which are sequentially mounted (Behrendt and Reichardt, 2000; Behrendt et al., 2002, 2004; Radlach et al., 2008). In front of the first rotational Raman channel, two identical interference filters IF2a and IF2b are used to achieve sufficient suppression of the elastic signal. In Table 1 all filter parameters are listed. The first filter pair has a transmission of 0.34 for 354.15 nm and 10^{-6} for 354.83 nm. The passbands have a full width at half maximum of 0.3 nm. The filter for extracting the second rotational Raman signal can be toggled between two distinct angles to optimize the performance of temperature measure-

ments during conditions of high and low background (see below). For the time being, the change of setting has to be done manually, but the angles are fixed by a pivot tooth. IF3 has a peak transmission of 0.52 and is 0.5 nm wide. The angles of incidence are 6° for the interference filters IF2a and b, and 4.8 and 6.2° for the second interference filter for the high- and low-background setting, respectively. The beam divergence in the polychromator is 0.45° as determined by experimentally validated ray tracing calculations. All narrowband interference filters were manufactured by Materion, Barr Precision Optics & Thin Film Coating. As photomultiplier for the rotational Raman signals, a Hamamatsu R1924P is used. The elastic channel is equipped with a neutral density filter (transmission of 0.2) to prevent saturation of the photomultiplier (Hamamatsu R7400-U02) in the presence of optically thick clouds in the near range.

In the branch of the water vapor channel, an interference filter (IF4) transmits the desired wavelength range; for details see Table 1. The total suppression has an efficiency better than 10^{-8} for 355 nm and 10^{-6} for other wavelengths. The signal is focused on a photomultiplier (Hamamatsu R1924P) for detection.

Presently, two data acquisition systems are used for the four lidar signals. First, there is a transient recorder (LICEL GmbH, Berlin) with three acquisition channels. Each photomultiplier signal is recorded in analog mode with 3.75 m range resolution and in photon-counting mode with range resolutions of 3.75 and 37.5 m (see Table 2). The measurement data shown here were all derived with the analog data. In standard operation, backscatter signals of 500 shots are averaged to get a profile with 10 s integration time. At the beginning of the HOPE campaign, the elastic signal and the two Raman channels were recorded with this system. From early May on, the water vapor detection channel signal was implemented and its signal was recorded with the LICEL data acquisition instead of the elastic signal. The strong elastic signal was then stored with a transient recorder system (Compuscope 14100 card of GaGe Applied Inc.) with resolutions of 3 m and 1 s, albeit only in analog mode.

The data analysis contains the following steps. First, the photon-counting data are corrected for photomultiplier dead-time effects. A dead time of 4.8 ns was determined by comparing the analog with the photon-counting signal and used

Table 2. Signal raw resolution.

Raw data	Temporal resolution	Spatial resolution	Recording mode
Elastic signal	10 s	3.75 m	Analog + photon-counting
	10 s	37.5 m	Photon-counting
	1 s	3 m	Analog
Rotational Raman 1	10 s	3.75 m	Analog + photon-counting
	10 s	37.5 m	Photon-counting
Rotational Raman 2	10 s	3.75 m	Analog + photon-counting
	10 s	37.5 m	Photon-counting
Vibrational water vapor	10 s	3.75 m	Analog + photon-counting

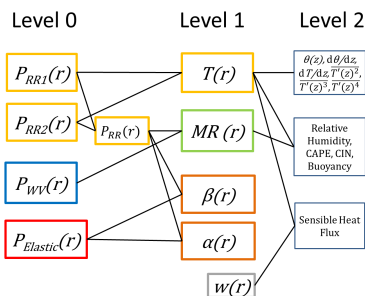


Figure 4. Diagram of the data products. Level 0 data are the background-corrected rotational Raman signals (yellow), the vibrational Raman signal of water vapor (blue), and the elastic backscatter signal (red). A temperature-independent reference signal P_{RR} is obtained from the temperature-dependent rotational Raman signals. Level 1 data products are temperature T , water vapor mixing ratio MR, particle backscatter coefficient β , and particle extinction coefficient α . Higher-level products derived from level 1 data: potential temperature θ , gradient of temperature and potential temperature, higher moments of turbulent temperature fluctuations T' , relative humidity, buoyancy, CAPE, and CIN. For deriving the sensible heat flux, profiles of the vertical wind w , e.g., from a Doppler lidar, are used.

for the correction. It has to be noted that the dead time not only is influenced by the photomultiplier alone but also depends on the data acquisition system. Then, the signals are background-corrected and smoothed in range and time with gliding average lengths that depend on the noise conditions and application. For example, for turbulence analysis (Behrendt et al., 2014) high temporal resolution of 10 s is needed, while for studies of the temperature gradient a low statistical error is essential. How the statistical error is affected by the averaging can be seen in Eq. (5). Temperature and other data products are then determined with the ana-

log and photon-counting signals separately and merged afterwards if needed. We found that the alternative approach of first merging the analog and photon-counting signals and then deriving the data products in a second step with the merged signals (Newsom et al., 2009) results in unstable temperature calibration functions because the merging procedure produces small erroneous fluctuations which influence the temperature measurements critically. To determine the statistical uncertainties of the data, the analog data are scaled to the photon-counting signals in order to attribute virtual count rates to the analog data (Whiteman et al., 2006). It turned out that this scaling results in accurate shot noise error estimates also for the analog data. In Behrendt et al. (2014) it is shown that the total statistical error depends mainly on the noise error. It is therefore possible to obtain a good error estimation by calculating the shot noise error through Poisson statistics.

From the combination of the two temperature-dependent signals, a temperature-independent molecular reference signal can also be obtained. The weighted sum of the signals with a weighting factor that depends on the system characteristics (Behrendt et al., 2002) can be used as a reference signal for the calculation of the water vapor MR, particle backscatter coefficient β , and extinction coefficient α (see also Fig. 4); no further vibrational nitrogen Raman signal like that used in other Raman lidar systems is needed. It should also be noted that the statistical uncertainty of the rotational Raman reference signals is lower than the uncertainty of the weaker nitrogen vibrational Raman signal.

The measured temperature profiles can be used to further derive, e.g., profiles of potential temperature θ , temperature gradients, variance, or other higher-order moments of turbulent temperature fluctuations (Behrendt et al., 2014). If profiles of vertical wind w are available with high temporal resolution, e.g., from a Doppler lidar, the sensible heat flux can be calculated. Also other products – like buoyancy (Corsmeier et al., 2011), CAPE (Convective Available Potential Energy), and CIN (Convective Inhibition) (Behrendt et al., 2011) – are possible.

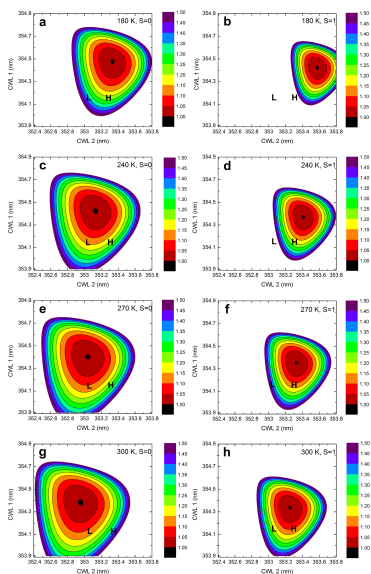


Figure 5. Statistical temperature uncertainty ΔT for different central wavelengths (CWL) of the RR filters. (a), (c), (e), and (g) are without background ($S = 0$); (b), (d), (f), and (h) are with background ($S = 1$). H denotes the configuration selected for high-background measurements, L the configuration for low-background measurements. The uncertainty values were normalized to the smallest value of each plot. The laser wavelength is 354.83 nm.

2.3 Determination of optimum configurations for low and high background

A switch for the central wavelength of the interference filter of the second rotational Raman channel was introduced during the HOPE campaign. By selecting lines for the second (high J) rotational Raman backscatter channel with larger spectral distance to the excitation wavelength, one can enhance the temperature sensitivity of the system. But while these lines are more temperature sensitive, they are also weaker in intensity. Consequently, there is a tradeoff between temperature dependence and signal intensity, which results in optimum settings which depend on the signal background relative to the Raman signal intensities (Radlach, 2009). In the following, refined simulation results on this

problem of lowest-possible statistical uncertainty of the temperature measurements depending on the background are presented. While the passband of the second rotational Raman channel is changed, the passband of the first rotational Raman channel (low J) stays constant. The RR1 channel is already so close to the laser wavelength that further change to weaker signals would decrease the blocking of the elastically backscattered light in the signal to critical values.

Refined simulations to what had already been described by Radlach et al. (2008) were performed for the present laser wavelength, with the goal of finding an optimum setting for the central wavelength of the second rotational Raman channel for high and low background. In the following the central wavelength of the first rotational Raman signal detection channel is called CWL1 and the second CWL2. From Eq. (4), the 1σ statistical uncertainty of temperature measurements can be calculated for two close temperatures T_1 and T_2 with

$$\Delta T = \frac{\partial T}{\partial Q} \Delta Q \approx \frac{(T_1 - T_2)}{(Q_1 - Q_2)} Q \sqrt{\frac{P_{RR1} + P_{B1}}{P_{RR1}^2} + \frac{P_{RR2} + P_{B2}}{P_{RR2}^2}}. \quad (10)$$

A simulation of the spectrum at two temperatures T_1 and T_2 5 K apart combined with the filter transmission curves gives the ratio Q of the two channels. Scaling parameters of the background are the ratio of the background per 0.1 nm filter bandwidth and the intensity P_J^{\max} of the strongest line of the rotational Raman spectrum (Radlach, 2009). This gives as a background

$$P_B = S \frac{\Delta\lambda_{\text{FWHM}}}{0.1 \text{ nm}} P_J^{\max}. \quad (11)$$

For the scaling factor S we chose 1 in the high-background case and 0 in the low-background case. As the intensity of the Raman signal depends on height but the background is constant for all height bins of a profile, the scaling factor S changes for the different heights of a measured profile and, of course, with the solar background and thus latitude, time of the day, and season as well as the laser power and receiver efficiency of the lidar system. During daytime, S will be nearly 0 at low altitudes for a well-designed high-power lidar with high signal to background ratio, but S will increase quickly with altitude as the signal intensity decreases. With optimizations to $S = 0$ and $S = 1$, one is even prepared for high-background conditions, e.g., near cumulus clouds at noon. It was found that larger values for S do not change the optimum central wavelengths significantly compared to $S = 1$. But as detailed in the following, the differences between $S = 0$ and $S = 1$ are significant, which is the motivation for the new switch.

In Fig. 5 the results of the simulations are presented for both high and low background for temperature regimes of 180, 240, 270, and 300 K. The simulation was performed assuming a beam divergence of 0.45° on the interference filters in the receiver, which modifies the filter transmission curves accordingly. The beam divergence was chosen in agreement

Table 3. Relative statistical temperature error for the high- and low-background setting of the center wavelength CWL2 of the interference filter of the second (high J) rotational Raman channel (H and L, respectively). S is the scaling factor for the background level (see text for details). While $S = 0$ stands for no background, $S = 1$ characterizes high-background conditions. The resulting relative errors for the selected configurations are bold. With the optimized settings for CWL2 the statistical errors do not exceed 20% higher values than the absolute optimum for atmospheric temperatures between 240 and 300 K.

	$S = 0$				$S = 1$			
CWL2	180 K	240 K	270 K	300 K	180 K	240 K	270 K	300 K
353.30 (H)	1.25	1.27	1.31	1.37	1.52	1.17	1.13	1.14
353.05 (L)	1.36	1.13	1.10	1.10	3.46	1.70	1.39	1.21

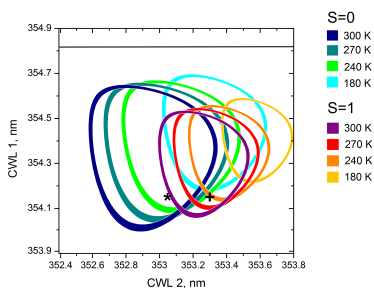


Figure 6. Overview of all cases shown in Fig. 5. The outer and inner borders of the rings mark 1.20 and 1.17 relative uncertainty, respectively. The selected configurations for high- and low-background conditions (marked with + and *, respectively) show lower relative uncertainties than 1.2 for all temperatures between 240 and 300 K (see also Table 3). The grey line marks the laser wavelength.

with the divergence in the polychromator in the current setup. For divergence values between 0.1 and 1.0°, the optimum wavelengths and iso-lines shift by 0.01 and 0.02 nm, respectively. The relative uncertainty ΔT is normalized to the smallest value in each case. The values of ΔT are of course lower during night- than during daytime, but this simulation is made to find an optimum setting within each regime and then compare the optimum settings. The central wavelengths of the first filter are limited to 354.2 nm and smaller to ensure that the elastic signal is blocked sufficiently for this channel.

The central wavelengths were 354.15 nm for CWL1 and 353.30 nm for CWL2 for high-background conditions for the measurements discussed here. With low background at night, this setting is not optimum, and therefore the pair of central wavelengths of 354.15 and 353.05 nm was used for low-background conditions. We use the corresponding angles of incidence mentioned in Table 1. In Fig. 6, an overview of all these temperature regimes is given. One can see that the measurements with our settings are not more than 20% higher

than the minimum uncertainty for all temperatures between 240 and 300 K. But this is only achieved by the two settings for CWL2.

To be able to use the advantages of both wavelengths, it is crucial to be able to toggle between the two settings in a short time period in order to avoid measurement gaps. Furthermore, the setting should be reproducible to avoid changes in calibration or overlap. This is realized by a filter holder which can be fixed by a pivot tooth at two positions. It was built in our workshop and tested on the campaign. Results are shown in Sect. 3.1.

3 Measurement examples

3.1 RR2 switch

To test the performance of the switch, a 24-h measurement was made including changes between the H and L setting. The switching time coincided with a radiosonde launch during nighttime. In general, “low-background” conditions are defined here as the time where the background is small compared to the rotational Raman signals in the altitude range of interest, i.e., between about half an hour after sunset and half an hour before sunrise. This was the case during the consecutive observation periods with a radiosonde launch at 20:00 UTC and early in the morning. All in all, there were three cases for the evaluation of the performance of the switch.

On average it took about 5 min to interrupt the data acquisition in a controlled way, change filter position, readjust the stray-light cover, and restart the data acquisition. When changing from high- to low-background setting, the signal intensity in the second Raman channel decreases, which results in a lower ratio Q (Fig. 7). But, as already discussed above, the relative sensitivity to temperature increases. The enhanced sensitivity is seen in Fig. 8, where the ratio between the two channels is normalized to the value at an arbitrary altitude (here the altitude was chosen in which the temperature profile of the radiosonde was 273 K, which was 2.6 km). In this visualization the different slope can be seen, which is larger for L than for H.

Finally, the Q vs. T curves from simulation and experiment (Fig. 9) are compared. For the experimental data, Q

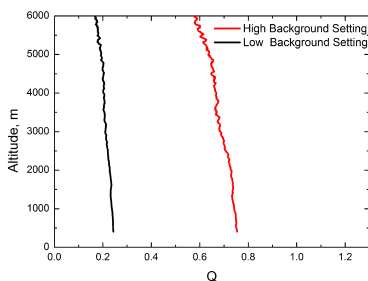


Figure 7. Measured ratio Q of the rotational Raman signals with the high- and low-background setting, H and L, respectively, at night. The data for the setting H were collected between 19:38 and 19:58 UTC on 18 May 2013, and data for the setting L just afterwards between 20:05 and 20:25 UTC. The intensity of the RR2 signal decreased by switching to L, hence the smaller ratio Q . The rotational signals were smoothed with a gliding average of 105 m height before the ratio was calculated.

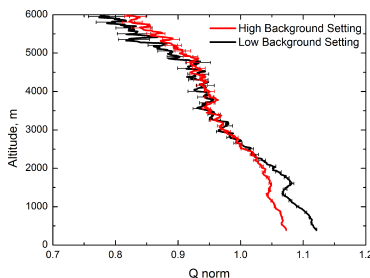


Figure 8. Same as Fig. 7 but normalized to 1 at a height of 2.6 km to illustrate the higher relative sensitivity of the low-background setting. Error bars show the statistical uncertainties.

values were assigned to T values of the radiosonde at the same height. The simulation calculates the resulting Q for temperatures from 240 to 300 K in 1 K steps for the actual filter curves including the central wavelengths. For the low-background setting, simulation and experiment agree very closely within the statistical error bars; for the high-background, a deviation of <1.5 K is found for Q values between 1.0 and 1.05. A comparison with Fig. 8 shows that this is the altitude region where an inversion layer was found. An inversion layer can lead to differences between

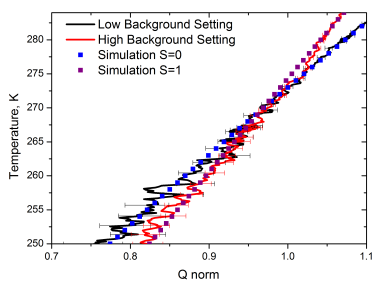


Figure 9. Same as Fig. 8 but against radiosonde temperature at the same height. In addition to the measurements, simulation data for the two settings are shown. In red and black are the measured values for Q with the statistical error, and in blue and violet the corresponding simulation.

radiosonde and lidar measurement due to averaging of the lidar data and sampling of a different air mass. The experimentally determined Q is linked to the temperature values of the radiosounding; a deviation of 1 to 2 K therefore can be attributed to the inversion. As there are for all other temperatures only deviations within the 1σ statistical uncertainties, we conclude that the agreement between experiment and simulation is good.

The statistical errors for different background values with the two settings were calculated. Nighttime measurements were used and, for the high-background case, background added according to a scaling factor of $S = 1$ at 1 km. In comparison with actually measured background values at noon with or without cloud coverage, the used background values are higher because the Raman signals of the UHOH RRL are quite strong. Thus, the comparison shows the performance in circumstances which can be considered a worst-case scenario.

Figure 10 shows the statistical errors with low background (measurement from 20:00 UTC, 20 min average) and both settings. Even during nighttime, there is a background of around 1 photon per bin for the integrated average over 500 laser pulses. Therefore S is not strictly equal to 0, but, in this case, S was less than 0.1 up to 2.1 km for the L setting and up to 3.2 km for the H setting. $S = 1$ was reached at 4.3 and 6.6 km. As expected, the setting L shows smaller errors for low altitudes and is favorable up to 7 km. The simulated error for high background is shown in Fig. 11. The absolute error values are in this case higher than in the case of low background. Below 1 km, S is less than 1, which results in a better performance of the low-background setting than the high-background setting. Above 1 km, S is larger than 1 and the

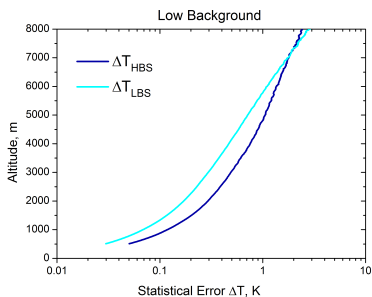


Figure 10. Comparison of the statistical error of the temperature measurements with both settings, ΔT_{HBS} and ΔT_{LBS} , at low-background conditions. The profiles were derived from data collected over about 20 min (55 000 laser shots) and with 105 m gliding average. Above 7 km altitude, the high-background configuration shows smaller errors due to the lower atmospheric temperatures at these heights and also the decrease in signal-to-noise ratio.

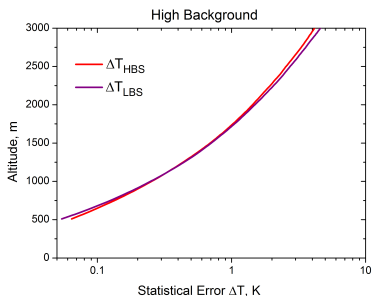


Figure 11. Same as Fig. 10 but for high-background conditions ($S = 1$ in 1 km altitude). The high-background setting is superior for measurements above 1 km altitude.

statistical errors are smaller with the high-background configuration.

To show the advantage of the new setting, the ratio between the error with high-background setting ΔT_{HBS} and the error with low-background setting ΔT_{LBS} was calculated for the different background conditions. The result is shown in Fig. 12. Using setting L is favorable during nighttime up to a height of 7 km, as already seen in Fig. 10. ΔT is reduced by 70 % for altitudes between 1 and 2 km. Above this altitude

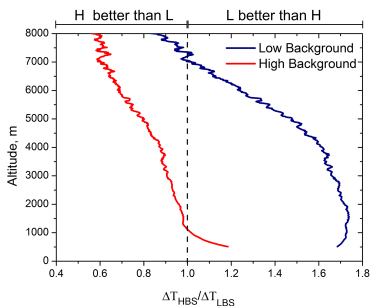


Figure 12. Ratio of high-background-setting uncertainties ΔT_{HBS} to low-background-setting uncertainties ΔT_{LBS} . A ratio above 1 shows better performance for the low-background setting compared to the high-background setting. In cases with no background, this advantage is clearly significant at lower altitudes but decreases with height. On the other hand, the high-background setting is superior already above 1 km in high-background conditions. But it should be noted that the altitude where the high-background setting becomes preferable depends on the signal-to-background ratio.

the advantage of L over H decreases. For high altitudes, H is still better than L even at night (see Fig. 6 for low temperatures < 240 K). This behavior is explained by the fact that the background factor S will be ≥ 1 at such altitudes. During daytime the signal intensity is high, such that $S < 1$ in low altitudes. Here both settings show similar statistical errors with advantages of up to 20 % (at 0.5 km) of the low-background configuration. With $S = 1$ at 1 km, the setting H is advantageous above this altitude.

Because the background factor S assumed in the simulations is higher than in reality for the strong signals which are obtained with the UHOH RRL during cloud-free conditions, the altitude where the high-background setting shows an advantage lies above 1 km unless clouds cause higher background by scattering sunlight. By applying the setting H during daytime, a good to optimum measurement performance can be guaranteed even under these very high background conditions. It is interesting to note that also smaller laser power would result in higher values of S for all background levels. Thus this optimization approach can be used to adapt the optimum receiver passbands to the system parameters of other lidars.

3.2 Temperature gradient and humidity

Figure 13 shows the water vapor MR and the temperature gradient during a 25 h measurement period between 18 May 2013 at 15:00 UTC and 19 May 2013 at 16:00 UTC. The li-

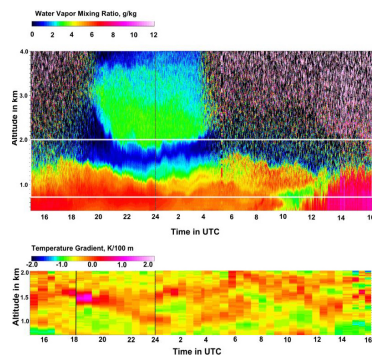


Figure 13. Time series of the water vapor mixing ratio (upper panel) and temperature gradient (lower panel) measured between 15:00 UTC on 18 May 2013 and 16:00 UTC on 19 May 2013. The white lines in the lower panel mark the height range of the data in the upper panel.

dar was pointing vertically during this time period. The setting of IF3 was changed at 20:00 UTC and at 05:00 UTC the next morning. MR data are shown with 1 min averaging. A 78 m gliding height average was applied to the data. The boundary layer top can be seen due to the gradient between the moist boundary layer and the lower values of MR in the free troposphere. The time series starts at 15:00 UTC, and the boundary layer is still convective at this time. The top of the boundary layer can be found around 1.6 km at 17:00 UTC. With sunset at 19:22 UTC there is a transition to a stable nocturnal boundary layer. Also a residual layer with a mixing ratio of 3 g kg^{-1} can be observed above the boundary layer with around 6 g kg^{-1} up to 1 km. Due to the lower solar background and the corresponding better measurement range a moist layer between 2 and 3 km can be observed at night. Sunrise is at 03:39 UTC, which can be seen by the increase of noise around this time. From 10:00 UTC on, the convective boundary layer starts to increase in altitude and shows higher values of mixing ratio (around 8 g kg^{-1}) than the day before. The height of the boundary layer top does not change significantly from 1.5 km after 14:00 UTC.

For the altitude region marked with the white box, the temperature gradient is shown in the lower panel. The resolution of temperature gradient data is 30 min and 105 m. These values have been chosen to monitor the mean boundary layer height continuously. A high positive gradient indicates a temperature inversion. Here one can see a positive gradient at 1.5 km with a value around $1.2 \text{ K (100 m)}^{-1}$ be-

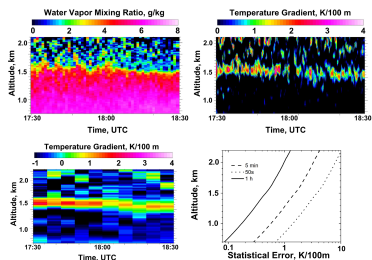


Figure 14. Detail from Fig. 13 of the time period from 17:30 to 18:30 UTC on 18 May. Upper left panel: water vapor mixing ratio with 1 min resolution; lower left panel: temperature gradient with 5 min; and upper left panel: 10 s profiles and 50 s gliding time average. Lower right panel: statistical error of temperature gradient measurements.

tween 17:30 and 19:00 UTC, which is remarkable to see in the late afternoon just before sunset. We would have not expected to find such high values in this altitude so late in the day. After sunset the gradient became weaker and split to the top of the nocturnal boundary layer and a residual layer at 1.7 km which was already observed with the water vapor mixing ratio time series. The residual layer stayed at this altitude during the whole measurement period. From 03:00 till 07:00 UTC another inversion can be seen between 1 and 1.3 km. A strong inversion was present on top of the growing convective boundary layer 10:00 till 15:00 UTC. This demonstrates that with the rotational Raman lidar temperature gradient layers can be identified and observed during longer time periods.

Figure 14 shows the time period from 17:30 to 18:30 UTC in more detail. The water vapor mixing ratio in the upper left panel has the same resolution as in Fig. 13. The temperature gradient is shown with two different temporal resolutions: 50 s gliding average over 10 s profiles on the upper right panel, 5 min on the lower left panel. The statistical uncertainty of the temperature gradient can be seen in the lower right panel. While the statistical error of the 5 min average is $1.1 \text{ K (100 m)}^{-1}$ at 1.5 km altitude, the 50 s average shows an error of 4 K (100 m)^{-1} . Therefore it can be used to determine qualitatively the altitude of the highest gradient, but not to identify absolute values. The altitude of the positive gradient and the top of the moist layer agree well for the shown time period even with this high temporal resolution.

The profiles of temperature, potential temperature, temperature gradient, and water vapor mixing ratio and their corresponding statistical uncertainties measured on 19 May 2013 between 13:00 and 13:30 UTC are shown in Fig. 15. This time period near local noon was chosen because the highest

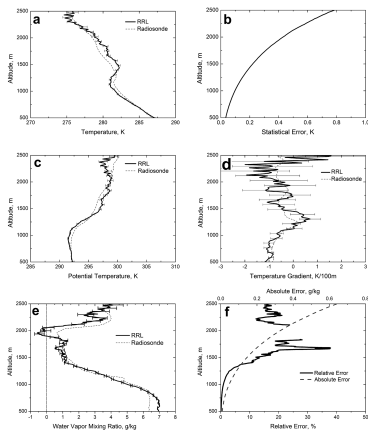


Figure 15. Measurements of the UHOH RRL between 13:00 and 13:30 UTC on 19 May 2013 with data of a local radiosonde launched at 13:00 UTC (dashed) for comparison. (a) Temperature, (b) statistical temperature error, (c) potential temperature (d), temperature gradient (e), water vapor mixing ratio, and (f) absolute and relative error of water vapor mixing ratio. Values of absolute error in the height range where the mixing ratio shows negative values are omitted. Error bars show the statistical errors of the lidar data. Altitudes below 500 m are affected by non-total overlap and are therefore not shown.

background values during the 25 h measurement period were found here; these examples thus illustrate the lower limit of the measurement performance, with all other periods having smaller statistical uncertainties. For the temperature profiles an average of 167 raw data profiles was used, and a gliding height average of 105 m was applied. A pressure profile measured by the radiosonde started at 13:00 UTC was used to calculate potential temperature. In the profiles of temperature, potential temperature, and temperature gradient one can see the characteristics of a well-mixed boundary layer up to about 1100 m. In the interfacial layer above, differences between the measurements of both instruments can be identified. As the lidar measurement is an average over half an hour and the radiosonde profile is just a snapshot, this is reasonable. For the water vapor profile measured with the lidar (Fig. 15e) a 154 m gliding average was applied. The moist boundary layer, a very dry layer just above, and a second moist layer above 2 km were found. In the dry layer, the uncertainty of the water vapor Raman lidar measurement gets larger in the absence of moisture due to the small water va-

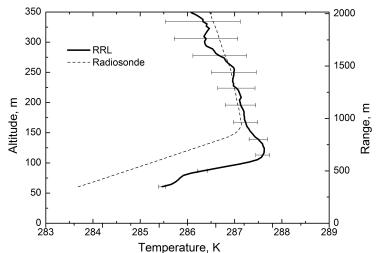


Figure 16. Results of low-elevation measurements: temperature measured with the UHOH RRL and a radiosonde (RS) against height a.g.l. The lidar data were collected from 02:40 to 02:57 UTC on 28 May 2013. The radiosonde measurement was started at 03:00 UTC. The altitude for the lidar profile is calculated from the range and corrected for topography. Lidar data at altitudes below 50 m are affected by overlap effects.

por Raman backscatter signal. In Fig. 15f the absolute and relative errors of the water vapor mixing ratio are shown. Of course, negative values of the water vapor mixing ratio are physically not possible. But in this case, they appear as measured values as a consequence of the small signal-to-noise ratio due to the small amount of water vapor at this height resulting in a signal which was hardly statistically distinguishable from the daylight background. Note that the 1σ statistical range indicates a probability of 68 % that the real value is found within. We do not want to shift these values to 0 because, in doing so, the mean of the data would be biased.

The profiles are shown with noise error bars derived by Eq. (4). A detailed error analysis including errors derived by turbulence analysis is discussed by Behrendt et al. (2014).

3.3 Low-elevation pointing

In vertical pointing mode low heights cannot be observed due to overlap effects. These effects can be corrected down to a certain altitude, but a minimum altitude of 300 m in the case of water vapor mixing ratio or temperature can unfortunately not be overcome with our single-telescope design. One solution for this problem is to perform measurements with small elevation angles. During the measurement shown in Fig. 16, the elevation angle was set to 10° . During HOPE, the measurement site was elevated above its surroundings by 10 to 15 m. This has been taken into account when transferring range to height above ground. The measurement geometry is illustrated in Fig. 17.

In Fig. 16 a comparison between the acquired lidar profile from 02:40 to 02:58 UTC and the radiosonde started at 03:00 UTC is shown. Raw data were treated like vertical ac-

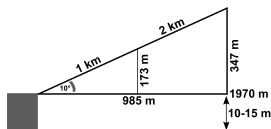


Figure 17. Illustration of the measurement geometry of Fig. 16.

quired profiles and projected to the vertical for the comparison. A positive gradient is present below 100 m in the lidar profile, whereas in the radiosonde profile it is shifted by 50 m to higher altitudes. The lidar profile is corrected for the altitude of the surrounding terrain. Whereas the altitudes of the inversion differ, the slope of the temperature profiles is identical. So we conclude that the observations indeed reveal differences of the temperature inversion profile of the nocturnal boundary layer.

4 Summary and outlook

In this paper the performance of the rotational Raman lidar of the University of Hohenheim during the HOPE campaign in April to May 2013 is presented.

To optimize the temperature measurements for both low and high background, a switch for the alignment of the interference filter for the second rotational Raman was implemented. It is possible to switch between the configurations in a short time period. The experimental data confirm the optimization simulations. The measurements proved the advantages of the new low-background configuration up to 7 km during night measurements, especially in altitudes below 4 km. An improvement of the statistical error up to 70 % can be found. Depending on the actual background level present during a measurement, the low-background configuration is also favorable in altitudes below 1 km during daytime. Due to the high signal intensities of the UHOH RRL, values of S less than 1 can be found in this altitude range. For larger background levels the improvement of the statistical error for using the H setting is up to 20 %. The advantage is not as large when changing from H to L, but one should keep in mind that a reduction of the statistical uncertainty by 20 % is equivalent to, e.g., an increase in laser power of 44 %.

The simulation was performed with the system parameters of the UHOH RRL. Therefore some points have to be taken into account when the results shown here are to be transferred to other systems. To get the exact values for another system, the simulation has to be repeated with the specific system parameters. However, the shifts from the excitation wavelength will be similar for other RRL systems operated in the UV. Additionally, the desired wavelength pairs depend on the temperature range being measured with the highest precision, including the background level in relation to the

signal intensity. Bearing all these factors in mind, one can estimate suitable wavelength pairs from Fig. 6.

Furthermore, the UHOH RRL was equipped with an additional channel to detect the vibrational Raman lines of water vapor and now delivers, as a product, the atmospheric water vapor mixing ratio of the atmospheric boundary layer and lower free troposphere during day- and nighttime. As a molecular reference signal, a temperature-independent combination of the two rotational Raman signals is used – not a vibrational Raman signal of nitrogen as commonly used. The statistical error depends on humidity. During daytime the lower 2 km of the atmosphere can be observed with a time and height averaging of 20 min and 154 m gliding average to achieve an absolute noise error less than 0.5 g kg^{-1} , which fulfills the requirements for boundary layer studies (Stull, 1988). Time series of water vapor mixing ratio and temperature gradient over a 25 h period were shown, and the diurnal changes in the boundary layer can be observed. Results from a low level measurement with capture of a strong inversion at 100 m show the capability to measure in a low-altitude range above ground with the beam steering unit.

Acknowledgements. The HOPE campaign was funded by the German Research Ministry under the project number 01LK1212 A. We thank KIT and the University of Cologne for performing the radiosonde launches.

Edited by: S. Buehler

References

- Achtert, P., Khaplanov, M., Khosravi, F., and Gumbel, J.: Pure rotational-Raman channels of the Esrange lidar for temperature and particle extinction measurements in the troposphere and lower stratosphere, *Atmos. Meas. Tech.*, 6, 91–98, doi:10.5194/amt-6-91-2013, 2013.
- Arshinov, J., Bobrovnikov, S., Serikov, I., Ansmann, A., Wandinger, U., Althausen, D., Mattis, I., and Müller, D.: Daytime operation of a pure rotational Raman lidar by use of a Fabry-Perot interferometer, *Appl. Optics*, 44, 17, 3593–3603, doi:10.1364/AO.44.003593, 2005.
- Avila, G., Fernandez, J. M., Tejada, G., and Montero, S.: The Raman Spectra and cross-sections of H_2O , D_2O , and HDO in the OH/OD-stretching regions, *J. Mol. Spectrosc.*, 228, 38–65, 2004.
- Balin, I., Serikov, I., Bobrovnikov, S., Simeonov, V., Calpini, B., Arshinov, Y., and van der Bergh, H.: Simultaneous measurement of atmospheric temperature, humidity, and aerosol extinction and backscatter coefficients by a combined vibrational-pure-rotational Raman lidar, *Appl. Phys. B*, 79, 775–782, 2004.
- Behrendt, A.: Temperature Measurements with Lidar, *Lidar: Range-Resolved Optical Remote Sensing of the Atmosphere*, Springer, New York, 2005.
- Behrendt, A. and Reichardt, J.: Atmospheric temperature profiling in the presence of clouds with a pure rotational Raman lidar by

- use of an interference-filter-based polychromator. *Appl. Optics*, 39, 1372–1378, 2000.
- Behrendt, A., Nakamura, T., Onishi, M., Baumgart, R., and Tsuda, T.: Combined Raman lidar for the measurement of atmospheric temperature, water vapor, particle extinction coefficient, and backscatter coefficient. *Appl. Optics*, 36, 7657–7666, 2002.
- Behrendt, A., Nakamura, T., and Tsuda, T.: Combined temperature lidar for measurements in troposphere, stratosphere and mesosphere. *Appl. Optics*, 14, 2930–2939, 2004.
- Behrendt, A., Wulfmeyer, V., Riede, A., Wagner, G., Pal, S., Bauer, H., Radlach, M., Späth, F.: Three-dimensional observations of atmospheric humidity with a scanning differential absorption lidar. *Proc. SPIE*, 7475, 74750L, doi:10.1117/12.835143, 2009.
- Behrendt, A., Pal, S., Aoshima, F., Bender, M., Blyth, A., Corsmeier, U., Cuesta, J., Dick, G., Dorninger, M., Flamant, C., Di Girolamo, P., Gorgas, T., Huang, Y., Kalthoff, N., Khodayar, S., Mannstein, H., Trümmer, K., Wieser, A., and Wulfmeyer, V.: Observation of convection initiation processes with a suite of state-of-the-art research instruments during COPS IOP 8b. *Q. J. Roy. Meteor. Soc.*, 137, 81–100, 2011.
- Behrendt, A., Wulfmeyer, V., Hammann, E., Muppa, S. K., and Pal, S.: Profiles of second- to third-order moments of turbulent temperature fluctuations in the convective boundary layer: first measurements with Rotational Raman Lidar. *Atmos. Chem. Phys. Discuss.*, 14, 29019–29055, doi:10.5194/acpd-14-29019-2014, 2014.
- Bhawar, R., Di Girolamo, P., Summa, D., Flamant, C., Althausen, D., Behrendt, A., Kiemle, C., Bossler, P., Cacciani, M., Champollion, C., Di Iorio, T., Engelmann, R., Herold, C., Pal, S., Riede, A., Wirth, M., and Wulfmeyer, V.: The water vapour intercomparison effort in the framework of the convective and orographically-induced precipitation study: airborne-to-ground-based and airborne-to-airborne lidar systems. *Q. J. Roy. Meteor. Soc.*, 137, 325–348, 2011.
- Cooney, J.: Measurement of atmospheric temperature profiles by Raman Backscatter. *J. Appl. Meteorol.*, 11, 108–112, 1972.
- Corsmeier, U., Kalthoff, N., Barthlott, C., Aoshima, F., Behrendt, A., Di Girolamo, P., Dorninger, M., Handwerker, J., Kottmeier, C., Mahike, H., Mobbs, S., Norton, E. G., Wickert, J., and Wulfmeyer, V.: Processes driving deep convection over complex terrain: a multi-scale analysis of observations from COPS IOP 9c. *Q. J. Roy. Meteor. Soc.*, 137, 137–155, 2011.
- Di Girolamo, P., Marchese, R., Whiteman, D. N., and Demoz, B. B.: Rotational Raman lidar measurements of atmospheric temperature in the UV. *Geophys. Res. Lett.*, 31, L01106, doi:10.1029/2003GL018342, 2004.
- Di Girolamo, P., Summa, D., and Ferretti, R.: Multiparameter Raman lidar measurements for the characterization of a dry stratospheric intrusion event. *J. Atmos. Ocean. Tech.*, 26, 1742–1762, 2009.
- Immler, F., Engelbart, D., and Schrems, O.: Fluorescence from atmospheric aerosol detected by a lidar indicates biogenic particles in the lowermost stratosphere. *Atmos. Chem. Phys.*, 5, 345–355, doi:10.5194/acp-5-345-2005, 2005.
- Kalthoff, N., Adler, B., Wieser, A., Kohler, M., Trümmer, K., Handwerker, J., Corsmeier, U., Khodayar, S., Lambert, D., Kopmann, A., Kunka, N., Dick, G., Ramatschi, M., Wickert, J., and Kottmeier, C.: KITcube – a mobile observation platform for convection studies deployed during HyMeX. *Meteorol. Z.*, 22, 633–647, 2013.
- Leblanc, T. and McDermid, I. S.: Accuracy of Raman lidar water vapor calibration and its applicability to longterm measurements. *Appl. Optics*, 30, 5592–5603, 2008.
- Lenschow, D. H., Wulfmeyer, V., and Senff, C.: Measuring second-through fourth-order moments in noisy data. *J. Atmos. Ocean. Tech.*, 17, 1330–1346, 2000.
- Lenschow, D. H., Lothon, M., Mayor, S. D., and Sullivan, P. P.: A comparison of higher-order vertical velocity moments in the convective boundary layer from lidar with in situ measurements and LES. *Bound.-Layer Meteorol.*, 143, 107–123, 2012.
- Mao, J., Hua, D., Wang, Y., Gao, F., and Wang, L.: Accurate temperature profiling of the atmospheric boundary layer using an ultraviolet rotational Raman lidar. *Opt. Commun.*, 282, 3113–3118, 2009.
- Melfi, S. H., Lawrence, J. D., McCormick, M. P.: Observation of Raman scattering by water vapor in the atmosphere. *Appl. Phys. Lett.*, 15, 295–297, 1969.
- Muppa, S. K., Behrendt, A., Späth, F., Wulfmeyer, V., Metzendorf, S., and Riede, A.: Turbulent humidity fluctuations in the convective boundary layer: case studies using DIAL measurements. *Bound. Layer Meteorol.*, submitted, 2014.
- Newsom, R. K., Turner, D. D., Mielke, B., Clayton, M., Ferrare, R., and Sivaraman, C.: Simultaneous analog and photon counting detection for Raman lidar. *Appl. Optics*, 20, 3903–3914, 2009.
- Pal, S., Behrendt, A., and Wulfmeyer, V.: Elastic-backscatter-lidar-based characterization of the convective boundary layer and investigation of related statistics. *Ann. Geophys.*, 28, 825–847, doi:10.5194/angeo-28-825-2010, 2010.
- Radlach, M.: A scanning eye-safe rotational Raman lidar in the ultraviolet for measurements of tropospheric temperature fields, doctoral thesis, Stuttgart, 2009.
- Radlach, M., Behrendt, A., and Wulfmeyer, V.: Scanning rotational Raman lidar at 355 nm for the measurement of tropospheric temperature fields. *Atmos. Chem. Phys.*, 8, 159–169, doi:10.5194/acp-8-159-2008, 2008.
- Schotland, R. M.: Errors in the lidar measurement of atmospheric gases by differential absorption. *J. Appl. Meteorol.*, 13, 71–77, 1974.
- Schwitalla, T. and Wulfmeyer, V.: Radar data assimilation experiments using the IPM WRF Rapid Update Cycle. *Meteorol. Z.*, 1, 79–102, 2014.
- Senff, C., Bösenberg, J., and Peters, G.: Measurements of water vapor flux profiles in the convective boundary layer with lidar and radar-RASS. *J. Atmos. Ocean. Tech.*, 11, 85–93, 1994.
- Sherlock, V., Garnier, A., Hauchecorne, A., and Keckhut, P.: Implementation and validation of a Raman lidar measurement of middle and upper tropospheric water vapor. *Appl. Optics*, 27, 5838–5850, 1999.
- Stevens, B. and Bony, S.: What are climate models missing?. *Science*, 340, 1053–1054, 2013.
- Stull, R. B.: *An Introduction to Boundary Layer Meteorology*, Springer, Heidelberg, New York, 1988.
- Su, J., McCormick, M. P., Wu, Y., Lee III, R. B., Lei, L., Liu, Z., and Leavor, K. R.: Cloud temperature measurement using rotational Raman lidar. *J. Quant. Spectrosc. Ra.*, 125, 45–50, 2013.
- Turner, D. D. and Goldsmith, J. E. M.: Twenty-four-hour Raman lidar water vapor measurements during the atmospheric radiation

- measurement program's 1996 and 1997 water vapor intensive observation periods, *J. Atmos. Ocean. Tech.*, 16, 1062–1076, 1999.
- Turner, D. D., Ferrare, R. A., Wulfmeyer, V., and Scarino, A. J.: Aircraft evaluation of ground-based Raman lidar water vapor turbulence profiles in convective mixed layers, *J. Atmos. Ocean. Tech.*, 31, 1078–1088, 2014a.
- Turner, D. D., Wulfmeyer, V., Berg, L. K., and Schween, J. H.: Water vapor turbulence profiles in stationary continental convective mixed layers, *J. Geophys. Res.*, 119, 11 pp., doi:10.1002/2014JD022202, 2014b.
- Wagner, G., Behrendt, A., Wulfmeyer, V., Späth, F., and Schiller, M.: High-power Ti:sapphire laser at 820 nm for scanning ground-based water–vapor differential absorption lidar, *Appl. Optics*, 52, 11, 2454–2469, 2013.
- Whiteman, D. N., Melfi, S. H., and Ferrare, R. A.: Raman lidar system for the measurement of water vapor and aerosols in the Earth's atmosphere, *Appl. Optics*, 31, 16, 3068–3082, 1992.
- Whiteman, D. N., Demoz, B., di Girolamo, P., Comer, J., Veselovskii, I., Evans, K., Wang, Z., Sabatino, D., Schwemmer, G., Gentry, B., Lin, R-F., Behrendt, A., Wulfmeyer, V., Browell, E., Ferrare, R., Ismail, S. and Wang, J.: Raman Lidar Measurements during the International H2O Project, Part II: Case Studies, *J. Atmos. Oceanic Technol.*, 23, 170–183, 2006.
- Wulfmeyer, V.: Investigation of turbulent processes in the lower troposphere with water-vapor DIAL and Radar-RASS, *J. Atmos. Sci.*, 56, 1055–1076, 1999a.
- Wulfmeyer, V.: Investigations of humidity skewness and variance profiles in the convective boundary layer and comparison of the latter with large eddy simulation results, *J. Atmos. Sci.*, 56, 1077–1087, 1999b.
- Wulfmeyer, V. and Bösenberg, J.: Ground-based differential absorption lidar for water-vapor profiling: assessment of accuracy, resolution, and meteorological applications, *Appl. Optics*, 37, 3825–3844, 1998.
- Wulfmeyer, V. and Feingold, G.: On the relationship between relative humidity and particle backscattering coefficient in the marine boundary layer determined with differential absorption lidar, *J. Geophys. Res.*, 105, 4729–4741, 2000.
- Wulfmeyer, V., Pal, S., Turner, D. D., and Wagner, E.: Can water vapour Raman lidar resolve profiles of turbulent variables in the convective boundary layer?, *Bound.-Lay. Meteorol.*, 136, 253–284, 2010.
- Zeyn, J., Lahmann, W., and Weitkamp, C.: Remote daytime measurements of tropospheric temperature profiles with a rotational Raman lidar, *Opt. Lett.*, 21, 16, 1301–1303, 1996.

4.3 Blocking capabilities of the new interference filter

To determine the remaining leakage, the signal in the first rotational Raman and in the elastic channel are compared. Figure 4.2 shows a comparison with the signals scaled to each other and the corresponding backscatter ratio. The clouds resulted in a backscatter ratio over one hundred and there was a fast extinction of the signals. In the remaining Raman signal a small peak corresponding to the peak in the elastic signal is apparent. As both signals are normalized to each other, it is possible to determine the fraction of the elastic signal which is transmitted. By normalization the influence of the different detection efficiencies is minimized. The Raman signal is approximately $3.33\text{E-}4$ of the elastic signal, if the filter efficiencies are taken into account. The ratio between the additional signal due to the cloud and the molecular signal is $1.61\text{E-}3$. This indicates an optical density of $5.4\text{E-}7$, which is superior to the OD6 which was guaranteed by the manufacturer.

4.4 Water vapor measurements

During September and October 2013 a campaign took place on the grounds of University of Hohenheim. It was focused on water vapor measurements. The measurement plan of this campaign can be found in Appendix B.2. In the course of the campaign several different water vapor distributions and absolute values were observed. Additionally, it was possible to compare the water vapor mixing ratio measured by the RRL with measurements of absolute humidity by the UHOH WV DIAL and a collocated radio sounding. Calibration of the RRL was performed with profiles from Vaisalla RS-92 radiosondes, which were launched directly on the site. In Fig. 4.3a a comparison with a profile measured by the UHOH WV DIAL is shown for a day with a dry free troposphere above a moist PBL. The DIAL is self-calibrating and is therefore an independent comparison. For the Raman lidar 20 minutes were averaged with a 154 m gliding average in height. In Fig. 4.3b a case with a distinct layer structure is shown.

It can be seen that the profiles match up to an altitude of 3 km. As

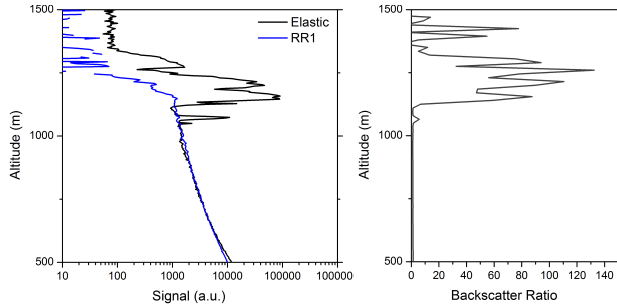


Figure 4.2: On the left side scaled elastic and rotational Raman signals from 19 August 2014 from 10:27 to 10:28 UTC. Right side shows the backscatter ratio. The backscatter ratio exceeds 100 in 1100 m altitude. From the leakage signal and the ratio between elastic and rotational Raman scattering the optical density is estimated.

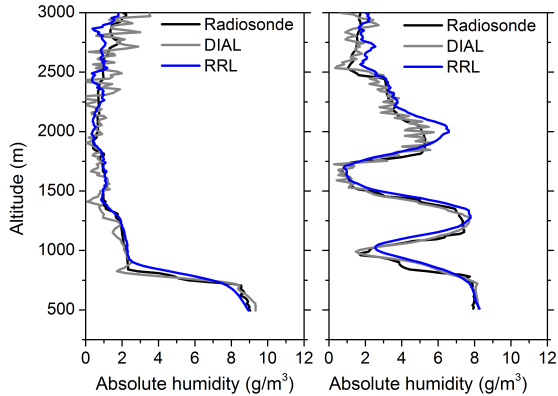


Figure 4.3: (a) Profile from 24 September 2013, 20 min profile starting 15:19 UTC. Absolute humidity measurement of the RRL in comparison with the calibration radiosonde and a WV DIAL measurement, 20 min and 154 m resolution. (b) same as (a), but for 22 September 2013 starting 14:04 UTC. Analog data were used, therefore the noise error is not available. For typical error values see next chapter. WV DIAL measurements provided by Florian Späth.

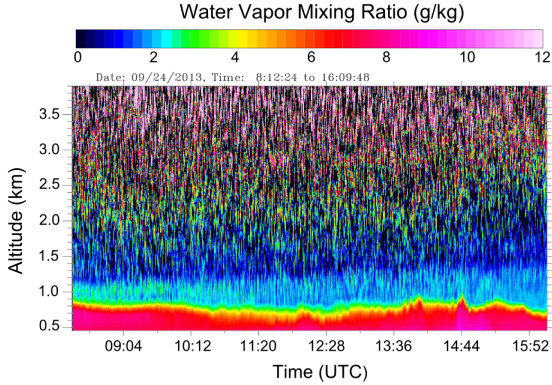


Figure 4.4: Time series of water vapor mixing ratio on 24 September 2013 with 30 s temporal resolution and 154 m gliding vertical average. The humidity is apparent in the shallow boundary layer and shows only in the late afternoon some turbulent features.

it is a daytime measurement, the vibrational Raman signal in these altitudes is weak in comparison with the background and the noise increases. While the layer structure is clearly visible, the gliding average seems to dislocate some of the extreme values. Alternatively it could be also an effect of the different sampled volumes of lidar and radiosonde. The profile measured by the WV DIAL with a higher vertical resolution (60 m) indicates that it is in fact a result from the averaging. In Fig. 4.4 and Fig. 4.5 two exemplary time series are shown with a 30 s temporal average. The profiles in Fig. 4.3 are extracts of these time series. While in Fig. 4.5 the layer structures and their variation through the course of the day can be identified, the overall smaller amount of water vapor in the free troposphere is low in the other case. In the afternoon some small convective structures can be observed.

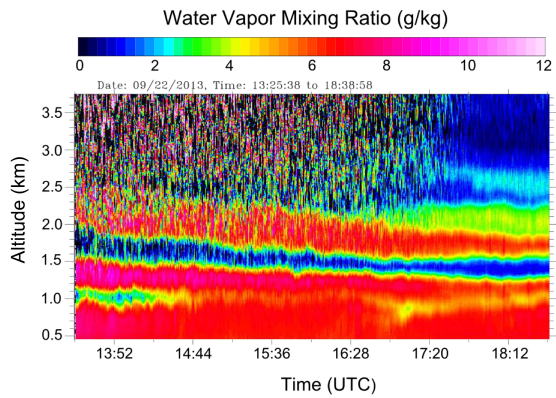


Figure 4.5: Time series of water vapor mixing ratio on 22 September 2013 with 30 s resolution and 154 m gliding vertical average. A humid layer between 2.0 km and 2.5 km altitude is visible the whole day.

Chapter 5 Planetary boundary layer and turbulence theory

The Institute of Physics and Meteorology of the University of Hohenheim has a research focus on the boundary layer processes. Planetary boundary layer (PBL) denotes the lowest layer of the atmosphere where exchange between surface and free atmosphere takes place [94]. The surface is the main humidity and heat source for the lower troposphere in case of low advection, therefore it is important to have a sufficient boundary layer scheme in weather and climate models. As it is challenging to observe the state of the PBL over the whole altitude range during fast changing processes, there is still a lack of measurement data. Most operational weather observations are located on the surface and only a few penetrate more than several meters into the PBL.

The PBL itself can be subdivided in several layers [20, 94]. The lowest sublayer is called surface layer and reaches up a few multiples of the obstacles and vegetation cover heights on the ground, as they are the dominating influence in this layer. The layer connecting boundary layer to the free troposphere above is called interfacial layer or entrainment zone, processes there drive the exchange between boundary layer and free troposphere [20]. The altitude of the boundary layer z_i depends on season, weather situation and time of the day. It can reach up to three kilometers over deserts and is especially shallow over oceans and during nighttime. z_i is identified by different methods based on e.g. high gradients in aerosol or moisture content, potential temperature or temperature gradient [94]. Many processes influence the state and altitude range of the PBL.

During night with no incoming radiation, the PBL is stable and there is almost no exchange between sublayers [94]. Residual layers sink down during night-time and the temperature profile shows often an inversion on top, as the surface cools down faster than the air above. With sunrise and incoming radiation, the PBL becomes thermodynamically unstable and the altitude of the layer top increases. Turbulent eddies develop in the PBL and the layer is also called convective boundary layer (CBL). Eddies transport mostly warm and humid air into the entrainment zone and into the free troposphere whereas colder and mostly drier air is mixed downwards. Entrainment fluxes describe these exchange rates.

Parameters describing the state of the convective boundary are the average eddy size, the integral length scale (IL), the variance and other higher order moments like skewness and kurtosis [94]. The variance is a measure of the strength of the fluctuations around an average value. It is supposed to show a distribution similar to a Gaussian, while the differences to the Gaussian are also of big interest. Different variables like temperature, water vapor or wind velocity show different variance profiles, e.g. in a well-mixed, convective boundary layer the maximum variance in the vertical wind velocity is expected to be found somewhere around one third of the total height z_i of the PBL, whereas for temperature and water vapor the maximum is found near the top of the PBL [122]. If the variance would be an ideal Gaussian, the fluctuations downward and upward would have all the same strength and size. In reality either small intense eddies or large weak eddies will have a higher appearance in a certain altitude. This property is described by the third order moment (TOM) or the skewness, which is the ratio between TOM and the variance. A TOM of zero describes a balance in the eddy sizes. It is expected that in the CBL the skewness is slightly negative for water vapor, that eddies evolving from the surface are quite large and bring a reasonable amount of temperature enhancement or humid air. On the other hand, cool and less moist entrainment from the troposphere is expected to be shorter in time and show more difference to the average value, leading to a positive skewness in the interfacial layer. Measurements show that this is valid for some cases with a well developed CBL at least for humidity q [123, 99, 77] and vertical wind u [98]. The fourth-order moment (FOM) is called

kurtosis, if divided by the variance, and describes the overall slope of the variance. A Gaussian distribution would result in a kurtosis of 3, which is not observed in atmospheric measurements.

5.1 Behrendt et al., 2015, Atmospheric Chemistry and Physics

The first turbulence analysis of temperature profiles acquired by lidar was performed and is presented in following publication. The necessary equations and methods are described in detail. My task in this was the measurement and the following derivation of temperature profiles.



Profiles of second- to fourth-order moments of turbulent temperature fluctuations in the convective boundary layer: first measurements with rotational Raman lidar

A. Behrendt¹, V. Wulfmeyer¹, E. Hammann¹, S. K. Muppa¹, and S. Pal²

¹University of Hohenheim, Institute of Physics and Meteorology, 70599 Stuttgart, Germany

²University of Virginia, Department of Environmental Sciences, Charlottesville, VA 22904, USA

Correspondence to: A. Behrendt (andreas.behrendt@uni-hohenheim.de)

Received: 9 July 2014 – Published in Atmos. Chem. Phys. Discuss.: 21 November 2014

Revised: 21 April 2015 – Accepted: 25 April 2015 – Published: 20 May 2015

Abstract. The rotational Raman lidar (RRL) of the University of Hohenheim (UHOH) measures atmospheric temperature profiles with high resolution (10 s, 109 m). The data contain low-noise errors even in daytime due to the use of strong UV laser light (355 nm, 10 W, 50 Hz) and a very efficient interference-filter-based polychromator. In this paper, the first profiling of the second- to fourth-order moments of turbulent temperature fluctuations is presented. Furthermore, skewness profiles and kurtosis profiles in the convective planetary boundary layer (CBL) including the interfacial layer (IL) are discussed. The results demonstrate that the UHOH RRL resolves the vertical structure of these moments. The data set which is used for this case study was collected in western Germany (50°53′50.56″ N, 6°27′50.39″ E; 110 m a.s.l.) on 24 April 2013 during the Intensive Observations Period (IOP) 6 of the HD(CP)² (High-Definition Clouds and Precipitation for advancing Climate Prediction) Observational Prototype Experiment (HOPE). We used the data between 11:00 and 12:00 UTC corresponding to 1 h around local noon (the highest position of the Sun was at 11:33 UTC). First, we investigated profiles of the total noise error of the temperature measurements and compared them with estimates of the temperature measurement uncertainty due to shot noise derived with Poisson statistics. The comparison confirms that the major contribution to the total statistical uncertainty of the temperature measurements originates from shot noise. The total statistical uncertainty of a 20 min temperature measurement is lower than 0.1 K up to 1050 m a.g.l. (above ground level) at noon; even for single 10 s temperature profiles, it is smaller than 1 K up to 1020 m a.g.l. Autocovariance and spectral analyses of the at-

mospheric temperature fluctuations confirm that a temporal resolution of 10 s was sufficient to resolve the turbulence down to the inertial subrange. This is also indicated by the integral scale of the temperature fluctuations which had a mean value of about 80 s in the CBL with a tendency to decrease to smaller values towards the CBL top. Analyses of profiles of the second-, third-, and fourth-order moments show that all moments had peak values in the IL around the mean top of the CBL which was located at 1230 m a.g.l. The maximum of the variance profile in the IL was 0.39 K² with 0.07 and 0.11 K² for the sampling error and noise error, respectively. The third-order moment (TOM) was not significantly different from zero in the CBL but showed a negative peak in the IL with a minimum of -0.93 K^3 and values of 0.05 and 0.16 K³ for the sampling and noise errors, respectively. The fourth-order moment (FOM) and kurtosis values throughout the CBL were not significantly different to those of a Gaussian distribution. Both showed also maxima in the IL but these were not statistically significant taking the measurement uncertainties into account. We conclude that these measurements permit the validation of large eddy simulation results and the direct investigation of turbulence parameterizations with respect to temperature.

1 Introduction

Temperature fluctuations and their vertical organization inherently govern the energy budget in the convective planetary boundary layer (CBL) by determining the vertical heat flux

and modifying the interaction of vertical mean temperature gradient and turbulent transport (Wyngaard and Cote, 1971; Wyngaard, 2010). Thus, the measurement of turbulent temperature fluctuations and characterizations of their statistics are essential for solving the turbulent energy budget closure (Stull, 1988). In situ measurements (near the ground, on towers, or on airborne platforms) sample certain regions of the CBL within certain periods and have been used for a long time for turbulence studies. But to the best of our knowledge, there are no previous observations based on a remote-sensing technique suitable for this important task, i.e., resolving temperature fluctuations in high resolution and covering simultaneously the CBL up to the interfacial layer (IL). In this work, it is demonstrated that rotational Raman lidar (RRL) (Cooney, 1972; Behrendt, 2005) can fill this gap.

By simultaneous measurements of turbulence at the land surface and in the IL, the flux divergence and other key scaling variables for sensible and latent heat entrainment fluxes can be determined, which is key for the evolution of temperature and humidity in the CBL and thus for verifying turbulence parameterizations in mesoscale models (Sorbjan, 1996, 2001, 2005).

Traditionally, studies of turbulent temperature fluctuations in the atmospheric CBL were performed with in situ instrumentation operated on tethered balloons, helicopters, and aircraft (e.g., Clarke et al., 1971; Muschinski et al., 2001) as well as recently with unmanned aerial vehicles (UAVs, e.g., Martin et al., 2011). However, it is not possible to obtain instantaneous profiles of turbulent fluctuations with in situ sensors and it is difficult to identify the exact location and characteristics of the IL. Recently, it was demonstrated that the combination of remote-sensing instruments (for guiding) and a UAV also allows for the study of entrainment processes at the CBL top (Martin et al., 2014). However, the UAV cannot continuously examine the processes due to its short endurance.

For studying turbulent processes and their parameterizations, however, it is essential that the turbulent transport and the temperature gradient are measured simultaneously in the same volume. Therefore, the shortcomings of in situ observations call for new remote-sensing technologies. These instruments can be operated on different platforms and can provide excellent long-term statistics, if applied from ground-based platforms. Passive remote-sensing techniques, however, show difficulties in contributing to turbulence studies because of their inherent limitation in range resolution which flattens turbulent fluctuations. Nevertheless, Kadyrov et al. (2003) published a study on turbulent temperature fluctuations based on passive remote-sensing techniques. The authors used a scanning microwave temperature profiler to investigate thermal turbulence and concluded that the spectral density of brightness temperature fluctuations at 75 m above ground indeed followed the expected $-5/3$ -power law of Kolmogorov (1991). Kadyrov et al. (2003) concluded that “measurements can be provided in all weather conditions,

but the technique has limitations in altitude range” as their turbulence studies could only reach up to a maximum height of 200 m.

In recent years, new insights in CBL turbulence were provided by studies based on active remote sensing with different types of radar and lidar systems. Radar wind profilers were used to study the vertical CBL wind profile and its variance (e.g., Angevine et al., 1994; Eng et al., 2000; Campistron et al., 2002). A radio-acoustic sounding system (RASS) provides profiles of virtual temperature which can be used as a scaling parameter for turbulence studies also in higher altitudes (e.g., Hermawan and Tsuda, 1999; Furomoto and Tsuda, 2001). But temperature and moisture fluctuations cannot be separated with RASS. Furthermore, the RASS profiles have typical resolutions of a few minutes which is too large to resolve the inertial subrange. In addition to radar, lidar techniques have also been used for turbulence studies: elastic backscatter lidar (Pal et al., 2010, 2013), ozone differential absorption lidar (ozone DIAL (Senff et al., 1996), Doppler lidar (e.g., Lenschow et al., 2000, 2012; Wulfmeyer and Janjic, 2005; O'Connor et al., 2010; Trümmer et al., 2015), water vapor differential absorption lidar (WV DIAL) (e.g., Senff et al., 1994; Kiemle et al., 1997; Wulfmeyer, 1999a; Lenschow et al., 2000; Muppa et al., 2015), and water vapor Raman lidar (e.g., Wulfmeyer et al., 2010; Turner et al., 2014a, b) have been employed or a combination of these techniques (e.g., Giez et al., 1999; Wulfmeyer, 1999b; Kiemle et al., 2007, 2011; Behrendt et al., 2011a; Kalthoff et al., 2013). However, so far, profiling of turbulent temperature fluctuations with active remote sensing was missing.

In general, daytime measurements are more challenging than nighttime measurements for lidar because of the higher solar background which increases the signal noise and even prohibits measurements for most Raman lidar instruments. In order to address the measurement needs, the University of Hohenheim (UHOH) RRL was optimized for high temperature measurement performance in daytime in the CBL (Radlach et al., 2008). The data of the UHOH RRL have already been used for studies on the characterization of transport and optical properties of aerosol particles near their sources (Behrendt et al., 2011b; Valdebenito et al., 2011), on the initiation of convection (Groenemeijer et al., 2009; Corsmeier et al., 2011), and on atmospheric stability indices (Behrendt et al., 2011; Corsmeier et al., 2011). Here, the formalism introduced by Lenschow et al. (2000) is applied for the first time to the data of an RRL to study the extension of the variable set of lidar turbulence studies within the CBL to temperature.

The measurements discussed here were carried out at around local noon (11:33 UTC) on 24 April 2013 during the Intensive Observations Period (IOP) 6 of the HD(CP)² (High-Definition Clouds and Precipitation for advancing Climate Prediction) Observational Prototype Experiment (HOPE), which is embedded in the project HD(CP)² of the German Research Ministry. The UHOH RRL was posi-

tioned during this study at 50°53′50.56″N, 6°27′50.39″E, 110 m a.s.l. near the village of Hambach in western Germany where it performed measurements between 1 April and 31 May 2013.

This paper is organized as follows. In Sect. 2, the setup of the UHOH RRL is described briefly; more details can be found in Hammann et al. (2015). The meteorological background and turbulence measurements are presented in Sect. 3. Finally, conclusions are drawn in Sect. 4.

2 Setup of the UHOH RRL

The RRL technique is based on the fact that different portions of the pure rotational Raman backscatter spectrum show different temperature dependence. By extracting signals out of these two portions and forming the signal ratio, one obtains a profile which, after calibration, yields a temperature profile of the atmosphere (see, e.g., Behrendt, 2005, for details).

A scheme of the UHOH RRL during HOPE is shown in Fig. 1. Key system parameters are summarized in Table 1. As laser source, an injection-seeded frequency-tripled Nd:YAG laser (354.8 nm, 50 Hz, 10 W), model GCR 290-50 of Newport Spectra-Physics GmbH, is used. The UV laser radiation is separated from the fundamental and frequency-doubled radiation near 532 and 1064 nm, respectively, with a Pellin–Broca prism (PBP), so that only the UV radiation is sent to the atmosphere. This improves eye safety significantly compared to systems which use harmonic beam splitters because there is definitely no potentially hazardous green laser light present in the outgoing laser beam. But the main reason for using UV laser radiation for the transmitter of the UHOH RRL is that the backscatter cross section is proportional to the inverse wavelength to the fourth power. This yields significantly stronger signals and thus lower statistical uncertainties of the measurements in the lower troposphere (see also Di Girolamo et al., 2004, 2006; Behrendt, 2005) when using the third harmonic instead of the second harmonic of Nd:YAG laser radiation. Behind the PBP, the laser beam is expanded 6.5-fold in order to reduce the beam divergence to < 0.2 mrad. The laser beam is then guided by three mirrors parallel to the optical axis of the receiving telescope (coaxial design) and reflected up into the atmosphere by two scanner mirrors inside of a so-called beam-steering unit (BSU). The same two mirrors reflect the atmospheric backscatter signals down to the receiving telescope which has a primary mirror diameter of 40 cm. The scanner allows for full hemispherical scans with a scan speed of up to $10^{\circ} \text{ s}^{-1}$. In the present case study, the scanner was pointing constantly in vertical direction. In the focus of the telescope, a field-stop iris defines the field of view. For the data shown here, an iris diameter of 3 mm was selected which yielded a telescope field of view of 0.75 mrad. The light is collimated behind the iris with a convex lens and enters a polychromator which contained three channels during the discussed measurements: one chan-

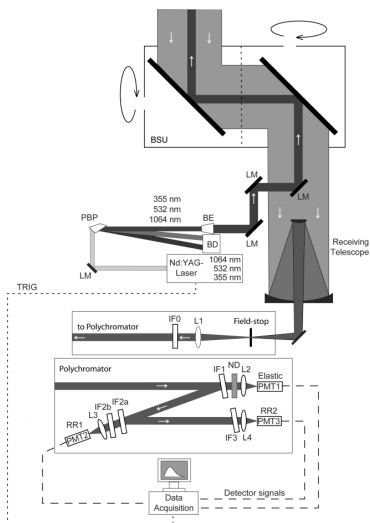


Figure 1. Scheme of the UHOH RRL. The beam-steering unit (BSU) consists of two plane mirrors which scan the laser beam and receiving telescope field-of-view. LM: laser mirror; PBP: Pellin–Broca prism; BE: beam expander; BD: beam dump; L1 to L4: lenses; IF0 to IF3: interference filters; PMT1 to PMT3: photomultiplier tubes; RR1 and RR2: rotational Raman channel 1 and 2, respectively. The beam splitter for the water vapor Raman channel between L1 and IF0 has been omitted for clarity here.

nel for collecting atmospheric backscatter signals around the laser wavelength (elastic channel) and two channels for two signals from different portions of the pure rotational Raman backscatter spectrum. During the HOPE campaign, the polychromator was later extended with a water vapor Raman channel; the beam splitter for this channel was already installed during the measurements discussed here. Within the polychromator, narrow-band multi-cavity interference filters extract in a sequence the elastic backscatter signal and the two rotational Raman signals with high efficiency. The filters are mounted at angles of incidence of about 5° . This setting allows for high reflectivity of the signals of the channels following in the chain (Behrendt and Reichardt, 2000; Behrendt et al., 2002, 2004). The filter passbands were optimized within detailed performance simulations for measurements in the CBL in daytime (Behrendt, 2005; Radlach et al.,

Table 1. Overview of key parameters of the rotational Raman lidar of University of Hohenheim (UHOH RRL) during the measurements discussed here.

Transmitter	Flash-lamp-pumped injection-seeded frequency-tripled Nd:YAG laser Pulse energy: ~ 200 mJ at 354.8 nm Repetition rate: 50 Hz Pulse duration: ~ 5 ns
Receiver	Diameter of primary mirror: 40 cm Focal length: 4 m Field of view: 0.75 mrad (selectable)
Scanner	Manufactured by the NCAR, Boulder, CO, USA Mirror coating: protected aluminum Scan speed: up to 10^6 s $^{-1}$
Detectors	Photomultiplier tubes, Hamamatsu R7400-U02 (Elastic), R1924P (RR1+2)
Data acquisition system	3-channel transient-recorder, LICEL GmbH, Germany
Range resolution	3.75 m in analog mode up to 30 km range 3.75 m in photon-counting mode up to 30 km range 37.5 m in photon-counting mode up to 75 km range

2008; Hammann et al., 2015). The new daytime/nighttime switch for the second rotational Raman channels (Hammann et al., 2015) was set to daytime optimizing the signal-to-noise ratio of the RR2 channel for high-background conditions. Further details on the receiver setup and the filter passbands can be found in Hammann et al. (2015).

3 Turbulence case study

3.1 Data set

The synoptic condition on 24 April 2013 was characterized by a large high-pressure system over central Europe. Because no clouds were forecasted for the HOPE region, this day was announced as Intensive Observation Period (IOP) 6 with the goal to study CBL development under clear-sky conditions. Indeed, undisturbed solar irradiance resulted in the development of a CBL which was not affected by clouds. A radiosonde launched at the lidar site at 11:00 UTC showed moderate westerly winds throughout the CBL and also in the lower free troposphere. The horizontal speeds were < 2 m s $^{-1}$ near the ground increasing to about 5 m s $^{-1}$ in the CBL between about 100 and 1000 m a.g.l. (above ground level). Between 1000 and 1300 m a.g.l., the horizontal wind increased further to about 10 m s $^{-1}$ while ranging between this value and 8 m s $^{-1}$ in the lower free troposphere; 3 m temperatures at the lidar site increased between 09:00 and 11:00 UTC from 280 to 294 K. The sensible heat flux at noon was about 170 W m $^{-2}$ at the lidar site.

The time–height plot of the particle backscatter coefficient β_{par} (Fig. 2) between 11:00 and 12:00 UTC shows the CBL height around local noon (11:33 UTC with a maximum solar elevation of 54 $^\circ$ on this day). β_{par} was measured with the

rotational Raman lidar technique by use of a temperature-independent reference signal (Behrendt et al., 2002). Data below 400 m were affected by incomplete geometrical overlap of the outgoing laser beam and the receiving telescope and have been excluded from this study.

As seen in Fig. 2, indeed no clouds were present in this period. The CBL is clearly marked by higher values of β_{par} which result from aerosol particles which are lifted up from the ground into the CBL. The instantaneous CBL height was determined with the Haar-wavelet technique which detects the strongest gradient of the aerosol backscatter signal as tracer (Pal et al., 2010, 2012; Behrendt et al., 2011a) (Fig. 2). The mean of the instantaneous CBL heights z_i in the observation period was 1230 m a.g.l. This value is used in the following for the normalized height scale z/z_i . The standard deviation of the instantaneous CBL heights was 33 m; the absolute minimum and maximum were 1125 and 1323 m a.g.l., i.e., the instantaneous CBL heights were within 200 m. Besides its vertical structure, the β_{par} field in the CBL also shows a temporal trend in this case which may be explained by changing aerosol number density or size distribution in the advected air over the lidar.

The temperature profile, which is the primary data product of the UHOH RRL, for the period of 11:00–11:20 UTC, is shown in Fig. 3 together with z_i and the data of a local radiosonde launched at the lidar site at 11:00 UTC. Calibration of the RRL temperature data used in this study was made with these radiosonde data in the CBL between 400 and 1000 m a.g.l.; the RRL data above result from extrapolation of the calibration function. For the calibration, we used a 20 min average of the RRL data in order to reduce sampling effects between the two data sets. Longer averaging periods for the RRL reduce the statistical uncertainty of the measure-

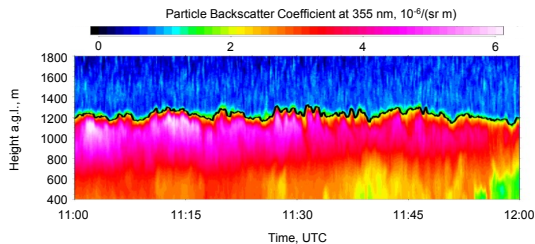


Figure 2. Time–height cross section of particle backscatter coefficient β_{par} at 354.8 nm measured with the UHOH RRL on 24 April 2013 between 11:00 and 12:00 UTC. The temporal and spatial resolution of the data is $\Delta t = 10$ s and $\Delta z = 3.75$ m with a gliding average of 109 m. The instantaneous CBL heights determined with the Haar-wavelet analysis of β_{par} profiles are marked. a.g.l. (above ground level).

ments but increase the sampling differences; shorter averaging results in larger statistical errors and additionally in sampling of fewer air masses which makes the comparison with the snapshot data of the radiosonde more difficult. It would be optimum, of course, to track the sonde with the RRL but such a synchronization of the lidar scanner with the sonde is not yet possible with the UHOH RRL.

The uncertainty of the calibration depends mainly on the calibration of the radiosonde; their uncertainty is < 0.2 K (see <http://www.graw.de/home/products2/radiosondes0/radiosondefdm-090/> and Nash et al., 2011). It is noteworthy that the accuracy of the measured temperature fluctuations do not depend on the absolute accuracy of the temperature measurements but on their relative accuracy. Even with an error of 1 K, the relative accuracy of the measured temperature fluctuations would be better than $(1 \text{ K}) / (250 \text{ K}) = 0.4\%$. For the statistical analysis of the turbulent temperature fluctuations, we then used this calibration for the 1 h RRL data set between 11:00 and 12:00 UTC. This 1 h period seems here to be a good compromise: for much longer periods, the CBL characteristics may change considerably while shorter periods would reduce the number of sampled thermals and thus increase the sampling errors.

The temperature profiles of RRL and radiosonde shown in Fig. 3 agree within fractions of 1 K in the CBL. Larger differences occur in the IL due to the different sampling methods: the mean lidar profile shows an average over 20 min, while the radiosonde data sample an instantaneous profile along the sonde's path which was determined by the drift of the sonde with the horizontal wind. In this case, the sonde needed about 5 min to reach the top of the boundary layer and drifted by about 1.6 km away from a vertical column above the site. Depending on the part of the thermal eddies in the CBL and the IL that are sampled, the radiosonde data thus represent different CBL features and are not representative for a mean profile (Weckwerth et al., 1996) which is a crucial point to be

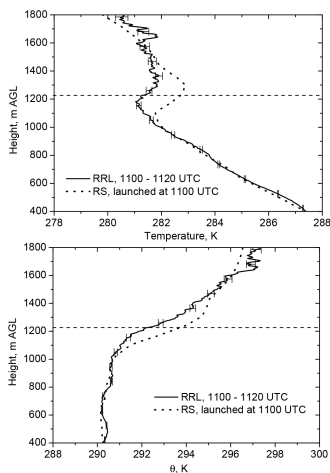


Figure 3. Upper panel: average temperature profile measured with the UHOH RRL on 24 April 2013 between 11:00 and 11:20 UTC and temperature profiles measured with a local radiosonde launched at the lidar site at 11:00 UTC. Lower panel: same but potential temperature profiles. The dashed line shows z_i for comparison. Error bars show the uncertainties derived with Poisson statistics from the intensities of the rotational Raman signals.

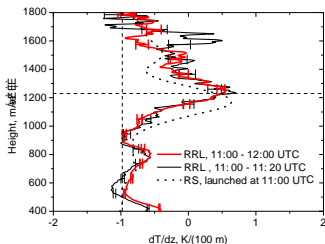


Figure 4. Average temperature gradients measured with the UHOH RRL on 24 April 2013 between 11:00 and 11:20 UTC, between 11:00 and 12:00 UTC and temperature gradient measured with a local radiosonde launched at the lidar site at 11:00 UTC. The horizontal dashed line shows z_i , the mean CBL top height for the period between 11:00 and 12:00 UTC, which agrees with the maximum temperature gradients of both RRL profiles. The vertical dashed line shows the dry-adiabatic temperature gradient. Error bars show the uncertainties derived with Poisson statistics from the intensities of the rotational Raman signals.

considered when using radiosonde data for scaling of turbulent properties in the CBL. Furthermore, averaged lidar temperature data are also more representative for a certain site for model validations.

Inside the CBL, the potential temperature (derived from the RRL temperature data with the radiosonde pressure profile) is nearly constant indicating a well-mixed CBL (Fig. 3, lower panel); z_i lies approximately in the middle of the temperature inversion in the IL (Fig. 3). Figure 4 shows the temperature gradients of the radiosonde and the RRL profiles, the latter for two averaging periods, namely, 11:00 to 11:20 UTC and 11:00 to 12:00 UTC. The maximum temperature gradient is in this case very similar for all three profiles, i.e., between 0.6 and 0.7 K/(100 m). It is interesting to note furthermore that the height of maximum temperature gradient agrees with z_i for both RRL profiles as determined with the Haar-wavelet technique. In contrast to this, the height of the maximum temperature gradient in the radiosonde profile is about 60 m lower. But, as already mentioned, the radiosonde data are not representative for a mean profile.

3.2 Turbulent temperature fluctuations

For CBL turbulence analyses, the instantaneous value of temperature $T(z)$ at height z is separated in a slowly varying component $\overline{T}(z)$ derived from applying a linear fit to the data typically over 30 to 60 min and the temperature fluctuation $T'(z)$ according to, e.g., Wyngaard (2010)

$$T(z) = \overline{T}(z) + T'(z). \quad (1)$$

Figure 5 shows the time–height cross sections of temperature, potential temperature, and detrended temperature fluctuations $T'(z)$ in the discussed period. For detrending, the same linear regression was applied to the temperature time series of all heights. Furthermore, the data set with the temperature fluctuations was gridded to exact 10 s time steps in order to ensure that all derived parameters are correct. (The vertical black lines in the lower panel of Fig. 5 are artifacts from this procedure.) One can see the positive and negative temperature fluctuations inside the CBL. In the IL, the fluctuations in the measured data become larger than in heights below. Above the CBL in the free troposphere, one finds fewer structures in the temperature fluctuations and mostly uncorrelated instrumental noise.

Lidar data contain significant stochastic instrumental noise, which has to be determined and for which has to be corrected in order to obtain the atmospheric fluctuation of a variable of interest. In general, the signal-to-noise ratio can be improved by averaging the signal in time and/or range but this in turn would of course reduce the ability to resolve turbulent structures. In principle, very high time resolution, i.e., the maximum allowed by the data acquisition system, is preferred in order to keep most frequencies of the turbulent fluctuations. But this is only possible as long as the derivation of temperature does not result in a non-linear increase of the noise errors; this noise regime should be avoided. A temporal resolution of 10 s turned out to be a good compromise for the temporal resolution of our data as explained below.

The variance of the atmosphere $\overline{(x'_a(z))^2}$ and the noise variance $\overline{(x'_n(z))^2}$ of a variable x are uncorrelated. Thus, we can write (Lenschow et al., 2000)

$$\overline{(x'_m(z))^2} = \overline{(x'_a(z))^2} + \overline{(x'_n(z))^2} \quad (2)$$

with $\overline{(x'_m(z))^2}$ for the measured total variance. Overbars denote here and in the following temporal averages over the analysis period. The separation of the atmospheric variance from the noise contribution can be realized by different techniques. Most straightforward is the autocovariance method, which makes use of the fact that atmospheric fluctuations are correlated in time while instrumental noise fluctuations are uncorrelated. Further details were introduced by Lenschow et al. (2000) so that only a brief overview is given here. The atmospheric variance can be obtained from the autocovariance function (ACF) of a variable by extrapolating the tails (non-zero lags) to zero lag with a power-law fit (see Eq. 32 of Lenschow et al., 2000). As the ACF at zero lag is the total variance, the instrumental noise variance is the difference of the two. Alternatively, one may calculate the power spectrum of the fluctuations and use Kolmogorov's (1991) $-5/3$ law within the inertial subrange in order to determine the noise level (e.g., O'Connor et al., 2010). We prefer the ACF method to the spectral analysis because the ACF method is less prone to errors since the statistical noise does not show

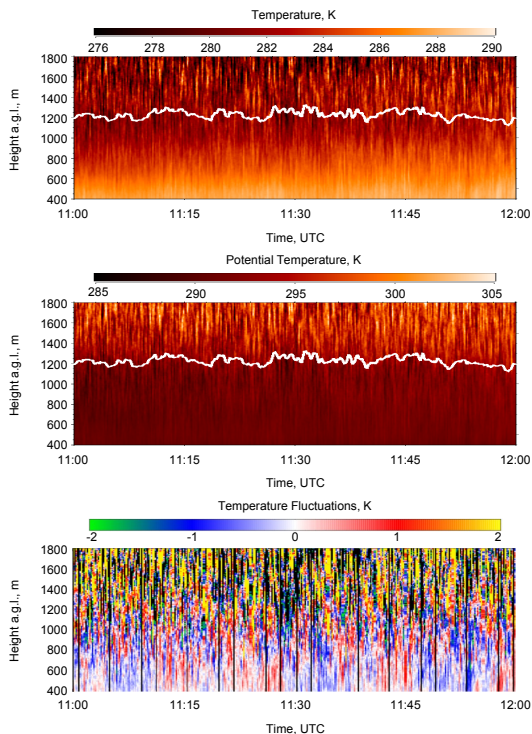


Figure 5. Same as Fig. 2 but for temperature, potential temperature, and detrended temperature fluctuations: time–height cross sections measured with the UHOH RRL on 24 April 2013 between 11:00 and 12:00 UTC. The temporal and spatial resolution of the data is $\Delta t = 10$ s and $\Delta z = 3.75$ m with a gliding average of 109 m. The instantaneous CBL heights determined with the Haar-wavelet analysis are marked (same as shown in Fig. 2), a.g.l. (above ground level). (Black vertical lines are gaps which result from gridding the data to exact 10 s intervals; these artifacts do not influence the turbulence analysis.)

up at the non-zero lags which are used for the fit; the determination of the statistical noise level from the power spectra is more prone to errors.

Figure 6 shows the ACF obtained from the measured temperature fluctuations for heights between 400 and 1230 m a.g.l., i.e., 0.3 to 1.0 z_i for time lags from -200 to 200 s. The increase of the values at zero lag with height shows mainly the increase of the statistical noise with height.

Different values of the ACF close to the zero lag show differences in the atmospheric variance at different heights.

The following question arises: what is the most suitable number of lags for the extrapolation of the structure function to lag zero? This has been discussed in Wulfmeyer et al. (2010) and Turner et al. (2014b) but here we are providing more details. We have applied the following procedure to the measured temperature fluctuations for the determination

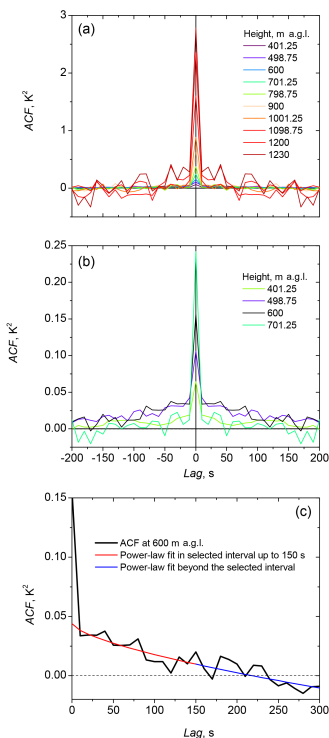


Figure 6. (a) Autocovariance functions (ACF) around the zero lag obtained at different heights from the temperature measurements shown in Fig. 5, i.e., with the data of 24 April 2013 between 11:00 and 12:00 UTC. (b) Zoom of (a) for lower heights only. (c) ACF with power-law fit for 600 m a.g.l.

of the integral scale, all higher-order moments, and for the separation of noise and atmospheric variances: first of all, the profile of the integral scale is derived using a standard number of lags. Usually, we are taking 20 time lags of 10 s covering thus 200 s, as this turned out from previous measurements to be a value which is typically appropriate. The resulting integral scale is a measure of the mean size of an

eddy in time. If the resulting integral scale is larger than the averaging time of the measured data, which is in this case 10 s, one can state that the most important part of the turbulent fluctuations is resolved. It can be theoretically shown that the zero crossing of the ACF appears at 2.5 times the integral scale (Wulfmeyer et al., 2015). Thus, we are choosing ≤ 2.5 times the mean value of the integral scale throughout the CBL as a reasonable number of fit lags. Please note that this refinement was not discussed in the literature before except only very recently by Turner et al. (2014b) and Wulfmeyer et al. (2015). Previously, very simple approaches were used such as just the value of the first lag as an approximation for the extrapolation to lag zero. Our approach is more appropriate and may further be refined by applying an iteration between the determination of the integral scale and the derivation of the optimal number of fit lags at each height. As the integral timescale has a mean of about 80 s in the CBL corresponding to a mean zero crossing of the ACF at 200 s, we finally decided to use 15 fit lags in this study (see Fig. 6c) which is on the safe side. We found that we can interrupt the iteration procedure in the first step because all resulting profiles are within the range of the noise error bars in this case regardless of whether we use 10, 15, or 20 fit lags. As a result, 15 fit lags finally seemed for us to be the best selection. For the higher-order moments, the same number of 15 fit lags was used as for the variance but here linear extrapolations to lag zero was applied (Lenschow et al., 2000). We consider this as best approach, as the shape of the higher-order structure function is still unknown to date.

3.3 Noise errors

The resulting profiles of the noise error of the temperature measurements

$$\Delta T(z) = \sqrt{\langle T_n^2(z) \rangle} \quad (3)$$

are shown in Fig. 7 together with profiles of the errors due to shot noise derived with Poisson statistics from the signal intensities (as detailed below). Both profiles are similar but it should be noted that the autocovariance technique specifies the total statistical error, while the shot-noise error is a part of the total statistical error.

For calculating the shot-noise errors from the signal intensities, the following approach was made: the lidar signals are detected simultaneously in analog and in photon-counting mode. As the intensities of our rotational Raman signals are too strong, the photon-counting signals are affected by dead-time effects in lower heights of about 6 km in daytime. Correction of these dead-time effects (Behrendt et al., 2004) is possible down to about 1.5 km. As this height limit is still too high for CBL studies, the analog signals have been used for the measurements of this study. In order to derive the shot-noise errors of the measurements with Poisson statistics, the analog signals of each 10 s profile were fitted to

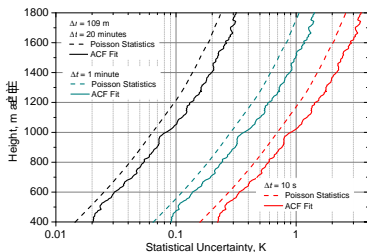


Figure 7. Statistical uncertainties of 10s, 1min, and 20min temperature profiles at noon determined with a $2/3$ -power-law fit of the ACF data (see Fig. 6). Shot-noise errors calculated by use of Poisson statistics from the detected signal intensities in each height are shown for comparison. It can be seen that the statistical uncertainty of the RRL temperature measurements is mainly governed by shot noise. The range resolution of the data was 109 m.

the photon-counting signals in heights between about 1.5 and 3 km, where both detection techniques were providing reliable data after dead-time correction of the photon-counting data. By this scaling, photon-counting rates could then be attributed to the analog signal intensities in lower altitudes. These attributed count rates were consequently used. The background photon-counting numbers were derived from the photon-counting signals detected from high altitudes.

The ratio of the two background-corrected photon-count numbers N_{RR1} and N_{RR2} of lower and higher rotational quantum transition channels

$$Q = \frac{N_{RR2}}{N_{RR1}} \quad (4)$$

is the measurement parameter which yields the atmospheric temperature profile after calibration of the system.

The shot-noise error of a signal with N photon counts according to Poisson statistics is

$$\Delta N(z) = \sqrt{N(z)}. \quad (5)$$

Error propagation for the RRL temperature data then yields (Behrendt et al., 2002)

$$\Delta T(z) = \frac{\partial T}{\partial Q} \frac{N_{RR2}(z)}{N_{RR1}(z)} \sqrt{\frac{N_{RR1}^*(z) + (\Delta \bar{B}_{RR1})^2}{(N_{RR1}(z))^2} + \frac{N_{RR2}^*(z) + (\Delta \bar{B}_{RR2})^2}{(N_{RR2}(z))^2}}, \quad (6)$$

with $N_{RR1}^*(z)$ and $N_{RR2}^*(z)$ for the photon counts in the two rotational Raman channels before background correction. $N_{RRi}(z) = N_{RRi}^*(z) - \bar{B}_{RRi}$ with $i = 1, 2$ are the signals which are corrected for background noise per range

bin \bar{B}_{RRi} . $\partial T / \partial Q$ is provided by the temperature calibration function. As outlined already above (see Sect. 3.1), the uncertainty of this calibration for the analysis of turbulent temperature fluctuations is negligible.

Since the background is determined over many range bins, the statistical uncertainty of the background can be neglected (Behrendt et al., 2004) so that one finally gets

$$\Delta T(z) = \frac{\partial T}{\partial Q} \frac{N_{RR2}(z)}{N_{RR1}(z)} \sqrt{\frac{N_{RR1}(z) + \bar{B}_{RR1}}{(N_{RR1}(z))^2} + \frac{N_{RR2}(z) + \bar{B}_{RR2}}{(N_{RR2}(z))^2}}. \quad (7)$$

The data in Fig. 7 show that the shot-noise errors calculated with Poisson statistics provide lower estimates for the total errors. But the comparison also confirms that the photon shot noise gives the major contribution (about 75 %) and that other statistical error sources (like the electric noise of the analog signals) are comparatively small. A similar result, also for analog signals which were glued to photon-counting signals, has already been obtained before for water vapor Raman lidar by Whiteman et al. (2006).

The background-corrected rotational Raman signals scale according to

$$N_{RRi}(z) \propto P \Delta t \Delta z \eta_t \eta_r A, \quad (8)$$

where $i = 1, 2$, P is laser power, Δt is measurement time, Δz is range resolution, η_t and η_r are transmitter and receiver efficiency, respectively, and A is receiving telescope area. The background counts in each signal range bin scale in a similar way but without being influenced by power P and η_t , so that we get

$$\bar{B}_{RRi}(z) \propto \Delta t \Delta z \eta_r A. \quad (9)$$

One can see from Eqs. (7) to (9) that the statistical measurement uncertainty scales consequently with the parameters which are found in both previous equations according to

$$\Delta T \propto \frac{1}{\sqrt{\Delta t \Delta z \eta_r A}}. \quad (10)$$

It is noteworthy, that increases of the laser power P and transmitter efficiency η_t are even more effective in reducing ΔT than increases of Δt , Δz , η_r , or A because the former improve only the backscatter signals and do not increase the background simultaneously like the latter. The value of the improvement obtained from increases of P or η_t , however, depends on the intensity of the background and thus on height and background-light conditions (see also Radlach et al., 2008; Hammann et al., 2015).

The statistical uncertainties for the RRL temperature measurements at noon shown in Fig. 7 were determined with 10s temporal resolution and for range averaging of

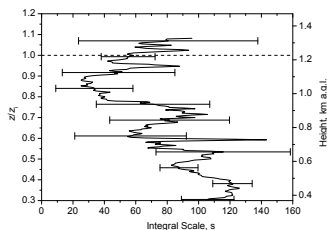


Figure 8. Integral scale of the temperature fluctuations shown in Fig. 5 (1 h period between 11:00 and 12:00 UTC, 24 April 2013). Error bars show the noise errors. The mean CBL height z_i of 1230 m (dashed line) was determined with the Haar-wavelet analysis of β_{par} and was used for the relative height scale z/z_i .

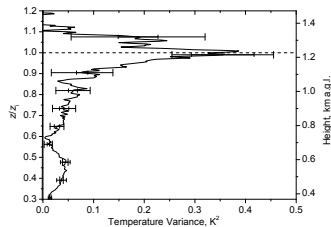


Figure 9. Profile of temperature variance (1 h period between 11:00 and 12:00 UTC, 24 April 2013). Error bars show the noise errors (thin error bars) and the sampling errors (thick error bars). The mean CBL height z_i of 1230 m (dashed line) was used for the relative height scale z/z_i .

109 m. The resulting error profiles for other temporal resolutions were then derived from the 10 s error profile by use of Eq. (10). The errors for other range resolutions can be easily obtained from Eq. (10) in a similar way.

The results of the error analysis show the very high performance of the UHOH RRL temperature data: with 10 s resolution, the total statistical uncertainty ΔT at noontime determined from the variance analysis of the temperature fluctuations is below 1 K up to 1020 m a.g.l. With 1 min resolution, ΔT is below 0.4 K up to 1000 m a.g.l. and below 1 K up to 1510 m a.g.l. With 20 min averaging, ΔT is below 0.1 and 0.3 K up to 1050 and 1710 m a.g.l., respectively.

3.4 Integral scale

Figure 8 shows the profile of the integral scale of the temperature fluctuations. It was obtained with the $2/3$ -power-law fit of the structure function to the ACF (Lenschow et al., 2000; Wulfmeyer et al., 2010). The integral scale is about 80 s in the mixed layer decreasing towards smaller values in the IL. At z_i , the integral scale was (56 ± 17) s. The integral scale is significantly larger than the temporal resolution of the UHOH RRL data of 10 s. This confirms that the resolution of our data is high enough to resolve the turbulent temperature fluctuations including the major part of the inertial subrange throughout the CBL. The integral timescale, which can be related to a length scale provided that the mean horizontal wind speed is known, is considered as a measure of the mean size of the turbulent eddies involved in the boundary layer mixing processes.

3.5 Temperature variance

To the best of our knowledge, the first profile of the temperature variance of the atmosphere $\overline{(T'_v(z))^2}$ measured with

a lidar system is shown in Fig. 9; the profile starts at about $0.3 z_i$ and covers the whole CBL. We found that between 0.3 and $0.9 z_i$, i.e., the major part of the CBL, the atmospheric variance was much smaller than in the IL. Here the values were only up to 0.1 K^2 (at $1100 \text{ m} = 0.9 z_i$ with 0.01 and 0.06 K^2 for the sampling and noise error, respectively). We also used the methods of Lenschow et al. (2000) for deriving these errors. While the noise errors denote the 1σ statistical uncertainties of the data product due to uncorrelated noise in the time series of the input data, the sampling errors describe those uncertainties resulting from the limited number of atmospheric eddies in the analysis period. Taking the error bars into account, one finds that the apparent minimum of the temperature variance profile at $0.6 z_i$ is only weakly significant. What remains is a profile with slightly increasing variance with height in the CBL and a clear maximum in the IL close to z_i . This maximum of the variance profile was 0.39 K^2 with a sampling error of 0.07 and 0.11 K^2 for the noise error (root-mean-square variability). Above, the variance decreased again. One expects such a structure for the variance profile: except at the surface, the temperature variance in the CBL is largest in the IL, since the temporal variability is driven by entrainment caused by turbulent buoyancy-driven motions acting against the temperature inversion at the top of the CBL (e.g., Deardorff, 1974; André et al., 1978; Stull, 1988; Moeng and Wyngaard, 1989).

For quantitative comparisons, often normalization of the temperature variance profile with T^* is used (Deardorff, 1970). But in the real world with its heterogeneous land use and soil properties and thus corresponding flux variability such scaling becomes difficult. Instead of a single scaling value, one could employ several flux stations and try to find a more representative scaling parameter by weighted averaging of the measurements made over different land-use types. But even then one expects that the scaled temperature vari-

ance profile depends on the ratio of the mean entrainment and surface flux (e.g., Moeng and Wyngaard, 1989). Thus, we decided not to scale the variance profile here and leave further generalizations to future studies based on more cases.

3.6 Third-order moment and skewness

The third-order moment (TOM) of a fluctuation is a measure of the asymmetry of the distribution. The skewness S is the TOM normalized by the variance to a dimensionless parameter defined for temperature as

$$S(z) = \frac{\overline{(T'(z))^3}}{(\overline{(T'(z))^2})^{3/2}}. \quad (11)$$

The normal distribution (Gaussian curve) has zero TOM and S . Positive values for TOM and S show a right-skewed distribution where the mode is smaller than the mean. If the mode is larger than the mean, TOM and S become negative (left-skewed distribution).

TOM and S profiles for the atmospheric temperature fluctuations of our case were derived with the technique of Lenschow et al. (2000), as explained in Sect. 3.2. The results are shown in Fig. 10. Up to about $0.9 z_i$, the TOM was not different to zero (taking the 1σ statistical uncertainties into account). In the IL, i.e., between 0.9 and $1.1 z_i$, a negative peak is found with values down to -0.93 K^3 with 0.05 and 0.16 K^3 for the sampling and noise errors, respectively. The skewness profile shows the same characteristics. Only data around $0.6 z_i$ had to be omitted from the skewness profile because the measured variance values are close to zero here and thus dividing by these values yields too large relative errors. At z_i , we found a skewness of -4.1 with 1.1 and 1.9 for the sampling and noise errors, respectively.

TOM and S profiles reveal interesting characteristics of the thermal plumes which were present in the CBL in this case. As rising plumes of warmer air are typically narrow and surrounded by larger areas of air close to the average temperature, one expects slightly positive temperature skewness in the major part of the CBL; e.g., Mironov et al. (1999) show values between 0 and 2 (see their Fig. 1b); they did not show negative values which would indicate narrow cold plumes. In the CBL up to about $0.9 z_i$, the measured values in our case agree with these data taking the uncertainties into account.

The negative minima of TOM and S in the IL above show a clear difference between the IL and the CBL below. Between 0.9 and $1.1 z_i$, negative and positive fluctuations were not symmetric but fewer very cold fluctuations were balanced by many warm fluctuations with less difference to the mean.

Because turbulent mixing occurs in the IL in a region of positive vertical temperature gradient, the air present in the free troposphere is warmer than the air in the CBL below. Consequently, the negative peak indicates that the cold overshooting updrafts in the IL were narrower in time than the downdrafts of warmer air.

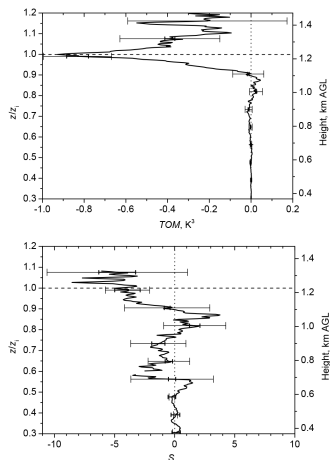


Figure 10. Same as Fig. 9 but profiles of the third-order moment (TOM) and the skewness S . Error bars show the noise errors (thin error bars) and the sampling errors (thick error bars). The mean CBL height z_i of 1230 m (dashed line) was used for the relative height scale z/z_i . The dotted vertical line marks zero skewness. Skewness data around 0.6 and above $1.1 z/z_i$ were omitted because the data were too noisy here due to variances close to zero.

Similar characteristics of the temperature TOM and skewness profiles in the IL were discussed, e.g., by Mironov et al. (1999), Canuto et al. (2001), and Cheng et al. (2005) who compare experimental data (tank, wind tunnel, airborne in situ), large eddy simulation (LES) data, and analytical expressions. Now, more comparisons can be performed between real atmospheric measurements and models.

Interestingly, an inverse structure of the TOM profile is found with respect to humidity fluctuations (Wulfmeyer, 1999b; Wulfmeyer et al., 2010; Turner et al., 2014b). Combining these results, it should be possible to perform very detailed comparisons with LES and to refine turbulence parameterizations. This concerns particularly the TKE (turbulent kinetic energy) 3.0 order schemes that are using the closure of the variance budget for determining the turbulent exchange coefficients.

3.7 Fourth-order moment and kurtosis

The fourth-order moment (FOM) is a measure of the steepness at the sides of the distribution and the corresponding

flatness of the peak. The kurtosis is the FOM normalized by the variance to a dimensionless parameter according to

$$\text{Kurtosis}(z) = \frac{\overline{(T'(z))^4}}{\left(\overline{(T'(z))^2}\right)^2}. \quad (12)$$

With this definition, the normal distribution (Gauss curve) has a kurtosis of 3. Equation (12) is also used by Lenschow et al. (2000); we follow this definition here. Please note that sometimes kurtosis is defined differently including a subtraction of 3 which then results in a kurtosis of 0 for the normal distribution, but mostly Kurtosis – 3 is called “excess kurtosis”.

Figure 11 shows FOM and kurtosis profiles of the measured temperature fluctuations of our case which have also been obtained with the method of Lenschow et al. (2000) for noise correction. For both FOM and kurtosis, the noise errors of the data are quite large; the importance of an error analysis becomes once more obvious. Throughout the CBL, no significant differences to the normal distribution are found. While the values for the FOM are close to zero in the CBL ($< 0.5 \text{ K}^4$ up to $0.9 z_i$), they appear larger in the IL, but the noise error does not allow for determining exact values, zero is still within the 1σ noise error bars. At z_i , FOM was 3.0 K^4 with 0.1 and 4.2 K^4 for the sampling and noise errors, respectively. The kurtosis at z_i was 23 with 8 and 35 for the sampling and noise errors, respectively. We conclude that the distribution of atmospheric temperature fluctuations was not significantly different to a Gaussian distribution (quasi-normal) regarding its fourth-order moment and kurtosis in our case.

Even if the data here are too noisy to identify non-zero FOM or kurtosis in the IL, it is interesting to note that higher values of kurtosis in the IL would reflect a situation for which a large fraction of the temperature fluctuations occurring in this region would exist due to infrequent, very large deviations in temperature; the related most vigorous thermals would then be capable to yield quite extreme temperature fluctuations, while mixing intensively in the IL with the air of the lower free troposphere. In contrast to this, the temperature fluctuations would be more moderate (Gaussian) in the CBL below.

4 Conclusions

We have shown that rotational Raman lidar provides a remote-sensing technique for the analysis of the turbulent temperature fluctuations within the well-developed CBL during noontime – even though the background-light conditions at noon are least favorable for the measurements. The required high temporal and spatial resolution combined with low-enough statistical noise of the measured data is reached by the UHOH RRL which is to the best of our knowledge for the first time. The data can thus be evaluated during all

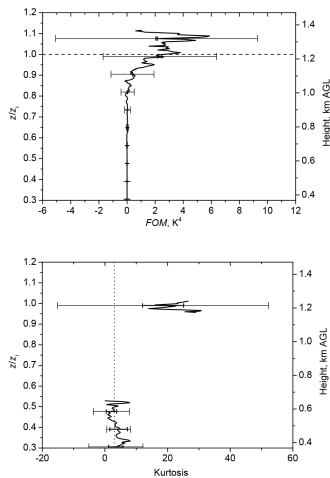


Figure 11. Same as Fig. 9 but profiles of the fourth-order moment (FOM) and kurtosis. Only kurtosis data below 0.55 and around $1.0 z/z_i$ are shown because other data are too noisy. The dotted vertical line in the lower panel marks a value of 3 which is the kurtosis of the normal distribution. Error bars show the noise errors (thin error bars) and the sampling errors (thick error bars). The mean CBL height z_i of 1230 m (dashed line in the upper panel) was used for the relative height scale z/z_i .

time periods of the day for studying the structure of the atmospheric boundary layer – of course also at night.

A case of the HOPE campaign was analyzed. The data were collected between 11:00 and 12:00 UTC on IOP 6, 24 April 2013, i.e., exactly around local noon (11:33 UTC). The UHOH RRL was located near the village of Hambach in western Germany ($50^\circ 53' 50.56'' \text{ N}$, $6^\circ 27' 50.39'' \text{ E}$; 110 m a.s.l.).

A profile of the noise variance was used to estimate the statistical uncertainty ΔT of the temperature data with a structure function fit to the ACF. A comparison with a ΔT profile derived with Poisson statistics demonstrated that the statistical error is mainly due to shot noise. The Haar-wavelet technique was applied to 10 s profiles of β_{par} and provided the mean CBL height over the observation period of $z_i = 1230 \text{ m a.g.l.}$ This value was used for normalizing the height scale. The integral scale had a mean of about 80 s in the CBL confirming that the temporal resolution of the RRL data of

10 s was sufficient for resolving the majority of turbulence down to the inertial subrange.

The results of this study give further information on turbulent temperature fluctuations and their statistics in the CBL and within the IL.

The atmospheric variance profile showed clearly the largest values close to z_i . A maximum of the variance of the atmospheric temperature fluctuations was found in the IL: 0.39 K^2 with a sampling and noise error of 0.07 and 0.11 K^2 , respectively.

Subsequently, also profiles of the third- and fourth-order moments were derived:

TOM and skewness were not significantly different to zero within the CBL up to about $0.9 z_i$. In the IL between 0.9 and $1.1 z_i$, a negative minimum was found with values down to -0.93 K^3 with 0.05 and 0.16 K^3 for the sampling and noise errors, respectively. Skewness at z_i was -4.1 and with 1.1 and 1.9 for the sampling and noise errors, respectively. We conclude that the turbulent temperature fluctuations were not significantly skewed in the CBL. In contrast to this, the atmospheric temperature fluctuations in the IL were clearly skewed to the left (negative skewness). This finding is related to narrower cold overshooting updrafts and broader downward mixing of warmer air from the free troposphere in the IL.

Throughout the CBL, no significant differences to the normal distribution were found for FOM and the kurtosis. For all moments but especially the FOM, the importance of an error analysis became once more obvious.

A quasi-normal FOM even when TOM is non-zero, agrees with the hypothesis of Millionshchikov (1941) which forms the basis for a large number of closure models (see Gryanik et al., 2005, for an overview). However, some recent theoretical studies, measurement data, and LES data suggest that this hypothesis would not be valid for temperature in the CBL (also see Gryanik et al., 2005, for an overview). Gryanik and Hartmann (2002) suggested furthermore a parameterization between the FOM, skewness, and variance of turbulent temperature fluctuations which can be tested as soon as a larger number of measurement cases on turbulent temperature fluctuations with rotational Raman lidar have become available.

It is planned to extend the investigation of CBL characteristics in future studies also by combining the UHOH RRL data with humidity and wind observations from water vapor DIAL (Behrendt et al., 2009; Wagner et al., 2013; Muppa et al., 2015) and Doppler lidar. Furthermore, also the scanning capability of the UHOH RRL will be used in the future to collect data closer to the ground and even the surface layer (Behrendt et al., 2012) in order to investigate heterogeneities over different terrain.

The combination of different turbulent parameters measured by lidar – preferably, at the same atmospheric coordinates simultaneously – promises to provide further understanding on the important processes taking place in the CBL including the IL. For instance, up until now, the key phys-

ical processes governing the IL and their relationships with other CBL properties unfortunately remain only poorly understood: they are oversimplified in empirical studies and poorly represented in the models. In consequence, more data should be evaluated to get the statistics of the turbulent temperature fluctuations under a variety of atmospheric conditions. We believe that corresponding measurements with RRL will contribute significantly to better understanding of boundary layer meteorology in the future – not only in daytime but also at night so that the entire diurnal cycle is covered and the characteristics of turbulent temperature fluctuations in different stability regimes can be observed.

Acknowledgements. The HOPE campaign was funded by the German Research Ministry under the project number 01LK1212 A. We thank the colleagues of Karlsruhe Institute of Technology (KIT) and the University of Cologne for performing the radiosonde launches. Furthermore, we like to thank the three anonymous reviewers for their helpful comments.

Edited by: S. Buehler

References

- André, J. C., De Moor, G., Lacarrère, P., Therry, G., and Du Vachat, R.: Modeling the 24-hour evolution of the mean and turbulent structures of the planetary boundary layer, *J. Atmos. Sci.*, 35, 1861–1883, 1978.
- Angevine, W. M., Doviak, R. J., and Sorbjan, Z. S.: Remote Sensing of Vertical Velocity Variance and Surface Heat Flux in a Convective Boundary Layer, *J. Appl. Meteorol.* 33, 977–983, 1994.
- Behrendt, A.: Temperature measurements with lidar, in: *Lidar: Range-Resolved Optical Remote Sensing of the Atmosphere*, edited by: Weikamp, C., Springer, New York, 273–305, 2005.
- Behrendt, A. and Reichardt, J.: Atmospheric temperature profiling in the presence of clouds with a pure rotational Raman lidar by use of an interference-filter-based polychromator, *Appl. Optics*, 39, 1372–1378, 2000.
- Behrendt, A., Nakamura, T., Onishi, M., Baumgart, R., and Tsuda, T.: Combined Raman lidar for the measurement of atmospheric temperature, water vapor, particle extinction coefficient, and particle backscatter coefficient, *Appl. Optics*, 41, 7657–7666, 2002.
- Behrendt, A., Nakamura, T., and Tsuda, T.: Combined temperature lidar for measurements in the troposphere, stratosphere, and mesosphere, *Appl. Optics*, 43, 2930–2939, 2004.
- Behrendt, A., Wulfmeyer, V., Riede, A., Wagner, G., Pal, S., Bauer, H., Radlach, M., and Späth, F.: 3-Dimensional observations of atmospheric humidity with a scanning differential absorption lidar, in: *Remote Sensing of Clouds and the Atmosphere XIV*, edited by: Picard, R. H., Schäfer, K., Comeron, A., and van Weele, M., SPIE Conference Proceeding Vol. 7475, ISBN: 9780819477804, 2009, Art. No. 74750L, doi:10.1117/12.835143, 2009.
- Behrendt, A., Pal, S., Aoshima, F., Bender, M., Blyth, A., Corsmeier, U., Cuesta, J., Dick, G., Dominger, M., Flamant, C., Di Girolamo, P., Gorgas, T., Huang, Y., Kalthoff, N.,

- Khodayar, S., Mannstein, H., Träumner, K., Wieser, A., and Wulfmeyer, V.: Observation of convection initiation processes with a suite of state-of-the-art research instruments during COPS IOP8b, Q. J. Roy. Meteor. Soc., 137, 81–100, doi:10.1002/qj.758, 2011a.
- Behrendt, A., Pal, S., Wulfmeyer, V., Valdebenito B., Á. M., and Lammel, G.: A novel approach for the characterisation of transport and optical properties of aerosol particles near sources, Part I: measurement of particle backscatter coefficient maps with a scanning UV lidar, Atmos. Environ., 45, 2795–2802, doi:10.1016/j.atmosenv.2011.02.061, 2011b.
- Behrendt, A., Hammann, E., Späth, F., Riede, A., Metzendorf, S., and Wulfmeyer, V.: Revealing surface layer heterogeneities with scanning water vapor DIAL and scanning rotational Raman lidar, in: Reviewed and Revised Papers Presented at the 26th International Laser Radar Conference (ILRC 2012), 25–29 June 2012, Porto Heli, Greece, edited by: Papayannis, A., Balis, D., and Amiridis, V., paper S7P-17, 913–916, 2012.
- Campistron, B., Bernard, S., Bénech, B., Arduhin-Girard, F., Dessens, J., Dupont, E., and Carissimo, B.: Turbulent Dissipation Rate In The Boundary Layer Via UHF Wind Profiler Doppler Spectral Width Measurements, Bound.-Lay. Meteorol., 103, 361–389, 2002.
- Canuto, V. M., Chang, Y., and Howard, A.: New third-order moments for the convective boundary layer, J. Atmos. Sci., 58, 1169–1172, 2001.
- Cheng, Y., Canuto, V. M., and Howard, A. M.: Nonlocal convective PBL Model based on new third- and fourth-order moments, J. Atmos. Sci., 62, 2189–2204, 2005.
- Clarke, R. H., Dyer, A. J., Brook, R. R., Reid, D. G., and Troup, A. J.: The Wangara experiment: Boundary layer data, Tech. Paper No. 19, CSIRO, Division of Meteorological Physics, Aspendale, Australia, 362 pp., 1971.
- Cooney, J.: Measurement of atmospheric temperature profiles by Raman backscatter, J. Appl. Meteorol., 11, 108–112, 1972.
- Corsmeier, U., Kalthoff, N., Barthlott, C., Behrendt, A., Di Girolamo, P., Dörninger, M., Aoshima, F., Handwerker, J., Kottmeier, C., Mahlike, H., Mobbs, S., Vaughan, G., Wickert, J., and Wulfmeyer, V.: Driving processes for deep convection over complex terrain: a multiscale analysis of observations from COPS-IOP 9c, Q. J. Roy. Meteor. Soc., 137, 137–155, doi:10.1002/qj.754, 2011.
- Deardorff, J. W.: Convective velocity and temperature scales for the unstable planetary boundary layer and for Rayleigh convection, J. Atmos. Sci., 27, 1211–1213, 1970.
- Deardorff, J. W.: Three-dimensional numerical study of turbulence in an entraining mixed layer, Bound.-Lay. Meteorol., 7, 199–226, 1974.
- Di Girolamo, P., Marchese, R., Whiteman, D. N., and Demoz, B.: Rotational Raman lidar measurements of atmospheric temperature in the UV, Geophys. Res. Lett., 31, L01106, doi:10.1029/2003GL018342, 2004.
- Di Girolamo, P., Behrendt, A., and Wulfmeyer, V.: Spaceborne profiling of atmospheric temperature and particle extinction with pure rotational Raman lidar and of relative humidity in combination with differential absorption lidar: performance simulations, Appl. Optics, 45, 2474–2494, 2006.
- Eng, K., Coulter, R., and Brutsaert, W.: Vertical Velocity Variance in the Mixed Layer from Radar Wind Profilers, J. Hydrol. Eng., 8, 301–307, 2003.
- Furumoto, J. and Tsuda, T.: Characteristics of energy dissipation rate and effect of humidity on turbulence echo power revealed by MU radar-RASS Measurements, J. Atmos. Terr. Sol.-Phys., 63, 285–294, 2001.
- Giez, A., Ehret, G., Schwiesow, R. L., Davis, K. J., and Lenschow, D. H.: Water vapor flux measurements from ground-based vertically pointed water vapor differential absorption and Doppler lidars, J. Atmos. Ocean. Tech., 16, 237–250, 1999.
- Groenemeijer, P., Barthlott, C., Behrendt, A., Corsmeier, U., Handwerker, J., Kohler, M., Kottmeier, C., Mahlike, H., Pal, S., Radlach, M., Trentmann, J., Wieser, A., and Wulfmeyer, V.: Multi-sensor measurements of a convective storm cluster over a low mountain range: adaptive observations during PRINCE, Mon. Weather Rev., 137, 585–602, doi:10.1175/2008MWR2562.1, 2009.
- Gryaniuk, V. M. and Hartmann, J.: A turbulence closure for the convective boundary layer based on a two-scale mass-flux approach, J. Atmos. Sci., 59, 2729–2744, 2002.
- Gryaniuk, V. M., Hartmann, J., Raasch, S., and Schröter, M.: A refinement of the Millionschikov Quasi-Normality Hypothesis for convective boundary layer turbulence, J. Atmos. Sci., 62, 2632–2638, 2005.
- Hammann, E., Behrendt, A., Le Mounier, F., and Wulfmeyer, V.: Temperature profiling of the atmospheric boundary layer with rotational Raman lidar during the HD(CP)² Observational Prototype Experiment, Atmos. Chem. Phys., 15, 2867–2881, doi:10.5194/acp-15-2867-2015, 2015.
- Hermawan, E. and Tsuda, T.: Estimation of turbulence energy dissipation rate and vertical eddy diffusivity with the MU radar RASS, J. Atmos. Sol.-Terr. Phys., 61, 1123–1130, doi:10.1016/S1364-6826(99)00075-9, 1999.
- Kadyrov, E. N., Shur, G. N., and Viazankin, A. S.: Investigation of atmospheric boundary layer temperature, turbulence, and wind parameters on the basis of passive microwave remote sensing, Radio Sci., 38, 8048, doi:10.1029/2002RS002647, 2003.
- Kalthoff, N., Träumner, K., Adler, B., Späth, S., Behrendt, A., Wieser, A., Handwerker, J., Madonna, F., and Wulfmeyer, V.: Dry and moist convection in the boundary layer over the Black Forest – a combined analysis of in situ and remote sensing data, Meteorol. Z., 22, 445–461, doi:10.1127/0941-2948/2013/0417, 2013.
- Kiemle, C., Ehret, G., Giez, A., Davis, K. J., Lenschow, D. H., and Oncley, S. P.: Estimation of boundary layer humidity fluxes and statistics from airborne differential absorption lidar (DIAL), J. Geophys. Res., 102, 29189–29203, 1997.
- Kiemle, C., Brewer, W. A., Ehret, G., Hardesty, R. M., Fix, A., Senff, C., Wirth, M., Poberaj, G., and LeMone, M. A.: Latent heat flux profiles from collocated airborne water vapor and wind lidars during IHOP 2002, J. Atmos. Ocean. Tech., 24, 627–639, 2007.
- Kiemle, C., Wirth, M., Fix, A., Rahm, S., Corsmeier, U., and Di Girolamo, P.: Latent heat fluxes over complex terrain from airborne water vapour and wind lidars, Q. J. Roy. Meteor. Soc., 137, 190–203, 2011.
- Kolmogorov, A. N.: The Local Structure of Turbulence in Incompressible Viscous Fluid for Very Large Reynolds Numbers, Proc.

- R. Soc. Lond., A 434, 1890, 9–13, doi:10.1098/rspa.1991.0075, 1991.
- Lenschow, D. H., Wulfmeyer, V., and Senff, C.: Measuring second through fourth-order moments in noisy data, *J. Atmos. Ocean. Tech.*, 17, 1330–1347, 2000.
- Lenschow, D. H., Lothon, M., Mayor, S. D., Sullivan, P. P., and Caunt, G.: A comparison of higher-order vertical velocity statistics in the convective boundary layer from lidar with in-situ measurements and large-eddy simulations, *Bound.-Lay. Meteorol.*, 143, 107–123, 2012.
- Martin, S., Bange, J., and Beyrich, F.: Meteorological profiling of the lower troposphere using the research UAV “M²AV Carolo”, *Atmos. Meas. Tech.*, 4, 705–716, doi:10.5194/amt-4-705-2011, 2011.
- Martin, S., Beyrich, F., and Bange, J.: Observing Entrainment Processes Using a Small Unmanned Aerial Vehicle: A Feasibility Study, *Bound.-Lay. Meteorol.*, 150, 449–467, 2014.
- Millionschikov, M. D.: On the Theory of Homogeneous Isotropic Turbulence, *Dokl. Akad. Nauk SSSR*, 32, 611–614, 1941.
- Mironov, D. V., Gryanik, M., Lykosov, V. N., and Zilitinkevich, S. S.: Comments on “A new second-order turbulence closure scheme for the planetary boundary layer”, *J. Atmos. Sci.*, 56, 3478–3481, 1999.
- Moeng, C.-H. and Wyngaard, J. C.: Evaluation of turbulent transport and dissipation closures in second-order modelling, *J. Atmos. Sci.*, 46, 2311–2330, 1989.
- Muppa, S. K., Behrendt, A., Späth, F., Wulfmeyer, V., Metzendorf, S., and Riede, A.: Turbulent humidity fluctuations in the convective boundary layer: Case studies using DIAL measurements, *Bound.-Lay. Meteorol.*, under review, 2015.
- Muschinski, A., Frehlich, R., Jensen, M., Hugo, R., Eaton, F., and Balsley, B.: Fine-scale measurements of turbulence in the lower troposphere: an intercomparison between a kite- and balloon-borne, and a helicopter-borne measurement system, *Bound.-Lay. Meteorol.*, 98, 219–250, 2001.
- Nash, J., Oakley, T., Vümel, H., and Li, W.: WMO Intercomparison of High Quality Radiosonde Systems, Published by the World Meteorological Organization (WMO), WMO/TD-No. 1580; Instruments and Observing Methods Report No. 107, 249 pp., 2011.
- O’Connor, E., Illingworth, A., Brooks, I., Westbrook, M., Christopher, D., Hogan, R., Davies, F., and Brooks, B.: A Method for Estimating the Turbulent Kinetic Energy Dissipation Rate from a Vertically Pointing Doppler Lidar, and Independent Evaluation from Balloon-Borne In Situ Measurements, *J. Atmos. Ocean. Tech.*, 27, 1652–1664, doi:10.1175/2010JTECHA1455.1, 2010.
- Pal, S., Behrendt, A., and Wulfmeyer, V.: Elastic-backscatter-lidar-based characterization of the convective boundary layer and investigation of related statistics, *Ann. Geophys.*, 28, 825–847, doi:10.5194/angeo-28-825-2010, 2010.
- Pal, S., Xueref-Remy, I., Ammoura, L., Chazette, P., Gibert, F., Royer, P., Dieudonné, E., Dupont, J. C., Haeffelin, M., Lac, C., Lopez, M., Morille, Y., and Ravetta, F.: Spatio-temporal variability of the atmospheric boundary layer depth over the Paris agglomeration: an assessment of the impact of the urban heat island intensity, *Atmos. Environ.*, 63, 261–275, 2012.
- Pal, S., Haeffelin, M., and Batchvarova, E.: Exploring a geophysical process-based attribution technique for the determination of the atmospheric boundary layer depth using aerosol lidar and near-surface meteorological measurements, *J. Geophys. Res.-Atmos.*, 118, 1–19, doi:10.1002/jgrd.50710, 2013.
- Radlach, M., Behrendt, A., and Wulfmeyer, V.: Scanning rotational Raman lidar at 355 nm for the measurement of tropospheric temperature fields, *Atmos. Chem. Phys.*, 8, 159–169, doi:10.5194/acp-8-159-2008, 2008.
- Senff, C. J., Bösenberg, J., and Peters, G.: Measurement of water vapor flux profiles in the convective boundary layer with lidar and Radar-RASS, *J. Atmos. Ocean. Tech.*, 11, 85–93, 1994.
- Senff, C. J., Bösenberg, J., Peters, G., and Schaberl, T.: Remote sensing of turbulent ozone fluxes and the ozone budget in the convective boundary layer with DIAL and radar-RASS: a case study, *Contrib. Atmos. Phys.*, 69, 161–176, 1996.
- Sorbjan, Z.: Effects caused by varying the strength of the capping inversion based on a large eddy simulation model of the shear-free convective boundary layer, *J. Atmos. Sci.*, 53, 2015–2024, 1996.
- Sorbjan, Z.: An evaluation of local similarity on the top of the mixed layer based on large-eddy simulations, *Bound.-Lay. Meteorol.*, 101, 183–207, 2001.
- Sorbjan, Z.: Statistics of scalar fields in the atmospheric boundary layer based on large-eddy simulations, Part I: free convection, *Bound.-Lay. Meteorol.*, 116, 467–486, 2005.
- Stull, R. B.: *An Introduction to Boundary Layer Meteorology*, Springer, Heidelberg, New York, 688 pp., 1988.
- Träumler, K., Damian, Th., Stawiarski, Ch., and Wieser, A.: Turbulent Structures and Coherence in the Atmospheric Surface Layer, *Bound.-Lay. Meteorol.*, 154, 1–25, doi:10.1007/s10546-014-9967-6, 2015.
- Turner, D. D., Ferrare, R. A., Wulfmeyer, V., and Scarino, A. J.: Aircraft evaluation of ground-Based Raman lidar water vapor turbulence profiles in convective mixed layers, *J. Atmos. Ocean. Tech.*, 31, 1078–1088, doi:10.1175/JTECH-D-13-00075.1, 2014a.
- Turner, D. D., Wulfmeyer, V., Berg, L. K., and Schween, J. H.: Water vapor turbulence profiles in stationary continental convective mixed layers, *J. Geophys. Res.*, 119, 1–15, doi:10.1002/2014JD022202, 2014b.
- Valdebenito, A. M., Pal, S., Lammel, G., Behrendt, A., and Wulfmeyer, V.: A novel approach for the characterisation of transport and optical properties of aerosol particles near sources: microphysics-chemistry-transport model development and application, *Atmos. Environ.*, 45, 2981–2990, doi:10.1016/j.atmosenv.2010.09.004, 2011.
- Wagner, G., Wulfmeyer, V., Späth, F., Behrendt, A., and Schiller, M.: Performance and specifications of a pulsed high-power single-frequency Ti:Sapphire laser for water-vapor differential absorption lidar, *Appl. Optics*, 52, 2454–2469, doi:10.1364/AO.52.002454, 2013.
- Weckwerth, T. M., Wilson, J. W., and Wakimoto, R. M.: Thermodynamic variability within the convective boundary layer due to horizontal convective rolls, *Mon. Weather Rev.*, 124, 769–784, 1996.
- Whiteman, D. N., Demoz, B., Di Girolamo, P., Comer, J., Veselovskii, I., Evans, K., Wang, Z., Sabatino, D., Schwemmer, G., Gentry, B., Lin, R.-F., Behrendt, A., Wulfmeyer, V., Browell, E., Ferrare, R., Ismail, S., and Wang, J.: Raman Lidar Measurements during the International H₂O Project. Part II: Case Studies, *J. Atmos. Ocean. Tech.*, 23, 170–183, 2006.

- Wulfmeyer, V.: Investigations of humidity skewness and variance profiles in the convective boundary layer and comparison of the latter with large eddy simulation results, *J. Atmos. Sci.*, 56, 1077–1087, 1999a.
- Wulfmeyer, V.: Investigation of turbulent processes in the lower troposphere with water-vapor DIAL and radar-RASS, *J. Atmos. Sci.*, 56, 1055–1076, 1999b.
- Wulfmeyer, V. and Janjic, T.: 24-h observations of the marine boundary layer using ship-borne NOAA high-resolution Doppler lidar, *J. Appl. Meteorol.*, 44, 1723–1744, 2005.
- Wulfmeyer, V., Pal, S., Turner, D. D., and Wagner, E.: Can water vapour Raman lidar resolve profiles of turbulent variables in the convective boundary layer?, *Bound.-Lay. Meteorol.*, 136, 253–284, doi:10.1007/s10546-010-9494-z, 2010.
- Wulfmeyer, V., Behrendt, A., Sorbian, Z., Turner, D. D., and Hardisty, R. M.: Determination of Convective Boundary Layer Entrainment Fluxes, Dissipation Rates, and the Molecular Destruction of Variances: Theoretical Description and a Strategy for its Confirmation with a Novel Lidar System Synergy, *J. Atmos. Sci.*, under review, 2015.
- Wyngaard, J. C.: *Turbulence in the Atmosphere*, Cambridge University Press, 2010.
- Wyngaard, J. C. and Cote, O. R.: The budgets of turbulent kinetic energy and temperature variance in the atmospheric surface layer, *J. Atmos. Sci.*, 28, 190–201, 1971.

5.2 Noise error of water vapor measurements

The instrumental noise error of water vapor measurements was investigated. In Fig. 5.1 the analyzed time series (19 May 2013, 13:00 to 13:40 UTC) with a gliding average of 154 m and 10 s time resolution is shown. The boundary layer became quasi-stationary during the observation period and updraft structures could be observed.

Due to the high background in the WV detection, the error cannot be estimated from the photon counting data. An autocovariance analysis is able to distinguish between instrumental and atmospheric noise in the data, as the instrumental noise is uncorrelated and the atmospheric noise correlated from time step to time step. In an auto-covariance calculation of the data in one altitude, the noise error is the value at zero lag whereas the atmospheric noise forms the overall shape of the function. The calculation is done for each altitude.

In Fig. 5.2 the statistical error of a 10 s measurement is shown. Additionally, the error was scaled to other temporal averages. In principle the error should also depend on the absolute water vapor content as this influences the signal counts. But in this case it seems that water vapor was more or less evenly distributed in the boundary layer. In the 10 s resolution, a noise error of 1 g/kg is reached already in 1 km altitude. It is still useful for turbulence studies, but only limited for other purposes. The 20 min average shows less than 1 g/kg error throughout the whole convective boundary layer. The measurement was at 13 UTC and the solar background was almost maximal around this time period, therefore this study is assumed to show the highest instrumental noise during the diurnal circle.

5.3 Higher order moments of temperature and water vapor mixing ratio

Temperature and water vapor are important variables in the atmosphere. For PBL studies knowledge of both variables is needed. In earlier studies of turbulent structures mostly only one variable was presented [123, 99, 17, 77] or several with a combination of different lidar systems [122]. With a RRL including vibrational Raman

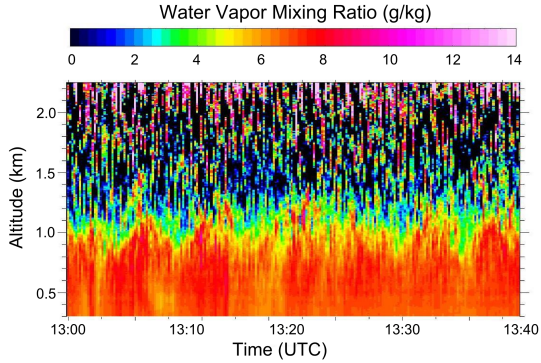


Figure 5.1: Water vapor mixing ratio time series with 10 s and 154 m gliding average. The time period from 13:00 till 13:40 UTC (19 May 2013) was chosen due to the constant boundary layer height. A z_i of 1075 m was determined for this time period.

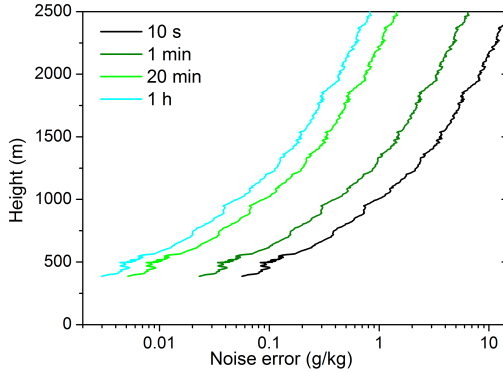


Figure 5.2: Statistical noise determined of a water vapor measurement with 154 m vertical resolution and a data point each 3.75 m. The error of a 10 s was scaled to other temporal averages. The measurement was done at 13 UTC, therefore the solar background is high and smaller noise error values are expected at other times of the day.

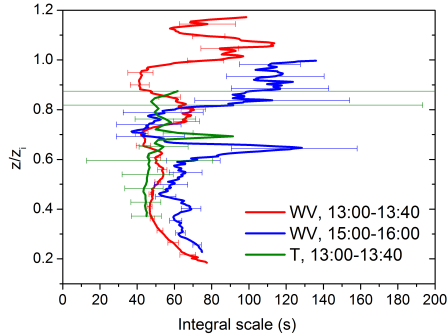


Figure 5.3: Integral scale profiles of temperature measurements between 13:00 and 13:40 UTC (green) and from water vapor measurements between 13:00 and 13:40 UTC (red) and between 15:00 and 16:00 UTC (blue). Error bars represent the sampling error.

water vapor measurements, temperature profiles as well as water vapor profiles are measured in a high resolution. In a comparison between profiles acquired with a set of lidars it could not be eliminated that slightly different volumes are sampled and therefore also slightly different turbulent structures. Here the measurements are definitely in the same volume. Such kind of measurements can be performed with the UHOH RRL since May 2013 and the presented variance and higher order moment profiles are the first evaluating the water vapor profiles of this system.

The water vapor detection channel was not yet installed on the IOP, which was used in section 5.1. Therefore the time period 19 May 2013, 13:00-13:40 UTC was chosen for the analysis, which was already shown in figure 4.1, and a later time period from 15:00 to 16:00 UTC on the same day. The temperature data were with 105 m gliding average over data points each 15 m and the water vapor data with 154 m gliding average and 3.75 m data points. Variance profiles are typically scaled by the height of the boundary layer z_i . It was derived by the Haar-Wavelet method with the elastic backscatter data of the WV DIAL (see also [17]). A z_i of 1075 m was determined for the first and 1316 m for the second time period.

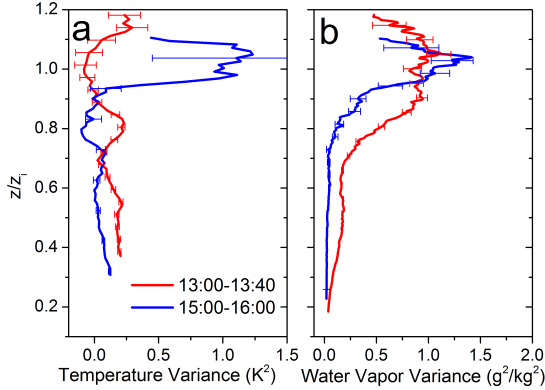


Figure 5.4: (a) Temperature variance profiles for both cases. While between 15:00 and 16:00 UTC (blue) the maximum variance is found at z_i , it is clearly lower at 13:00 to 13:40 UTC (red). (b) Water vapor mixing ratio variance for both time periods with highest values round z_i . Error bars represent the sampling error.

In the following graphs the altitude is given in dependency of this height.

In the first step the profiles were gridded to achieve a constant time step between profiles of 10.0 seconds. A second step despiked the data and removed a linear trend. Then the mean is subtracted to get the deviations from the mean. From these data the auto-covariance is calculated for each altitude from 50 lags and the first 20 lags fitted to derived the variance.

The integral length scale describes the typical scale of an eddy. It is shown in Fig. 5.3 for temperature at 13:00 UTC and water vapor for 13:00 and 15:00 UTC. As can be seen, for 13:00 UTC the profiles show a values of approximately 40 to 50 s in the lower PBL for both the temperature and the water vapor mixing ratio and up to 70 s at $0.8 z_i$. The values in the second time period are 70 s below $0.7 z_i$ and lower above. The temperature profile for the second case is not shown due to large error bars.

In Fig. 5.4 the variance profiles are plotted. Maximum variance

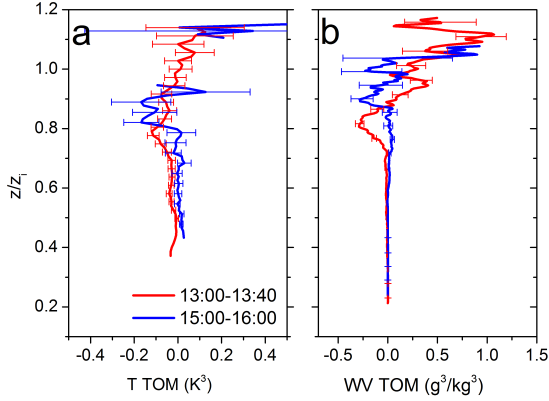


Figure 5.5: (a) Third order moment of temperature for both time periods. In the red curve the TOM shows a small negative peak at z_i , like expected from the variance profile. Negative values are found below the boundary layer top for the blue curve. Values at z_i are missing due to large error bars. (b) TOM of water vapor mixing ratio with negative values below z_i and positive values in the entrainment zone. Error bars represent the sampling error.

is expected around z_i , which is the case in both water vapor variance profiles and in the temperature variance profile for 15:00 till 16:00 UTC. In the other case the maximum is found at a lower altitude. That could be caused by the inhomogeneous boundary layer with a higher impact of processes in lower heights. It seems that the mixing of free tropospheric air with the CBL air takes place lower in case of temperature than for particles. The maximum values of $0.23 \pm 0.03 K^2$ and $1.23 \pm 0.71 K^2$ are comparable to the value $0.39 K^2$ found in [17]. For the water vapor profiles the highest variance values are found between 0.8 and 1.2 z_i . The variance at z_i is $0.94 \pm 0.05 (g/kg)^2$ and $1.41 \pm 0.22 (g/kg)^2$, respectively, which is in comparison with the cases in [123, 77] and [122] a relatively high value. Here values between $0.3 (g/kg)^2$ [77] and $3.5 (g/kg)^2$ [123] are reported. A comparison between the two time steps reveals, that the sampling error is larger for the second time period.

Figure 5.5 shows the corresponding third order moment profiles. The TOM of temperature is expected to be around zero in the mixed

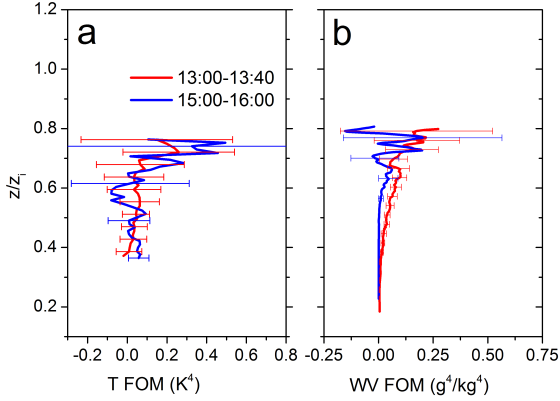


Figure 5.6: (a) Fourth-order moment of temperature. Values above $0.8 z_i$ are too noisy. (b) FOM of water vapor mixing ratio. Error bars represent the sampling error.

boundary layer with negative values at z_i [17]. This behavior can be observed in the red curve. A negative peak is observable at $0.8 z_i$ corresponding to the variance profile. Unfortunately the error bars of the blue curve were large at z_i therefore these values are not shown for clarity. But there are already negative values at $0.8 z_i$, so it seems that it is not a typical case.

The water vapor profiles show negative values down to $-0.25 (g/kg)^3$ at z_i and positive values above. Like already seen in the variance profile, the processes at the boundary top are not clearly defined. Also here the transition is found at a lower altitude ($0.85 z_i$) as expected. The TOM values are in comparison with [77] high, therefore the eddy structure seems to be more asymmetric in this case. Already in the time series shown in Fig. 5.1 the single eddies are apparent and the whole time series looks inhomogeneous.

In Fig. 5.6 the fourth-order moment is shown. Like expected in typical convective cases, the fourth-order moment is small inside the boundary layer with higher values above. While the error bars in the water vapor FOM allow to identify the shape, the error bars in the temperature FOM are larger than the values itself.

The study shows that it is possible to derive the higher order moments of water vapor profiles from the recent measurements with the RRL. The noise error is a limitation, but the performance is comparable with vibrational Raman lidars applied in other studies. In combination with the simultaneous measured temperature profiles, this system is a valuable tool in turbulence studies.

5.4 Wulfmeyer et al., 2016, Journal of Atmospheric Sciences

Part of the data acquired during HOPE is used in a publication about parametrization schemes for the boundary layer. Additional to the proposed equations the results are compared between the methods. I provided the temperature profiles.

© Copyright 2016 American Meteorological Society (AMS). Permission to use figures, tables, and brief excerpts from this work in scientific and educational works is hereby granted provided that the source is acknowledged. Any use of material in this work that is determined to be “fair use” under Section 107 of the U.S. Copyright Act September 2010 Page 2 or that satisfies the conditions specified in Section 108 of the U.S. Copyright Act (17 USC §108, as revised by P.L. 94-553) does not require the AMS’s permission. Reproduction, systematic reproduction, posting in electronic form, such as on a web site or in a searchable database, or other uses of this material, except as exempted by the above statement, requires written permission or a license from the AMS. Additional details are provided in the AMS Copyright Policy, available on the AMS Web site located at (<http://www.ametsoc.org/>) or from the AMS at 617-227-2425 or copyrights@ametsoc.org.

Determination of Convective Boundary Layer Entrainment Fluxes, Dissipation Rates, and the Molecular Destruction of Variances: Theoretical Description and a Strategy for Its Confirmation with a Novel Lidar System Synergy

VOLKER WULFMAYER

*Institute of Physics and Meteorology, University of Hohenheim, Stuttgart, Germany, and
Cooperative Institute for Research in Environmental Sciences, Boulder, Colorado*

SHRAVAN KUMAR MUPPA, ANDREAS BEHRENDT, EVA HAMMANN, AND FLORIAN SPÄTH

Institute of Physics and Meteorology, University of Hohenheim, Stuttgart, Germany

ZBIGNIEW SORBJAN

Physics Department, Marquette University, Milwaukee, Wisconsin

DAVID D. TURNER

NOAA/National Severe Storms Laboratory, Norman, Oklahoma


R. MICHAEL HARDESTY

NOAA/Earth System Research Laboratory, Boulder, Colorado

(Manuscript received 22 December 2014, in final form 20 October 2015)

ABSTRACT

Atmospheric variables in the convective boundary layer (CBL), which are critical for turbulence parameterizations in weather and climate models, are assessed. These include entrainment fluxes, higher-order moments of humidity, potential temperature, and vertical wind, as well as dissipation rates. Theoretical relationships between the integral scales, gradients, and higher-order moments of atmospheric variables, fluxes, and dissipation rates are developed mainly focusing on the entrainment layer (EL) at the top of the CBL. These equations form the starting point for tests of and new approaches in CBL turbulence parameterizations. For the investigation of these relationships, an observational approach using a synergy of ground-based water vapor, temperature, and wind lidar systems is proposed. These systems measure instantaneous vertical profiles with high temporal and spatial resolution throughout the CBL including the EL. The resolution of these systems permits the simultaneous measurement of gradients and fluctuations of these atmospheric variables. For accurate analyses of the gradients and the shapes of turbulence profiles, the lidar system performances are very important. It is shown that each lidar profile can be characterized very well with respect to bias and system noise and that the constant bias has negligible effect on the measurement of turbulent fluctuations. It is demonstrated how different gradient relationships can be measured and tested with the proposed lidar synergy within operational measurements or new field campaigns. Particularly, a novel approach is introduced for measuring the rate of destruction of humidity and temperature variances, which is an important component of the variance budget equations.

 Denotes Open Access content.

Corresponding author address: Volker Wulfmeyer, Institute of Physics and Meteorology, University of Hohenheim, Garbenstraße 30, 70599 Stuttgart, Germany.
E-mail: volker.wulfmeyer@uni-hohenheim.de

DOI: 10.1175/JAS-D-14-0392.1

© 2016 American Meteorological Society

1. Introduction

The turbulent transport of heat, matter, and momentum in the convective boundary layer (CBL) is essential for many key processes in the atmosphere. It determines the horizontal and vertical distribution of scalars such as humidity and other constituents as well as the vertical

stability. Particularly critical are the entrainment fluxes at the CBL top, as they influence the 3D fields of water vapor, temperature, and horizontal wind in the lower troposphere in both vertical directions: above the CBL by entrainment processes and from the CBL top down to the surface and the soil–vegetation layers by its coupling with the surface fluxes and the closure of the surface energy balance. The resulting 3D fields characterize the preconvective environment and influence thunderstorm initiation as well as the development of clouds and precipitation.

Generally, the grid increments of state-of-the-art weather forecast and climate models are too large to resolve small-scale boundary layer turbulence. Consequently, turbulence parameterizations (TP) are essential components of almost all weather and climate models. To a great extent, the TP determines the quality of the simulation of land surface–atmosphere feedback (e.g., Milovac et al. 2014). A particular weakness of the models is the parameterization of entrainment fluxes, which is required for a high quality of simulations on all time scales. On short time scales, an incorrect simulation of entrainment leads to erroneous evolutions of CBL moisture and temperature as well as the convective available potential energy and convective inhibition, which results in poor skill of predicting convection initiation. On longer time scales, incorrect entrainment fluxes cause errors in the vertical distribution of water vapor with negative consequences for the simulation of climate statistics with respect to radiative transfer and the evolution of clouds and precipitation. This concerns reanalyses, regional dynamical downscaling, and global climate change projections. The high sensitivity of NWP model forecast quality on the CBL TP was demonstrated by, for example, Hong et al. (2006), Hill and Lackmann (2009), and Xie et al. (2012) and with respect to the performance of regional climate models by, for example, Dethloff et al. (2001), Park and Bretherton (2009), and Samuelsson et al. (2011).

Models for entrainment fluxes were derived in various publications (Van Zanten et al. 1999; Fedorovich et al. 2004), and relationships useful for applications in NWP models were proposed (Noh et al. 2003). For instance, in the nonlocal Yonsei University (YSU) TP (Hong et al. 2006), the water vapor entrainment flux is the product of an entrainment velocity and the moisture jump at the CBL top. The entrainment velocity is estimated by assuming a constant ratio between the surface and the entrainment heat fluxes of -0.15 and by diagnosing the temperature jump at the CBL top. However, it is unclear whether this constant ratio holds in a real atmospheric boundary layer where gravity waves and wind shear are expected to have a great influence on entrainment fluxes (Wulfmeyer 1999a; Conzemius and Fedorovich 2006).

Particularly, it is expected that the temperature flux ratio decreases to approximately -0.3 during shear convection and even more during forced convection with dramatic consequences on moistening or drying conditions (Sorbjan 2005, 2006).

Sorbjan (2001, 2005, 2006) developed CBL scaling laws for deriving profiles of fluxes and higher-order moments of atmospheric variables. These scaling approaches relate fluxes and higher-order moments of atmospheric variables to their gradients in the entrainment layer (EL). Furthermore, these relationships include dependencies of fluxes and variances on the gradient Richardson number so that the influence of wind shear can also be included. If these relationships are valid, simple tests of existing TPs will be possible.

Advanced CBL TPs with refined representation of entrainment may be derived and incorporated in mesoscale models. This will be possible for hierarchies of model simulations from relatively coarse grid increments to the gray zone (e.g., Saito et al. 2013) where turbulent fluctuations become resolved. Gray-zone experiments are a very important area of research, as both regional climate models and NWP models will reach the corresponding grid increments on the order of 1 km within the next years. Therefore, the representation of land–atmosphere feedback of this new model generation has to be studied in great detail and to be optimized, including a realistic simulation of clouds and precipitation.

A prerequisite of the application of new scaling relationships is their verification. This can be realized by performing large-eddy simulations (LESs) and the confirmation of their results by dedicated observations. Since the 1970s, LES has been used for studying the CBL under various conditions (Deardorff 1970). Advances in computing power and model developments enable the resolution of turbulence above the surface layer throughout the CBL including the EL. Most of the runs have been performed under strong convective conditions with homogeneous surface heat fluxes (Wyngaard and Brost 1984). The results were used for deriving parameterizations of fluxes and variances (Moeng and Sullivan 1994; Ayotte et al. 1996) and their dependence on varying strengths of the inversion (Sorbjan 1996). Detailed studies of entrainment processes were presented by Sullivan et al. (1998) and Kim et al. (2003). First studies are available considering the heterogeneity of surface fluxes (Maronga and Raasch 2013). The similarity relationships derived in Sorbjan (2005, 2006) were tested by only a few dedicated LESs so that it is still not clear whether these relationships are generally applicable.

However, it must be considered that most of the LES results introduced above were based on periodic

boundary conditions, homogeneous land surface conditions, and specific assumptions of the interaction of the free troposphere (damping layers) with the CBL. Effects of land surface heterogeneity, interaction of gravity waves with CBL turbulence, wind shear in the EL, inversion strengths, and large-scale forcing have often not been considered in detail. Only a few studies considering realistic heterogeneous surface were performed (e.g., Hechtel et al. 1990; Maronga and Raasch 2013) and these were used primarily to study the surface energy balance closure problem (Kanda et al. 2004). Thus, more realistic LES studies are still required, for example, by nesting them in mesoscale environments or by gray-zone experiments of limited area or even with global models.

Further progress has recently been achieved by the direct numerical simulation (DNS) of entrainment processes (e.g., Waggy et al. 2013; Garcia and Mellado 2014). These results have been applied to derive further insight in the dependence of entrainment velocities, variances, and fluxes as well as eddy diffusivity on scaling variables. Similar to LES, additional studies are required to study the validity of DNS results in inhomogeneous terrain and in dependence of the mesoscale environment.

Models are only as good as the data used for their verification. The only way to confirm similarity relationships, LES, and DNS of turbulent transport and exchange processes are observations with sufficient resolution and accuracy. This verification should be performed under a range of different meteorological conditions, both at the surface and throughout the mixed layer (ML) and the EL. The observations should provide not only measurements of profiles and gradients of atmospheric variables but also their turbulent fluctuations. Reaching the CBL top is possible with aircraft in situ or remote sensing instrumentation as well as ground-based, vertically steering, or scanning lidar or clear-air radar systems. Unfortunately, dedicated observations for studying LES and TPs are relatively sparse. Still, to date, most of the studies were performed using aircraft in situ turbulence sensors (e.g., Lenschow et al. 1994). Here, it is very challenging to derive instantaneous profiles of turbulent quantities owing to sampling issues and complex flight patterns with the operations of in situ sensors only. Furthermore, it is difficult to measure the distance between the flight lag and the CBL depth z_i , which is important to parameterize variables as functions of z/z_i (e.g., Turner et al. 2014a). Aircraft equipped with lidar systems flying close to the CBL top can deliver both vertical profiles and measurements of the spatial inhomogeneities (Crum and Stull 1987; Crum et al. 1987; Kiemle et al. 1997; Couvreux et al. 2005). However, aircraft campaigns are

expensive and relatively sparse so that it is difficult to relate the results to a variety of meteorological conditions. Mounting in situ sensors on tethered balloons may be another option but it is challenging to reach the CBL top, which can typically range up to 2000 m or more in some locations.

Therefore, for turbulence studies, it is worthwhile to apply a synergy of in situ measurements with airborne and ground-based remote sensing. Passive remote sensing systems such as Fourier-transform infrared (FTIR) (Turner and Löhnert 2014) spectroscopy and microwave radiometers (MWRs) (Löhnert et al. 2009) demonstrated great potential for ABL profiling. However, the vertical resolution of the retrievals, which are based on the inversion of the radiative transfer equation, is limited by the width of weighting functions to 500 m or more in the EL so that gradients of humidity and temperature are mostly averaged out (Wulfmeyer et al. 2015a). Furthermore, the retrievals are generally too noisy for resolving turbulent fluctuations (Kalthoff et al. 2013).

Clear-air radars observe either the refractive index structure parameter or reflectivity from insects (Emeis 2011). These features can be used to retrieve line-of-sight wind velocities or vertical wind speed. Clear-air radar does not provide direct measurements of wind speed because, in the case of structure parameter measurements, the first moment of the Doppler spectrum is influenced by covariances between reflectivity and radial velocity fluctuations (Muschinski and Sullivan 2013). Nevertheless, volume imaging of wind fields is possible with a resolution of a few seconds (e.g., Mead et al. 1998). In the case of insect backscatter, it is questionable whether these can be considered as tracers for atmospheric motion. Therefore, cloud radar signals are usually not evaluated with respect to wind speed in the clear CBL but in clouds.

The relation between the refractive index structure parameter and temperature and moisture gradients can also be applied for retrieving temperature and moisture profiles (Tsuda et al. 2001). However, this method relies on additional reference measurements of humidity and knowledge of the sign of the refractive index gradient so that its accuracy is limited and routine application is difficult. For temperature profiling, the radar acoustic sounding system (RASS) has been developed (e.g., Matuura et al. 1986). These systems measure the propagation speed of sound so that it is possible to retrieve the virtual temperature profile. This technique is limited by the altitude coverage when high horizontal winds carry the sound waves outside of the radar beam. Nevertheless, in the CBL, measurements of temperature profiles with turbulence resolution have been demonstrated (Angevine et al. 1993; Wulfmeyer 1999a).

Lidar systems measure range-resolved signals, which are directly related to atmospheric dynamics and thermodynamics. Thus, these have a great potential for deriving gradients and turbulent fluctuations of humidity, temperature, and wind, simultaneously. For decades, Doppler lidar (DL) systems, which measure the Doppler shift of aerosol particle backscatter by heterodyne detection, have been used for the profiling of higher-order turbulent moments of vertical wind and turbulent kinetic energy dissipation rate (Frehlich et al. 1998; Lenschow et al. 2000; Frehlich and Cornman 2002; Wulfmeyer and Janjić 2005; Hogan et al. 2009; Lothon et al. 2009; Tucker et al. 2009; Ansmann et al. 2010; Träumner et al. 2011; Lenschow et al. 2012). The routine operation of Doppler lidar systems is now possible, as these systems are commercially available and affordable from various companies.

With respect to water vapor profiling, two different lidar options are available. These are water vapor differential absorption lidar (WVDIAL) or water vapor Raman lidar (WVRL), which both can measure profiles and gradients of absolute humidity or mixing ratio as well as turbulent moments in the CBL (Wulfmeyer 1999b; Wulfmeyer et al. 2010; Turner et al. 2014a,b; Muppa et al. 2015). Combinations of these systems have been applied for ground-based profiling of the latent heat flux (Senff et al. 1994; Wulfmeyer 1999a; Giez et al. 1999; Linné et al. 2007; Behrendt et al. 2011) and higher-order moments (Wulfmeyer 1999b; Lenschow et al. 2000). The high accuracies and turbulence resolutions of WVDIAL and Doppler lidar from aircraft have also been used for latent heat flux profiling (Kiemle et al. 2007, 2011) and for detailed comparisons with LES (Couvreur et al. 2005, 2007). Particularly exciting is the fact that recently temperature rotational Raman lidar (TRRL) reached the resolution needed for temperature turbulence profiling as well (Hammann et al. 2015; Behrendt et al. 2015).

In this work, we are focusing on the capabilities and performances of ground-based lidar systems of this kind because these have the advantage that they can provide continuous profiling of mean profiles, gradients, and turbulence profiles improving sampling statistics during similar meteorological conditions. These systems are becoming available in different climate regimes: at the Atmospheric Radiation Measurement (ARM) Program Southern Great Plains site in Oklahoma, United States; in tropical regions such as the ARM site in Darwin, Australia (www.arm.gov/sites); operated from December 2010 until December 2014; Ackerman and Stokes 2003; Mather and Voyles 2013); and in the midlatitudes at various observatories such as Lindenberg, Germany, and Cabauw, the Netherlands; as well as during field campaigns such as the

Convective and Orographically-induced Precipitation Study (COPS) (Wulfmeyer et al. 2008, 2011) (www.uni-hohenheim.de/cops), the High Definition Clouds and Precipitation [HD(CP)²] Observational Prototype Experiment (HOPE) (<https://hdcp2.zmaw.de>), and the recent Surface Atmospheric Boundary Layer Exchange (SABLE) campaign (Wulfmeyer et al. 2015b).

We demonstrate that this novel synergy of lidar systems consisting of DL, WVDIAL/WVRL, and TRRL provides a complete dataset of gradients and turbulent moments for the verification of LES and similarity relationships. We focus on ground-based observations, as it is possible to deploy these lidar systems very close to each other for simultaneous measurements of covariances between different atmospheric variables. Furthermore, measurements can be collected under a variety of different conditions producing robust statistics of turbulent quantities in an affordable manner.

This study is organized as follows: In section 2, we derive an advanced set of scaling relationships in the CBL. Particularly, we derive relationships of momentum, latent heat, and sensible heat fluxes as well as higher-order moments to mean wind, temperature, and moisture gradients with particular emphasis on the EL. Furthermore, new equations for relating integral scales to turbulent quantities are derived. Particularly, what is to our knowledge for the first time, a novel technique for measuring the molecular destruction rates of water vapor and temperature variances is developed that are important components of the variance budget equations.

In section 3, we analyze the capabilities of DL, WVDIAL, WVRL, and TRRL for profiling vertical wind, water vapor, and temperature as well as their higher-order moments. We show how the lidar measurements can be combined for deriving fluxes and higher-order moments using measurements of vertical gradients of mean profiles. The results demonstrate that the proposed lidar synergy is necessary but also sufficient for providing a complete set of measurements for studying and verifying the proposed similarity relationships. It is also shown that these synergetic lidar measurements open up new possibilities for thorough comparisons with LES and detailed studies of TPs.

In section 4, we present first results using WVDIAL and TRRL for studying turbulence profiles up to the third order and their relationship to water vapor and temperature gradients as well as entrainment fluxes. We also get first insight into molecular destruction rates.

In section 5, the results are summarized. A series of new field campaigns in different climate regions is proposed as contributions to studies of land-atmosphere

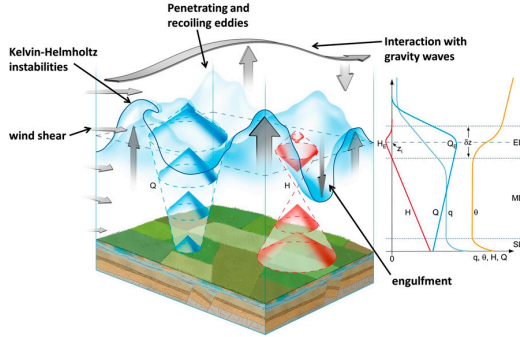


FIG. 1. The convective boundary layer: vertical structure and key processes. The cones on the left side of the figure indicate the mean direction (arrows) and the mean strength (diameters) of either the sensible heat (red) or the latent heat (blue) fluxes.

interaction as well as theories and parameterizations of turbulence in the CBL. In the appendix, the sensitivity of the results on systematic and noise errors is investigated and it is confirmed that the current state-of-the-art lidar systems are able to measure profiles and moments with high accuracy and resolution.

2. Convective boundary layer structure and entrainment

a. Vertical structure

The vertical structure and the turbulent activity of the CBL is depicted in Fig. 1. In a horizontally homogeneous, quasi-stationary, and well-mixed CBL it is expected that the mean potential temperature θ profile can be characterized by a negative gradient in the surface layer (SL), a constant in the ML, and an increase in the EL due to the temperature inversion.

Here, we define the entrainment zone as the region, in which a nonturbulent fluid from the free troposphere is mixed into the CBL and remains part of the CBL afterward. This can occur far downward in the CBL by engulfment, as often observed by remote sensing systems. In contrast, the EL or the interfacial layer is the region around the inversion at the CBL top, which can be used to locate the instantaneous and mean gradients as well as the mean entrainment flux (LeMone 2002).

In the SL, the mean specific humidity q profile should have a negative gradient as well, as long as significant

evapotranspiration is present, a slight negative gradient in the ML, and a stronger negative gradient in the EL. Well-mixed conditions are usually achieved after threefold to fourfold eddy turnover time or the CBL time scale $t^* \approx z_i/w_*$, where z_i is the mean CBL depth and w_* the convective velocity scale:

$$w_* = \left(\frac{G}{\bar{\theta}_v} z_i H_{v,0} \right)^{1/3}. \tag{1}$$

Here, G is the acceleration due to gravity, $\bar{\theta}_v$ is the mean virtual potential temperature in the CBL, and $H_{v,0}$ is surface buoyancy flux. Typical values of w_* in a well-developed CBL range between approximately 1 and 2 m s⁻¹.

In the absence of significant horizontal advection, the evolutions of θ and q are driven by the vertical divergences of the sensible and latent heat flux profiles (H and Q), respectively. Their absolute mean values and directions (the spectra and sizes are not shown) are indicated in Fig. 1 by the diameters and the directions of the cones, respectively. Whereas $H(z)$ must have a negative slope reaching a negative value in the EL, $Q(z)$ can have a negative or positive slope depending on whether the difference between the entrainment flux Q_E and the surface flux Q_0 is negative or positive. In any case, as long as there is a negative slope of q in the EL, then $Q_E > 0$. The understanding and the parameterization of these flux divergences—also for momentum—is the essence of TPs, which are fundamental for weather and climate modeling.

In the SL, the vertical stability can be characterized by the bulk Richardson number,

$$Ri_b = \frac{G}{\theta_a} z \frac{\theta_{vw} - \theta_{vg}}{U_{SL}^2}, \quad (2)$$

where θ_a is the potential temperature in the surface layer; z is height above the displacement height in the canopy or in other land cover; θ_{vw} and θ_{vg} are the virtual potential temperatures of the air and the land surface, respectively; and U_{SL} is the horizontal wind speed in the SL at height z . The depth of the SL can be defined by the extent to which the vertical change of fluxes is less than 10%. Over a homogeneous surface, the resulting vertical profiles of wind, temperature, and humidity can be described by the Monin–Obukhov similarity theory (MOST), which relates their gradients to surface fluxes and stability functions given for different ranges of Ri_b (Grachev et al. 2000; Poulos et al. 2002; Jiménez et al. 2012). The study and measurements of these relationships in the surface layer is possible by using scanning lidar systems and eddy covariance instrumentation and is subject of future publications.

In the ML, θ is nearly constant with height, indicating a well-mixed boundary layer. Vertical flux profiles are evolving in time and are well defined for a specific domain and time average. This can be studied by deriving integral length and temporal scales for the higher moments of the atmospheric variables and their covariances, which can be related to their sampling errors (Lenschow et al. 1994). Typically, 30–60-min averaging time is needed for deriving profiles of turbulent quantities with low noise and acceptable sampling errors on the order of 10%–20%. However, this averaging time may increase further at lower horizontal wind speed U . The amount and the gradient of q are strongly dependent on the ratio between the fluxes in the SL and the EL. As it is particularly challenging and crucial to derive entrainment fluxes, we will focus on vertical exchange processes in the EL.

b. The entrainment layer

The EL separates the ML from the free troposphere by a temperature inversion. The strength of this inversion and the entrainment flux are the result of a variety of interacting processes. These are indicated in Fig. 1 and are mainly due to four effects: 1) the engulfment of air from the free troposphere mixed downward in the turbulent CBL, 2) instabilities induced by wind shear at the EL interface such as Kelvin–Helmholtz and Holmboe waves, 3) penetrating and recoiling convective eddies, and 4) the propagation and excitation of wave modes such as gravity waves and their interaction with the turbulent eddies.

Consequently, various local and nonlocal processes are contributing to the fluxes, which are neither well understood nor accurately parameterized in state-of-the-art mesoscale models. Therefore, sophisticated theoretical concepts are necessary to understand the turbulent variables in the EL. These concepts have to be verified by new combinations of measurements.

1) HIGHER-ORDER MOMENTS AND ENTRAINMENT FLUXES

It can be expected that the flux Q through an interface such as the EL is related to the mean gradient of the variable of interest q so that

$$Q = -\frac{1}{R} \nabla q, \quad (3)$$

where R is the resistance of the interface. This relationship from stochastic physics is not only used for studying turbulent transport in the atmosphere but also water transport in the soil or fluxes at the land surface (Zehe et al. 2014). The challenge is to relate in a comprehensive and physical way the resistance R to parameters that are expected to influence the entrainment fluxes. Thus, it is desirable to derive a closed set of scaling variables in the EL so that their gradients can be related to fluxes and higher-order turbulent moments. A corresponding set of equations was proposed by Sorbjan (1996, 2001, 2005, 2006) and reads

$$S_w = w_*, \quad (4)$$

$$S_L = \frac{w_*}{N_E}, \quad (5)$$

$$S_\theta = S_L \gamma_E = w_* \frac{\gamma_E}{N_E}, \quad \text{and} \quad (6)$$

$$S_q = S_L g_E = w_* \frac{g_E}{N_E}, \quad (7)$$

where S_w , S_L , S_θ , and S_q are the scaling variables for vertical velocity w statistics, the EL length scale L , the potential temperature θ , and the specific humidity q . The index E denotes that all variables and gradients are taken in the EL. The gradients of θ and q in the EL are γ_E and g_E , respectively. Alternatively, it may be reasonable to replace w_* by the standard deviation of the vertical velocity fluctuations $\sqrt{w'^2_E}$, which is easy to do in all following scaling relationships. For now, we stick with the hypothesis that w_* is the appropriate EL scaling variable.

The Brunt–Väisälä frequency N_E depends on the inversion strength in the EL according to

$$N_E = \sqrt{\beta_E \gamma_E}, \quad (8)$$

with the buoyancy parameter $\beta := G/\theta$.

This scaling [Eqs. (4)–(7)] is based on the following assumptions: 1) the turbulent fluctuations of the vertical wind in the EL scale with the buoyant forcing from the land surface and the CBL depth but not with the wind shear, 2) the time scale of fluctuations of atmospheric variables is the inverse of the Brunt–Väisälä frequency, 3) the most important scaling variable for temperature fluctuations is the mean potential temperature gradient at z_i , 4) the most important scaling variable for moisture fluctuations is its mean moisture gradient at z_i , and 5) despite the complex and different physical processes leading to local transport as depicted in Fig. 1, mean but not local gradients remain the most important scaling variables determining the entrainment flux averaged in time or in space over a homogeneous region.

Based on Eqs. (4)–(7), relationships for entrainment fluxes and higher-order moments can be derived. Entrainment fluxes for momentum $M_{u,v,E}$, temperature H_E , and moisture Q_E can be written by the combination of the scaling variables as

$$\begin{aligned} M_{u,v,E} &= -C_M S_E^2 s_{u,v,E}^2 f_M(\text{Ri}_E) \\ &= -C_M \left(\frac{w_{\oplus}}{N_E}\right)^2 s_{u,v,E}^2 f_M(\text{Ri}_E) \equiv -\frac{1}{R_{M,E}} s_{u,v,E}, \quad (9) \end{aligned}$$

$$\begin{aligned} H_E &= -C_H S_w S_{\theta H} f_H(\text{Ri}_E) \\ &= -C_H w_{\oplus}^2 \frac{\gamma_E}{N_E} f_H(\text{Ri}_E) \equiv -\frac{1}{R_{H,E}} \gamma_E, \quad \text{and} \quad (10) \end{aligned}$$

$$\begin{aligned} Q_E &= -C_Q S_w S_{qQ} f_Q(\text{Ri}_E) \\ &= -C_Q w_{\oplus}^2 \frac{g_E}{N_E} f_Q(\text{Ri}_E) \equiv -\frac{1}{R_{Q,E}} g_E, \quad (11) \end{aligned}$$

where $M_{u,v,E}$ denotes the momentum fluxes in two horizontal wind directions described by the indices u and v . The constants C_M , C_H , and C_Q are positive and s_E is the wind shear in the EL such that

$$s_E^2 = \left(\frac{du}{dz}\right)^2 + \left(\frac{dv}{dz}\right)^2 =: (s_{u,E})^2 + (s_{v,E})^2. \quad (12)$$

By comparing Eqs. (9)–(11) with Eq. (3), indeed resistances with respect to each turbulent flux can be defined. Particularly, we expect that the resistances are functions of the gradient Richardson number

$$\text{Ri}_E = \frac{N_E^2}{s_E^2}, \quad (13)$$

which is conceptually similar to Eq. (2). In shearless conditions (free-convection limit) $s_E \rightarrow 0$; thus, $\text{Ri}_E \rightarrow \infty$. In this case, the functions $f_{M,H,Q}$ should reach the constant

value $\lim_{\text{Ri}_E \rightarrow \infty} f_{M,H,Q} = 1$. It may be worthwhile to absorb the constants C_M , C_H , and C_Q in these functions.

For the momentum flux M_E , Sorbjan (2009) analyzed LES datasets and found $C_M \cong 0.2$ and

$$f_M(\text{Ri}_E) = 1 - \frac{1}{\text{Ri}_E}, \quad (14)$$

which is proposed for $\text{Ri}_E > 1$.

For the interfacial heat and humidity fluxes, Sorbjan (2005, 2006) estimated $C_H \cong 0.012$ and $C_Q \cong 0.025$ as well as the dependence of the fluxes on Ri_E by LES and achieved

$$f_{H,Q}(\text{Ri}_E) = \frac{1 + c_{H,Q}/\text{Ri}_E}{\sqrt{1 + 1/\text{Ri}_E}}, \quad (15)$$

where the coefficients $c_{H,Q}$ were assessed to be $c_H \cong c_Q \cong 8$.

In an analogous way, second-order moments of the vertical wind, temperature, and humidity fluctuations can be arranged as follows:

$$\overline{w^2}_E = C_w s_w^2 f_w^2(\text{Ri}_E) = C_w s_w^2 f_w^2(\text{Ri}_E), \quad (16)$$

$$\overline{\theta^2}_E = C_{\theta^2} S_{\theta^2}^2 f_{\theta^2}(\text{Ri}_E) = C_{\theta^2} w_{\oplus}^2 \left(\frac{\gamma_E}{N_E}\right)^2 f_{\theta^2}(\text{Ri}_E), \quad \text{and} \quad (17)$$

$$\overline{q^2}_E = C_{q^2} S_{q^2}^2 f_{q^2}(\text{Ri}_E) = C_{q^2} w_{\oplus}^2 \left(\frac{g_E}{N_E}\right)^2 f_{q^2}(\text{Ri}_E). \quad (18)$$

In the case of EL temperature and humidity variances, Sorbjan (2006) suggested $C_{\theta^2} \cong 0.04$ and $C_{q^2} \cong 0.175$ as well as a functional dependence on Ri_E of the form

$$f_{\theta^2,q^2}(\text{Ri}_E) = \frac{1 + c_{\theta^2,q^2}/\text{Ri}_E}{1 + 1/\text{Ri}_E}. \quad (19)$$

The coefficients c_{θ^2} and c_{q^2} have still to be estimated. For vertical wind, both the function $f_w(\text{Ri}_E)$ and the coefficient C_w need to be determined as well.

Figure 2 presents the dependence of the functions f_M , $f_{H,Q}$, and f_{θ^2,q^2} on Ri_E for typical ranges of the proposed constants. The function f_M shows a strong nonlinear behavior for $\text{Ri}_E < 10$ and the momentum flux decreases between $1 < \text{Ri}_E < 10$ by more than an order of magnitude. The other functions show basically three regimes, which may be related to different entrainment processes. In the first regime for $\text{Ri}_E \leq 0.1$, the function f_{θ^2,q^2} is leveling off and approaches the constant value c_{θ^2,q^2} . This may be the range where entrainment is mainly determined by the engulfment of overturning eddies. In contrast, $f_{H,Q}$ is not converging to a limited value but to ∞ for $\text{Ri}_E \rightarrow 0$. It is very important to test this different

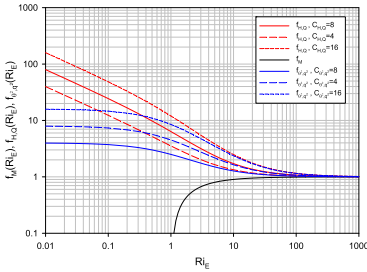


FIG. 2. The functions f_M , $f_{H,Q}$, and f_{θ^2,q^2} for scaling fluxes and variance in dependence of Ri_E . The functions $f_{H,Q}$ and f_{θ^2,q^2} are presented around constants derived by LES.

behavior of the flux and variance scaling functions by additional LES and observations. In the transition regime from $0.1 < Ri_E < 10$, different processes may be responsible for the strength of entrainment simultaneously. Finally, for $Ri_E > 10$, both functions $f_{H,Q}$ and f_{θ^2,q^2} are converging to unity and entrainment may mainly be determined by Kelvin–Helmholtz instabilities and interaction with gravity waves. Please note that these results depend on the grid resolution of the corresponding LES. Further refinements are required by LES with increased grid resolution or DNS. It is also important to explore the difference in scaling using Ri_E , which is proposed here and the bulk Richardson number, which was used, for example, in Sullivan et al. (1998) and Trümmer et al. (2011).

A similar approach as for the variances may be used to describe the third moments of w , θ' , and q' in the EL:

$$\overline{w^3}_E = C_w S_w^3 f_w(Ri_E) = C_w S_w^3 f_w(Ri_E), \tag{20}$$

$$\overline{\theta'^3}_E = C_\theta S_\theta^3 f_\theta(Ri_E) = C_\theta W_\theta^3 \left(\frac{2E}{N_E}\right)^3 f_\theta(Ri_E), \text{ and } \tag{21}$$

$$\overline{q'^3}_E = C_q S_q^3 f_q(Ri_E) = C_q W_q^3 \left(\frac{gE}{N_E}\right)^3 f_q(Ri_E). \tag{22}$$

However, this hypothesis would need to be tested extensively to ensure that the magnitude of the third moments is indeed proportional to the cubes of the gradients for θ and q at z , as well as to determine the dependence on Ri_E and the coefficients C_w , C_θ , and C_q .

2) DETERMINATION OF INTEGRAL SCALES AS WELL AS DISSIPATION AND DESTRUCTION RATES

We start with the evaluation of stationary turbulence. This is the case if the time series of the fluctuating variable $q(t)$ can be separated into

$$q(t) = q'(t) + \overline{q(t)}, \tag{23}$$

where $\overline{q(t)}$ is a slowly varying component, which can be derived by low-pass filtering or subtracting a linear trend, and $q'(t) = 0$. Of course, this analysis can be performed at each height level in the CBL including the EL; however, for the sake of simplicity we omit an index for the height level in the following. The autocovariance function A of this time series is defined as

$$A_q(t_1, t_2) = \overline{[q(t_1) - \overline{q(t_1)}][q(t_2) - \overline{q(t_2)}]}. \tag{24}$$

If the time series $q(t)$ is stationary then

$$A_q(t_1, t_2) = A_q(t_1 - t_2) = A_q(t_2 - t_1) = A_q(\tau) \tag{25}$$

with $|A_q(\tau)| \leq A_q(0)$.

The structure function D of a variable q is defined according to

$$D_q(t_1, t_2) = \overline{[q(t_1) - q(t_2)]^2} \text{ or } D_q(\tau) = \overline{[q(t + \tau) - q(t)]^2}. \tag{26}$$

If the time series is stationary, it is easy to show

$$D_q(\tau) = 2[A_q(0) - A_q(\tau)] \text{ and } A_q(\tau) = A_q(0) - 0.5D_q(\tau). \tag{27}$$

In the spatial domain, the structure function reads

$$D_q(\mathbf{r}_1, \mathbf{r}_2) = \overline{[q(\mathbf{r}_1) - q(\mathbf{r}_2)]^2} \tag{28}$$

and if the field is locally homogeneous and isotropic then

$$D_q(\mathbf{r}_1, \mathbf{r}) = \overline{[q(\mathbf{r}_1 + \mathbf{r}) - q(\mathbf{r}_1)]^2} \equiv D_q(r) \tag{29}$$

and the relations

$$D_q(r) = 2A(0) - 2A_q(r) \text{ and } A_q(r) = A_q(0) - 0.5D_q(r) \tag{30}$$

hold.

In the following, we assume that either by high-resolution modeling or measurements, the inertial subrange is resolved for a sufficient short lag of the time series. The inertial subrange lies in between the inner and outer scales of turbulence where it is assumed locally homogeneous and isotropic. Now, we can analyze these equations with respect to the time series of vertical wind, humidity, and temperature at different heights. It was shown in Tatarski (1961) and Monin and Yaglom (1975) that

$$D(\tau) = C^2 \tau^{2/3} \quad (31)$$

The autocorrelation function AC is defined as

with the structure parameters C^2 for vertical wind velocity

$$AC(\tau) = 1 - \frac{k}{\nu_a} \tau^{2/3}. \quad (39)$$

$$C_w^2 \cong C_K \varepsilon^{2/3}, \quad (32)$$

The root of this equation is

humidity

$$\tau_0 = \left(\frac{\nu_a}{k} \right)^{3/2} \quad (40)$$

$$C_q^2 \cong a_q^2 \frac{\overline{N}_q}{\varepsilon^{1/3}}, \quad (33)$$

so that the respective integral time scale can be estimated according to

and potential temperature

$$C_\theta^2 \cong a_\theta^2 \frac{\overline{N}_\theta}{\varepsilon^{1/3}}, \quad (34)$$

$$\mathcal{T} = \int_0^{\tau_0} AC(\tau) d\tau = \int_0^{\tau_0} \left(1 - \frac{k}{\nu_a} \tau^{2/3} \right) d\tau, \quad (41)$$

which yields

$$\mathcal{T} = \frac{2}{5} \left(\frac{\nu_a}{k} \right)^{3/2}. \quad (42)$$

where ε is the turbulent kinetic energy (TKE) dissipation rate, and \overline{N}_q and \overline{N}_θ are the destruction rates of humidity and potential temperature variances due to molecular processes, respectively. The constants in Eqs. (32)–(34) are considered universal in the inertial subrange. The Kolmogorov constant $C_K \cong 2$ and the constants a_q^2 and a_θ^2 are expected to be in the range 2.8–3.2 (Stull 1988).

Please note that this integration is an approximation of the integral scale of the turbulence fluctuations because we do not integrate to infinity but to the first zero crossing of $AC(\tau)$. However, this turned out as a good compromise for separating turbulent fluctuations from mesoscale variability and for getting robust results under the presence of significant system noise (Lenschow et al. 2000; Wulfmeyer et al. 2010; Behrendt et al. 2015).

Consequently, one way of determining dissipation and destruction rates is to start with the autocovariance function A in the time domain and to assume Taylor's hypothesis of frozen turbulence in the inertial subrange. Then,

$$A_w(\tau) = \overline{w^2} - \varepsilon^{2/3} U^{2/3} \tau^{2/3}, \quad (35)$$

If the shape of AC is mainly controlled by homogeneous and isotropic turbulence, the ratio between the root and the integral scale gives an estimate of how many lags should be used for the interpolation of the structure function. One natural choice is to take approximately $2\mathcal{T}/\Delta t$ lags, where Δt is the resolution of the time series. If the shape of AC is contaminated by mesoscale variability, then an iteration between the fit of the structure function and the determination of the integral scale may be necessary, resulting in a reduction of the number of lags.

$$A_q(\tau) = \overline{q^2} - 0.5 a_q^2 \frac{\overline{N}_q}{\varepsilon^{1/3}} U^{2/3} \tau^{2/3}, \quad \text{and} \quad (36)$$

$$A_\theta(\tau) = \overline{\theta^2} - 0.5 a_\theta^2 \frac{\overline{N}_\theta}{\varepsilon^{1/3}} U^{2/3} \tau^{2/3}. \quad (37)$$

Using these equations, the atmospheric variance, the dissipation and destruction rates, and the integral scales can be determined, respectively, if the autocorrelation functions and the horizontal wind profile $U(z)$ are known.

The integration of AC yields the dependence of \mathcal{T} or the integral length scales $\mathcal{R} \cong U\mathcal{T}$ on atmospheric variables:

This can be shown as follows: all autocovariance functions have the form

$$A(\tau) = \nu_a - k\tau^{2/3}, \quad (38)$$

insofar that distortions by mesoscale variability in the inertial subrange can be neglected. In the following, we assume that this is the case, which can be tested by studying the shape of A for $\tau < \mathcal{T}$, where \mathcal{T} is the integral time scale. If the shapes of the data and the fit agree well, the extrapolation of the structure function fit to the autocovariance data to lag zero yields the atmospheric variance ν_a and the coefficient of the structure function k . This technique separates the atmospheric and the noise variance at lag 0, which is necessary as the latter can often not be neglected [see also the appendix and Eq. (A9)].

$$\mathcal{T}_w = \frac{2}{5} \left(\frac{\nu_a}{\varepsilon U} \right)^{3/2}, \quad \mathcal{R}_w = \frac{2}{5} \left(\frac{\nu_a}{\varepsilon} \right)^{3/2} \frac{1}{U}, \quad (43)$$

$$\mathcal{T}_q = \frac{2\sqrt{8}}{5a_q^2} \left(\frac{\nu_a}{\varepsilon} \right)^{3/2} \sqrt{\frac{\varepsilon}{\overline{N}_q^3}} \frac{1}{U},$$

$$\mathcal{R}_q = \frac{2\sqrt{8}}{5a_q^2} \left(\frac{\nu_a}{\varepsilon} \right)^{3/2} \sqrt{\frac{\varepsilon}{\overline{N}_q^3}}, \quad \text{and} \quad (44)$$

$$\mathcal{T}_\theta = \frac{2\sqrt{8}}{5a_\theta^2} \left(\frac{\nu_a}{\varepsilon} \right)^{3/2} \sqrt{\frac{\varepsilon}{\overline{N}_\theta^3}} \frac{1}{U}, \quad \mathcal{R}_\theta = \frac{2\sqrt{8}}{5a_\theta^2} \left(\frac{\nu_a}{\varepsilon} \right)^{3/2} \sqrt{\frac{\varepsilon}{\overline{N}_\theta^3}}, \quad (45)$$

For the vertical wind, its integral time scale is inversely proportional to the dissipation rate and proportional to the 3/2 power of the variance. It can be expected that variance and dissipation are related variables (larger variance leading to larger dissipation), which can be investigated now with our methodology.

In contrast, the integral scales for humidity and potential temperature are proportional to the square root of the TKE dissipation rate and inversely proportional to the 3/2 power of their destruction rates, respectively. The dependence on the variance profiles is the same as for vertical wind. In the future, it will be very interesting to compare the behavior of molecular destruction and TKE dissipation rates and their dependence on various atmospheric conditions. The results can be used for studying the processes controlling their height dependence.

This can be realized in the following way. Combining the fit of the AC functions or the resulting integral scales with the coefficients of the structure functions permits the direct estimation of dissipation rates. For example, for vertical velocity

$$k_w = \varepsilon^{2/3} U^{2/3} \quad \text{and} \quad (46)$$

$$\varepsilon = \frac{k_w^{3/2}}{U} \quad (47)$$

$$= \frac{2}{5} \frac{(\sqrt{w^2})^3}{U \mathcal{F}_w} = \frac{2}{5} \frac{(\sqrt{w^2})^3}{\mathcal{H}_w}. \quad (48)$$

As the integral scale for vertical wind generally varies less than a factor of 2 with height in the mixed layer and the EL (Lenschow et al. 2000; Lothon et al. 2006), the shape of the ε profile is mainly determined by the profile of the vertical velocity variance.

Correspondingly, for humidity

$$k_q = \frac{1}{2} a_q^2 \frac{\overline{N}_q}{\varepsilon^{1/3}} U^{2/3}, \quad (49)$$

elimination of U with Eq. (47)

$$\frac{k_q}{k_w} = \frac{1}{2} a_q^2 \frac{\overline{N}_q}{\varepsilon}, \quad (50)$$

or elimination of ε with Eq. (47)

$$k_q = \frac{1}{2} a_q^2 \frac{\overline{N}_q}{\sqrt{k_w}} U, \quad (51)$$

thus

$$\overline{N}_q = \frac{2k_q \sqrt{k_w}}{a_q^2} \frac{1}{U}, \quad (52)$$

or using Eqs. (43) and (44)

$$\overline{N}_q = \frac{4}{5} \frac{\theta^2 \sqrt{w^2}}{a_q^2 \mathcal{F}_q^{2/3} \mathcal{F}_w^{1/3} U} = \frac{4}{5} \frac{\theta^2 \sqrt{w^2}}{a_q^2 \mathcal{H}_q^{2/3} \mathcal{H}_w^{1/3}}. \quad (53)$$

In an analogous way for potential temperature

$$k_\theta = \frac{1}{2} a_\theta^2 \frac{\overline{N}_\theta}{\varepsilon^{1/3}} U^{2/3}, \quad (54)$$

$$\frac{k_\theta}{k_w} = \frac{1}{2} a_\theta^2 \frac{\overline{N}_\theta}{\varepsilon}, \quad (55)$$

$$\overline{N}_\theta = \frac{2k_\theta \sqrt{k_w}}{a_\theta^2} \frac{1}{U}, \quad (56)$$

or using Eqs. (43) and (45)

$$\overline{N}_\theta = \frac{4}{5} \frac{\theta^2 \sqrt{w^2}}{a_\theta^2 \mathcal{F}_\theta^{2/3} \mathcal{F}_w^{1/3} U} = \frac{4}{5} \frac{\theta^2 \sqrt{w^2}}{a_\theta^2 \mathcal{H}_\theta^{2/3} \mathcal{H}_w^{1/3}}. \quad (57)$$

Using Eqs. (49) and (54) we achieve

$$\frac{k_q}{k_\theta} \approx \frac{\overline{N}_q}{\overline{N}_\theta}. \quad (58)$$

Obviously, LES and DNS output or simultaneous measurements of wind, humidity, and potential temperature profiles at high temporal and spatial resolution permit the estimation of the ratio of dissipation rates [Eqs. (50) and (55)] as well as their absolute values [Eqs. (47) and (48), Eqs. (52) and (53), and Eqs. (56) and (57)] provided that accurate measurements of horizontal wind are available. Of course, these equations are only applicable if the conditions of locally homogeneous and isotropic turbulence as well as Taylor's hypothesis are valid.

3) DISCUSSION

For deriving quantitative results, it is essential that all the turbulent quantities introduced above are estimated as accurate and as general as possible. This may be accomplished with turbulence theory, by dedicated LES and DNS studies, and by measurements. As we are not aware of a turbulence theory that permits the derivation of the unknown resistances and dissipation/destruction rates, these relationships need to be tested considering different heterogeneous land surface forcings, stabilities in EL, wind shear, and gravity wave conditions. Furthermore, it is necessary to explore dependencies of fluxes and higher-order moments on different definitions of the Richardson number in the EL and to refine the functional dependence of fluxes and variances on the Richardson number. From the modeling perspective, this requires a chain of mesoscale model simulations

down to the gray zone or the LES scale in order to imbed the model domain with turbulence resolution in a realistic synoptic and mesoscale environment. It is worthwhile to note that the relationships introduced in sections 2b(1) and 2b(2) also provide essential components of CBL energy and water budgets. For instance, dissipation and molecular destruction rates as well as flux divergences are part of these budgets.

Either using idealistic LES and DNS or gray-zone simulations, the results have to be verified by observations. Gradients play an important role in the magnitude of the variances and fluxes, so accurate profiles of horizontal wind, humidity, and potential temperature in the ML, the EL, and the lower free troposphere are critical (Sorbján 2009). Here, we are focusing on turbulent processes around the EL. So far, particularly in this region, field experiments have not provided suitable datasets that are capable to confirm the complete set of relationships between gradients, variances, fluxes, and dissipation/destruction rates. In the following, we demonstrate that this can be accomplished with a new synergy of lidar systems.

3. Lidar synergy for studying entrainment fluxes as well as dissipation and variance destruction rates

a. Basic observational requirements

To study the relationships between fluxes and gradients [Eqs. (9)–(11)], variances and gradients [Eqs. (16)–(18)], and even higher-order moments [Eqs. (20)–(22)], it is necessary that four conditions are fulfilled: 1) wind, temperature, and humidity profiles must be measured simultaneously with small and height-independent bias in the ML, the EL, and the lower free troposphere; 2) the vertical resolution of the measurements must be high enough to resolve the gradients in the profiles, particularly in the EL; 3) the temporal resolutions of the measurements must be high enough to resolve turbulent fluctuations; and 4) the precision of the measurements must be high enough so that vertical structures in the turbulence profiles can be resolved.

Currently, it is hardly possible to realize this with airborne in situ or remote sensing measurements. Research aircraft with in situ sensors provide measurements of the required variables but only at a specific height level. Therefore, it is difficult to derive a comprehensive dataset of gradient, variance, and flux profiles under different meteorological conditions especially at a range of heights in the ML and the EL. The horizontal and vertical structure of the CBL can be studied by lidar systems deployed on aircraft but these campaigns are sparse and expensive. Another option is a combination of ground-based scanning lidar systems but their development and

application is still at its infancy. The height of meteorological towers is generally too low to reach the daytime EL, except special meteorological conditions over land (Zhou et al. 1985), so that these structures also do not come into consideration for deriving comprehensive statistics. Tethered balloons with a combination of in situ sensors may be an option but it will be difficult to get vertical profiles and to reach the CBL top, especially in continental CBLs that can be 2 km deep or more.

Passive infrared and microwave spectrometers may be an approach for retrieving temperature and humidity profiles; however, it has been shown that their temporal and vertical resolution is neither capable of resolving gradients nor turbulent fluctuations in the EL (Wulfmeyer et al. 2015a). In the following, we demonstrate that a synergy of active lidar remote sensing systems with the required vertical and temporal resolutions should be able to provide the desired data.

b. Properties and performance of lidar systems

Recent advances in lidar technology permitted the development of three types of lidar systems, which can measure wind, humidity, and temperature profiles with high resolution and accuracy. The DL can measure either vertical wind profiles in the vertical steering mode or horizontal wind profiles in the velocity azimuth display (VAD or scanning in azimuth at a fixed off-zenith elevation) mode. The signal-to-noise ratio (SNR) of the line-of-sight wind measurements is high enough to reach resolutions of 1 s and 30 m with noise errors on the order of 0.1 m s^{-1} . Systematic errors in line-of-sight (LOS) wind measurements are typically on the order of a few centimeters per second. This performance has been demonstrated for decades using research systems like the high-spectral-resolution Doppler lidar (HRDL) of the National Oceanic and Atmospheric Administration (NOAA) (Lenschow et al. 2000; Wulfmeyer and Janjić 2005; Lothon et al. 2009; Lenschow et al. 2012). Furthermore, horizontal wind profiles can be measured by VAD scans. A recent breakthrough in the development of compact, efficient, and eye-safe laser transmitters such as Er-doped fiber lasers permitted the development of very compact, all-solid-state systems, which are now commercially available from different companies (e.g., Philippov et al. 2004; Kameyama et al. 2007).

With respect to water vapor profiling, two methods are available: WVDIAL and WVRL. WVRLs measure profiles of water vapor mixing ratio m . As mixing ratio m can be readily converted to specific humidity q in the CBL by standard pressure and temperature profiles, in the following, we consider only q as the measured variable.

Operational WVRLs have been installed at only a few sites such as the ARM Program Southern Great Plains (SGP) WVRL (Turner et al. 2002). The design and installation of WVRL systems is usually the result of a special project. Extensive research led to a routine technique for the calibration of mixing ratio measurements, which is necessary for WVRL, with an accuracy of approximately 5% (Turner and Goldsmith 1999; Ferrare et al. 2006). Optimization of daytime performance, which is particularly critical for Raman lidar, was mainly achieved with the SGP Raman lidar and has not been accomplished at all sites. Typically, in the daytime, the noise error is less than 1 g kg^{-1} up to the CBL top using a combination of temporal and vertical resolutions of 10 s and 75 m, respectively. For the SGP WVRL, Wulfmeyer et al. (2010) and Turner et al. (2014a,b) demonstrated that this performance is sufficient for measuring profiles of higher-order moments of mixing ratio in the CBL. These higher-order moments derived from noisy lidar observations have also been validated with in situ measurements (Turner et al. 2014a). Furthermore, ARM has operated a nearly identical Raman lidar at Darwin, Australia, which provides a tropical dataset to complement the SGP midlatitude one.

The WVDIAL technique measures the absolute humidity ρ as a function of range. Similar to WVRL, it is straightforward to convert ρ in q with high accuracy by standard pressure and temperature profiles so that we continue to consider q as the measured variable. The technologically more demanding WVDIAL technique is less mature. To the best of our knowledge, just one ground-based system exists worldwide at the Institute of Physics and Meteorology (IPM) of the University of Hohenheim (UHOH) that has daytime turbulence resolution. Currently, this system has the highest temporal and spatial resolution of ground-based water vapor remote sensing systems (Behrendt et al. 2009; Wulfmeyer et al. 2015a). As DIAL does not need a calibration with respect to system constants, a very high accuracy of absolute humidity measurements is achieved. Recently, Späth et al. (2014) demonstrated by theoretical considerations and comparisons with soundings a systematic error of 2%. Because of the high signal-to-noise-ratio of the backscatter signals during daytime, the noise error is about an order of magnitude lower than WVRL using the same combination of vertical and temporal resolutions (Wulfmeyer et al. 2015a). Therefore, WVDIAL is an excellent instrument for measuring water vapor profiles, gradients, and higher-order moments (Muppa et al. 2015).

The TRRL technique is currently the only remote sensing technique that permits the profiling of temperature, its higher-order turbulent moments, and its gradient

in the lower troposphere with high vertical resolution (Wulfmeyer et al. 2015a). Because of a recent breakthrough in system design and performance at IPM, Hammann et al. (2015) demonstrated that it is now possible to determine the strength of the inversion layer during daytime. Comparisons with soundings, which are necessary for the calibration of TRRL, revealed a systematic error of less than 1 K. The noise error of temperature profiles is less than 2 K using resolutions of 10 s and 100 m up to 2 km, which permitted the first profiling of higher-order moments of temperature (Behrendt et al. 2015). Noise error propagation [see Eq. (A14)] explains that it is still possible to extract accurate atmospheric variance measurements at this noise level and that these measurements are particularly significant in the EL. Therefore, the TRRL method is now suited to provide the temperature measurements necessary for the turbulence studies that are subject of this work. As it is easily possible to convert temperature profiles measured with TRRL into profiles of potential temperature and their fluctuations (Behrendt et al. 2011), we continue to use the variable θ in our considerations. Furthermore, the combination of WVRL, WVDIAL, and TRRL permits a straightforward interchange of the different humidity variables m , ρ , and q . Although none of these systems is commercially available yet, new technologies are emerging having this potential (e.g., Spuler et al. 2015).

A single lidar system does not measure fluxes directly. However, the combination of high-resolution vertical wind measurements by DL or a radar wind profiler with WVDIAL or WVRL and TRRL permits the determination of latent and sensible heat flux profiles with the eddy correlation (EC) technique directly, which was originally pioneered in Senff et al. (1994) and also demonstrated by Wulfmeyer (1999a) and Giez et al. (1999). The confirmation that sensible heat flux profiles can be measured by a DL–TRRL combination was recently provided by Wulfmeyer et al. (2015b).

Furthermore, the instantaneous CBL height $z_i(t)$ and correspondingly the mean z_i during the averaging period can be measured very accurately (e.g., Pal et al. 2010). Different methods using vertical gradients of mean profiles and variance profiles can also be compared. This is important for appropriate CBL scaling and for the localization of the EL.

c. Proposed experimental design

A considerable advantage of the application of the lidar system synergy in the CBL is its capability to profile atmospheric variables, their gradients, turbulent moments, and fluxes simultaneously. The combination of these lidar measurements permits a thorough study of

EL scaling by testing different combinations of the equations above allowing both the general relationships (e.g., is the water vapor variance proportional to the square of the mean gradient?) to be evaluated and estimates of the coefficients to be made.

For instance, the combination of lidar systems permits a complete verification of the set of Eqs. (9)–(11), Eqs. (16)–(18), and even Eqs. (20)–(22). If lidar systems demonstrate that these relationships are valid, their measurements can be used for deriving unique quantitative results with respect to fluxes and higher-order moments, as various constants can be determined by means of comparisons.

We recommend the following combination of lidar instruments:

- One scanning Doppler lidar for determining wind profiles in the CBL and the wind shear in the EL. This lidar would primarily perform VAD scans so that horizontal wind profiles could be derived.
- One vertically pointing Doppler lidar for vertical wind measurements and profiling of its higher-order moments. It may be possible to perform these measurements with a single Doppler lidar by switching between vertical and VAD operation modes, if the SNR is high enough. This would need to be investigated by studying the performance characteristics of the particular DL that would be used.
- One vertically pointing DIAL or WVRL with sufficient resolution measuring profiles of q and g as well as profiles of higher-order moments of q .
- One vertically pointing TRRL with sufficient resolution for measuring θ and γ profiles as well as higher-order moments of θ .

In addition to allowing the equations for fluxes and higher-order moments to be investigated, this combination permits a direct measurement of Ri as well as dissipation and molecular destruction rates.

d. Strategy for investigation of CBL scaling based on lidar synergy

Three important contributions of lidar measurements are possible: 1) the direct measurement and independent development of CBL similarity relationships based on the lidar synergy proposed above, 2) the test of the CBL relationships introduced in section 2b, and 3) use of these measurements for model verification. The direct determination of CBL similarity relationships is being addressed by field campaign data such as HOPE in spring 2013, SABLE in August 2014 in Germany, and at the ARM operational sites at SGP and Darwin, from which measurements of a combination of gradients and higher-order turbulent moments of atmospheric variables are available.

In this case, the following data analysis procedure is suggested:

- 1) Determination of all profiles of mean variables, their gradients, and higher-order moments and their characterization with respect to their errors, as discussed in sections 3c(1) and 3c(2).
- 2) Investigation of integral scales for making sure that the major part of the turbulent fluctuations is resolved.
- 3) Performance of the same procedure for the combined variables such as fluxes and dissipation and molecular destruction rates [sections 2b(1), 2b(2), and 3c(2)].

Using these results, the data can be combined and correlated in different ways in order to search for their relationships.

1) RICHARDSON NUMBER RELATIONSHIPS

For studying the relationships introduced in section 2b, first of all, it is essential to study the Ri_E dependence of variances and third-order moments. For instance, using Eqs. (16)–(18), we get

$$f_{w^2}(Ri_E) = \frac{1}{C_{w^2}} \frac{w^2_E}{w_*^2}, \tag{59}$$

$$f_{\theta^2}(Ri_E) = \frac{1}{C_{\theta^2}} \frac{\theta^2_E}{w_*^2 (\gamma_E/N_E)^2}, \text{ and} \tag{60}$$

$$f_{q^2}(Ri_E) = \frac{1}{C_{q^2}} \frac{q^2_E}{w_*^2 (g_E/N_E)^2}. \tag{61}$$

For example, if the relationship for moisture [Eq. (19)] is valid, we find

$$Ri_E = \frac{1}{C_{q^2}} \frac{q^2_E}{w_*^2 (g_E/N_E)^2} - c_{q^2} \frac{1}{1 - \frac{1}{C_{q^2}} \frac{q^2_E}{w_*^2 (g_E/N_E)^2}}. \tag{62}$$

This equation makes a direct measurement of Ri_E possible merely based on a combination of temperature and water vapor lidar systems. This same approach allows for determining the values of the coefficients C_{q^2} and c_{q^2} as measurements of Ri_E will be available directly from the combination of DL and TRRL [Eq. (13)]. Naturally, many cases would be needed to develop uncertainty estimates for these coefficients and to see if these coefficients have any dependence on the meteorological regime. An analogous equation can be derived for Ri_E in dependence of temperature variance and gradients.

2) HIGHER-ORDER MOMENT RELATIONSHIPS

By the combination of gradient and variance measurements as well as the knowledge of Ri_E , Eqs. (16)–(18) can be studied. First attempts have already been performed by Wulfmeyer et al. (2010) and Turner et al. (2014b). However, for these studies neither wind nor temperature profiles were available yet, so further refinements and the use of more expanded datasets are necessary.

The question arises whether measurements of higher-order moments are helpful to get additional insight regarding turbulence in the EL. These lidar studies may lead to a refinement of the similarity relationships. For instance, focusing on humidity, if Eqs. (18) and (22) are valid, the skewness \mathcal{S}_q in the EL should be negative because

$$\mathcal{S}_q := \frac{\overline{q^3}_E}{(\overline{q^2}_E)^{3/2}} \quad (63)$$

$$= \frac{C_q w_*^3 (g_E/N_E)^3 f_q(\text{Ri})}{[C_q w_*^2 (g_E/N_E)^2 f_q(\text{Ri})]^{3/2}} \quad (64)$$

$$= -\frac{C_q}{C_q^3} \frac{f_q(\text{Ri})}{[f_q(\text{Ri})]^{3/2}} \quad (65)$$

$$\cong -\frac{C_q}{C_q^3}, \quad (66)$$

where the last equation holds in the case of free convection. Under these conditions, the dependence on gradients is eliminated because the relationships are self-similar. Obviously, the similarity relationships propose a negative \mathcal{S}_q in the EL. However, we already know from our measurements that this is not correct but \mathcal{S}_q changes sign from negative to positive in the EL typically just below z_i (Wulfmeyer 1999a; Lenschow et al. 2000; Wulfmeyer et al. 2010; Turner et al. 2014b). The reason for this discrepancy is likely the inappropriate expansion of the scaling relationship for the variance [Eq. (18)] to the third-order moment [Eq. (22)]. This is a first interesting test of the similarity relationships demonstrating the potential of the lidar observations. Additionally, if the coefficients and the dependencies on Ri_E are known, Eq. (65) provides another estimate of Ri_E , which may be useful for studying the consistency of the set of equations.

For vertical wind, it is straightforward to see that the relationships prescribe that $\mathcal{S}_w > 0$. Indeed, this can be confirmed by most measurements (Lenschow et al. 2000, 2012). However, while \mathcal{S}_w remains positive in the EL, there seems to be a negative slope leading to a reduction in the EL, which is not predicted. Thus, a very important topic will be the study of the behavior of third-order moments in the EL of the CBL.

3) FLUX RELATIONSHIPS

Particularly interesting is the application of EL scaling in a way that a minimum set of lidar systems can be applied for deriving fluxes taking advantage of their measurements of higher-order moments. There is indeed an interesting potential because, for example, the combination of Eq. (11) and the square root of Eq. (18) yields

$$Q_E = \frac{C_Q}{\sqrt{C_q}} w_* \sqrt{q^2}_E \frac{1 + c_Q/Ri_E}{\sqrt{1 + c_q/Ri_E}} \quad (67)$$

$$= \frac{0.025}{\sqrt{0.175}} w_* \sqrt{q^2}_E \frac{1 + 8/Ri_E}{\sqrt{1 + c_q/Ri_E}} \quad (68)$$

$$= 0.06 w_* \sqrt{q^2}_E \frac{1 + 8/Ri_E}{\sqrt{1 + c_q/Ri_E}} \quad (69)$$

$$\cong 0.06 w_* \sqrt{q^2}_E, \quad (70)$$

where the Eq. (70) holds in the case of free convection. In the case of significant wind shear, Eq. (67) and the studies of Ri_E in section 3d(1) or Eq. (62) can be combined so that it may be possible to use a WVDIAL and a TRRL for the direct determination of entrainment moisture fluxes.

Another possibility is to relate the flux with variance and gradients by eliminating w_* :

$$Q_E = -\frac{C_Q}{C_q} \frac{N_E}{g_E} \overline{q^2}_E \frac{1 + c_Q/Ri_E}{1 + c_q/Ri_E} \sqrt{1 + \frac{1}{Ri_E}}, \quad (71)$$

$$Q_E \cong -\frac{C_Q}{C_q} \frac{N_E}{g_E} \overline{q^2}_E \sqrt{1 + \frac{1}{Ri_E}}, \quad \text{and} \quad (72)$$

$$Q_E \cong -\frac{C_Q}{C_q} \frac{N_E}{g_E} \overline{q^2}_E \cong -0.14 \frac{N_E}{g_E} \overline{q^2}_E, \quad (73)$$

again where the last equation is proposed to be valid in the free convection limit. Comparing Eqs. (71)–(73) with the surface latent heat flux, it can be determined whether the CBL is drying or moistening, as long as moisture advection can be neglected. Obviously, the CBL is moistening if the ratio $V = Q_E/Q_0 < 1$, which translates to

$$V = \frac{Q_E}{Q_0} = 0.06 \frac{w_* \sqrt{q^2}_E}{Q_0} \frac{1 + 8/Ri_E}{\sqrt{1 + c_q/Ri_E}} \quad (74)$$

$$= 0.06 \frac{\sqrt{q^2}_E}{q_*} \frac{1 + 8/Ri_E}{\sqrt{1 + c_q/Ri_E}} \quad (75)$$

$$\cong 0.06 \frac{\sqrt{q^2}_E}{q_*}, \quad (76)$$

with the last equation holding in the case of free convection.

Of course, if the relationships for Q_E are verified, they can also be used for determining the flux divergence in the CBL, which is extremely important for CBL TP. Assuming a linear flux profile, the flux divergence is simply

$$\frac{\partial}{\partial z} w'q' = \frac{Q_E - Q_0}{z_i} \quad (77)$$

$$\approx \frac{0.06\sqrt{q_E^2 w_{*g}^2 - Q_0}}{z_i}. \quad (78)$$

Obviously, a couple of comprehensive relationships can be derived, which are worth an extensive evaluation.

In an additional step, it is also possible to investigate the closure of the budget equations for mean variables, as demonstrated in Senff et al. (1994), Wulfmeyer (1999a,b), as well as for higher-order moments and fluxes.

4) DISSIPATION AND MOLECULAR DESTRUCTION RATES

The lidar measurements allow the profiling of the integral scales throughout the CBL including the EL. If the major part of the turbulent fluctuations is resolved, the parameters of the structure function can be determined. Therefore, we are proposing here a new technique for the combination DL, TRRL, and WVDIAL or WVRL in order to determine TKE dissipation rates as well as the destruction rates of temperature and humidity variances based on Eqs. (43)–(45), Eqs. (47) and (48), Eq. (52) and (53), and Eqs. (56) and (57).

4. First results using WVDIAL and TRRL

a. Dataset

We present data collected during intensive observations period (IOP) 5 of HOPE, which was performed in spring 2013 close to the city of Jülich, Germany. IOP5 was executed on 20 April 2013. We focus on a dataset collected with the IPM WVDIAL and the TRRL between 1130 and 1230 UTC. The lidar systems were located at site close to the village of Hambach near Research Centre Jülich at 50°53'50.56"N, 6°27'50.39"E and 110 m above sea level.

During IOP5, the HOPE domain was under the influence of a high pressure system over the Baltic Sea and a cold front over the Alps to the southeast. The local conditions were measured by a weather and energy balance closure station a few meters from the site. The surface pressure at the measurement site was $p_0 \approx 1020$ hPa. The horizontal wind speed at 5-m height was 1.5 m s^{-1} from northeast turning to eastern directions at the CBL top, as

revealed by a radio sounding launched at the measurement site at 1300 UTC. The surface temperature was low with 284 K. Because of the large-scale conditions, rather dry air was advected into the region resulting in a surface specific humidity of merely 3.4 g kg^{-1} corresponding to a relative humidity (rh) of approximately 43%. Further details concerning the meteorological conditions are found in Muppa et al. (2015).

Except for a few cirrus clouds, the atmosphere was cloud free and contained only a few aerosol layers in the free troposphere. The surface heating was significant resulting in sensible heat flux of 247 W m^{-2} , whereas the evapotranspiration was modest with 89 W m^{-2} . The friction velocity was $u_* \approx 0.7 \text{ m s}^{-1}$, corresponding to a Monin–Obukhov length of $L \approx -126 \text{ m}$.

b. Results derived by lidar synergy

We are focusing on the synergy of the IPM WVDIAL and the TRRL systems. Doppler lidar data had to be excluded because the vertical velocity variance and skewness, as well as the horizontal winds, have not been processed in detail yet. Therefore, a full analysis of fluxes and variances, and their relationships with gradients and dependences on Ri_E , is not possible. In any event, a full exploitation of all equations presented in sections 2 and 3 is beyond the scope of this work and subject of future activities.

However, even without the knowledge of Ri_E , a large number of relations could be studied for the first time here. This is due to the fact that the WVDIAL and TRRL measurements are providing mean profiles and their vertical gradients of specific humidity and potential temperature, variance profiles, and insight into structure coefficients in the same vertical air column, simultaneously. For this study, both the WVDIAL and the TRRL data were processed with a temporal resolution of 10 s and vertical resolutions of 100 m allowing for a consistent analysis of gradients and turbulent moments. Additionally, the TRRL data were corrected with respect to systematic errors induced by incomplete overlap between laser transmitter and field of view of the telescope up to 800 m with a time-independent correction function (Hammann et al. 2015). Afterward, the WVDIAL absolute humidity measurements and the TRRL temperature measurements were transformed into specific humidity and potential temperature using a hydrostatic pressure profile.

The mean specific humidity, potential temperature, and relative humidity profiles and their gradients during the measurement period are presented in Fig. 3 (top). The system noise errors and the estimate of the mean CBL depth z_i are also indicated. As mentioned above, the specific humidity in the ML was rather low with

3 g kg^{-1} . Toward the entrainment layer already a strong decrease of the specific humidity was observed decreasing further to 0.1 g kg^{-1} in the lower free troposphere. This resulted in a strong reduction of rh around the EL as well. The potential temperature profile shown in Fig. 3 shows a well-mixed CBL (as also confirmed by soundings) up to 1000 m with a mean $\theta \approx 282.5 \text{ K}$. The moisture decrease above and the large vertical extent of the region with increasing potential temperature likely indicates an entrainment drying CBL.

During the time period of interest, the CBL was well developed and reached a quasi-stationary depth, as confirmed by the lidar backscatter profiles (not shown). Whereas many different definitions of z_i are available (e.g., Cohn and Angevine 2000; Pal et al. 2010) and some uncertainties remain, we could take advantage of the synergy of our measurements. For this purpose, we evaluated the gradients of the lidar backscatter signals, the minimum of the mean water vapor gradient, and the maximum of the potential temperature gradient in the EL as well as the locations of the maxima of the variance profiles. This resulted in $z_i \approx 1280 \text{ m}$ with a standard deviation of 60 m derived from the instantaneous $z_i(t)$ values of the backscatter gradients. The latter value multiplied by 2 can be considered as an estimate of the mean EL thickness and resulted in $\Delta_{\text{EL}} \approx 120 \text{ m}$. This result of z_i was consistent within 20 m with the radio sounding launched at 1300 UTC.

Using the estimate of z_i , we derived a vertical velocity scale of $w_* \approx 2 \text{ m s}^{-1}$, a convective time scale of $t_* \approx 10.7 \text{ min}$, a humidity scale of $q_* \approx 0.015 \text{ g kg}^{-1}$, and a potential temperature scale of $\theta_* \approx 0.1 \text{ K}$. Furthermore, we estimated the corresponding temperature gradient by taking the range $z_i - \Delta_{\text{EL}}/2$, $z_i + \Delta_{\text{EL}}/2$, which yielded $\gamma_E \approx 0.02 \text{ K m}^{-1}$ or a temperature jump of approximately 2 K in the EL. This resulted in a Brunt–Vaisala frequency of $N_E \approx 0.026 \text{ Hz}$ and a local Richardson number $\text{Ri}_l = \Delta\theta/\theta_* \approx 20$. As shown in Fig. 3, the minimum specific humidity gradient in the EL was approximately $-0.012 \text{ g kg}^{-1} \text{ m}^{-1}$ and the averaged gradient in the EL yielded $g_E \approx -0.01 \text{ g kg}^{-1} \text{ m}^{-1}$.

By means of the analyses described in section b of the appendix (see also Lenschow et al. 2000; Wulfmeyer et al. 2010), we derived profiles of the integral scales, variances, and third-order moments of potential temperature and specific humidity. In all these figures, black error bars indicate noise errors and the colored error bars the sampling errors.

Figure 4 presents the profiles of the integral scales \mathcal{T}_θ (top panel) and \mathcal{T}_q (bottom panel). In these panels, we also compared their determination by a numerical integration from lag 0 to the first zero crossing of the autocovariance function with the theoretical result given in

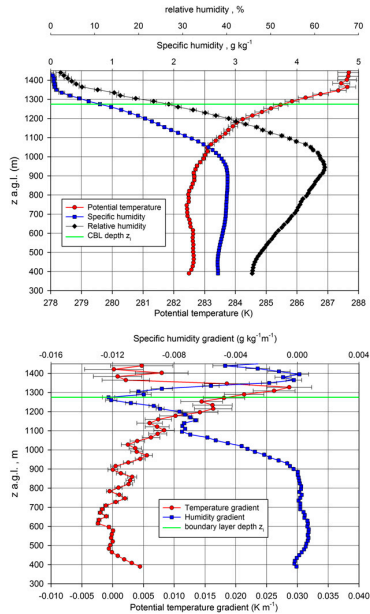


Fig. 3. (top) Mean profiles of specific humidity and potential temperature during IOP5 (1130–1230 UTC). (bottom) Corresponding vertical gradient profiles. The error bars due to system noise and the estimate of z_i are also indicated.

Eq. (42). The outliers in the numerical integration are due to systematic errors, if very low variance levels are determined by the extrapolation of the autocovariance function, as in the numerical integration the autocorrelation function must be used [see Eq. (41) and Fig. A1]. We recommend the use of Eq. (42) because it gives more robust results at low variance levels and compares very well with the numerical integration otherwise.

For potential temperature, a rather constant profile in the CBL was determined with $\mathcal{T}_\theta \approx 50 \text{ s}$. In contrast, \mathcal{T}_q showed a reduction from the ML to the EL from approximately 150 to 50 s. In both profiles, fine structures appear, which are not fully understood yet. Currently, we suppose that these are due to sampling statistics. These results also confirm that the resolution of the lidar profiles was high enough to resolve the temperature and

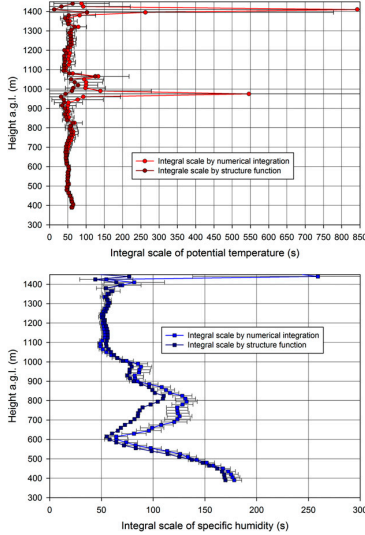


FIG. 4. (top) Potential temperature integral scale derived using the integration of the autocovariance function to the first zero crossing or using the new Eq. (42). (bottom) As in (top), but for specific humidity.

humidity fluctuations into the inertial subrange even in the EL.

The potential temperature and specific humidity variance profiles are depicted in Fig. 5. To demonstrate the high SNR of the measurements, the profiles are plotted on a logarithmic scale. Again, some fine structures in the profiles are found, which may be due to sampling statistics or a too-strong noise correction at low variance level. Otherwise, the potential temperature variance profiles show a nearly constant variance of 0.07 K^2 in the ML and the expected peak in the EL with an amount of 0.5 K^2 . In contrast, the specific humidity variance profile is generally increasing from very low levels by an order of magnitude to $0.1 \text{ g}^2 \text{ kg}^{-2}$ in the ML. In the EL, the typical peak is reached with a value of $0.5 \text{ g}^2 \text{ kg}^{-2}$. It is likely a coincidence in this case that the absolute values of potential temperature and specific humidity variances in the EL are similar.

Profiles of the third-order moments are presented in Fig. 6. In the ML, both profiles indicate a symmetric

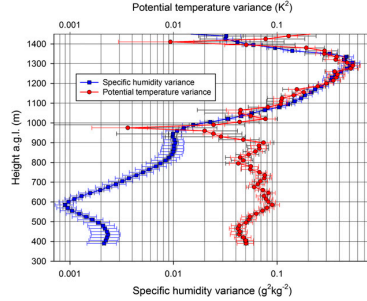


FIG. 5. The specific humidity and potential temperature variance profiles. The error bars in the same color as the plots are the sampling errors and the black error bars are the noise errors.

distribution of the fluctuations. However, in the EL, below z_i the third-order moment turns positive for the potential temperature and negative for the specific humidity fluctuations. Close to z_i , the moments show a zero crossing and are changing sign above, which is clearly visible in the specific humidity but less pronounced in potential temperature, however, likely as a result of a larger noise level in the latter.

c. Discussion

The results presented in Figs. 3–6 can be used to evaluate several relationships proposed in this work. The necessity to derive improved relationships for exchange and turbulent processes in the EL becomes already evident by noting that the standard potential temperature and specific humidity scales derived in section 4b cannot explain the observed variances in this layer.

The main weakness in our study is the lack of knowledge of Ri_E . However, the local $Ri_l \approx 20$ and the lack of strong shear in the radiosonde data indicate that the case was not too far from the free-convection limit. Therefore, in the following, we disregard any Ri_E dependencies. Furthermore, we assume that w_{*s} is a reasonable scaling variance for the vertical wind fluctuations even in the EL.

Considering these uncertainties, we start with an evaluation of the variances in the EL. Using Eqs. (17) and (18) and the proposed coefficients C_θ and C_q , we get estimates of $\overline{\theta'^2} \approx 0.1 \text{ K}^2$ and $\overline{q'^2} \approx 0.1 \text{ g}^2 \text{ kg}^{-2}$. Thus, we achieved an underestimation of the variances in the EL by a factor of 5. Obviously, at least one of the assumptions, the validity of the free convection limit, the scaling with w_{*s} , or the values of the constants derived by LES were not valid.

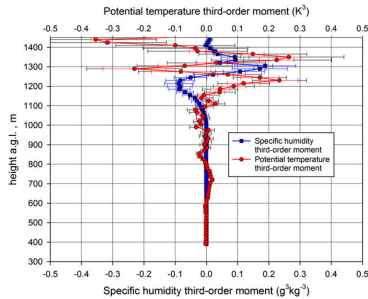


FIG. 6. The specific humidity and potential temperature third-order-moment profiles. The same convention for the colors and error bars is used as in Fig. 5.

We also tested Eqs. (70) and (73) for the water vapor entrainment flux Q_E . Using Eq. (70) we achieved $Q_E \approx 210 \text{ W m}^{-2}$ and using Eq. (73) we got $Q_E \approx 450 \text{ W m}^{-2}$. In both cases, an entrainment drying CBL was confirmed [see also Eq. (76)]. However, because of the strong drying at the CBL top (see Fig. 3), the latter value was likely closer to reality. This indicates that we may have to go away from the scaling using w_σ in the EL and it is better to use potential temperature and specific humidity gradients.

Using Fig. 6, we can evaluate also the scaling proposed in Eqs. (21), (22), and (66). It turns out that the gradient scaling does not work in the case of third-order moments because the third-order moment changes sign in the EL leading to a complex structure of the profiles. With respect to water vapor, this structure was also found in other lidar measurements (Wulfmeyer 1999b; Wulfmeyer et al. 2010; Turner et al. 2014b) so that this seems to be common in the CBL. With respect to temperature, we are confirming this complex structure for the second time using active remote sensing—the first time it was shown using TRRL measurement by Behrendt et al. (2015) albeit with different values of the negative and positive maxima. Couvreux et al. (2007) detected and analyzed this structure by LES. They argued that this behavior is due to the deformation of eddies in the region of the inversion causing different updraft and recoiling structures. In the future, further insight in and quantification of the behavior of third-order moments should be collected by additional observations and dedicated LES and DNS runs by analyzing the third-order moment budgets.

The use of Eq. (39) in combination with Eq. (A9) also allowed us to get some insight in the profiles of the structure function coefficients k_q and k_θ . Figure 7 presents the results. In the top panel, except at very low variance levels, we found a striking linear relationship between these coefficients and the corresponding variances with a very similar slope for specific humidity and potential temperature. By a linear fit, we found $\overline{q^2} \approx 26.5 \text{ s}^{2/3} k_q$ and $\overline{\theta^2} \approx 26.2 \text{ s}^{2/3} k_\theta$. Furthermore, we studied the ratio k_q/k_θ between these coefficients, which corresponds to the ratio of the molecular destruction rates of humidity and temperature variances. The results are presented in the bottom panel of Fig. 7. Except some outliers due to low SNR and taking a ratio of noisy signals, in the ML, the destruction rate is much smaller for humidity than for temperature. However, in the EL, the ratio reaches approximately the same value of 1 so that the destruction rates are becoming similar.

Despite some missing information, we demonstrated first results comparing profiles of gradients, variances, and the coefficient of the structure function from the ML through the EL in a quasi-stationary CBL. Whereas the variances in the EL were underestimated by the gradient function relationships in comparison to the measurements, reasonable results were achieved for the water vapor entrainment flux. The structure of the third-order moments in the EL is more complex than can be described by gradient relationships. Interesting results were found with respect to the behavior of the structure function coefficients showing a different ratio of molecular destruction rates in the ML and the EL. In the future, it is essential that these studies are extended by simultaneous measurements of wind profiles and vertical velocity statistics because the dependence of the relationships on the functions $f(\text{Ri}_E)$ for variances and fluxes as well as the validity of scaling with the convective velocity scale have to be investigated. For this purpose, continuous measurements of the daily cycle of the CBL during field campaigns and/or observatories with sufficient equipment of lidar systems are necessary. Furthermore, the dependence of the results on the resolution of the lidar systems and of dedicated LES runs needs to be explored.

5. Summary and outlook

In this work, we presented methodologies for improving the representation of turbulent transport processes and entrainment in weather and climate models for advanced simulations of water and energy cycles. Usually, turbulent transport processes are represented by the turbulence parameterization (TP), as long as the model grid increment is approximately 1 km or more.

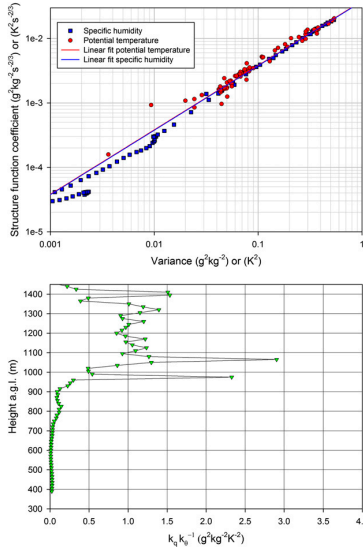


FIG. 7. (top) Relation between variances and structure function coefficients for potential temperature and specific humidity. Additionally, the results of a linear fit are shown. (bottom) The ratio between the coefficient in dependence of height.

However, it is controversial at what grid increment the turbulence should be explicitly simulated without any TP so that the model is running in the large-eddy simulation (LES) mode. Because over many regions of Earth, convection initiation in the daytime is critical for the formation of clouds and precipitation, we are focusing on the investigation of turbulence in the daytime atmospheric convective boundary layer (CBL) with low cloud coverage.

Studies of turbulent transport processes and entrainment can be performed either by LES or high-resolution observations. LES has been used for the investigation of turbulence for a long time, and many aspects of TPs have been derived from the corresponding results. However, it should not be forgotten that a detailed simulation of land surface-atmosphere exchange and feedback requires a realistic representation of the heterogeneity of the land surface with respect to soil properties, land cover, and orography. Furthermore, it is fundamental to

include the simulation of gravity waves at the CBL top, as these are contributing to the strength of entrainment. Only a few LES studies—if any—have been performed that fulfill these requirements. Therefore, strong efforts are still needed to improve LES by imbedding the simulations in a realistic large-scale environment. The latter is leading to the so-called gray-zone experiments where a chain of models resolving down to the LES scale can be compared with respect to their performance in a realistic synoptic setting. In any case, model simulations either in the form of gray-zone experiments or more idealistic LES must be verified with respect to their performance. Furthermore, any TPs require physically based relationships concerning entrainment processes, which must be verified by observations.

We present a new approach for the understanding and simulation of entrainment in the EL at the top of the CBL. After a discussion of the vertical structure of the CBL, EL scaling variables are introduced, which can be combined to derive a series of equations for determining variances and fluxes. These are related to gradients of wind, temperature, and humidity in the EL. It is also shown that the vertical exchange through the EL should contain a functional dependence of the gradient Richardson number Ri_E . Suggestions for these relationships are made. Furthermore, the autocovariance functions of the variables are considered, which can be modeled in the inertial subrange with the structure function for stationary and homogeneous turbulent processes. Physical relationships between the integral temporal and spatial scales and the turbulent quantities are derived, which can be tested by observations. New equations are introduced for profiling the TKE dissipation rate as well as the molecular destruction rates of humidity and temperature variances.

The verification of the relationships requires the measurements of wind, temperature, and humidity profiles as well as their gradients in the CBL including the EL. It is necessary that the corresponding instruments resolve their fluctuations for determining profiles of higher-order moments and of fluxes simultaneously.

We demonstrate that these verification efforts can be realized by a new synergy of DL for profiling the vertical and horizontal wind, WVDIAL or WVRL for humidity profiling, and TRRL for temperature profiling. This combination of instruments is essential but also sufficient for a complete analysis of the similarity relationships. A thorough analysis of the new generation of WVRL, WVDIAL, and TRRL lidar systems, where the last two of them have been developed at the IPM of the UHOH, demonstrates that these systems are capable of fulfilling the measurement needs. A detailed analysis of systematic and noise errors of mean profiles, their

gradients, higher-order moments, fluxes, and dissipation and molecular destruction rates is presented, which can be used to confirm the sufficient performance of these lidar systems.

A straightforward strategy of using the data from these lidar systems is developed. After all profiles of interest are determined and their error bars are characterized, the results can be combined in different ways. For instance, the data can be used for determining Ri_E to study the functional dependence of Ri_E influencing variance and flux profiles. A series of equations is derived to investigate variance- and third-order moment-gradient relationships, flux-variance relationships, and flux-gradient relationships.

We demonstrate that the DL–WVDIAL/WVRL–TRRL synergy has at least three functions: 1) a complete set of equations can be tested for deriving variances and fluxes by gradient relationships; 2) LES can be verified in great detail by studying profiles of second-, third-, and fourth-order moments; and 3) new relationships for fluxes and variances can be derived forming the basis for budget analyses and new TPs.

First tests of these relationships were presented using a dataset from HOPE. Simultaneous measurements of mean profiles and gradients of potential temperature as well as specific humidity and their variances are shown and analyzed. We showed that the similarity relationships underestimate the measured variance, if the free-convection limit was present and the constants previously derived by LES are valid. Furthermore, we assumed that the convective velocity scale is an appropriate scaling variable. The application of a gradient-variance similarity relationship for the entrainment water vapor flux gave reasonable results and indicated an entrainment-drying CBL during the measurement period. The variances were proportional to the fit coefficients of the structure function and the molecular destruction rates of potential temperature and specific humidity variances became similar in the EL. In the future, measurements of additional scaling variables using DL have to be added to refine these studies.

So far, this combination of measurements has only been realized during the HOPE and SABLE field campaigns. Further datasets are available from observatories such as the ARM SGP and Darwin sites but may require some redesign and improvement of instrument equipment and performance there. We propose to perform dedicated field campaigns for studying the proposed relationships and to extend current observatories to fulfill the required measurement needs. Ideally, the operation of this basic synergy of active instruments should be supported by airborne in situ as well as passive and active remote sensing measurements

using a combination of lidar and radar systems extending the measurements in clouds. These efforts should be accompanied by gray-zone simulations down to the LES or even the DNS scale. The relationships and equations in this work as well as simulations of the same scales will enable us to reach a new level of detail and accuracy for testing and developing advanced TPs in the CBL.

Acknowledgments. This work was supported by the Cooperative Institute for Environmental Studies (CIRES) in Boulder, Colorado, by a Visiting Fellow Award for the first author. Furthermore, this study was performed within the German Science Foundation (DFG) Research Unit FOR1695 “Regional Climate Change” and the Federal Ministry of Education and Research (BMBF) program High Definition Clouds and Precipitation (HD(CP)²). This research was also supported by the National Severe Storms Laboratory (NSSL) in Norman, Oklahoma, and the U.S. Department of Energy (DOE) Atmospheric System Research (ASR) via Grant DE-SC0006898.

APPENDIX

Error Analysis of Lidar Profiles

a. Systematic errors

For all lidar systems introduced above, stable system performance has been demonstrated so that any systematic errors should be constant in time during turbulence measurements. The corresponding errors of wind, humidity, and temperature profiles can be taken from the specifications summarized in section 3b. As the height dependence of these errors is very low as well, their effect on gradients can be neglected. It is interesting to investigate the effect of systematic errors on turbulent quantities as well. If the systematic error is just a constant offset, it does not have an influence on the fluctuations so that this effect can be neglected. However, in many lidar systems and other calibrated observing systems, systematic deviations from the mean can be caused by errors in a calibration constant. In this case, the error of the fluctuations can be analyzed as follows using q as an example. If q_T and q_M are the true and the measured values then

$$q_T(t) = q_M(t) + Fq_M(t), \quad (\text{A1})$$

where F is the relative systematic error of the measurement of q_M . Then

$$q_T'(t) = q_T(t) - \bar{q}_T \quad \text{and} \quad (\text{A2})$$

$$q_M'(t) = q_M(t) - \bar{q}_M. \quad (\text{A3})$$

Thus, the systematic error $\Delta q'_M$ in the measurement of the fluctuations of q reads

$$\Delta q'_M(t) = q'_T(t) - q'_M(t) = q_T(t) - \bar{q}_T - [q_M(t) - \bar{q}_M]. \quad (\text{A4})$$

Using Eq. (A1), it follows

$$\Delta q'_M(t) = q_M(t) + Fq_M(t) - \bar{q}_M - F\bar{q}_M - q_M(t) + \bar{q}_M \quad (\text{A5})$$

$$= Fq_M(t) - F\bar{q}_M = F[q_M(t) - \bar{q}_M] \quad (\text{A6})$$

$$= Fq'_M(t). \quad (\text{A7})$$

Applying Eq. (A7) to the derivation of variances, we get

$$\overline{q'^2_M} = (1 + F)^2 \overline{q'^2_T} \simeq (1 + 2F) \overline{q'^2_T}, \quad (\text{A8})$$

where $\overline{q'^2_M}$ is the variance measured including the systematic effect by F , for example, by an inaccurate calibration. Basically, the systematic error doubles, if variances are considered. As F is constant in time and just a few percent for all lidar systems (DL, WVDIAL, WVRL, and TRRL) considered here, systematic errors in the measurements of fluctuations can be neglected.

b. Sampling and noise errors

Error bars due to sampling and noise statistics have to be derived and considered for all profiles in order to specify the significance of the results. Sampling errors are critical for ground-based measurements owing to the considerable integration time to collect turbulent fluctuations with high statistical certainty. Sampling errors can be reduced by performing many measurements under similar meteorological conditions or by the design and operation of ground-based networks. Sampling errors were derived for all kinds of turbulent profiles and specified in [Lenschow et al. \(1994, 2000\)](#); therefore, they are not repeated here.

For all lidar-derived profiles, noise error bars have also to be specified, as their propagation into turbulence profiles is still significant. It is the strength of the lidar technique that these error bars can be derived for each turbulence profile under the current meteorological conditions without any additional assumptions. A very convenient and robust technique for determining noise error profiles was introduced in [Lenschow et al. \(2000\)](#) and applied there to DL and WVDIAL measurements. [Wulfmeyer et al. \(2010\)](#) extended this technique to WVRL and [Behrendt et al. \(2015\)](#) to TRRL turbulence measurements.

This technique is based on the extrapolations of the measured autocovariance functions to lag 0 by the structure functions given in Eqs. (35)–(37). We assume

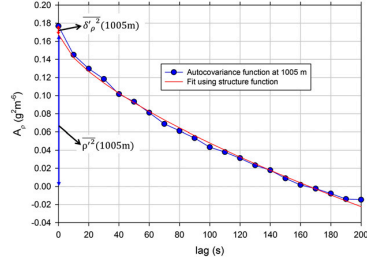


FIG. A1. Separation of atmospheric and noise variance by the fit of the structure function to the autocovariance function A_q for absolute humidity measured with the IPM WVDIAL.

that the noise errors between different lags are uncorrelated, which is the case for all lidar systems of interest here. It follows, for example, for specific or absolute humidity ρ measurements at lag 0:

$$A_q(0) = \overline{q'^2} + \delta^2 \quad \text{or} \quad A_q(0) = \overline{\rho'^2} + \delta_\rho^2, \quad (\text{A9})$$

where δ^2 and δ_ρ^2 are the specific or absolute humidity system noise variances at the corresponding temporal and range resolutions. [Figure A1](#) demonstrates this technique for a WVDIAL absolute humidity measurement performed during the SABLE campaign at 1100–1200 UTC 21 August 2014 at a height of 1005 m using a temporal resolution of 10 s. Clearly the noise and the atmospheric variances can be separated. The turbulence is well resolved, as observed by the good fit to the structure function, and the noise contribution is very small. The fit results in $\overline{\rho'^2} \simeq 0.17 \text{ g}^2 \text{ m}^{-6}$ and a noise variance of $\delta_\rho^2 \simeq 0.01 \text{ g}^2 \text{ m}^{-6}$, which corresponds to a noise error standard deviation of just $\delta_\rho \simeq 0.1 \text{ g m}^{-3}$.

Extended studies of this technique (e.g., [Turner et al. 2014b](#)) demonstrated that this separation is routinely possible at all height levels, at much higher noise levels, and even in the presence of clouds. As it was not explicitly mentioned in [Lenschow et al. \(2000\)](#), we are deriving here the error propagation for noise errors of gradients of humidity and temperature profiles as well as for errors of third- and fourth-order moments of atmospheric variables. Noise errors of fluxes as well as dissipation and molecular destruction rates are also considered.

1) GRADIENTS

Gradients of humidity and temperature are derived from absolute humidity or mixing ratio profiles (WVDIAL or WVRL) or from temperature profiles (TRRL). In contrast

to radio soundings, the representativeness is improved by continuous measurements of profiles of the variable of interest with a temporal resolution of 1–10 s and averaging them over time periods of 30–120 min, typically. The gradient, for example, for humidity, can be approximated by calculating the differential quotient

$$g(\bar{z}) = \frac{q(z + \Delta z) - q(z)}{\Delta z}, \quad (\text{A10})$$

where Δz is the range resolution of the lidar measurement and the gradient is located at \bar{z} , the mean value between z and $z + \Delta z$. After determination of the noise variance δ^2 at each vertical bin of humidity profile, the error σ_g of the gradient reads

$$\sigma_g \approx \sqrt{\frac{\delta^2}{N}} \frac{\sqrt{2}}{\Delta z}, \quad (\text{A11})$$

considering that the noise errors at the range bins $z + \Delta z$ and z are nearly the same and statistically independent. Here, N is the number of samples during the averaging time for the determination of the gradient and turbulent quantities.

2) HIGHER-ORDER MOMENTS

Using the error propagation for the fluctuation q' of water vapor, higher-order moment profiles can be characterized with respect to noise errors. For instance, for the noise error $\sigma_{q'^2}$ of the variance we consider that noise errors are independent in each sample q'_i of the fluctuations and achieve by error propagation

$$\sigma_{q'^2}^2 \approx \frac{1}{N^2} \sum_i \left[\frac{\partial}{\partial q'_i} (q_i^2) \right]^2 \delta_i^2 \approx \frac{4}{N^2} \sum_i (q'_i)^2 \delta_i^2 \approx \frac{4}{N} q'^2 \delta^2. \quad (\text{A12})$$

Thus,

$$\sigma_{q'^2} \approx 2\sqrt{q'^2} \sqrt{\frac{\delta^2}{N}} \quad \text{and} \quad (\text{A13})$$

$$\sigma_{q'^2} \approx 2q'^2 \sqrt{\frac{\delta^2}{q'^2 N}}. \quad (\text{A14})$$

Applying these equations to the example from Fig. A1, which used a time resolution of 10 s and an averaging time of 1 h ($N = 360$), we get an absolute error of $\sigma_{q'^2} \approx 0.004 \text{ g}^2 \text{ m}^{-6}$ and a relative error of $\sigma_{q'^2}/q'^2 \approx 3\%$, which is quite acceptable and demonstrates the low noise of the IPM WVDIAL.

Applying the same principle of Eq. (A12) to higher-order moments, we get for the noise error $\sigma_{q'^n}$ of the third-order moment

$$\sigma_{q'^3} \approx 3\sqrt{\frac{\delta^2}{q'^4}} \approx 3\sqrt{3q'^2} \sqrt{\frac{\delta^2}{N}}. \quad (\text{A15})$$

We applied the Isserlis theorem to the fourth-order moment as $q'^4 \approx 3q'^2$ assuming that higher-order moments do not deviate too much from a Gaussian distribution.

Then, Eq. (A15) can also be written in the following forms:

$$\sigma_{q'^3} \approx \frac{3}{2}\sqrt{3}\sqrt{q'^2}\sigma_{q'^2} \quad (\text{A16})$$

or

$$\frac{\sigma_{q'^3}}{q'^3} \approx 3\sqrt{3} \frac{1}{\mathcal{S}_q} \sqrt{\frac{\delta^2}{q'^2 N}} \quad (\text{A17})$$

by introducing the skewness \mathcal{S}_q of the time series.

The noise error of the fourth-order moment is calculated accordingly and we derive

$$\sigma_{q'^4} \approx 4\sqrt{q'^6} \sqrt{\frac{\delta^2}{N}} \approx 4\sqrt{15q'^2} \sqrt{\frac{\delta^2}{N}} \quad (\text{A18})$$

again using an Isserlis theorem but here for $q'^6 \approx 15q'^2$. Analogous to the third-order moment we get the following relationships:

$$\sigma_{q'^4} \approx \frac{\sqrt{15}}{2} q'^2 \sigma_{q'^2} \quad (\text{A19})$$

or

$$\frac{\sigma_{q'^4}}{q'^4} \approx 4\sqrt{15} \frac{1}{\mathcal{K}} \sqrt{\frac{\delta^2}{q'^2 N}} \quad (\text{A20})$$

with the kurtosis \mathcal{K} of the time series. Obviously, the noise errors of the n th moment scale approximately with

$$\sigma_{q'^n} \propto \sqrt{q'^2}^{\frac{(n-2)}{2}} \sigma_{q'^2} \quad \text{for } n \in \mathbb{N} \geq 2. \quad (\text{A21})$$

Using these relationships, a full error propagation is possible for all vertical profiles of higher-order moments and their vertical gradients so that errors can be derived for all variables presented in the equations above. The errors scale with the standard deviation of noise during the averaging time. Consequently, as long as no nonlinearities occur in the derivation of fluctuations, it is better to maximize the time resolution so that the atmospheric variability is resolved as far as possible into the inertial subrange. Furthermore, the noise errors of the turbulent moments scale with powers of

atmospheric variances so that the noise errors remain small in the EL.

3) FLUXES

It is also important to study noise errors in fluxes. Here, we achieve

$$\sigma_{w'q'} \simeq \sqrt{q^2 \frac{\delta_w^2}{N} + w^2 \frac{\delta_q^2}{N}} \tag{A22}$$

$$\simeq \sqrt{q^2 w^2} \sqrt{\frac{\delta_w^2}{Nw^2} + \frac{\delta_q^2}{Nq^2}} \tag{A23}$$

$$\begin{aligned} &\simeq \frac{1}{r} q' w' \sqrt{\frac{\delta_w^2}{Nw^2} + \frac{\delta_q^2}{Nq^2}} \\ &= \frac{1}{r} q' w' \sqrt{\left(\frac{\delta_w^2}{w^2} + \frac{\delta_q^2}{q^2}\right) \frac{1}{N}}, \end{aligned} \tag{A24}$$

where r is the correlation coefficient between vertical wind and water vapor fluctuations. The same equations hold for sensible heat fluxes replacing q' by θ' . Here, for low noise in the flux profiles, a large correlation coefficient and low relative noise error with respect to the atmospheric variances are important.

4) DISSIPATION AND MOLECULAR DESTRUCTION RATES

Finally, we derive the noise error for the dissipation rates based on Eqs. (47), (52), and (56). We achieve

$$\sigma_{\varepsilon} \simeq \varepsilon \sqrt{\frac{9}{4} \left(\frac{\sigma_{k_w}}{k_w}\right)^2 + \left(\frac{\sigma_U}{U}\right)^2}, \tag{A25}$$

$$\sigma_{\bar{N}_\theta} \simeq \bar{N}_\theta \sqrt{\left(\frac{\sigma_{k_\theta}}{k_\theta}\right)^2 + \frac{1}{4} \left(\frac{\sigma_{k_w}}{k_w}\right)^2 + \left(\frac{\sigma_U}{U}\right)^2}, \text{ and} \tag{A26}$$

$$\sigma_{\bar{N}_q} \simeq \bar{N}_q \sqrt{\left(\frac{\sigma_{k_q}}{k_q}\right)^2 + \frac{1}{4} \left(\frac{\sigma_{k_w}}{k_w}\right)^2 + \left(\frac{\sigma_U}{U}\right)^2}. \tag{A27}$$

In this case, σ_{k_w} , σ_{k_θ} , and σ_{k_q} are the errors in the determination of the fit coefficients to the structure function by the regression analysis, and σ_U is an error estimate for the horizontal wind profile.

REFERENCES

Ackerman, T. P., and G. M. Stokes, 2003: The Atmospheric Radiation Measurement Program—To predict reliably what increased greenhouse gases will do to global climate, we have to understand the crucial role of clouds. *Phys. Today*, **56**, 38–46, doi:10.1063/1.1554135.

Angevine, W., S. Avery, and G. Kok, 1993: Virtual heat flux measurements from a boundary-layer profiler-RASS compared to

aircraft measurements. *J. Appl. Meteor.*, **32**, 1901–1907, doi:10.1175/1520-0450(1993)032<1901:VHFMA>2.0.CO;2.

Ansmann, A., J. Fruntke, and R. Engelmann, 2010: Updraft and downdraft characterization with Doppler lidar: Cloud-free versus cumuli-topped mixed layer. *Atmos. Chem. Phys.*, **10**, 7845–7858, doi:10.5194/acp-10-7845-2010.

Ayotte, K. W., and Coauthors, 1996: An evaluation of neutral and convective planetary boundary-layer parameterizations relative to large eddy simulations. *Bound.-Layer Meteor.*, **79**, 131–175, doi:10.1007/BF00120078.

Behrendt, A., V. Wulfmeyer, A. Riede, G. Wagner, S. Pal, H. Bauer, M. Radlach, and F. Späth, 2009: Three-dimensional observations of atmospheric humidity with a scanning differential absorption Lidar. *Remote Sensing of Clouds and the Atmosphere XIV*, R. H. Picard, K. Schäfer, and A. Cameron et al., Eds., International Society for Optical Engineering (SPIE Proceedings, Vol. 7475), 74750L, doi:10.1117/12.835143.

—, and Coauthors, 2011: Observation of convection initiation processes with a suite of state-of-the-art research instruments during COPS IOP 8b. *Quart. J. Roy. Meteor. Soc.*, **137**, 81–100, doi:10.1002/qj.758.

—, E. Hammann, S. K. Muppa, S. Pal, and V. Wulfmeyer, 2015: Profiles of second- to fourth-order moments of turbulent temperature fluctuations in the convective boundary layer: First measurements with rotational Raman lidar. *Atmos. Chem. Phys.*, **15**, 5485–5500, doi:10.5194/acp-15-5485-2015.

Cohn, S., and W. Angevine, 2000: Boundary layer height and entrainment zone thickness measured by lidars and wind-profiling radars. *J. Appl. Meteor.*, **39**, 1233–1247, doi:10.1175/1520-0450(2000)039<1233:BLHAEZ>2.0.CO;2.

Conzemius, R. J., and E. Fedorovich, 2006: Dynamics of sheared convective boundary layer entrainment. Part I: Methodological background and large-eddy simulations. *J. Atmos. Sci.*, **63**, 1151–1178, doi:10.1175/JAS3691.1.

Couvreux, F., F. Guichard, J.-L. Redelsperger, C. Kiemle, V. Masson, J.-P. Lafore, and C. Flamant, 2005: Water-vapour variability within a convective boundary-layer assessed by large-eddy simulations and IHOP_2002 observations. *Quart. J. Roy. Meteor. Soc.*, **131**, 2665–2693, doi:10.1256/qj.04.167.

—, —, V. Masson, and J.-L. Redelsperger, 2007: Negative water vapour skewness and dry tongues in the convective boundary layer: Observations and large-eddy simulation budget analysis. *Bound.-Layer Meteor.*, **123**, 269–294, doi:10.1007/s10546-006-9140-y.

Crum, T., and R. Stull, 1987: Field measurements of the amount of surface layer air versus height in the entrainment zone. *J. Atmos. Sci.*, **44**, 2743–2753, doi:10.1175/1520-0469(1987)044<2743:FMOTAO>2.0.CO;2.

—, —, and E. Eloranta, 1987: Coincident lidar and aircraft observations of entrainment into thermals and mixed layers. *J. Climate Appl. Meteor.*, **26**, 774–788, doi:10.1175/1520-0450(1987)026<0774:CLAAOO>2.0.CO;2.

Deardorff, J., 1970: A three-dimensional numerical investigation of the idealized planetary boundary layer. *Geophys. Fluid Dyn.*, **1**, 377–410, doi:10.1080/03091927009365780.

Dethloff, K., C. Abegg, A. Rinke, I. Hebestadt, and V. F. Romanov, 2001: Sensitivity of Arctic climate simulations to different boundary-layer parameterizations in a regional climate model. *Tellus*, **53A**, 1–26, doi:10.1034/j.1600-0870.2001.01073.x.

Emeis, S., 2011: *Surface-Based Remote Sensing of the Atmospheric Boundary Layer*. Atmospheric and Oceanographic Sciences Library, Vol. 40, Springer, 174 pp.

- Fedorovich, E., R. Conzemius, and D. Mironov, 2004: Convective entrainment into a shear-free, linearly stratified atmosphere: Bulk models reevaluated through large eddy simulations. *J. Atmos. Sci.*, **61**, 281–295, doi:10.1175/1520-0469(2004)061<0281:CEIASL>2.0.CO;2.
- Ferrare, R., and Coauthors, 2006: Evaluation of daytime measurements of aerosols and water vapor made by an operational Raman lidar over the Southern Great Plains. *J. Geophys. Res.*, **111**, D05S08, doi:10.1029/2005JD005836.
- Frehlich, R., and L. Cornman, 2002: Estimating spatial velocity statistics with coherent Doppler lidar. *J. Atmos. Oceanic Technol.*, **19**, 355–366, doi:10.1175/1520-0426.19.3.355.
- , S. M. Hannon, and S. W. Henderson, 1998: Coherent Doppler lidar measurements of wind field statistics. *Bound.-Layer Meteorol.*, **86**, 233–256, doi:10.1023/A:1000676021745.
- García, J. R., and J. P. Mellado, 2014: The two-layer structure of the entrainment zone in the convective boundary layer. *J. Atmos. Sci.*, **71**, 1935–1955, doi:10.1175/JAS-D-13-0148.1.
- Giez, A., G. Ehret, R. L. Schwiesow, K. J. Davis, and D. H. Lenschow, 1999: Water vapor flux measurements from ground-based vertically pointed water vapor differential absorption and Doppler lidars. *J. Atmos. Oceanic Technol.*, **16**, 237–250, doi:10.1175/1520-0426(1999)016<0237:WVFMFG>2.0.CO;2.
- Grachev, A. A., C. W. Fairall, and E. F. Bradley, 2000: Convective profile constants revisited. *Bound.-Layer Meteorol.*, **94**, 495–515, doi:10.1023/A:1002452529672.
- Hammann, E., A. Behrendt, F. Le Mouineur, and V. Wulfmeyer, 2015: Temperature profiling of the atmospheric boundary layer with rotational Raman lidar during the HD(CP)² Observational Prototype Experiment. *Atmos. Chem. Phys.*, **15**, 2867–2881, doi:10.5194/acp-15-2867-2015.
- Hechtel, L., C.-H. Moeng, and R. Stull, 1990: Temperature profiling of the atmospheric boundary layer with rotational Raman lidar during the HD(CP)² Observational Prototype Experiment. *J. Atmos. Sci.*, **47**, 1721–1741, doi:10.1175/1520-0469(1990)047<1721:TEONSF>2.0.CO;2.
- Hill, K. A., and G. M. Lackmann, 2009: Analysis of idealized tropical cyclone simulations using the Weather Research and Forecasting Model: Sensitivity to turbulence parameterization and grid spacing. *Mon. Wea. Rev.*, **137**, 745–765, doi:10.1175/2008MWR2220.1.
- Hogan, R. J., A. L. M. Grant, A. J. Illingworth, G. N. Pearson, and E. J. O'Connor, 2009: Vertical velocity variance and skewness in clear and cloud-topped boundary layers as revealed by Doppler lidar. *Quart. J. Roy. Meteor. Soc.*, **135**, 635–643, doi:10.1002/qj.413.
- Hong, S.-Y., Y. Noh, and J. Dudhia, 2006: A new vertical diffusion package with an explicit treatment of entrainment processes. *Mon. Wea. Rev.*, **134**, 2318–2341, doi:10.1175/MWR3199.1.
- Jiménez, P. A., J. Dudhia, J. F. González-Rouco, J. Navarro, J. P. Montávez, and E. García-Bustamante, 2012: A revised scheme for the WRF surface layer formulation. *Mon. Wea. Rev.*, **140**, 898–918, doi:10.1175/MWR-D-11-00056.1.
- Kalthoff, N., and Coauthors, 2013: Dry and moist convection in the boundary layer over the Black Forest—A combined analysis of in situ and remote sensing data. *Meteor. Z.*, **22**, 445–461, doi:10.1127/0941-2948/2013/0417.
- Kameyama, S., T. Ando, K. Asaka, Y. Hirano, and S. Wadaka, 2007: Compact all-fiber pulsed coherent Doppler lidar system for wind sensing. *Appl. Opt.*, **46**, 1953–1962, doi:10.1364/AO.46.001953.
- Kanda, M., A. Inagaki, M. O. Letzel, S. Raasch, and T. Watanabe, 2004: LES study of the energy imbalance problem with eddy covariance fluxes. *Bound.-Layer Meteorol.*, **110**, 381–404, doi:10.1023/B:BOUN.0000007225.45548.7a.
- Kiemle, C., G. Ehret, A. Giez, K. Davis, D. Lenschow, and S. P. Oncley, 1997: Estimation of boundary layer humidity fluxes and statistics from airborne differential absorption lidar (DIAL). *J. Geophys. Res.*, **102**, 29 189–29 203, doi:10.1029/97JD01112.
- , and Coauthors, 2007: Latent heat flux profiles from collocated airborne water vapor and wind lidars during IHOP_2002. *J. Atmos. Oceanic Technol.*, **24**, 627–639, doi:10.1175/JTECH1997.1.
- , M. Wirth, A. Fix, S. Rahm, U. Corsmeier, and P. Di Girolamo, 2011: Latent heat flux measurements over complex terrain by airborne water vapour and wind lidars. *Quart. J. Roy. Meteor. Soc.*, **137**, 190–203, doi:10.1002/qj.757.
- Kim, S.-W., S.-U. Park, and C.-H. Moeng, 2003: Entrainment processes in the convective boundary layer with varying wind shear. *Bound.-Layer Meteorol.*, **108**, 221–245, doi:10.1023/A:1024170229293.
- LeMone, M., 2002: Convective boundary layer. *Encyclopedia of Atmospheric Sciences*, 1st ed. J. Holton and J. Curry, Eds., Academic Press, 250–257.
- Lenschow, D. H., J. Mann, and L. Kristensen, 1994: How long is long enough when measuring fluxes and other turbulence statistics? *J. Atmos. Oceanic Technol.*, **11**, 661–673, doi:10.1175/1520-0426(1994)011<0661:HLILEW>2.0.CO;2.
- , V. Wulfmeyer, and C. Senff, 2000: Measuring second-through fourth-order moments in noisy data. *J. Atmos. Oceanic Technol.*, **17**, 1330–1347, doi:10.1175/1520-0426(2000)017<1330:MSTFOM>2.0.CO;2.
- , M. Lothon, S. D. Mayor, P. P. Sullivan, and G. Canut, 2012: A comparison of higher-order vertical velocity moments in the convective boundary layer from lidar with in situ measurements and large-eddy simulation. *Bound.-Layer Meteorol.*, **143**, 107–123, doi:10.1007/s10546-011-9615-3.
- Linné, H., B. Hennemuth, J. Bösenberg, and K. Ertel, 2007: Water vapour flux profiles in the convective boundary layer. *Theor. Appl. Climatol.*, **87**, 201–211, doi:10.1007/s00704-005-0191-7.
- Löhnert, U., D. D. Turner, and S. Crewell, 2009: Ground-based temperature and humidity profiling using spectral infrared and microwave observations. Part I: Simulated retrieval performance in clear-sky conditions. *J. Appl. Meteor. Climatol.*, **48**, 1017–1032, doi:10.1175/2008JAMC2060.1.
- Lothon, M., D. H. Lenschow, and S. D. Mayor, 2006: Coherence and scale of vertical velocity in the convective boundary layer from a Doppler lidar. *Bound.-Layer Meteorol.*, **121**, 521–536, doi:10.1007/s10546-006-9077-1.
- , —, and —, 2009: Doppler lidar measurements of vertical velocity spectra in the convective planetary boundary layer. *Bound.-Layer Meteorol.*, **132**, 205–226, doi:10.1007/s10546-009-9398-y.
- Maronga, B., and S. Raasch, 2013: Large-eddy simulations of surface heterogeneity effects on the convective boundary layer during the LITFASS-2003 experiment. *Bound.-Layer Meteorol.*, **146**, 17–44, doi:10.1007/s10546-012-9748-z.
- Mather, J. H., and J. W. Voyles, 2013: The ARM Climate Research Facility: A review of structure and capabilities. *Bull. Amer. Meteor. Soc.*, **94**, 377–392, doi:10.1175/BAMS-D-11-00218.1.
- Matuura, M., Y. Masuda, H. Inuki, S. Kato, S. Fukao, T. Sato, and T. Tsuda, 1986: Radio acoustic measurement of temperature profile in the troposphere and stratosphere. *Nature*, **323**, 426–428, doi:10.1038/323426a0.
- Mead, J., G. Hopcraft, S. Frasier, B. Pollard, C. Cherry, D. Schaubert, and R. McIntosh, 1998: A volume-imaging radar wind profiler for atmospheric boundary layer turbulence studies.

- J. Atmos. Oceanic Technol.*, **15**, 849–859, doi:10.1175/1520-0426(1998)015<0849:AVIRWP>2.0.CO;2.
- Milovac, J., K. Warrach-Sagi, J. Ingwersen, A. Behrendt, F. Späth, V. Wulfmeyer, and H. D. Wizemann, 2014: Sensitivity of the WRF model to boundary layer and land surface parameterizations: Comparisons with differential absorption lidar and eddy covariance measurements. *21st Symp. on Boundary Layers and Turbulence*, Leeds, United Kingdom, Amer. Meteor. Soc., 26. [Available online at <https://ams.confex.com/ams/21BLT/webprogram/Paper248146.html>.]
- Moeng, C.-H., and P. P. Sullivan, 1994: A comparison of shear- and buoyancy-driven planetary boundary layer flows. *J. Atmos. Sci.*, **51**, 999–1022, doi:10.1175/1520-0469(1994)051<0999:ACOSAB>2.0.CO;2.
- Monin, A. S., and A. Yaglom, 1975: *Statistical Fluid Mechanics*. Vol. 2, *Mechanics of Turbulence*, MIT Press, 896 pp.
- Muppa, S. K., A. Behrendt, F. Späth, V. Wulfmeyer, S. Metzendorf, and A. Riede, 2015: Turbulent humidity fluctuations in the convective boundary layer: Case studies using water vapour differential absorption lidar measurements. *Bound.-Layer Meteor.*, doi:10.1007/s10546-015-0078-9, in press.
- Muschinski, A., and P. Sullivan, 2013: Using large-eddy simulation to investigate intermittency fluxes of clear-air radar reflectivity in the atmospheric boundary layer. *Proc. Antennas and Propagation Society Int. Symp. (APSURSI)*, Orlando, FL, IEEE, 2321–2322, doi:10.1109/APS.2013.6711819.
- Noh, Y., W. G. Cheon, S. Y. Hong, and S. Raasch, 2003: Improvement of the K-profile model for the planetary boundary layer based on large eddy simulation data. *Bound.-Layer Meteor.*, **107**, 401–427, doi:10.1023/A:1022146015946.
- Pal, S., A. Behrendt, and V. Wulfmeyer, 2010: Elastic-backscatter-lidar-based characterization of the convective boundary layer and investigation of related statistics. *Ann. Geophys.*, **28**, 825–847, doi:10.5194/angeo-28-825-2010.
- Park, S., and C. S. Bretherton, 2009: The University of Washington shallow convection and moist turbulence schemes and their impact on climate simulations with the Community Atmosphere Model. *J. Climate*, **22**, 3449–3469, doi:10.1175/2008JCLI2557.1.
- Philippov, V., C. Codemard, Y. Jeong, C. Alegria, J. K. Sahu, J. Nilsson, and G. N. Pearson, 2004: High-energy in-fibre pulse amplification for coherent lidar applications. *Opt. Lett.*, **29**, 2590–2592, doi:10.1364/OL.29.002590.
- Poulos, G. S., and Coauthors, 2002: CASES-99: A comprehensive investigation of the stable nocturnal boundary layer. *Bull. Amer. Meteor. Soc.*, **83**, 555–581, doi:10.1175/1520-0477(2002)083<0555:CACTOT>2.3.CO;2.
- Saito, K., and Coauthors, 2013: Super high-resolution mesoscale weather prediction. *J. Phys.: Conf. Ser.*, **454**, 012073, doi:10.1088/1742-6596/454/1/012073.
- Samuelsson, P., and Coauthors, 2011: The Rossby Centre Regional Climate model RCA3: Model description and performance. *Tellus*, **63A**, 4–23, doi:10.1111/j.1600-0870.2010.00478.x.
- Senff, C., J. Bösenberg, and G. Peters, 1994: Measurement of water vapor flux profiles in the convective boundary layer with lidar and radar-RASS. *J. Atmos. Oceanic Technol.*, **11**, 85–93, doi:10.1175/1520-0426(1994)011<0085:MOWVFP>2.0.CO;2.
- Sorbjan, Z., 1996: Effects caused by varying the strength of the capping inversion based on a large eddy simulation model of the shear-free convective boundary layer. *J. Atmos. Sci.*, **53**, 2015–2024, doi:10.1175/1520-0469(1996)053<2015:ECBVTS>2.0.CO;2.
- , 2001: An evaluation of local similarity on the top of the mixed layer based on large-eddy simulations. *Bound.-Layer Meteor.*, **101**, 183–207, doi:10.1023/A:1019260632125.
- , 2005: Statistics of scalar fields in the atmospheric boundary layer based on large-eddy simulations. Part I: Free convection. *Bound.-Layer Meteor.*, **116**, 467–486, doi:10.1007/s10546-005-0907-3.
- , 2006: Statistics of scalar fields in the atmospheric boundary layer based on large-eddy simulations. Part II: Forced convection. *Bound.-Layer Meteor.*, **119**, 57–79, doi:10.1007/s10546-005-9014-8.
- , 2009: Improving non-local parameterization of the convective boundary layer. *Bound.-Layer Meteor.*, **130**, 57–69, doi:10.1007/s10546-008-9331-9.
- Späth, F., A. Behrendt, S. K. Muppa, S. Metzendorf, A. Riede, and V. Wulfmeyer, 2014: High-resolution atmospheric water vapor measurements with a scanning differential absorption lidar. *Atmos. Chem. Phys. Discuss.*, **14**, 29 057–29 099, doi:10.5194/acpd-14-29057-2014.
- Spuler, S. M., K. S. Repasky, B. Morley, D. Moen, M. Hayman, and A. R. Nehrir, 2015: Field-deployable diode-laser-based differential absorption lidar (DIAL) for profiling water vapor. *Atmos. Meas. Tech.*, **8**, 1073–1087, doi:10.5194/amt-8-1073-2015.
- Stull, R. B., 1988: *An Introduction to Boundary Layer Meteorology*. Atmospheric and Oceanographic Sciences Library, Vol. 13, Springer, 670 pp.
- Sullivan, P. P., C.-H. Moeng, B. Stevens, D. H. Lenschow, and S. D. Mayor, 1998: Structure of the entrainment zone capping the convective atmospheric boundary layer. *J. Atmos. Sci.*, **55**, 3042–3064, doi:10.1175/1520-0469(1998)055<3042:SOTEZC>2.0.CO;2.
- Tatarski, V. I., 1961: *Wave Propagation in a Turbulent Medium*. McGraw-Hill, 285 pp.
- Träumner, K., C. Kottmeier, U. Corsmeier, and A. Wieser, 2011: Convective boundary-layer entrainment: Short review and progress using Doppler lidar. *Bound.-Layer Meteor.*, **141**, 369–391, doi:10.1007/s10546-011-9657-6.
- Tsuda, T., M. Miyamoto, and J. Furumoto, 2001: Estimation of a humidity profile using turbulence echo characteristics. *J. Atmos. Oceanic Technol.*, **18**, 1214–1222, doi:10.1175/1520-0426(2001)018<1214:EOAHPU>2.0.CO;2.
- Tucker, S. C., W. A. Brewer, R. M. Banta, C. Senff, S. P. Sandberg, D. C. Law, A. M. Weickmann, and R. M. Hardesty, 2009: Doppler lidar estimation of mixing height using turbulence, shear, and aerosol profiles. *J. Atmos. Oceanic Technol.*, **26**, 673–688, doi:10.1175/2008JTECHA1157.1.
- Turner, D. D., and J. E. M. Goldsmith, 1999: Twenty-four-hour Raman lidar water vapor measurements during the Atmospheric Radiation Measurement Program's 1996 and 1997 water vapor intensive observation periods. *J. Atmos. Oceanic Technol.*, **16**, 1062–1076, doi:10.1175/1520-0426(1999)016<1062:TFHRLW>2.0.CO;2.
- , and U. Löhnert, 2014: Information content and uncertainties in thermodynamic profiles and liquid cloud properties retrieved from the ground-based Atmospheric Emitted Radiance Interferometer (AERI). *J. Appl. Meteor. Climatol.*, **53**, 752–771, doi:10.1175/JAMC-D-13-0126.1.
- , R. A. Ferrare, L. A. Heilman Brasseur, W. F. Feltz, and T. P. Tooman, 2002: Automated retrievals of water vapor and aerosol profiles over Oklahoma from an operational Raman lidar. *J. Atmos. Oceanic Technol.*, **19**, 37–50, doi:10.1175/1520-0426(2002)019<0037:AROWVA>2.0.CO;2.
- , —, V. Wulfmeyer, and A. J. Scarino, 2014a: Aircraft evaluation of ground-based Raman lidar water vapor turbulence profiles in convective mixed layers. *J. Atmos. Oceanic Technol.*, **31**, 1078–1088, doi:10.1175/JTECH-D-13-00075.1.
- , V. Wulfmeyer, L. K. Berg, and J. H. Schween, 2014b: Water vapor turbulence profiles in stationary continental convective

- mixed layers. *J. Geophys. Res. Atmos.*, **119**, 11 151–11 165, doi:10.1002/2014JD022202.
- Van Zanten, M. C., P. G. Duynkerke, and J. W. M. Cuijpers, 1999: Entrainment parameterization in convective boundary layers. *J. Atmos. Sci.*, **56**, 813–828, doi:10.1175/1520-0469(1999)056<0813:EPICBL>2.0.CO;2.
- Waggy, S. B., S. Biringen, and P. Sullivan, 2013: Direct numerical simulation of top-down and bottom-up diffusion in the convective boundary layer. *J. Fluid Mech.*, **724**, 581–606, doi:10.1017/jfm.2013.130.
- Wulfmeyer, V., 1999a: Investigation of turbulent processes in the lower troposphere with water vapor DIAL and radar-RASS. *J. Atmos. Sci.*, **56**, 1055–1076, doi:10.1175/1520-0469(1999)056<1055:TOTPIT>2.0.CO;2.
- , 1999b: Investigations of humidity skewness and variance profiles in the convective boundary layer and comparison of the latter with large eddy simulation results. *J. Atmos. Sci.*, **56**, 1077–1087, doi:10.1175/1520-0469(1999)056<1077:IOHSAV>2.0.CO;2.
- , and T. Janjić, 2005: Twenty-four-hour observations of the marine boundary layer using shipborne NOAA high-resolution Doppler lidar. *J. Appl. Meteor.*, **44**, 1723–1744, doi:10.1175/JAM2296.1.
- , and Coauthors, 2008: The Convective and Orographically Induced Precipitation Study: A research and development project of the World Weather Research Program for improving quantitative precipitation forecasting in low-mountain regions. *Bull. Amer. Meteor. Soc.*, **89**, 1477–1486, doi:10.1175/2008BAMS2367.1.
- , S. Pal, D. D. Turner, and E. Wagner, 2010: Can water vapour Raman lidar resolve profiles of turbulent variables in the convective boundary layer? *Bound.-Layer Meteor.*, **136**, 253–284, doi:10.1007/s10546-010-9494-z.
- , and Coauthors, 2011: The Convective and Orographically-induced Precipitation Study (COPS): The scientific strategy, the field phase, and first highlights. *Quart. J. Roy. Meteor. Soc.*, **137**, 3–30, doi:10.1002/qj.752.
- , and Coauthors, 2015a: A review of the remote sensing of lower tropospheric thermodynamic profiles and its indispensable role for the understanding and the simulation of water and energy cycles. *Rev. Geophys.*, **53**, 819–895, doi:10.1002/2014RG000476.
- , and Coauthors, 2015b: New concepts for studying land-surface-atmosphere feedback based on a new lidar synergy and grey zone simulations. *Geophysical Research Abstracts*, Vol. 17, Abstract EGU2015-5054. [Available online at <http://meetingorganizer.copernicus.org/EGU2015/EGU2015-5054.pdf>.]
- Wyngaard, J. C., and R. A. Brost, 1984: Top-down and bottom-up diffusion of a scalar in the convective boundary layer. *J. Atmos. Sci.*, **41**, 102–112, doi:10.1175/1520-0469(1984)041<0102:TDABUD>2.0.CO;2.
- Xie, B., J. C. H. Fung, A. Chan, and A. Lau, 2012: Evaluation of nonlocal and local planetary boundary layer schemes in the WRF model. *J. Geophys. Res.*, **117**, D12103, doi:10.1029/2011JD017080.
- Zehe, E., and Coauthors, 2014: From response units to functional units: A thermodynamic reinterpretation of the HRU concept to link spatial organization and functioning of intermediate scale catchments. *Hydrol. Earth Syst. Sci.*, **18**, 4635–4655, doi:10.5194/hess-18-4635-2014.
- Zhou, M. Y., D. H. Lenschow, B. B. Stankov, J. C. Kaimal, and J. E. Gaynor, 1985: Wave and turbulence structure in a shallow baroclinic convective boundary layer and overlying inversion. *J. Atmos. Sci.*, **42**, 47–57, doi:10.1175/1520-0469(1985)042<0047:WATSIA>2.0.CO;2.

Chapter 6 Measurement of surface layer temperature gradients

In atmospheric models the planetary boundary layer is mostly not simulated in detail due to processing time. To describe the processes in the PBL, the grid size of a typical weather forecast model mentioned in [121] of several kilometers is too large. One solution are LES (Large Eddy Simulations) runs with higher resolution, in other cases the boundary layer is treated with parametrizations and assumptions. If simulations are performed with high resolution, also the surface conditions including orography and vegetation cover are needed as input.

6.1 Surface flux theory

Main energy source of the Earth is the sun. Depending on surface cover and soil moisture some of the sun energy will lead to evapotranspiration, evaporation of soil moisture and transpiration of the vegetation. This source of humidity is especially important during summer (growing vegetation) after rain (water availability). One part of the energy is heating the upper soil layers. In principle, the energy balance between incoming net radiation from the sun and the atmospheric and soil fluxes should be closed in case of no advection, but measurements with Eddy-Covariance (EC) stations show an energy gap, which is not completely understood yet [38, 42, 43]. Measurement of fluxes in the atmosphere is quite challenging. Sensible heat flux can be derived with temperature profiles from Raman lidar or estimated from ground measurements in combination with a

Doppler lidar [27]. Some approaches in measuring latent heat fluxes were already done [33, 25, 32, 26].

Whereas the two campaigns in 2013 were focused on vertical profiling of the boundary layer to derive entrainment fluxes, the surface fluxes were of main interest during the SABLE campaign. Surface to atmosphere exchange processes are important for the modeling of small scale processes. Land use can influence the surface fluxes immensely. Whereas the latent heat flux will be the main energy flux above vegetation (if there is enough humidity), sensible heat flux has more influence over a bare surface or in case of drought. Therefore also the properties of the surface and even the upper soil level have to be taken into account in studies of the boundary layer. In the research unit ‘Regionaler Klimawandel’ the link between atmosphere properties, crops and soil is studied with additional focus on climate change and its consequences on farming. It is also studied how farming influences the regional climate by growing certain crops. To assist the model evaluation, measurements of surface fluxes over different surfaces in combination with knowledge of the entrainment fluxes were performed. Several EC stations were placed in two different regions of Baden-Württemberg, near Nellingen (Swabian Alb, rough climate) and near Pforzheim (Kraichgau, mild climate). Differences in the surface fluxes between certain crops could be recorded [117]. These efforts were accompanied by a campaign with lidars performed in August 2014. Additional to the RRL and the DIAL of UHOH, also a CO₂-DIAL [47, 45] and Doppler lidar from LMD (Parisienne, France), a Doppler lidar from KIT Garmisch-Partenkirchen (HALO) and a Doppler-Lidar from Leosphere participated. Derivation of surface fluxes uses the roughness wind speed u_* [60]. Therefore the Doppler lidars were positioned so that their line of sights could intersect and a full data set was achieved. RRL and DIAL scanned the surface layer with low elevation (0-12°) over one of the EC-stations and the line of sight of the Doppler lidars intersected this line up to 7 times. Because both surface and entrainment fluxes had to be measured, scanning and vertical measurements were alternated every hour and radiosondes started within the vertical measurement periods (see measurement plan in Appendix B.3).

During the HOPE campaign the two positions for the highJ filter

were experimentally characterized. Simulations showed that for the RRL the signal to noise ratio is high enough in the lowest 2 km to measure also at daytime with the so called low background configuration. This was realized during the whole measurement period of SABLE except of SOP1, when clear sky measurement with both configurations and the new lowJ filter were performed.

6.2 Low level scans

The scan pattern of the RRL was initiated like following: The azimuth angle was chosen in direction to the EC station EC1. As the station was in a maize field and too narrow to be in the line of sight of the lidars, a tower on a near hill was used as reference and the scan direction determined as an angular deviation from the tower. With this method it could be realized that the four participating lidars were directed correctly. RHI (Range-Height-Indicator) scans were performed with 0.2° steps from 0° to 12° (61 steps in total) and 480 shots per direction. The angle range was chosen to reach 100 m altitude above ground in around 500 m distance. With this scan pattern it was possible to acquire 6 complete scans in one hour, which resulted in one minute integrated profiles per elevation angle. Unfortunately it was not possible to measure with the same azimuth angle vertically, as wires of a power line were in the outgoing beam, resulting in severe power losses (signal intensity reduced by 30%). Therefore the scanner had to be positioned at another azimuth angle for vertical measurements.

Low level scans were performed every other hour on all IOP days. In the following two examples are shown, from the 12 August 2014 and the 19 August 2014. It is expected that the temperature will decrease slowly with altitude if no inversion is present [94]. The case from 12 August 2014 is such an ideal case. On 19 August a case with a inversion in 40 meters altitude was recorded. This was also confirmed by a radio sounding.

To achieve a better representativeness of the results, several scan steps were fused together to get a coarser angle resolution. After calculation of temperature (including gliding average, overlap cor-

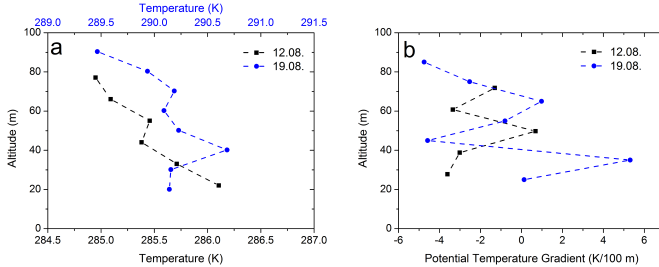


Figure 6.1: (a) Surface temperature profiles derived from low elevation measurements. Data from 12 and 19 August 2014, 11-12 UTC, details can be found in the text. (b) Potential temperature gradient from the profiles shown in (a).

rection) the data was arranged in a grid with 50 m grid size in horizontal direction (x). This is sufficient to resolve the different surface types, in our case maize, bare soil and forest. In y -direction, vertical to the ground, a finer resolution is required. A fit to the values is the input in the equations for deriving the surface flux with Monin-Obukhov theory [75, 34, 26, 21, 60]. Therefore a resolution between 10 and 15 m seems reasonable. For further analysis several grid boxes in x -direction can be averaged. For the surface temperature profiles shown in Fig. 6.1a, the grid in x -direction was 50 m and in y -direction 11 m. Data were from 12 August, 11-12 UTC in the distance between 500 and 600 m and from 19 August, same time and distance. Data below 30 m were erroneous due to a slight increase of ground level in scan direction, which reached 20 m in 800 m distance. In this time of the year the maize was fully grown and had a height of 3-4 m depending on the exact location. For comparison the respective potential temperature gradients are shown in Fig. 6.1b. Here the inversion in the second case results in positive values. At around 70 m above ground the temperature seems to stagnate or rather follows an adiabatic gradient like expected in a well mixed boundary layer. That point is interpreted as the upper border of the surface layer and determination of the sensible heat flux has to be done below this level.

In comparison with the low level measurement shown in [53], it is possible to evaluate the profile for different land uses as the range in-

formation (distance to lidar) is not lost. That measurement resolved an inversion on top of nocturnal boundary layer while here the day time boundary layer is sampled. There were no cloud-free IOPs during SABLE, therefore the cases cannot be classified as perfect convection cases. During 19 August an inversion could be observed till 15 UTC. For further evaluation u_* has to be known, which is currently not the case. With u_* it would be possible to derive the surface sensible heat flux. As the prominent weather situation was cool and humid, the EC station measurements of sensible heat fluxes showed untypical low values for August. Measured sensible heat fluxes were in the range of 100 to 150 W/m² while the latent heat flux was approximately two times higher. It is therefore challenging to measure these small fluxes with a new technique. Further analysis will show if the sensible heat flux can be derived or if the measurements method has to be refined in respect to scan steps and time per direction.

Chapter 7 Discussions

7.1 Comparison between the performance in the years 2007 and 2014

A direct comparison of the measurement performance was difficult as the count rates and statistical errors are also influenced by the atmospheric conditions. The laser power was not constant over time and the power values were not logged, therefore only an estimation of the improvements are possible. Table 7.1 shows a comparison between the system parameters in 2007 [81] and the subsequently improved system.

For single update-steps comparison were made e.g. the introduction of the background switch in [53]. In further steps the new lowJ filter was implemented. The implementation took more than one hour, therefore immediate comparisons between both filters were not manageable. In the strength of the raw signal an enhancement from 568 counts (in range bin 300) to 792 counts could be observed. It results in an reduction of the statistical error of 20% for similar atmospheric conditions. The resulting difference in the statistical error provided by the exchange of IF2 and the switching of IF3 are presented in Fig. 7.1.

	COPS (2007)	HOPE (2013)	SABLE (2014)
Laser Power	9 W	10 W	10 W
Dichroic mirror replaced	-	-	+
PMT power supply exchange	-	+	+
Water vapor channel	-	-/+	+
LowJ transmission	0.34	0.34	0.52
HighJ switch	-	+	+
LICEL updated	-	-	+

Table 7.1: System parameters 2007, 2013 and 2014. In red before improvement, in yellow ambiguous states and in green the improved characteristics.

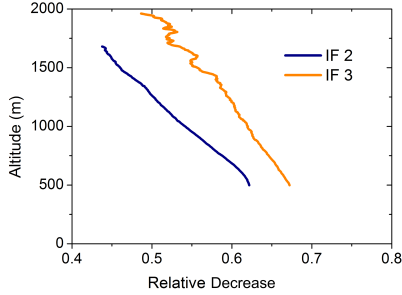


Figure 7.1: Improvement of the relative error due to the filter exchange (IF2) and use of alternative filter passband (IF3)[55].

7.2 Outline of possible further technical improvements

7.2.1 Increase of laser power

In chapter 3 the recent upgrades of the system are described with the main focus on the detection. Another possibility for improvements would be the laser source. The statistical noise error ΔT_{stat} is given by

$$\Delta T_{stat} = \frac{\delta T(Q)}{\delta Q} \Delta Q = \frac{\delta T(Q)}{\delta Q} Q \sqrt{\frac{P_{lowJ} + P_{B1}}{P_{lowJ}^2} + \frac{P_{highJ} + P_{B2}}{P_{highJ}^2}}, \quad (7.1)$$

with P_{lowJ} and P_{highJ} the background-corrected signal counts in the respective channels and Q the ratio between them. P_B is the background count rate, respectively. If the signal count rate is much higher than the background count rate, ΔT_{stat} is proportional to the inversion of $\sqrt{P_{\lambda_0}}$. This relation is only valid if the repetition rate is preserved. In the exact derivation, the amount of background is crucial especially if signal and background are in the same order of magnitude, which will certainly be the case in altitudes above a few kilometers in daytime. An increase of the repetition rate also increases the background count rate by the same factor. Therefore an improvement of the average laser power should be examined in

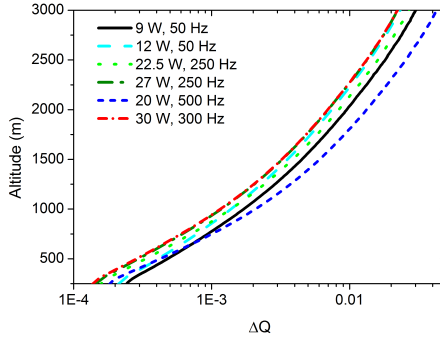


Figure 7.2: Comparison of the ΔQ of the current laser performance (9 W, 50 Hz) in black and other power/frequency combinations. In low altitudes the laser power is the dominating indicator, with increasing altitude the pulse frequency becomes more significant. Background counts from 19 May 2013, 11 UTC, count rates simulated from measurements during this time period with the GCR290-50.

respect to both parameters.

It was discussed to implement another laser source with 250 Hz repetition rate into the system, therefore a simulation regarding the minimal power at a higher repetition rate to conserve the measurement performance at daytime was performed. Data from 19 May 2013 at 11 UTC was used to have realistic daylight background. In Fig. 7.2 the ΔQ of several repetition rates and power combinations are shown. The statistical error was calculated by scaling the factors to the actual measured signal strength. The count rates were acquired with a 9 W and 50 Hz laser source. In lower altitudes with a high signal to noise ratio the relative error is determined by the laser power. Depending on the background, higher repetition rates and therefore higher background counts counteract the primary laser power. As can be seen the relative error of 12 W and 50 Hz follows the lines of combinations with significant higher laser power (27 W, 250 Hz), while the (22.5 W, 250 Hz) combination is in between the (9 W, 50 Hz) and the other mentioned. The combination (20 W, 500 Hz) only decreases ΔQ for altitudes below 700 m. The exact

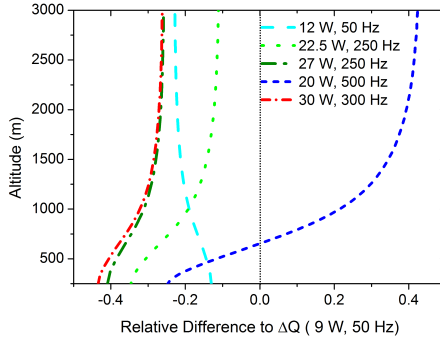


Figure 7.3: Relative difference to (9 W, 50 Hz) statistical error of the simulated power-frequency combinations shown in Fig. 7.2.

altitudes, where these intersections occur, are related to the solar background and the temperature range.

In Fig. 7.3 the relative difference in ΔQ is shown. The corresponding difference of ΔT_{stat} is proportional to the relative difference of ΔQ (see Eq. 7.1). It seems that each line converges to a constant value, which is not strictly correlated to the power or the pulse energy of the laser. In conclusion, to estimate the improvement of the statistical error by implementation of a new laser, not only the power, but also the repetition rate should be taken into account. This is especially important for daytime measurements, for nighttime measurements the stronger laser power is in every case advantageous.

7.2.2 Detection

Concerning the detection the biggest issue is the temperature stability of the laboratory. In theory the interference filters show only a small temperature sensitivity [81], but they seem to have deteriorated as the calibration parameter changes slightly during the diurnal circle. This could be caused by the varying temperature in the truck.

It has to be seen if manufacturers succeed in the future to produce

interference filters for UV wavelengths with even higher transmission and blocking capabilities and increase the quantum efficiency of photomultipliers. Concerning the further development of interference filter, we found already enhanced products like the new filter (see section 3.2.2). In case of photomultiplier, it seems that the development is stagnating.

7.2.3 Additional wavelengths

In the moment only the third harmonic of the Nd:YAG is transmitted to the atmosphere and the emission of the other two wavelengths is dumped. Future additions could include also the transmission and detection of 532 nm or 1064 nm. The laser emits these wavelengths already and in the detection a beam splitter would not decrease the measurement performance in the UV significantly. It has to be taken into account, that in this case it is necessary to adapt the beam expanding optics to avoid chromatic effects and take care of the changed eye safety issues.

A detection of other wavelengths would make it possible to extract additional information about aerosol particles [29][76]. An improvement in temperature measurements is not to be expected as long as the results are not combined after data analysis. As alternative during night time it should be possible to use the elastic backscatter from 532 nm to derive additional temperature profiles using the inversion method (see section 2.2).

Chapter 8 Summary and outlook

The RRL of UHOH was modified in several aspects since the COPS campaign. The modifications improved the temperature measurement performance and also included the addition of a water vapor mixing ratio measurement channel [53]. The higher measurement performance could be realized with a better signal to noise ratio and a corresponding lower statistical error. Modifications like the redesign of the polychromator made it possible to derive first time temperature profiles with a sufficient temporal and vertical resolution for the derivation of higher order moments of temperature [17]. Additionally, complete diurnal circles of temperature and water vapor mixing ratio were measured. For that purpose also the nighttime performance of the system was important and a switch was implemented [53], which optimized the passband shift regarding the background. With this second configuration, the statistical error of nighttime measurements was decreased up to 70% due to the higher sensitivity. The disadvantage of this configuration is the lower signal intensity due to the application of rotational Raman lines with higher J values, which limits the usability of the configuration at daytime. It is only recommended to use in daytime, if the measurement focus is on the first few kilometers in altitude where the signal intensity is significantly higher than the background values. With these considerations, it was decided to measure during the SABLE campaign with the low background configuration.

A new interference filter in the first Raman channel made it possible to derive profiles in a cloudy boundary layer [55]. This filter has a suppression of the elastic backscatter of more than 10^6 with a peak transmission of 52%, which is superior to the former combination of

two filters with a final peak transmission of 34% and the required blocking of six orders of magnitude.

The system was part of three measurement campaigns and more than 300 hours of data is available. Most of the measurements are vertical profiles, but especially during the SABLE campaign scanning measurements were performed.

After exact characterization of the laser wavelength the optimum passbands for temperature measurements were determined for the temperature range 270 to 300 K and for day- and nighttime solar background, respectively. The next step was the generalization of the simulation for arbitrary wavelengths and a parametrization in respect to temperature range and signal to background ratio [52]. It was found that the optimum passbands are almost independent on the filter passband curve and that the two already mentioned parameters are sufficient to describe the passband shift with less than 2% deviation to the exact simulation. With a linear dependency on temperature and an exponential dependency on the background level, the results can easily be transferred to other systems. It has to be mentioned, that the relations are given not only for the optimum passband combination, but also for a combination with a relative uncertainty of 120% of the optimum. This combination does not suffer from probable leakage of elastic backscatter into the filter passband next to the excitation wavelength. The shift of the optimum passband is too small to guarantee the needed optical blocking of up to 10^6 in case of additional particle scattering.

High-resolution measurements of temperature and water vapor mixing ratio were used to derive variance profiles and profiles of higher order moments. In case of temperature variance it were the first variance profiles derived from lidar data. Temperature profiles from scanning measurements were used to derive surface layer temperature gradients. Temperature profiles were assimilated into WRF to show the impact on the model. Sensible heat fluxes in the boundary layer were derived.

Next steps would be the overall stabilization of the system. The detection needs to be temperature stabilized as the transmission properties of the interference filters are temperature and humidity sensitive. This could be the cause for unstable calibration values

and has to be solved if the system should measure unattended. Additional detection channels for polarization measurements or other Nd:YAG harmonics are possible but not implemented yet as the research focus is on temperature and moisture and not on aerosols. Improvements are not limited to technical aspects but also include measurement scenarios and modes. Of high interest are profiles of the lower boundary layer especially in the transition phases at sunset and sunrise. There is also a big interest in surface layer measurements for which the scan modes should be optimized. In general, all measurements up-to-date faced special conditions like being near a coal pit (HOPE), unusual cool and humid for the season (SABLE) and it is therefore suggested to repeat the measurements over homogenous surface in highly convective weather conditions. This should provide measurements which compare better to theoretical approaches based on idealized cases.

The available data sets were used in several publications, but there are far more cases to be analyzed in respect to convective processes and boundary layer meteorology. The possibility to measure temperature and moisture profiles in a temporal resolution suitable for these processes make the system valuable for many purposes, especially in combination with a Doppler lidar, which are nowadays already commercially available. On the other side, when built more stable and compact, the technique is suitable to provide temperature profiles of the boundary layer in a higher temporal resolution on a regular basis. The influence of hourly assimilated profiles was shown in [5, 4] and promises a high impact in the model output. A small automatic system is also suitable for networks and can therefore enhance significantly the data base for weather forecasts.

Bibliography

- [1] ACHTERT, P., KHAPLANOV, M., KHOSRAWI, F., AND GUMBEL, J. Pure rotational-Raman channels of the Esrange lidar for temperature and particle extinction measurements in the troposphere and lower stratosphere. *Atmospheric Measurement Techniques* 6 (2013), 91–98.
- [2] ADAM, M., DEMOZ, B. B., WHITEMAN, D. N., VENABLE, D. D., JOSEPH, E., GAMBACORTA, A., WEI, J., SHEPARD, M. W., MILOSHEVICH, L. M., BARNET, C. D., HERMAN, R. L., FITZGIBBON, J., AND CONNELL, R. Water Vapor Measurements by Howard University Raman Lidar during the WAVES 2006 Campaign. *Journal of Atmospheric and Oceanic Technology* 27 (2009), 42–60.
- [3] ADAM, S. Assimilation von Lidar Temperaturdaten in das WRF-Modell. Master’s thesis, University of Hohenheim, 2014.
- [4] ADAM, S., BEHRENDT, A., SCHWITALLA, T., HAMMANN, E., AND WULFMAYER, V. First Assimilation of Temperature Lidar Data into an NWP Model: Impact on the Simulation of the Temperature Field, Inversion Strength, and PBL Depth. *QJRM*S (2016).
- [5] ADAM, S., SCHWITALLA, T., HAMMANN, E., BEHRENDT, A., AND WULFMAYER, V. First Assimilation of rotational Raman lidar temperature data. In *Proceedings of the 27th ILRC* (2015).
- [6] ALPERS, M., EIXMANN, R., FRICKE-BEGEMANN, C., GERDING, M., , AND HÖFFNER, J. Temperature lidar

- measurements from 1 to 105 km altitude using resonance, Rayleigh, and Rotational Raman scattering. *Atmos. Chem. Phys.* 4 (2004), 793–800.
- [7] ANSMANN, A., AND MÜLLER, D. *in Weitkamp: Lidar - Range-resolved optical remote sensing of the atmosphere.* Springer, 2005, ch. 4.
- [8] APITULEY, A., WILSON, K. M., POTMA, C., VOLTEN, H., AND DE GRAAF, M. Performance assessment and application of Caeli-A high-performance Raman lidar for diurnal profiling of water vapour, aerosols and clouds. In *Proceedings of the 8th International Symposium on Tropospheric Profiling, Delft, Netherlands, 19-23 Oct.* (2009).
- [9] ARNOLD, K. S., AND SHE, C. Y. Metal Fluorescence lidar (light detection and ranging) and the middle atmosphere. *Contemporary Physics* 44, 1 (2003), 35–49.
- [10] AVILA, G., FERNANDEZ, J. M., TEJEDA, G., AND MONTERO, S. The Raman Spectra and cross-sections of H₂O, D₂O, and HDO in the OH/OD-stretching regions. *Journal of Molecular Spectroscopy* 228 (2004), 38–65.
- [11] BALIN, I., SERIKOV, I., BOBROVNIKOV, S., SIMEONOV, V., CALPINI, B., ARSHINOV, Y., AND VAN DEN BERGH, H. Simultaneous measurement of atmospheric temperature, humidity, and aerosol extinction and backscatter coefficients by a combined vibrational-pure-rotational raman lidar. *Applied Physics B* 79 (2004), 775–782.
- [12] BEHRENDT, A. *in Weitkamp: Lidar: Range-Resolved Optical Remote Sensing of the Atmosphere.* Springer, 2005, ch. 10, Temperature Measurements with Lidar.
- [13] BEHRENDT, A., HAMMANN, E., SPÄTH, F., RIEDE, A., METZENDORF, S., AND WULFMAYER, V. Revealing surface layer heterogenities with scanning Water Vapor DIAL and scanning rotational Raman LIDAR. In *Proceedings of the 26th ILRC* (2012).

- [14] BEHRENDT, A., AND NAKAMURA, T. Calculation of the calibration constant of polarization lidar and its dependency on atmospheric temperature. *Opt. Express* 10, 16 (Aug 2002), 805–817.
- [15] BEHRENDT, A., NAKAMURA, T., ONISHI, M., BAUMGART, R., AND TSUDA, T. Combined Raman lidar for the measurement of atmospheric temperature, water vapor, particle extinction coefficient, and particle backscatter coefficient. *Appl. Opt.* 41, 36 (Dec 2002), 7657–7666.
- [16] BEHRENDT, A., AND REICHARDT, J. Atmospheric temperature profiling in the presence of clouds with a pure rotational Raman lidar by use of an interference-filter-based polychromator. *Appl. Opt.* 39, 9 (Mar 2000), 1372–1378.
- [17] BEHRENDT, A., WULFMEYER, V., HAMMANN, E., MUPPA, S. K., AND PAL, S. Profiles of second- to fourth-order moments of turbulent temperature fluctuations in the convective boundary layer: first measurements with rotational Raman lidar. *Atmospheric Chemistry and Physics* 15, 10 (2015), 5485–5500.
- [18] BEHRENDT, A., WULFMEYER, V., HAMMANN, E., MUPPA, S. K., SPÄTH, F., METZENDORF, S., RIEDE, A., KALTHOFF, N., MAURER, V., AND WIESER, A. Atmospheric boundary layer studies with combined temperature rotational Raman lidar, water vapor DIAL and Doppler lidar. In *Proceedings of the 27th ILRC* (2015).
- [19] BÖSENBERG, J., MATTHIAS, V., AND ET AL. EARLINET: A European Aerosol Research Lidar Network to Establish an Aerosol Climatology. *MPI Report 348* (2003).
- [20] BRUTSAERT, W. *Evaporation into the Atmosphere*. D. Reidel Publishing Company, 1982.
- [21] BUSINGER, J. A., WYNGAARD, J. C., IZUMI, Y., AND BRADLEY, E. F. Flux-Profile Relationships in the Atmospheric Surface Layer. *Journal of the Atmospheric Sciences* 28 (1971), 181–189.

- [22] CADEDU, M. P., PECKHAM, G. E., AND GAFFARD, C. The vertical resolution of ground-based microwave radiometers analyzed through a multiresolution wavelet technique. *IEEE Trans. Geosci. Remote Sens.* 40 (2002), 531–540.
- [23] CADET, B., GIRAUD, V., HAEFFELIN, M., KECKHUT, P., RECHOU, A., AND BALDY, S. Improved retrievals of the optical properties of cirrus clouds by a combination of lidar methods. *Appl. Opt.* 44, 9 (Mar 2005), 1726–1734.
- [24] COONEY, J. Measurement of atmospheric temperature profiles by Raman Backscatter. *Journal of Applied Meteorology* 11 (1972), 108–112.
- [25] COOPER, D., EICHINGER, W., KAO, J., HIPPS, L., REISNER, J., SMITH, S., SCHAEFFER, S., AND WILLIAMS, D. Spatial and temporal properties of water vapor and latent energy flux over a riparian canopy. *Agricultural and Forest Meteorology* 105 (2000), 161–183.
- [26] COOPER, D. I., EICHINGER, W. E., ARCHULETA, J., HIPPS, L., NEALE, C. M. U., AND PRUEGE, J. H. An Advanced Method for Deriving Latent Energy Flux from a Scanning Raman Lidar. *Agron. J.* 99 (2007), 272–284.
- [27] DAVIS, J. C., COLLIER, C. G., DAVIES, F., PEARSON, G. N., BURTON, R., AND RUSSEL, A. Doppler lidar observations of sensible heat flux and intercomparisons with a ground-based energy balance station and WRF model output. *Meteorologische Zeitschrift* 18, 2 (2009), 155–162.
- [28] DI GIROLAMO, P., MARCHESE, R., WHITEMAN, D. N., AND DEMOZ, B. B. Rotational Raman lidar measurements of atmospheric temperature in the UV. *Geophysical Research Letter* 31 (2004), L01106.
- [29] DI GIROLAMO, P., SUMMA, D., AND FERRETTI, R. Multiparameter Raman Lidar Measurements for the Characterization of a Dry Stratospheric Intrusion Event. *Journal of Atmospheric and Oceanic Technology* 26 (2009), 1742–1762.

- [30] DI GIROLAMO, P., SUMMA, D., LIN, R.-F., MAESTRI, T., RIZZI, R., AND MASIELLO, G. UV Raman lidar measurements of relative humidity for the characterization of cirrus cloud microphysical properties. *Atmospheric Chemistry and Physics* 9, 22 (2009), 8799–8811.
- [31] DINOEV, T., SIMEONOV, V., ARSHINOV, Y., BOBROVNIKOV, S., RISTORI, P., CALPINI, B., AND M. PARLANGE, H. v. D. B. Raman Lidar for Meteorological Observations, RALMO - Part 1: Instrument description. *Atmospheric Measurement Techniques* 6, 5 (2013), 1329–1346.
- [32] EICHINGER, W., COOPER, D., HIPPS, L., KUSTAS, W., NEALE, C., AND PRUEGER, J. Spatial and temporal variation in evapotranspiration using Raman lidar. *Advances in Water Resources* 29 (2006), 369–381.
- [33] EICHINGER, W., COOPER, D., KAO, J., CHEN, L., HIPPS, L., AND PRUEGER, J. Estimation of spatially distributed latent heat flux over complex terrain from a Raman lidar. *Agricultural and Forest Meteorology* 105 (2000), 145–159.
- [34] EICHINGER, W. E., COOPER, D. I., FORMAN, P. R., GRIEGOS, J., OSBORN, M. A., RICHTER, D., TELLIER, L. L., AND THORNTON, R. The Development of a Scanning Raman Water Vapor Lidar for Boundary Layer and Tropospheric Observations. *Journal of Atmospheric and Oceanic Technology* 16 (1999), 1754–1766.
- [35] ELORANTA, E. E. in *Weitkamp: Lidar: Range-Resolved Optical Remote Sensing of the Atmosphere*. Springer, 2005, ch. 5, High Spectral Resolution Lidar.
- [36] ENDEMANN, M., AND BYER, R. L. Simultaneous remote measurements of atmospheric temperature and humidity using a continuously tunable IR lidar. *Appl. Opt.* 20, 18 (Sep 1981), 3211–3217.
- [37] FIOCCO, G., BENEDETTI-MICHELANGELI, G., MAISCHBERGER, K., AND MADONNA, E. Measurement of Tem-

- perature and Aerosol to Molecule Ratio in the Troposphere by Optical Radar. *Nature Physical Science* 229 (1971), 78–79.
- [38] FOKEN, T. The Energy Balance Closure Problem: An Overview. *Ecological Applications* 18, 6 (2008), 1351–1367.
- [39] FOTH, A., BAARS, H., DI GIROLAMO, P., AND POSPICHAL, B. Water vapour profiles from Raman lidar automatically calibrated by microwave radiometer data during HOPE. *Atmospheric Chemistry and Physics* 15 (2015), 7753–7763.
- [40] FRICKE, K. H., AND ZAHN, U. Mesopause temperatures derived from probing the hyperfine structure of the D₂ resonance line of sodium by lidar. *J. Atmos. Terr. Phys.* 47 (1985), 499–512.
- [41] FROIDEVAUX, M., HIGGINS, C. W., SIMEONOV, V., RISTORI, P., PARDYJAK, E., SERIKOV, I., CALHOUN, R., VAN DEN BERGH, H., AND PARLANGE, M. B. A Raman lidar to measure water vapor in the atmospheric boundary layer. *Advances in Water Resources* 51 (2013), 345–356.
- [42] GAYLER, S., INGWERSEN, J., PRIESACK, E., WOHLING, T., WULFMEYER, V., AND STRECK, T. Assessing the relevance of subsurface processes for the simulation of evapotranspiration and soil moisture dynamics with CLM3.5: comparison with field data and crop model simulations. *Environ. Earth Sci.* 69 (2013), 415–427.
- [43] GAYLER, S., WOHLING, T., GRZESCHIK, M., INGWERSEN, J., WIZEMANN, H.-D., PETRA, H., ATTINGER, S., STRECK, T., AND WULFMEYER, V. Incorporating dynamic root growth enhances the performance of Noah-MP ensemble simulations at two contrasting winter wheat field sites. *Water Res. Res.* 50 (2014), 1337–1356.
- [44] GIANNAKAKI, E., BALIS, D. S., AMIRIDIS, V., AND ZEREFOS, C. Optical properties of different aerosol types: seven years of combined Raman-elastic backscatter lidar measurements in Thessaloniki, Greece. *Atmos. Meas. Tech.* 3 (2010), 569–578.

- [45] GIBERT, F., EDOUART, D., CÉNAC, C., AND LE MOUNIER, F. Lidar reveals CO₂ concentration field anomalies in the atmosphere. In *EGU General Assembly Conference Abstracts* (May 2014), vol. 16 of *EGU General Assembly Conference Abstracts*, p. 2608.
- [46] GIBERT, F., EDOUART, D., CENAC, C., PELLEGRINO, J., MOUNIER, F. L., AND DUMAS, A. 2-mm coherent DIAL for CO₂, H₂O and wind field profiling in the lower atmosphere: Instrumentation and results. In *Proceedings of the 27th ILRC* (2015).
- [47] GIBERT, F., FLAMANT, P., CUESTA, J., AND BRUNEAU, D. Vertical 2- μ m heterodyne differential absorption lidar measurements of mean CO₂ mixing ratio in the troposphere. *J. Atmos. Ocean. Technology* (2008).
- [48] GIBSON, A. J., THOMAS, L., AND BHATTACHARYYA, S. K. Laser observations of the ground-state hyperfine structure of sodium and of temperatures in the upper atmosphere. *Nature* 281 (1979), 131–132.
- [49] GUSTAFSSON, N., CAPALDO, M., ESTRADA, B. O., AND QUIBY, J. *Position paper - requirements of observations for regional NWP*. World Meteorological Organization, 2001.
- [50] HAIR, J. W., CALDWELL, L. M., KRUEGER, D. A., AND SHE, C.-Y. High-Spectral-Resolution Lidar with Iodine-Vapor Filters: Measurement of Atmospheric-State and Aerosol Profiles. *Appl. Opt.* 40, 30 (Oct 2001), 5280–5294.
- [51] HAIR, J. W., HOSTETLER, C. A., COOK, A. L., HARPER, D. B., FERRARE, R. A., MACK, T. L., WELCH, W., IZQUIERDO, L. R., AND HOVIS, F. E. Airborne High Spectral Resolution Lidar for profiling aerosol optical properties. *Appl. Opt.* 47, 36 (Dec 2008), 6734–6752.
- [52] HAMMANN, E., AND BEHRENDT, A. Parametrization of optimum filter passbands for rotational Raman temperature measurements. *Optics Express* 23, 24 (2015), 30766–30782.

- [53] HAMMANN, E., BEHRENDT, A., LE MOUNIER, F., AND WULFMEYER, V. Temperature profiling of the atmospheric boundary layer with rotational Raman lidar during the HD(CP)² Observational Prototype Experiment. *Atmospheric Chemistry and Physics* 15, 5 (2015), 2867–2881.
- [54] HAMMANN, E., BEHRENDT, A., RIEDE, A., GEISLER, A., RADLACH, M., AND WULFMEYER, V. Scanning rotational Raman Lidar with daytime/nighttime optimization switch. In *Proceedings of the 26th ILRC* (2012).
- [55] HAMMANN, E., BEHRENDT, A., AND WULFMEYER, V. Recent upgrades of the rotational Raman lidar of University of Hohenheim for the measurement of temperature profiles in the surface layer. In *Proceedings of the 27th ILRC* (2015).
- [56] HAUCHECORNE, A., AND CHANIN, M.-L. Density and temperature profiles obtained by lidar between 35 and 70 km. *Geophysical Research Letters* 7, 8 (1980), 565–568.
- [57] HAUCHECORNE, A., CHANIN, M. L., KECKHUT, P., AND NEDELJKOVIC, D. LIDAR Monitoring of the Temperature in the Middle and Lower Atmosphere. *Appl. Phys. B* 55 (1992), 29–34.
- [58] HUA, D., UCHIDA, M., AND KOBAYASHI, T. Ultraviolet Rayleigh–Mie lidar for daytime-temperature profiling of the troposphere. *Appl. Opt.* 44, 7 (2005), 1315–1322.
- [59] HUA, D., UCHIDA, M., AND KOBAYASHI, T. Ultraviolet Rayleigh–Mie lidar with Mie-scattering correction by Fabry–Perot etalons for temperature profiling of the troposphere. *Appl. Opt.* 44, 7 (2005), 1305–1314.
- [60] JIMENEZ, P. A., DUDHIA, J., GONZALEZ-RUOCO, J. F., NAVARRO, J., MONTAVEZ, J. P., AND GARCIA-BUSTAMANTE, E. A Revised Scheme for the WRF Surface Layer Formulation. *Monthly Weather Review* 140 (2012), 898–918.

- [61] KALTHOFF, N., ADLER, B., WIESER, A., KOHLER, M., TRÄUMNER, K., HANDWERKER, J., CORSMEIER, U., KHODAYAR, S., LAMBERT, D., KOPMANN, A., KUNKA, N., DICK, G., RAMATSCHI, M., WICKERT, J., AND KOTTMEIER, C. KITcube-a mobile observation platform for convection studies deployed during HyMeX. *Meteorologische Zeitschrift* 6, 22 (2013), 633–647.
- [62] KECKHUT, P., CHANIN, M. L., AND HAUCHECORNE, A. Stratosphere temperature measurement using Raman lidar. *Appl. Opt.* 29, 34 (Dec 1990), 5182–5186.
- [63] KIEHL, J. T., AND TRENBERTH, K. E. Earth’s annual global mean energy budget. *Bull. Am. Meteorol. Soc.* 78 (1997), 197–208.
- [64] KLETT, J. D. Stable analytical inversion solution for processing lidar returns. *Appl. Opt.* 20, 2 (Jan 1981), 211–220.
- [65] KÖPP, F., RAHM, S., AND SMALIKHO, I. Characterization of Aircraft Wake Vortices by 2-micro m Pulsed Doppler Lidar. *Journal of Atmospheric and Oceanic Technology* 21 (2004), 194–206.
- [66] LANDULFO, E., DA SILVA LOPES, F. J., DE ARRUDA MOREIRA, G., MARQUES, M. T. A., OSNEIDE, M., ANTUNA, J. C., ARREDONDO, R. E., RASCADO, J. L. G., ALADOS-ARBOLEDAS, L., BASTIDAS, A., NISPERUZA, D., BEDOYA, A., MUNERA, M., ALEGRIA, D., FORNO, R. N., SANCHEZ, M. F., LAZCANO, O., MONTILLA-ROSETO, E., SILVA, A., JIMENEZ, C., QUEL, E., RISTORI, P., OTERO, L., BARBOSA, H. M., GOUVEIA, D. A., AND BARJA, B. ALINE/LALINET NETWORK STATUS. In *Proceedings of the 27th ILRC* (2015).
- [67] LEBLANC, T., AND MCDERMID, I. S. Accuracy of Raman Lidar water vapor calibration and its applicability to long term measurements. *Applied Optics* 30 (2008), 5592–5603.

- [68] LIU, F., AND YI, F. Lidar-measured atmospheric N₂ vibrational rotational Raman spectra and consequent temperature retrieval. *Optics Express* 23, 22 (2014).
- [69] LIU, Z., CHEN, W., ZHANG, T., HAIR, J., AND SHE, C. An incoherent Doppler lidar for ground-based atmospheric wind profiling. *Appl. Phys. B* 64 (1997), 561–566.
- [70] LÖHNERT, U., TURNER, D. D., AND CREWELL, S. Ground-based temperature and humidity profiling using spectral infrared and microwave observations. Part I: Simulated retrieval performance in clear-sky conditions. *J. Appl. Meteorol. Climatol.* 48 (2009), 1017–1032.
- [71] MAO, J., HUA, D., WANG, Y., GAO, F., AND WANG, L. Accurate temperature profiling of the atmospheric boundary layer using an ultraviolet rotational Raman lidar. *Optic Communications* 282 (2009), 3113–3118.
- [72] MATTIS, I., ANSMANN, A., ALTHAUSEN, D., JAENISCH, V., WANDINGER, U., MÜLLER, D., ARSHINOV, Y. F., BOBROVNIKOV, S. M., AND SERIKOV, I. B. Relative-humidity profiling in the troposphere with a Raman lidar. *Appl. Opt.* 41, 30 (Oct 2002), 6451–6462.
- [73] MEASURES, R. M. *Laser Remote Sensing*. John Wiley, 1984.
- [74] MELFI, S., LAWRENCE, J. D., AND MCCORMICK, M. P. Observation of Raman Scattering By Water Vapor In The Atmosphere. *Applied Physics Letters* 9, 15 (1969).
- [75] MONIN, A., AND OBUKHOV, A. Basic laws of turbulent mixing in the surface layer of the atmosphere. *Tr. Akad. Nauk SSSR Geophys. Inst.* 151, 24 (1954), 163–187.
- [76] MÜLLER, D., WANDINGER, U., ALTHAUSEN, D., MATTIS, I., AND ANSMANN, A. Retrieval of physical particle properties from lidar observations of extinction and backscatter at multiple wavelengths. *Appl. Opt.* 37, 12 (Apr 1998), 2260–2263.

- [77] MUPPA, S. K., BEHRENDT, A., SPÄTH, F., WULFMEYER, V., METZENDORF, S., AND RIEDE, A. Turbulent Humidity Fluctuations in the Convective Boundary Layer: Case Studies Using Water Vapour Differential Absorption Lidar Measurements. *Boundary Layer Meteorology* (2015).
- [78] NEWSOM, R. K., TURNER, D. D., MIELKE, B., CLAYTON, M., FERRARE, R., AND SIVARAMAN, C. Simultaneous analog and photon counting detection for Raman lidar. *Applied Optics* 20 (2009), 3903–3914.
- [79] PAL, S. *A mobile, scanning eye-safe lidar for the study of atmospheric aerosol particles and transport processes in the lower troposphere*. PhD thesis, University of Hohenheim, Stuttgart, 2009.
- [80] PAL, S., BEHRENDT, A., AND WULFMEYER, V. Elastic-backscatter-lidar-based characterization of the convective boundary layer and investigation of related statistics. *Annales Geophys.* 28 (2010), 825–847.
- [81] RADLACH, M. *A scanning eye-safe rotational Raman lidar in the ultraviolet for measurements of tropospheric temperature fields*. PhD thesis, University of Hohenheim, Stuttgart, 2009.
- [82] RADLACH, M., BEHRENDT, A., AND WULFMEYER, V. Scanning rotational Raman lidar at 355 nm for the measurement of tropospheric temperature fields. *Atmospheric Chemistry and Physics* 8, 2 (2008), 159–169.
- [83] RAIMONDI, V., CECCHI, G., PANTANI, L., AND CHIARI, R. Fluorescence lidar monitoring of historical buildings. *Appl. Opt.* 37 (1998), 1089–1098.
- [84] REICHARDT, J., WANDINGER, U., KLEIN, V., MATTIS, I., HILBER, B., AND BEGBIE, R. RAMSES: German Meteorological Service autonomous Raman lidar for water vapor, temperature, aerosol, and cloud measurements. *Appl. Opt.* 51 (2012), 8111–8131.

- [85] SCHOTLAND, R. M. Errors in the Lidar Measurement of Atmospheric Gases by Differential Absorption. *Journal of Applied Meteorology* 13 (1974), 71–77.
- [86] SENFF, C., II, R. A., MAYOR, S., AND ZHAO, Y. Ozone Flux Profiles in the Boundary Layer Observed with an Ozone DIAL/Doppler Lidar Combination. In *Advances in Atmospheric Remote Sensing with Lidar*, A. Ansmann, R. Neuber, P. Rairoux, and U. Wandinger, Eds. Springer Berlin Heidelberg, 1997, pp. 363–366.
- [87] SHE, C. Y. Remote Measurement of atmospheric parameters: new applications of physics with lasers. *Contemporary Physics* 31, 4 (1990), 247–260.
- [88] SHE, C.-Y. Spectral structure of laser light scattering revisited: bandwidths of nonresonant scattering lidars. *Appl. Opt.* 40, 27 (Sep 2001), 4875–4884.
- [89] SHE, C. Y., II, R. J. A., CALDWELL, L. M., AND KRUEGER, D. A. High spectral resolution Rayleigh-Mie Lidar measurement of aerosol and atmospheric profiles. *Opt. Lett.* 17 (1992), 541–543.
- [90] SHERLOCK, V., GARNIER, A., HAUCHECORNE, A., AND KECKHUT, P. Implementation and Validation of a Raman lidar measurement of middle and upper tropospheric water vapor. *Applied Optics* 27 (1999), 5838–5850.
- [91] SHIMIZU, H., LEE, S. A., AND SHE, C. Y. High spectral resolution lidar system with atomic blocking filters for measuring atmospheric parameters. *Applied Optics* 22 (1983), 1373–1381.
- [92] SOBCYK, A. Atmosphärische Wasserdampfmessung mit einem Rotations-Raman Lidar im Rahmen der Messkampagne HOPE, 2013.
- [93] STOKES, G. M., AND SCHWARTZ, S. E. The Atmospheric Radiation Measurement (ARM) Program: Programmatic background and design of the cloud and radiation test bed. *Bull. Am. Meteorol. Soc.* 75 (1994), 1201–1221.

- [94] STULL, R. B. *An Introduction to Boundary Layer Meteorology*. Springer, 1988.
- [95] SU, J., MCCORMICK, M., WU, Y., LEE III, R., LEI, L., LIU, Z., AND LEAVOR, K. Cloud temperature measurement using rotational Raman lidar. *Journal of Quantitative Spectroscopy & Radiative Transfer* 125 (2013), 45–50.
- [96] SVANBERG, S. Fluorescence lidar monitoring of vegetation status. *Phys. Scr. T58* (1995), 79–85.
- [97] THEOPOLD, F. A., AND BÖSENBERG, J. Differential absorption lidar measurements of atmospheric temperature profiles: theory and experiment. *J. Atmos. Ocean. Technol.* 10 (1993), 165–179.
- [98] TRÄUMNER, K., DAMIAN, T., STAWIARSKI, C., AND WIESER, A. Turbulent Structures and Coherence in the Atmospheric Surface Layer. *Boundary Layer Meteorology* 154 (2015), 1–25.
- [99] TURNER, D., FERRARE, R., WULFMAYER, V., AND SCARINO, A. J. Aircraft evaluation of ground-Based Raman lidar water vapor turbulence profiles in convective mixed layers. *Journal of Atmospheric and Oceanic Technologies* 31 (2014), 1078–1088.
- [100] TURNER, D., AND GOLDSMITH, J. Twenty-Four-Hour Raman Lidar Water Vapor Measurements during the Atmospheric Radiation Measurement Program’s 1996 and 1997 Water Vapor Intensive Observation Periods. *Journal of Atmospheric and Oceanic Technologies* 16 (1999), 1062–1076.
- [101] TURNER, D., WULFMAYER, V., BERG, L., AND SCHWEEN, J. Water vapor turbulence profiles in stationary continental convective mixed layers. *Journal of Geophysical Research* 119 (2014).
- [102] VAUGHAN, G., WAREING, D. P., PEPLER, S. J., THOMAS, L., AND MITEV, V. Atmospheric temperature measurements

- made by rotational Raman scattering. *Applied Optics* 32 (1993), 2758–2764.
- [103] VEBERIČ, D. Maximum-likelihood reconstruction of photon returns from simultaneous analog and photon-counting lidar measurements. *Appl. Opt.* 51, 2 (Jan 2012), 139–147.
- [104] VENABLE, D. D., WHITEMAN, D. N., CALHOUN, M. N., DIRISU, A. O., CONNELL, R. M., AND LANDULFO, E. Lamp mapping technique for independent determination of the water vapor mixing ratio calibration factor for a Raman lidar system. *Appl. Opt.* 50, 23 (Aug 2011), 4622–4632.
- [105] VON ZAHN, U., VON COSSART, G., FIEDLER, J., FRICKE, K. H., NELKE, G., BAUMGARTEN, G., REES, D., HAUCHECORNE, A., AND ADOLFSEN, K. The ALOMAR Rayleigh/Mie/Raman lidar: objectives, configuration, and performance. *Ann. Geophysicae* 18 (2000), 815–833.
- [106] WAGNER, G., BEHRENDT, A., WULFMAYER, V., SPÄTH, F., AND SCHILLER, M. High-power Ti:sapphire laser at 820 nm for scanning ground-based water-vapor differential absorption lidar. *Applied Optics* 11, 52 (2013), 2454–2469.
- [107] WALKER, M., VENABLE, D., AND WHITEMAN, D. N. Gluing for Raman lidar systems using the lamp mapping technique. *Appl. Opt.* 53, 36 (Dec 2014), 8535–8543.
- [108] WANG, Y., CAO, X., HE, T., GAO, F., HUA, D., AND ZHAO, M. Observation and analysis of the temperature inversion layer by Raman lidar up to the lower stratosphere. *Applied Optics* 54, 34 (2015), 10079–10088.
- [109] WEIBRING, P., EDNER, H., AND SVANBERG, S. Versatile mobile lidar system for environmental monitoring. *Appl. Opt.* 42, 18 (2003), 3583–3594.
- [110] WEITKAMP, C., Ed. *Lidar:Range-Resolved Optical Remote Sensing of the Atmosphere*. Springer, 2005.

- [111] WHITEMAN, D. N., DEMOZ, B., DI GIROLAMO, P., COMER, J., VESELOVSKII, I., EVANS, K., WANG, Z., SABATINO, D., SCHWEMMER, G., GENTRY, B., LIN, R.-F., BEHRENDT, A., WULFMEYER, V., BROWELL, E., FERRARE, R., ISMAIL, S., AND WANG, J. Raman Lidar Measurements during the International H2O Project. Part II:Case Studies. *J. Atmos. Oceanic Technol.* *23* (2006), 170–183.
- [112] WHITEMAN, D. N., DEMOZ, B., GIROLAMO, P. D., COMER, J., VESELOVSKII, I., EVANS, K., WANG, Z., CADIROLA, M., RUSH, K., SCHWEMMER, G., GENTRY, B., MELFI, S. H., MIELKE, B., VENABLE, D., AND VAN HOVE, T. Raman Lidar Measurements during the International H2O Project. Part I: Instrumentation and Analysis Techniques. *Journal of Atmospheric and Oceanic Technology* *23* (2006), 157–169.
- [113] WHITEMAN, D. N., MELFI, S. H., AND FERRARE, R. A. Raman lidar system for the measurement of water vapor and aerosols in the Earth’s atmosphere. *Applied Optics* *16*, 31 (1992), 3068–3082.
- [114] WHITEMAN, D. N., RUSH, K., RABENHORST, S., WELCH, W., CADIROLA, M., MCINTIRE, G., RUSSO, F., ADAM, M., VENABLE, D., CONNELL, R., VESELOVSKII, I., FORNO, R., MIELKE, B., STEIN, B., LEBLANC, T., MCDERMID, S., AND VÖMEL, H. Airborne and Ground-Based Measurements Using a High-Performance Raman Lidar. *Journal of Atmospheric and Oceanic Technology* *27* (2010), 1781–1800.
- [115] WITSCHAS, B., GU, Z., AND UBACHS, W. Temperature retrieval from Rayleigh-Brillouin scattering profiles measured in air. *Optics Express* *22*, 24 (2014), 29655–29667.
- [116] WITSCHAS, B., LEMMERZ, C., AND REITEBUCH, O. Day-time measurements of atmospheric temperature profiles (2-15 km) by lidar utilizing Rayleigh-Brillouin scattering. *Opt. Lett.* *39*, 7 (2014), 1972–1975.
- [117] WIZEMANN, H. D., INGWERSEN, J., HÖGY, P., WARRACH-SAGI, K., STRECK, T., AND WULFMEYER, V. Three year

- observations of water vapor and energy fluxes over agricultural crops in two regional climates of Southwest, Germany. *Met. Z.* *24*, 1 (2015), 29–59.
- [118] WU, D., WANG, Z., LIU, D., XIE, C., AND WANG, Y. Independent calibration of water vapor Raman lidar by using additional elastic measurements at water vapor Raman wavelength. In *Proceedings of the 27th ILRC* (2015).
- [119] WULFMEYER, V. Investigations of humidity skewness and variance profiles in the convective boundary layer and comparison of the latter with large eddy simulation results. *Journal of Atmospheric Sciences* *56* (1999), 1077–1087.
- [120] WULFMEYER, V., AND BÖSENBERG, J. Ground-based differential absorption lidar for water-vapor profiling: assessment of accuracy, resolution, and meteorological applications. *Applied Optics* *18*, 37 (1998), 3825–3844.
- [121] WULFMEYER, V., HARDESTY, R. M., TURNER, D. D., BEHRENDT, A., CAEDDU, M. P., GIROLAMO, P. D., SCHLÜSSEL, P., BAELEN, J. V., AND ZUS, F. A review of the remote sensing of lower tropospheric thermodynamic profiles and its indispensable role for the understanding and the simulation of water and energy cycles. *Review of Geophysics* *53* (2015).
- [122] WULFMEYER, V., MUPPA, S., BEHRENDT, A., HAMMANN, E., SPÄTH, F., SORBJAN, Z., TURNER, D. D., AND HARDESTY, R. M. Determination of Convective Boundary Layer Entrainment Fluxes, Dissipation Rates, and the Molecular Destruction of Variances: Theoretical Description and a Strategy for its Confirmation with a Novel Lidar System Synergy. *Journal of the Atmospheric Sciences* *73* (2016), 667–692.
- [123] WULFMEYER, V., PAL, S., TURNER, D. D., AND WAGNER, E. Can Water Vapour Raman Lidar Resolve Profiles of Turbulent Variables in the Convective Boundary Layer? *Boundary Layer Meteorology* *136* (2010), 253–284.

List of own publications

Publications as first author

- Hammann et al., *Proceedings of ILRC 26th*, 2012 [54]
- Hammann et al., *Atmos. Chem. Phys.*, 2015 [53]
- Hammann et al., *Proceedings of ILRC 27th*, 2015 [55]
- Hammann and Behrendt, *Opt. Express*, 2015 [52]

Publications as co-author

- Behrendt et al., *Proceedings of ILRC 26th*, 2012 [13]
- Behrendt et al., *Atmos. Chem. Phys.*, 2015 [17]
- Behrendt et al., *Proceedings of ILRC 27th*, 2015 [18]
- Adam et al., *Proceedings of ILRC 27th*, 2015 [5]
- Wulfmeyer et al., *J. Atmos. Sci.*, 2015 [122]
- Adam et al., *QJRMS*, 2016 [4]

List of Figures

3.1	Photograph of the mobile platform of the UHOH RRL. The beam steering unit is dismounted during the transport.	35
3.2	Rotational Raman spectrum including the current filter positions and shapes. Two different positions for the highJ filter (IF3) are realized for different background conditions. The lowJ filter (IF2) as the newest has almost a rectangular transmission pass-band [55].	40
4.1	Range corrected elastic backscattered signal from 19 May 2013, 13:00-13:40 UTC.	43
4.2	On the left side scaled elastic and rotational Raman signals from 19 August 2014 from 10:27 to 10:28 UTC. Right side shows the backscatter ratio. The backscatter ratio exceeds 100 in 1100 m altitude. From the leakage signal and the ratio between elastic and rotational Raman scattering the optical density is estimated.	61

4.3	(a) Profile from 24 September 2013, 20 min profile starting 15:19 UTC. Absolute humidity measurement of the RRL in comparison with the calibration radiosonde and a WV DIAL measurement, 20 min and 154 m resolution. (b) same as (a), but for 22 September 2013 starting 14:04 UTC. Analog data were used, therefore the noise error is not available. For typical error values see next chapter. WV DIAL measurements provided by Florian Späth.	61
4.4	Time series of water vapor mixing ratio on 24 September 2013 with 30 s temporal resolution and 154 m gliding vertical average. The humidity is apparent in the shallow boundary layer and shows only in the late afternoon some turbulent features.	62
4.5	Time series of water vapor mixing ratio on 22 September 2013 with 30 s resolution and 154 m gliding vertical average. A humid layer between 2.0 km and 2.5 km altitude is visible the whole day.	63
5.1	Water vapor mixing ratio time series with 10 s and 154 m gliding average. The time period from 13:00 till 13:40 UTC (19 May 2013) was chosen due to the constant boundary layer height. A z_i of 1075 m was determined for this time period.	84
5.2	Statistical noise determined of a water vapor measurement with 154 m vertical resolution and a data point each 3.75 m. The error of a 10 s was scaled to other temporal averages. The measurement was done at 13 UTC, therefore the solar background is high and smaller noise error values are expected at other times of the day.	84
5.3	Integral scale profiles of temperature measurements between 13:00 and 13:40 UTC (green) and from water vapor measurements between 13:00 and 13:40 UTC (red) and between 15:00 and 16:00 UTC (blue). Error bars represent the sampling error.	85

5.4	(a) Temperature variance profiles for both cases. While between 15:00 and 16:00 UTC (blue) the maximum variance is found at z_i , it is clearly lower at 13:00 to 13:40 UTC (red). (b) Water vapor mixing ratio variance for both time periods with highest values round z_i . Error bars represent the sampling error.	86
5.5	(a) Third order moment of temperature for both time periods. In the red curve the TOM shows a small negative peak at z_i , like expected from the variance profile. Negative values are found below the boundary layer top for the blue curve. Values at z_i are missing due to large error bars. (b) TOM of water vapor mixing ratio with negative values below z_i and positive values in the entrainment zone. Error bars represent the sampling error.	87
5.6	(a) Fourth-order moment of temperature. Values above $0.8 z_i$ are too noisy. (b) FOM of water vapor mixing ratio. Error bars represent the sampling error.	88
6.1	(a) Surface temperature profiles derived from low elevation measurements. Data from 12 and 19 August 2014, 11-12 UTC, details can be found in the text. (b) Potential temperature gradient from the profiles shown in (a).	120
7.1	Improvement of the relative error due to the filter exchange (IF2) and use of alternative filter passband (IF3)[55].	124
7.2	Comparison of the ΔQ of the current laser performance (9 W, 50 Hz) in black and other power/frequency combinations. In low altitudes the laser power is the dominating indicator, with increasing altitude the pulse frequency becomes more significant. Background counts from 19 May 2013, 11 UTC, count rates simulated from measurements during this time period with the GCR290-50.	125

7.3	Relative difference to (9 W, 50 Hz) statistical error of the simulated power-frequency combinations shown in Fig. 7.2.	126
A.1	Measurement of the pulse height distribution for four illumination levels.	155
A.2	Differential of Fig. A.1 for the three higher illumination levels. The minimum shows suitable discriminator levels. It can be seen best in the 0.2 illumination and is located between 8 and 10. The illumination level of 0.01 is not shown due to a too low total count rate.	155
A.3	Determination of dead times for a photomultiplier-transient recorder combination. (a) for the elastic signal, (b) for the first rotational Raman channel. In black the scaled analog signal, in colors the photon counting profiles for different dead time corrections. The shape is best matched with the 4.4 ns and 4.8 ns dead time correction, respectively.	157

List of Tables

2.1	Overview of existing temperature rotational Raman lidars with focus on measurements in the lower troposphere	14
3.1	Parameters and chosen AOI of the interference filters. CWL: central wavelength, FWHM: full width at half maximum	41
7.1	System parameters 2007, 2013 and 2014. In red before improvement, in yellow ambiguous states and in green the improved characteristics.	123

Appendices

Appendix A Updated programs and data acquisition

In the course of the thesis it was necessary to update data analysis tools and develop new ones. Data analysis is done with IDL (Interactive Data Language). The data acquisition and programs, written in LabVIEW, were also modified.

A.1 Choice of discriminator level

The discriminator level in the transient recorder determines the voltage level which a peak in the signal from the photomultiplier must excel to be counted as photon. If the level is set too low, noise from the photomultiplier is counted as additional photons; if it is too high, signal is lost. Therefore a level has to be chosen which minimizes both noise and signal loss. The optimum setting is determined by measuring a constant signal with variation of the discriminator level. The procedure is described in the manual from Licel GmbH. The product is the so-called pulse height distribution. In Fig. A.1 such a measurement is shown. The count rate decreases with first increasing steps of the discriminator levels (reduction of noise) and levels out (device noise and signal left) for even higher discriminator levels. The first derivative of that curve shows a minimum for the optimum discriminator setting.

As can be seen in Fig. A.2, the minimum is not clearly located at one specific level, but at least at the same discriminator level range for different intensities of illumination. Based on these measurements a discriminator level of 10 was chosen for further

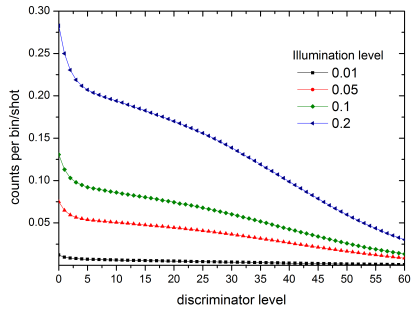


Figure A.1: Measurement of the pulse height distribution for four illumination levels.

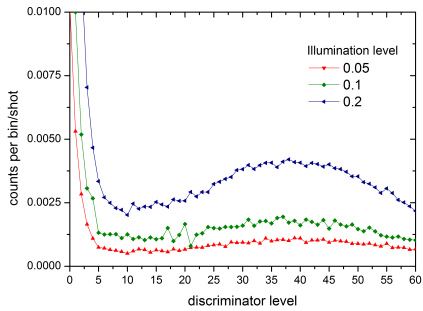


Figure A.2: Differential of Fig. A.1 for the three higher illumination levels. The minimum shows suitable discriminator levels. It can be seen best in the 0.2 illumination and is located between 8 and 10. The illumination level of 0.01 is not shown due to a too low total count rate.

measurements.

A.2 Data Acquisition and beam steering

The transient recorder (LICEL GmbH) was equipped with a new Ethernet controller to reduce the time needed for data transfer to the PC. It took almost 1 s, therefore the time between two 500 shot sequences (10 s summation time) was 11 s. With the updated controller this could be reduced to 0.2 s, so that with a summation over 490 shots the time step between sequential vertical profiles was exact 10.0 s. The LabView-program addressing the scanner was simplified. As the scan pattern for this campaign needed only movements in one angle (elevation or azimuth) at a time, some control steps could be omitted. Before the simplification the program was more than 50% of the time occupied with moving the scanner and not acquiring data, this could be improved to less than 10% time loss due to scanner movement.

A.3 Program to glue analog and photon-counting data

Lidar signals cover a large range in photon count rates. Whereas signals from low altitudes nearly saturate the photomultipliers or avalanche photo diodes, it is single photon counting in higher altitudes. Dividing the signal with two telescope in near and far field and usage of neutral density filters in front of the near field detection (to avoid saturation of the photomultiplier), is one solution. Another method is to apply transient recorders. The signal is recorded not only as single photon counts, if the signal from the photomultiplier exceeds the discriminator threshold, but also as analog signal, which is an integral over the whole signal in one time bin. With this method sampling of high count rates as well as small count rates in the same profile is possible. The analog signal has a comparatively high noise level and is therefore not useful if the mean count rates are very low. For data analysis both signals are combined to have one profile which includes both advantages.

Prior to further data analysis, the photon-counting signal has to be dead-time corrected. We use the approach of a non-paralyzing

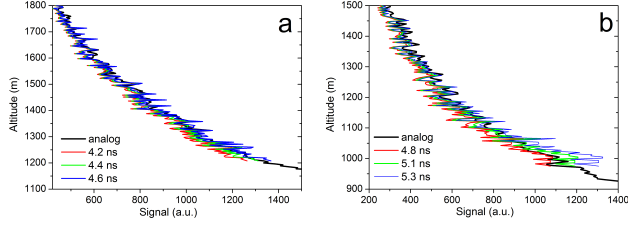


Figure A.3: Determination of dead times for a photomultiplier-transient recorder combination. (a) for the elastic signal, (b) for the first rotational Raman channel. In black the scaled analog signal, in colors the photon counting profiles for different dead time corrections. The shape is best matched with the 4.4 ns and 4.8 ns dead time correction, respectively.

photomultiplier [14]:

$$N = N_c \exp(-N_c \tau), \quad (\text{A.1})$$

with the measured count rate N and the corrected count rate N_c and the dead time τ . The dead time was first measured by the manufacturer of the data acquisition system (LICELE, see also [81]) and they determined 5.55 ns for the Raman channels and 4.1 ns for the elastic channel. Careful reanalysis showed that the actual dead times are 4.8 ns for the RR channels and 4.4 ns for the elastic channel (Fig. A.3). The determination includes a comparison of the slope of the photon counting data, depending on supposed dead time with the slope of the analog signal. In case of correct dead time they should be identical.

Dead time correction works only up to a maximum number of counts, therefore the photon-counting has to be glued to the analog signal for the lower altitudes [103]. The merging itself is done like described in [78]. Background corrected analog and photon-counting signals are compared in an altitude range where both are valid and the analog signal can be expressed as a virtual count rate. Then the profiles are fused with virtual count rates below and photon-counting data above the fusion altitude. This method even gives good error estimates for temperature [17] and water vapor [112] measurements.

Another possibility is to use the method described by [103],

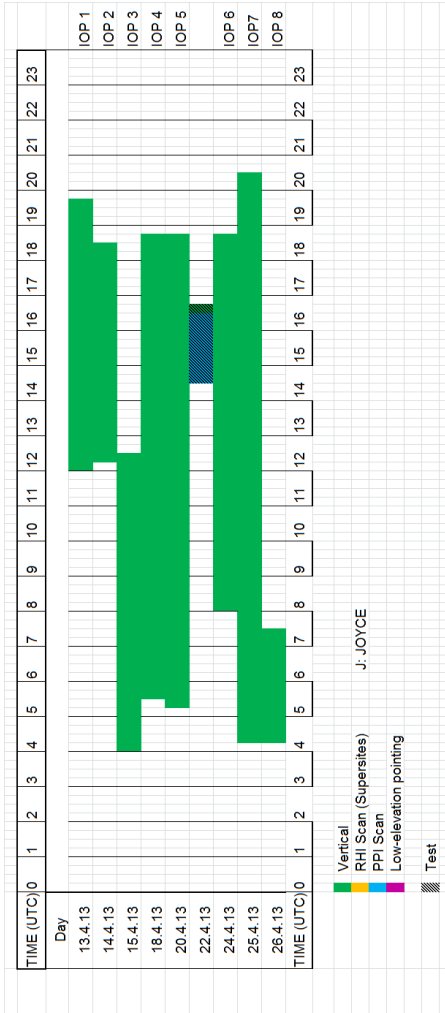
where a maximum likelihood estimation is applied. The lamp mapping technique (LMT) described in [104, 107] is based on the application of a lamp to vary the count number instead of using measured profiles to derive the glue coefficients. It is supposed to be more stable as the effects of solar background and eventual aerosol load are avoided.

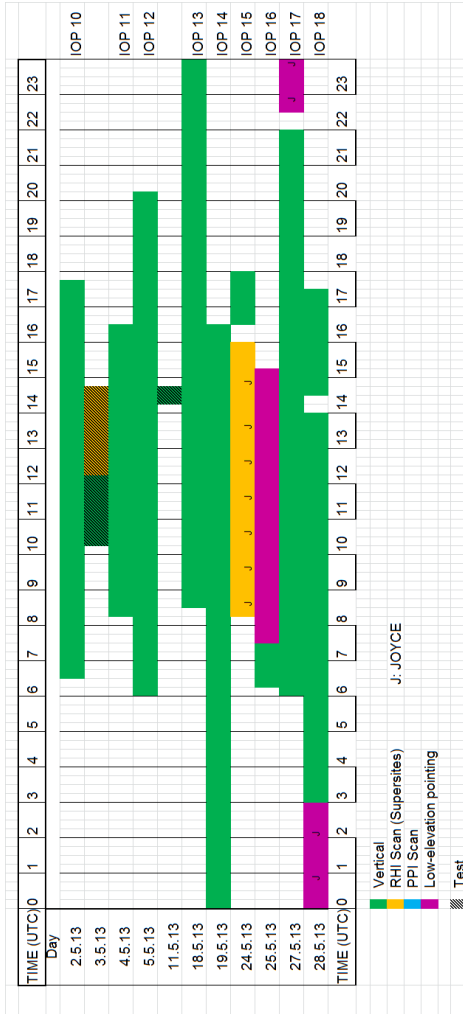
A.4 Retrieval of water vapor mixing ratio

In May 2013 the RRL was upgraded with a detection channel for the vibrational Raman signal from water vapor. While the technique is well established [74, 113, 90, 67], the IDL program for the derivation had to be written and the calibration to a radio sounding established. This was topic of a bachelor thesis [92], which showed that the water vapor mixing ratio can be retrieved in all day-times and also during scans with an average time of several minutes. Another result was that the calibration constant is not as stable as anticipated and that it is therefore advisable to compare lidar and radiosonde profiles regularly. For further analysis including corrections for the different extinctions, the basic program was rewritten and the derivation of absolute humidity was added to simplify the comparison with DIAL data. Results from May 2013 derived with these programs including a comparison with radio sounding can be found in [53]. Even more water vapor measurement days were done in the autumn the same year in Hohenheim (see section 4.4).

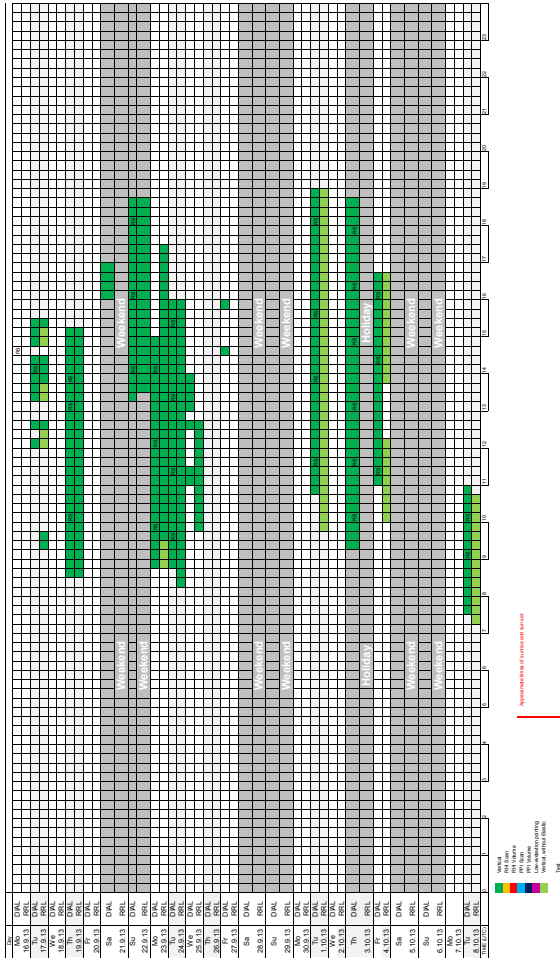
Appendix B Measurement plans

B.1 HOPE, April and May 2013

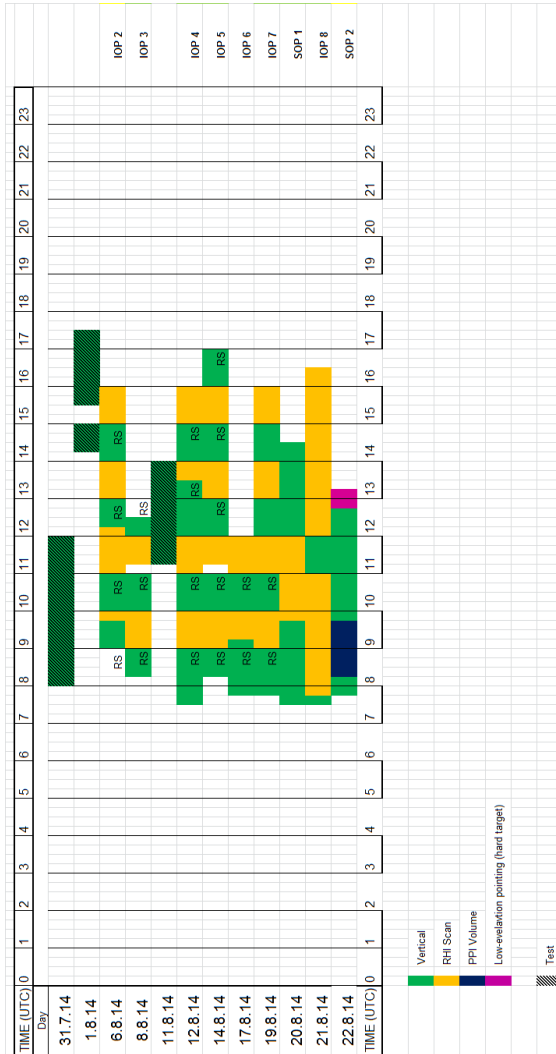




B.2 Hohenheim, September and October 2013



B.3 SABLE, August 2014



Lebenslauf

Eva Maria Hammann
geboren am 31.08.1985 in Stuttgart

- 2011-2016** Doktorandin am Institut für Physik und Meteorologie der Universität Hohenheim
Titel der Dissertation: 'High-resolution measurements of temperature and humidity fields in the atmospheric boundary layer with scanning rotational Raman lidar'
- 2010-2011** Diplomarbeit am 3. Physikalischen Institut der Universität Stuttgart
Titel der Arbeit: 'Temperaturabhängige Rotationen einzelner F_1F_0 -ATP-Synthasen'
- 2008** Auslandssemester an der Universität Oslo, Norwegen
- 2005-2010** Studium im Diplomstudiengang Physik an der Universität Stuttgart
- 2005** Abitur am Friedrich-Schiller-Gymnasium, Marbach am Neckar

Acknowledgments

I would like to thank Professor Volker Wulfmeyer for giving me the opportunity to write a PhD-thesis in the Institute of Physics and Meteorology and to be my advisor. His support was very valuable. Many thanks to Professor Paolo Di Girolamo and Professor Thilo Streck for their readiness to be reviewers of the thesis. Vielen Dank auch an Professor Lutz Graeve für seine Bereitschaft das Dekanat zu vertreten.

I thank Dr. Andreas Behrendt for his guidance he provided as my co-advisor. His knowledge of Raman lidars was of great help. Especially for his support in writing publications I am very grateful. Special thanks to the whole remote sensing team for all their assistance, namely Simon Metzendorf, Florian Späth, Dr. Andrea Riede and Dr. Shraavan Muppa. They were there every time I was too short, too weak or in need of a second pair of hands. Measurement campaigns would not have been possible without you. Thank you very much for making me 'honorary' DIAL team member. There were many good times with you all.

Zudem möchte ich mich bei sämtlichen Mitarbeitern am Institut bedanken, für deren Unterstützung in technischen und Verwaltungsanliegen und für die freundliche Aufnahme.

Vielen Dank an meine Freunde, die mir Mut zugesprochen haben, wenn mal wieder der Laser nicht kooperativ war.

Ein ganz besonderer Dank an meine Familie, für die Möglichkeit zu studieren und zu promovieren. Ohne eure Unterstützung wäre alles nicht möglich gewesen.